Mesospheric Turbulence: The Role in the Creation of Mesospheric Inversion Layers and Statistical Results

Dissertation
zur Erlangung des akademischen Grades
doctor rerum naturalium (Dr. rer. nat.)
der Mathematisch-Naturwissenschaftlichen Fakultät der Universität Rostock

vorgelegt von
Artur Szewczyk,
geboren am 24. May 1981 in Gniezno, Polen
wohnhaft in Rostock

1. Gutachter: Prof. Dr. Markus Rapp,
Ludwig-Maximilians-Universität München

2. Gutachter: Prof. Dr. Gerald Lehmacher,
Clemson University

Datum des Einreichens der Arbeit: 26. Juni 2015
Datum der Verteidigung: 16. November 2015

urn:nbn:de:gbv:28-diss2015-0226-7

Contents

1. Introduction **5**

2. Turbulence **9**
2.1. Energy Spectrum 9
2.2. Characteristic Scales 10
2.3. Strength of Turbulence 12
2.4. Sources of turbulence in the MLT region 13
2.5. In-situ soundings in the MLT region 13
2.6. Theoretical lower limit for the turbulence energy dissipation rate 14
2.7. Theoretical relation between turbulence dissipation rate and variability dissipation rate 18
2.8. Mesospheric turbulence: main questions addressed in this work 19

3. Mesospheric Inversion Layers **21**
3.1. Overview of MIL and its importance 21
3.2. Processes responsible for MIL creation 23
3.3. MIL observations 25

4. New Statistical Turbulence Analysis **27**
4.1. General algorithm for data treatment in wavelet turbulence dissipation rate analysis 27
4.2. Error treatment 32
4.3. Data weighting 34
4.4. Noise level and fitting ranges 39
4.5. Criteria used to distinguish turbulent and non-turbulent spectra 39
4.6. Demonstration of the functioning of the New Statistical Turbulence Analysis using synthetic signals 45

5. Geophysical results **51**
5.1. Simultaneous observations of a Mesospheric Inversion Layer and turbulence during the ECOMA-2010 rocket campaign 51
5.1.1. Campaign overview 51
5.1.2. Experimental results 52
5.1.3. Discussion 60
5.2. New Statistical Turbulence Analysis - results 63
5.2.1. Comparison of ε mean profiles for winter and summer obtained using the new and old analyses 64
5.2.2. Discrepancies between the ε-values obtained using Fourier and wavelet technique 66
5.2.3. Turbulent layer thickness and turbulence layer inhomogeneity 69
5.2.4. Turbulence found in the regions with adiabatic temperature lapse rate 74

5.2.5. ε climatologies for winter and summer . . . 75
5.2.6. Turbulence statistics . . . 79
5.2.7. Summary . . . 82
5.3. Comparison of the experimental and model results . . . 84

6. Summary and outlook **87**
6.1. Summary . . . 87
6.2. Outlook . . . 89

A. Flights list **93**

B. PCM formats description **95**
B.1. Old PCM Format . . . 95
B.2. New PCM format . . . 97
B.3. Wadis PCM format . . . 98

C. The ionization gauges TOTAL and CONE **101**
C.1. Background parameters . . . 103

D. Analysis techniques **105**
D.1. Fourier . . . 105
D.2. Wavelet . . . 105
D.2.1. Wavelet analysis: Definitions . . . 106

E. Experimental relation between turbulence dissipation rate and variability dissipation rate **111**

F. Buoyancy frequency climatology from rocket temperature data **113**

G. Overview of remote atmosphere measurements **115**
G.1. Radar technique . . . 115
G.2. ALOMAR RMR-Na lidar . . . 115
G.3. MLS instrument onoard NASA EOS satellite . . . 116

H. Results from PHOCUS campaign in June/July 2011 **117**
H.1. Campaign overview . . . 117
H.2. Measurements . . . 117
H.2.1. Background atmosphere . . . 117
H.2.2. Turbulence . . . 118
H.3. Summary . . . 120

I. Turbulence occurrence rate and variability during MIDAS/MACWAVE campaign **121**
I.1. Turbulence dissipation rate variability . . . 121
I.2. Turbulence occurrence rate . . . 122

J. ε and temperature profiles for individual flights. **123**

Chapter 1.

Introduction

Phenomenon of turbulence in the the mesosphere/lower thermosphere (MLT) region (roughly from 50 to 120 km) is of great scientific interest. It is responsible for several important atmospheric processes. The momentum transfer from waves to the background flow via turbulence drives a summer-to-winterpole residual circulation, which induces downwelling and adiabatic warming in winter, as well as upwelling and adiabatic cooling in summer. The latter results in the fact that the coldest part of Earth's atmosphere is the polar summer mesopause (e.g., *Lübken*, 1999), a fact that is seemingly counterintuitive. Turbulence also plays a role in the process of vertical redistribution of atmospheric trace constituents and is directly heating and cooling the atmosphere in the processes of turbulent dissipation and turbulent diffusion (e.g., *Liu et al.*, 2000). Turbulence heating can take part in the process of creation of Mesospheric Inversion Layers (MILs) (e.g., *Meriwether and Gerrard*, 2004), which are common phonomena in the MLT region. *Liu et al.* (2000) suggest that process of turbulent heating with high enough heating rates alone can create MIL. Turbulence is also known to take part in the creation of the PMSE, Polar Mesospheric Summer Echoes (e.g., *Rapp and Lübken*, 2004), and is proposed to take part in the creation of the PMWE, Polar Mesospheric Winter Echoes (e.g., *Rapp et al.*, 2011). Despite its significance, turbulence in the MLT region remains one of the least known processes in the Earth's atmosphere. The main reason for this is the fact that turbulence at these altitudes is very hard to investigate, both in-situ and remotely. The turbulence cascade, which is a characteristic feature of turbulence, extends to small scales, in the MLT region down to several meters, hence to investigate it in sufficient detail in-situ measurements are the only possibility. Remote studies of turbulence, i.e. radar turbulence measurements (e.g., *Nastrom*, 1997; *Nastrom and Eaton*, 1997; *Nastrom and Tsuda*, 2001), are still in development and do not possess sufficient resolution to investigate turbulence in high detail.

In-situ measurements of turbulence in the MLT region in polar latitudes have been intensively conducted since 1990 with use of the TOTAL (*Hillert et al.*, 1994) and the CONE (*Giebeler et al.*, 1993) ionization gauges. Due to numerous rocket soundings, it was possible for *Lübken* (1997) and *Lübken et al.* (2002) to make the first statistical analysis of the turbulence measurements in the mesosphere for winter and summer, respectively. These statistics were a landmark in the MLT region turbulence research, despite the fact that the set of in-situ turbulence data used for the analysis was limited to 12 flights for winter and 8 flights for summer, conducted in Andøya Rocket Range (69^o N) and Esrange (68^o N). The mean profiles for winter and summer obtained from these flights by *Lübken* (1997) and *Lübken et al.* (2002) are shown in Fig. 1.1 with blue and red lines respectively. They used Fourier turbulence analysis technique introduced by *Lübken* (1992) which had 1 km altitude resolution. From current theoretical understanding of turbulence in the MLT region it is apparent that this resolution is not enough to investigate turbulence inhomogeneity and turbulence layer thickness in sufficient detail. Theoretical studies, e.g., by *Weinstock*

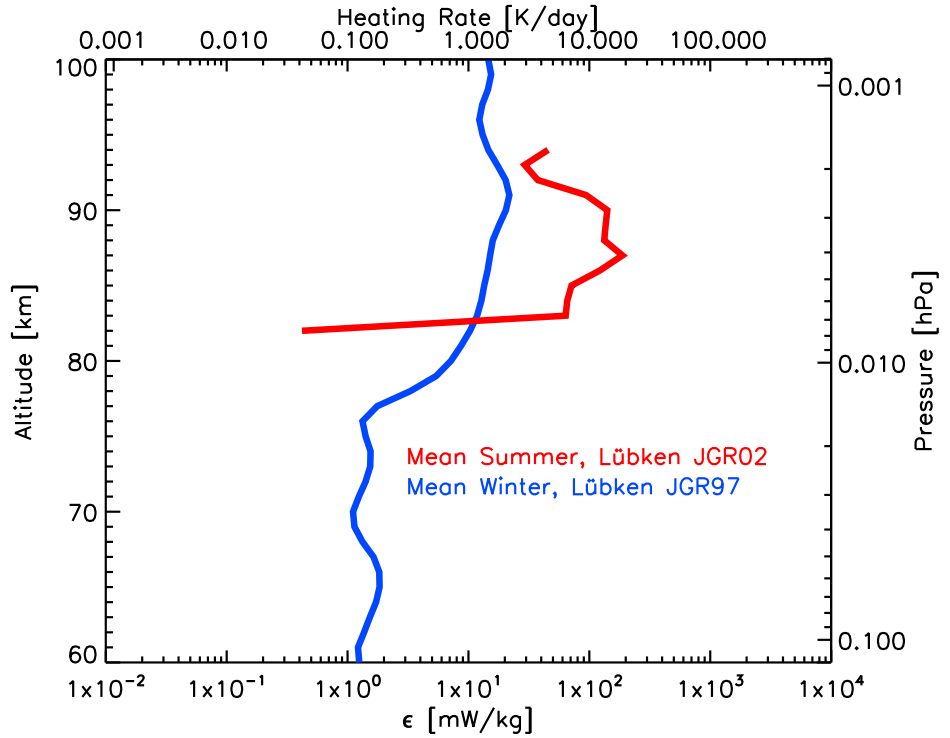

Figure 1.1 Climatologies for turbulence dissipation rate, ε, (heating rate on the top abscissa) obtained at high latitudes by *Lübken* (1997) and *Lübken et al.* (2002) for winter (blue line) and summer (red line) respectively. On the right ordinate approximate atmospheric pressure is shown as a vertical coordinate.

(1978) and *Hocking* (1999), as well as direct numerical simulations made by *Fritts et al.* (2003, 2009a, 2013a,b), suggest that thickness of the turbulent layer can be on order down to tens of meters and as well turbulence exhibits inhomogeneity on these scales. Because of its limited altitude resolution Fourier technique is not able to detect the turbulence layers significantly thinner than its vertical resolution of 1 km. Since publication of *Lübken* (1997) and *Lübken et al.* (2002) a new turbulence analysis technique has been developed, which utilizes wavelet analysis technique (*Strelnikov et al.*, 2003), with improved vertical resolution of 100 m. Also the experimental database was extended by several flights that were conducted since the published climatologies.

This altogether has motivated a new statistical analysis of turbulence measurements in the MLT region, with use of wavelet analysis and extended flights' database. This analysis is the main part of this thesis and is referred here as the New Statistical Turbulence Analysis. To conduct this analysis, several improvements to turbulence derivation technique has been developed. The turbulence dissipation rate, ε, is obtained by fitting theoretical model to the spectrum obtained after wavelet transform of the residuals of neutral density fluctuations measured during a rocket flight. Since the new data set is very extensive (35 flights in the altitude range from 60 to 100 km divided into 100 m altitude bins gives more than 10000 individual spectra to analyze) automatization of the fitting process and derivation of ε-values from the fit has been made. Besides, also improvement in turbulent dissipation rate error, ε_{ERR}, derivation was made, and set of criteria to distinguish between turbulent and non turbulent spectra was established. In the results obtained using the new analysis, which shows

general agreement with the old analysis, several new features were found, including existence of turbulence layers in summer below 82 km, existence of turbulence inhomogeneities on scales of below 1 km, and as well the clear exponential increase of winter ε-values with altitude until the turbopause, which was not found by *Lübken* (1997). Also, the experimental results were compared with the results obtained using KMCM (Kühlungsborn Mechanistic Circulation Model).

Apart from the improvements already mentioned concerning the previous analysis, this work also presents extended turbulence statistics in addition to turbulence mean profiles. The publications of *Lübken* (1997) and *Lübken et al.* (2002), apart from presenting climatologies, were very limited in showing other statistics. These extended statistics can be useful to understand various phenomena in the MLT region. Turbulence occurrence rate statistics are compared with the PMSE and PMWE occurrence rate statistics. Turbulence variation with altitude helps to quantify turbulence processes, and statistics on turbulence layer thickness gives insight into turbulence inhomogeneity. Particularly interesting is the role of turbulence for the creation of MILs. As mentioned, large turbulent heating rates values, on the order of $\approx$ 10 K/h (240 K/day), are thought to create the MIL event itself (*Liu et al.*, 2000). These high ε-values are much higher than the mean profiles presented by *Lübken* (1997) and *Lübken et al.* (2002), and were never found using the Fourier analysis. However using wavelet analysis they are already observed, e.g., during ECOMA09 flight, where a MIL event was accompanied by strong turbulence, with heating rates exceeding 10 K/h (240 K/day). These results are described in the frame of this work (see Sec. 5.1). Once again it has to be stressed that only using in-situ mesurements and spectral analysis with high enough vertical resolution (wavelet analysis in our case) it is possible to detect such high ε-values.

Although significant advances in theoretical understanding of the role of turbulence in the MLT region have been achieved, this work contains very important and comprehensive set of in-situ measurements that consistently supports our current understanding of the significance of MLT turbulence in the atmospheric system.

This thesis is organized as follows. After the introduction, in Chap. 2 description of neutral air turbulence, which is a major topic of this manuscript is given. This part is followed by a short review of our current knowledge of MILs and their possible formation mechanisms, including that by turbulence (Chap. 3). Afterwards, in Chap. 4 description of the New Statistical Turbulence Analysis, including deriving of ε_{ERR} based on weights, procedure of automatically setting fitting ranges and set of criteria to distinguish between turbulent and non turbulent spectra is given. Chap. 5 contains geophysical results. First results obtained during ECOMA09 flight conducted in 2010 in ARR are given, where a MIL with accompanying strong turbulence was detected and investigated. Afterwards turbulence climatologies for winter and summer obtained using the New Statistical Turbulence Analysis, and also extended set of statistics for turbulence obtained in the frame of this analysis is presented. Chap. 6 summarizes the results of this work, which is followed by an outlook to a future use of the obtained results and upcoming rocket campaigns which will investigate the MLT region's turbulence.

Chapter 2.

Turbulence

This chapter presents an introduction of the basic concept and equations, which will help to describe the neutral air turbulence. Also theoretical considerations regarding the measurements of MLT region's turbulence are introduced and discussed here.

2.1. Energy Spectrum

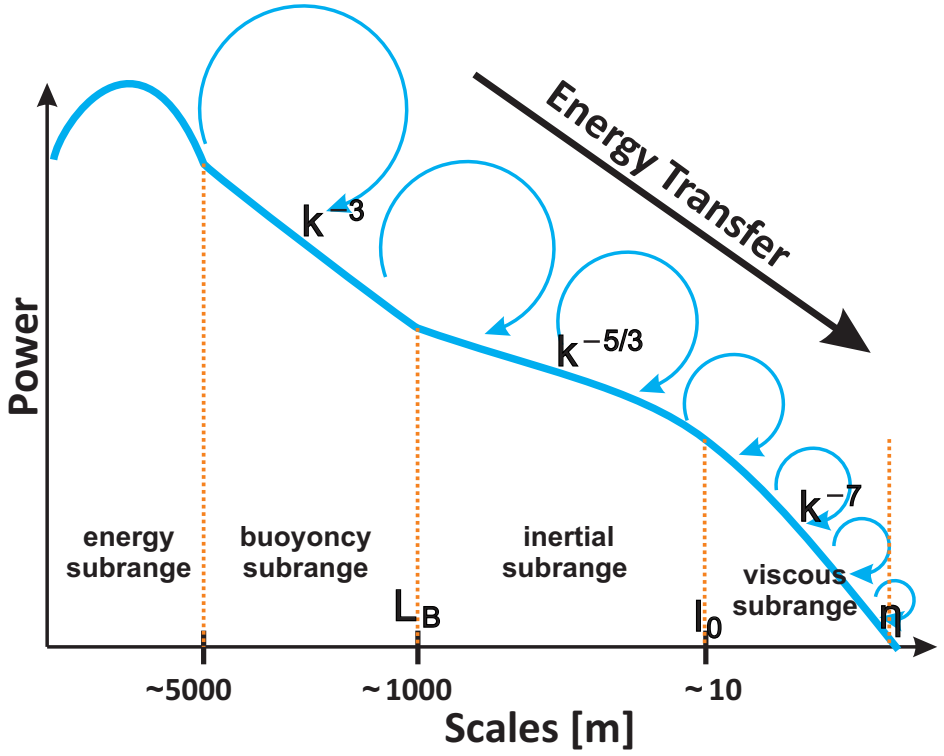

Figure 2.1 Schematic representation of energy spectrum for turbulence (with typical scales for the neutral turbulence in the mesosphere). The inertial and viscous subranges of the spectrum represent the spectral model of *Heisenberg* (1948). In the spectrum characteristic scales for turbulence: turbulence outer scale, L_B, turbulence inner scale, l_0, and Kolmogorov microscale, η, are marked. Both axes are shown on logarithmic scales. The thick black arrow denotes the direction of energy transfer from large to small scales. Circled blue arrows are shown as a convention to denote decreasing size of turbulent eddies along the turbulence cascade.

It is commonly accepted that turbulence gets energy at the low wave number range. The

turbulent kinetic energy is then cascading down to larger wave numbers and, when reaching the wave numbers where viscosity dominates, this energy is dissipated into heat. The kinetic energy distribution in the turbulent flow field can be described by the energy spectrum shown in Fig. 2.1. It shows how the turbulent kinetic energy is distributed over the structures of different scales (eddies of different size, denoted as blue circled arrows in figure). The scales shown for this energy spectrum are typical for the mesosphere. The ordinate shows the power spectral density, P, whereas the abscissa represents the spatial scales of turbulent structures, l, which are related to the wave number as $l = 2\pi/k$. This spectrum can be split into different parts based on the physical processes that dominate at the considered scales. The left-most part of the spectrum (the largest scales) is called energy subrange and is the part where turbulence gets its energy (mainly from gravity waves or wind shear). This acquired kinetic energy is then transferred to the smaller scales by a process generally known as the energy cascade. The next part of the spectrum is called the buoyancy subrange, since buoyancy forces are dominating over viscosity and inertia. The next two and the most important parts for our study are the inertial and viscous subranges. In the inertial subrange the motion of the turbulent eddies is dominated by inertial forces and energy is transported from larger scales to smaller ones by means of vortex stretching due to the non-linear terms in the Navier-Stokes equations (e.g., *Burchard*, 2002). The underlying idea is that a given turbulent eddy is stretched by the shear stress induced by a larger eddy. In the viscous subrange the viscous dissipation plays a significant role: that is, the kinetic energy is dissipated to heat by viscous forces. The inertial and viscous energy subranges are further considered here in more detail, since our measurement technique (as well as most of the turbulent models) deals with these parts of the energy spectrum. A mathematical description of the inertial subrange was first derived by *Kolmogorov* (1941) from dimensional reasoning and is well accepted to be $E(k) \propto k^{-5/3}$ for a one-dimensional spectrum. *Kolmogorov* (1941) also estimated that the viscous part of the energy spectrum should have a much steeper slope. This part can be well described by an exponential law, $E(k) \propto exp(k^{-2})$ (e.g., *Batchelor*, 1953; *Novikov*, 1961; *Tatarskii*, 1971; *Hill and Clifford*, 1978; *Driscoll and Kennedy*, 1983). The energy spectrum in the viscous subrange, however, can also be estimated from the dimensional reasoning, which yields $E(k) \propto k^{-7}$ (*von Weizsäcker*, 1948; *Heisenberg*, 1948). One has to mention that even though the latest is not a mathematically rigorous description of the viscous subrange, it agrees reasonably well with the experimental results.

2.2. Characteristic Scales

The subranges of the energy spectrum are limited by characteristic scales. These scales can be thought of as the sizes of the turbulent eddies. The smallest possible size of a turbulent motion is estimated by the Kolmogoroff scale (smaller eddies are destroyed by the molecular diffusion):

$$\eta = (\frac{\nu^3}{\varepsilon})^{1/4} \tag{2.1}$$

where $\nu = \mu/\rho$ is the kinematic viscosity, μ is the dynamic viscosity, ρ is the mass density of air, and ε is the turbulent energy dissipation rate (described in the next section). The inertial forces, which drive the eddy's motion in the inertial subrange, begin to be dominated by the viscous forces at certain scales. This transition region defines the inner scale, l_0. The

inner scale is defined differently in different models. The inner scales, can be derived from the models of *Heisenberg* (1948); *Tatarskii* (1971); *Driscoll and Kennedy* (1983), which yield (after *Lübken*, 1993):

$$l_0^H = 9.90 \cdot \eta \tag{2.2}$$

$$l_0^T = 7.06 \cdot \eta \tag{2.3}$$

$$l_0^D = 6.66 \cdot \eta \tag{2.4}$$

respectively. The superscript designates the model. By comparing the inner scales of turbulence, one has to refer to the model used for the calculation and (if different models are used) take into account the discrepancy in l_0 values shown above. For equal input parameters, however, these models result in a close η and, subsequently, ε-values because of the slightly different spectral shape in the viscous subrange and within the inertial to viscous subrange transition scales (for comparison of the l_0, η, and ε-values, derived using different models see e.g., *Lübken et al.*, 1993; *Lübken*, 1993; *Giebeler*, 1995). In the frame of this work only *Heisenberg* (1948) model is used, therefore the inner scale is denoted here simply as l_0.

The largest scales within the inertial subrange are defined by the outer (buoyancy) scale, L_B. Various formulas are used in the literature for determination of the buoyancy scale (see e.g., *Weinstock*, 1978; *Lübken et al.*, 1993; *Hocking*, 1999). L_B values presented in the literature are, therefore, ambiguous and have to be considered only as an estimate of this scale. *Weinstock* (1978); *Lübken* (1992, 1993) used the following formula:

$$L_B = 9.97 \cdot \sqrt{\frac{\varepsilon}{N^3}} \tag{2.5}$$

where N is the Brunt-Väisälä (buoyancy) frequency.

In Fig. 2.2 length scales of importance for turbulence in the MLT region obtained in the work of *Lübken* (1993) are shown. Mean free path is denoted as l_{MFP} and given by equation:

$$l_{MFP} = \frac{k_B \cdot T}{\sqrt{2} \cdot \pi \cdot d^2 \cdot p} \tag{2.6}$$

where k_B is the Boltzmann constant, T is the temperature, p is pressure, and d is the diameter of the gas particles in meters. The atmospheric background parameters were taken from CIRA-1986 for March, 70 °N. A constant energy dissipation rate of $\varepsilon = 0.1$ W/kg was assumed at all altitudes. The inertial subrange is shown as hatched area.

In Fig. 2.2 it can be seen that the typical length scales of the smallest turbulent eddies (Kolmogorov scale, η) in the MLT region vary from tens of centimeters to tens of meters. The inner scale, l_0, of MLT turbulence can vary from meters to hundreds of meters. The estimate of the outer (buoyancy) scale, L_B, gives values from hundreds of meters to some kilometers for ε-values exhibiting in the mesosphere (L_B value in the figure is shown for constant ϵ value, hence it does not change with the altitude).

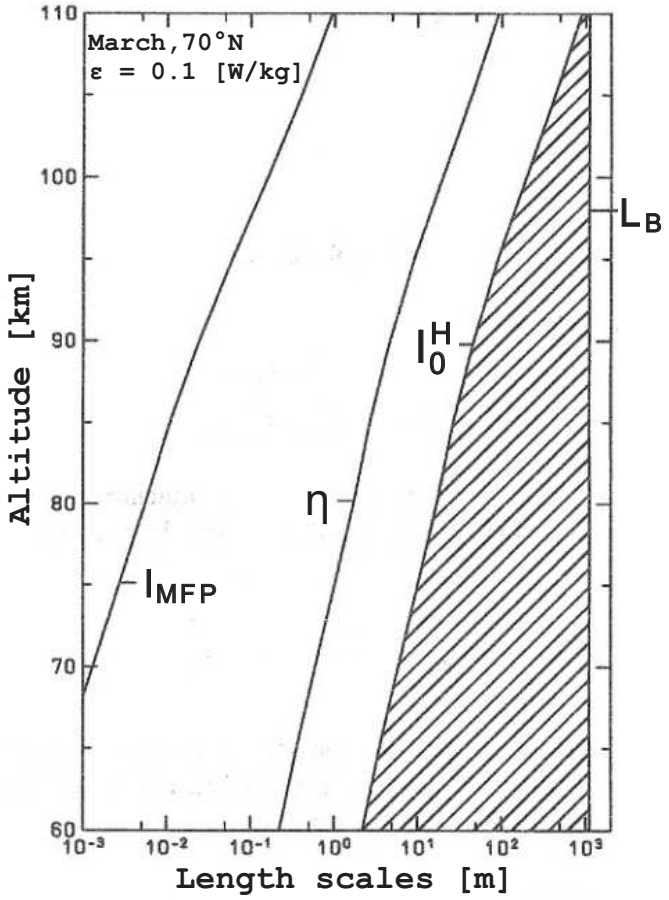

Figure 2.2 Length scales of importance for turbulence (after *Lübken*, 1993): L_B: outer scale; l_0^H: inner scale; η: Kolmogoroff microscale, l_{MFP}: mean free path. The atmospheric background parameters are taken from CIRA-86 (March, 70 °N, *CIRA Working Group* (1992)). A constant energy dissipation rate of $\varepsilon = 0.1$ W/kg was assumed at all altitudes. The inertial subrange is shown as hatched area.

2.3. Strength of Turbulence

The turbulent energy dissipation rate, ε, describes the rate at which the kinetic turbulent energy is transferred into heat. By using this quantity the influence of turbulence on the mesosphere can be quantified. ε is defined as (e.g., *Landau et al.*, 1961):

$$\varepsilon = \frac{\nu}{2}\overline{(\frac{\partial u_i}{\partial x_j})^2} \tag{2.7}$$

where, u_i is i-th component of the velocity, and x_j is the j-th Cartesian coordinate. This quantity can also be converted to heating rate, which is considered to be an equivalent characteristic:

$$Heating\ Rate \equiv \frac{\partial T}{\partial t} = \frac{\varepsilon}{c_p} \tag{2.8}$$

where $c_p \approx 1004$ J kg^{-1} K^{-1} is the heat capacity of air at a constant pressure.

Turbulence can also be described in terms of eddy diffusion, which is analogous with the molecular diffusion. This introduces the turbulence (eddy) diffusion coefficient for momentum, K, which is discussed in more details in Sec. 2.6.

2.4. Sources of turbulence in the MLT region

Gravity wave breaking and Kelvin-Helmholtz shear instability are believed to be the two major sources of turbulence generation in the MLT region (see e.g., *Fritts et al.*, 2003). These two sources share common characteristics related to turbulence transition, evolution, and duration, and they exhibit a number of differences that have important implications for atmospheric observations at mesopause altitudes and for layered structures. Common features related to layering include a clear spatial separation of the maxima of turbulent kinetic energy dissipation and thermal dissipation accompanying vigorous turbulence, as well as sharp local gradients in turbulent kinetic energy production, dissipation, and magnitude (*Fritts et al.*, 2003). Differences arise because gravity wave breaking leads to a maximum of turbulence activity that moves with the phase of the wave (*Fritts et al.*, 2003; *Achatz*, 2005), whereas shear instabilities cause turbulence and mixing confined by stratification to a narrow layer. As a result, the effects of turbulence due to shear instability likely persist for much longer time than those of turbulence due to gravity wave breaking (see e.g., *Müllemann et al.*, 2003, where different sources of MLT turbulence were experimentally identified).

2.5. In-situ soundings in the MLT region

Experimental studies of turbulence at the northern latitudes in the MLT region have been intensively conducted since 1990. Due to numerous rocket soundings, the observational data base of the in-situ measured turbulence parameters has grown (list of all the flights that investigated the turbulence at polar latitudes is given in App. A).

Lübken (1997) and *Lübken et al.* (2002) made the first statistical analysis of turbulence in the atmosphere in the winter and summer respectively. For this analysis, the set of in-situ turbulence data was limited to 12 flights for winter and 8 flights for summer period, conducted in Andøya Rocket Range, (69^o N) and Esrange, (68^o N, 2 summer flights only). The mean profiles for winter and summer obtained from these flights are shown in Fig. 1.1. It is worth to note, that these in-situ measurements also show that turbulence appears in layers with a typical vertical extent of several kilometers. The results of the turbulence measurement contained in these statistics yielded the following:

- ε profiles with vertical resolution of one kilometer derived from the in-situ measurements of neutral density fluctuations
- Estimate of characteristic scales of mesospheric turbulence
- Comparison of the results deduced from the measurements of the different tracers: plasma and neutrals
- Comparison of the results deduced using different methods and spectral models

At the moment of the publication of turbulence statistics for winter and summer by *Lübken* (1997) and *Lübken et al.* (2002) the brief status of the knowledge about mesospheric turbulence was the following (after *Strelnikov*, 2006)):

- At polar latitudes in summer, turbulence always exists around the mesopause heights
- Typical turbulence energy dissipation rates lie within the range 0.5 - 200 mW/kg (heating rate $\approx$ 0.05 - 20 K/d)
- The corresponding inner scales, l_0, range from $\approx$ 10 to $\approx$ 50 m. Kolmogoroff microscale, η, from $\approx$ 1 to $\approx$ 5 m
- The vertical extent of a single turbulent patch varies from at least 1 km (vertical resolution of the measurements technique) to $\approx$ 9 km
- At polar latitudes, the entire region of the turbulence activity in summer is confined to the altitudes from 82 to 95 km. In winter it extends over the whole measurements area, from 60 to 100 km

In the current thesis, new statistical turbulence analysis is made, using the wavelet analysis technique in place of the Fourier analysis technique used by *Lübken* (1997) and *Lübken et al.* (2002). One of the advantages of the wavelet technique is better vertical resolution of the ε measurements. For the statistics, data set of 35 flights (16 for winter and 19 for summer) was used (App. A). This new analysis can further address the questions regarding turbulence in the MLT region (see Sec. 2.8).

2.6. Theoretical lower limit for the turbulence energy dissipation rate

From physical considerations there should be a minimal limit for ε. This limit was proposed by *Lübken* (1993) to be:

$$\varepsilon_{min} = \nu \cdot N^2 \tag{2.9}$$

There are two physical explanations for this limit:

- the turbulent diffusion coefficient, K, cannot be smaller than the the molecular diffusion coefficient, D, because the molecular diffusion would destroy turbulent eddies immediately (*Lübken*, 1993)
- the turbulence inner scale, l_0, cannot be larger than the turbulence outer scale, L_B, which would mean that there is no inertial subrange in the turbulence spectra (*Strelnikov*, 2006)

In this section we will discuss if this limit is a precise analytical definition and show that it is derived theoretically using coefficients and relations that are oversimplified and should not be applied for each measured ε value. We will also present experimental results for the energy dissipation rate, ε, available in the literature, which are significantly below this theoretical limit.

Theoretical assumptions

For deriving eq. 2.9 *Lübken* (1993) uses equation given by *Weinstock* (1978):

$$K = 0.81 \cdot \frac{\varepsilon}{N^2} \tag{2.10}$$

Lübken (1993) notices that the turbulent diffusion coefficient K cannot be smaller than the molecular diffusion coefficient D. Therefore:

$$K_{min} \approx D \tag{2.11}$$

Since in the atmosphere $D \approx \nu$ (e.g., *Lübken*, 1993), this also gives a lower estimate for ε:

$$\varepsilon_{min} \approx K_{min} \cdot N^2 \approx \nu \cdot N^2 \tag{2.12}$$

Eq. 2.10 is derived by *Weinstock* (1978, eq. 31b). This equation comes from the relation for diffusion by inertial subrange turbulence (i.e. isotropic, homogeneous and stationary turbulence) proposed by *Zimmerman and Loving* (1975):

$$K = \alpha^{1/2} \cdot C_1 \cdot C^{-4/3} \cdot \left(\frac{\varepsilon}{N^2} \right) \tag{2.13}$$

where $\alpha \approx 1.5$ is Kolmogoroff constant, C_1 is an undetermined constant that occurs in *Heisenberg* (1948) dimensional relation for K, and C is coming from *Lumley* (1964) and *Shur* (1962) buoyancy transition wavelength. Constant C_1 is derived in the process of absolute evaluations of the Lagrangian velocity correlation function (*Weinstock*, 1978). Constant C is determined analytically by a modification of the Lumley-Shur theory by *Weinstock* (1978) to be $C \approx \alpha^{-3/2} \approx 0.62$ for stably stratified fluids. It can be seen that the expression for ε_{MIN} (Eq. 2.9) depends on the determination of the constants included in eq. 2.13 ($\alpha^{1/2} \cdot C_1 \cdot C^{-4/3}$).

General appliance of eq. 2.13 was addressed by *Hocking* (1999). He discussed the assumptions for the middle atmosphere turbulence case made in developing this formula. *Hocking* (1999) remarked that eq. 2.13 appears to be exquisitely simple, yet hides a multitude of complexity. It raises many issues, e.g.,is the derivation too simplistic? Is it valid at all? If it is valid, what should be the "constants" $\alpha^{1/2} \cdot C_1 \cdot C^{-4/3}$? *Hocking* (1999) did not dwell too much on the actual value of these constants. Rather than asking the question what this value is, he asked whether eq. 2.13 applies at all. He pointed out that the methods by which diffusion can take place are far more complex than simple three dimensional turbulent diffusion as assumed in derivation of eq. 2.13. As reasons for this fact he pointed out two main factors: first, turbulence is very intermittent both temporally and spatially, and very often occurs in thin layers in the middle atmosphere. These thin layers are often separated by regions which are either only weakly turbulent or even laminar (as it is discussed in Sec. 5.2.3). Secondly, the processes which induce diffusion can themselves be scale-dependent.

Hocking (1999) concluded by simply noting that the relation between rates of diffusion and energy dissipation rate, eq. 2.13, is not simple as was assumed by *Weinstock* (1978) and in fact is both scale and species dependent. This is still an area which deserves much research, and the key point to note is that the visualizations and parameterizations of these processes have been grossly oversimplified in the past. Therefore, proposed ε_{MIN}, which is derived directly from this equation, is not a precise analytical definition and should not be applied to each individual measured ε value.

Another way of deriving the lower limit for ε is to compare the outer and inner scales of turbulence, L_B and l_0 respectively, as it was done by *Strelnikov* (2006). The equation for L_B, eq. 2.5, is derived there with the use of the relation from *Weinstock* (1981) (eq. 2.14 given in the next section), where the constant C also appears (doubts about the appliance of this constant are discussed above and in the next section).

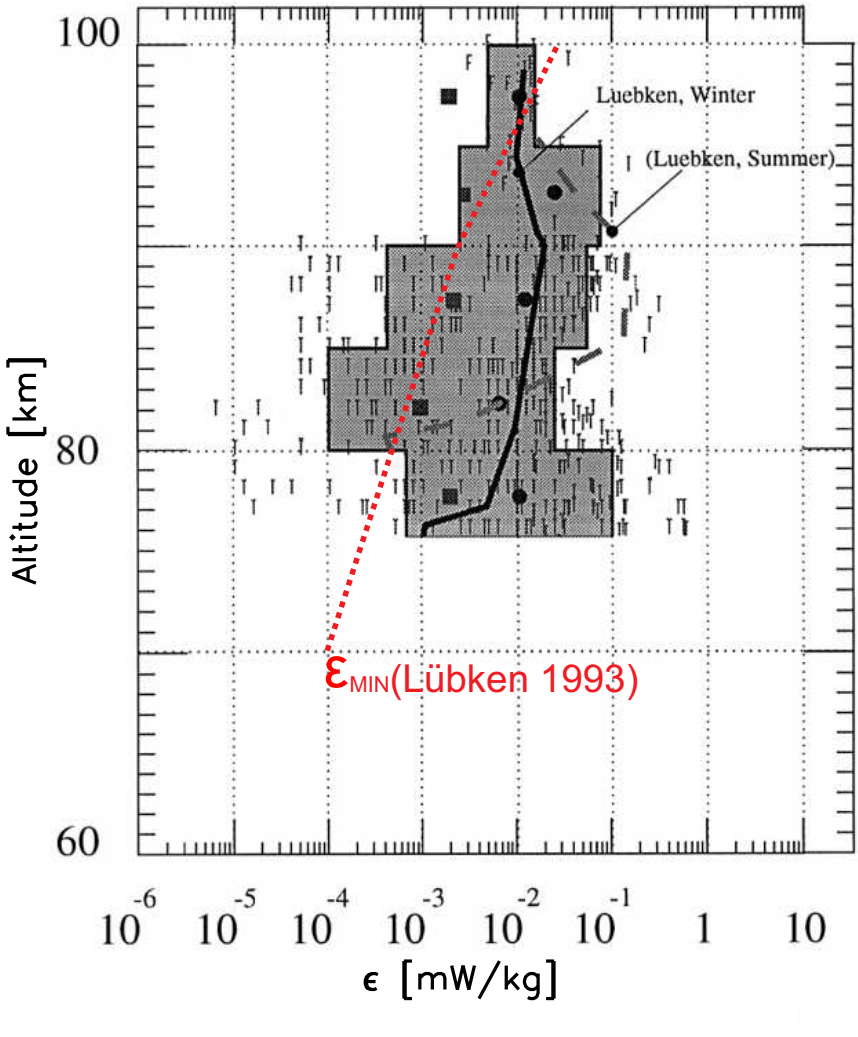

Figure 2.3 Energy dissipation rates from *Dickinson et al.* (1985), *Lübken et al.* (1987), *Blix et al.* (1990) gathered and rescaled by *Hocking* (1999). Rescaled raw data are shown by "T" symbols. The filled squares show median values of ε given by the authors. The solid circles show median values re-calculated using theory presented in *Hocking* (1999). The dashed gray and solid black lines show ε mean values from *Lübken* (1997) for summer and winter respectively. The red, dotted line showing the ε_{MIN} limit from *Lübken* (1993) was sketched by the author for comparison. For more details see *Hocking* (1999)

Experimental results

The in-situ measured values for the turbulence dissipation rate, ε, were presented in the past in several articles. *Hocking* (1999) gathered data presented by *Dickinson et al.* (1985), *Lübken et al.* (1987) and *Blix et al.* (1990) and rescaled these data to present it together in one plot (Fig. 2.3). In this plot the mean values for winter and summer from *Lübken* (1997) are shown as black solid and grey dashed lines, respectively. ε mean values for summer presented in *Lübken* (1997) are obtained from the same data set with a different statistical approach as the mean values for summer obtained in *Lübken et al.* (2002) and differ only slightly from the latter. The median values of ε given by authors listed above are shown

as filled black squares and median values obtained using theory given by *Hocking* (1999) are shown as black filled circles (these values are not discussed here). The red dotted line showing the ε_{MIN} values from *Lübken* (1993) is drawn for comparison only. The individual measured values of ε from the three works mentioned above are shown as "T" symbols and are of particular interest for us. It can be noted, that the measured ε exhibit values of up to two orders of magnitude below the theoretical ε_{MIN} limit.

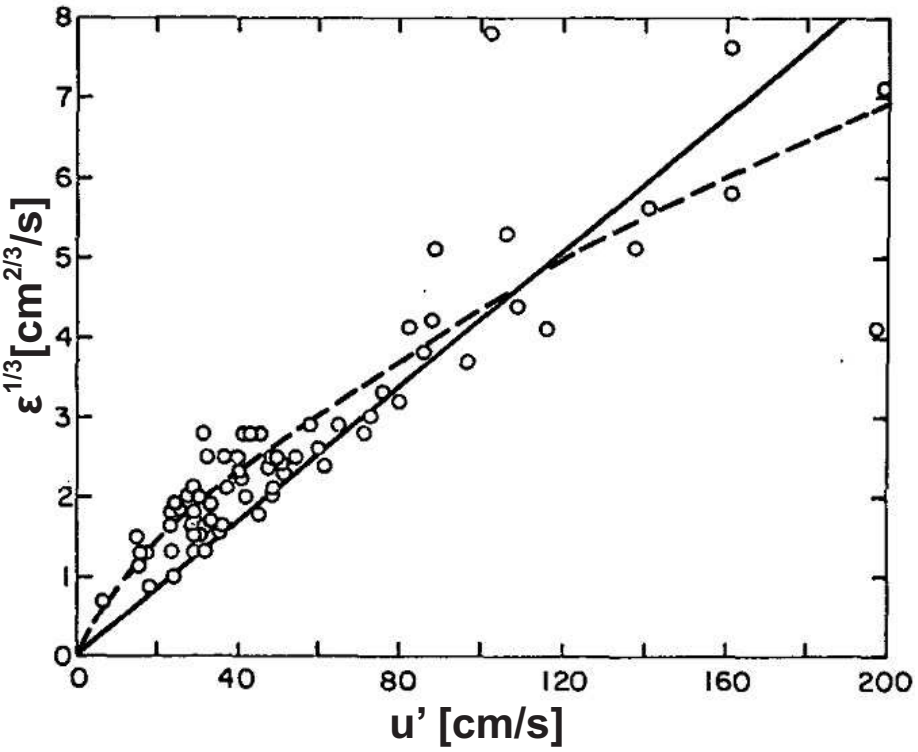

Figure 2.4 Graph of $\varepsilon^{1/3}$ vs u' reproduced from *Heck and Panofsky* (1975). The circles represent observations, the dashed line represents a fit of eq. 2.14 with $C = 0.37$. The solid line represents other fit which is not discussed here.

.

Weinstock (1981) discusses an other issue. He uses data from the project HICAT (High Altitude Clear Air Turbulence) (*Crooks*, 1967) to provide an empirical value for constant C and discuss applicability of the C to the atmospheric diffusion and clear air turbulence. The resulting value of $C \approx 0.37$ is comparable with the theoretical value discussed in the previous subsection. This empirical value of C was derived by fitting equation:

$$\varepsilon = C \cdot (u')^2 \cdot N \tag{2.14}$$

where u' is the variance of vertical velocity, to the set of turbulence data obtained from the HICAT project for upper troposphere/lower stratosphere. This fit is shown in Fig. 2.4 reproduced from *Heck and Panofsky* (1975). Note different scales of ε and u' in Fig. 2.4 and Eq. 2.14. The circles represent observation values, the fit of eq. 2.14 is shown as a dashed line for $C = 0.37$. The solid line represents another fit which is not discussed here. It can be seen in Fig. 2.4 that there exist particular ε-values, especially for the small u' values, which

are up to one order of magnitude smaller than the values for the fitted equation. This means that, according to eqs. 2.14, 2.13, and 2.12, particular C, K and ε_{min} values, respectively, could be lower by the same magnitude. It is worth to note that *Weinstock* (1981) did not question the possibility of the low ε-values obtained in this experiment. The possibility that the C constant is significantly lower than the theoretical value derived by *Weinstock* (1978) additionally gives weight to the statements about eq. 2.13 and the derivation of the constants it contains, which are discussed in previous subsection.

The experimental results discussed above further confirm that the expression for ε_{MIN} should not be applied as a strict limit for atmospheric turbulence data. There are several published, experimentally determined ε-values well below the ε_{MIN} limit. Also, constant C obtained by fitting into experimental data from *Heck and Panofsky* (1975) can have significantly lower values.

Summary

From the considerations above, it can be stated that the expression for ε_{MIN}, proposed by *Lübken* (1993), while good as approximation for ε limit, should not be used as a strict limit for individual experimentally measured ε-values. This limit was derived using theoretical assumptions, which are valid only for stably stratified atmosphere with the inertial subrange and are found by *Hocking* (1999) to be oversimplified for a general atmospheric case. The comparison of the experimental results made by *Weinstock* (1981) and *Hocking* (1999) shows that indeed ε-values below this limit were already measured and were not questioned by the authors. Note also, that from the definition of turbulence energy dissipation rate (eq. 2.7), there is no global minimum in the ε-field. Based on this conclusion, in the presented work we will show the full scope of the derived ε-values, and not ignore the smallest ones, i.e. $\varepsilon < \varepsilon_{MIN}$. To increase the confidence in derived ε-values a rigorous error discussion is presented in Sec. 4.2.

2.7. Theoretical relation between turbulence dissipation rate and variability dissipation rate

Variability dissipation rate for tracer θ, abbreviated in this work as N_θ, is the rate at which fluctuations of the tracer θ are destroyed by molecular diffusion. This is analogous to velocity fluctuations dissipated into heat. Turbulence dissipation rate, ε, and variability dissipation rate, N_θ, can be compared using two equations from *Lübken* (1993):

$$C_n^2 = \frac{a^2 \cdot N_\theta}{\varepsilon^{1/3}} \tag{2.15}$$

and

$$\varepsilon = \left(\frac{Pr^{tur}}{f_\alpha \cdot a^2 \cdot B \cdot Ri} \right)^{3/2} \cdot (C_n^2)^{3/2} \cdot \left(\frac{g}{N} \right)^3 \tag{2.16}$$

where a is a numerical constant discussed in *Lübken* (1993), factor B considers the degree of anisotropy and can have values between 1 (horizontally stratified) and 3 (isotropic), Pr^{tur}

is a turbulent Prandtl number, f_α is normalization constant discussed in *Lübken* (1993), C_n^2 is structure function constant, g is acceleration due to gravity.

After inserting C_n^2 from Eq. 2.15 into Eq. 2.16 we obtain:

$$\varepsilon = \left(\frac{Pr^{tur}}{f_\alpha \cdot a^2 \cdot B \cdot Ri}\right)\left(\frac{g^2}{N^2}\right) \cdot a^2 \cdot N_\theta \tag{2.17}$$

Now by applying to eq. 2.17 different constants' values available in the literature, one can set theoretical limits of ε in terms of N_θ.

Range of values for expression:

$$\left(\frac{Pr^{tur}}{f_\alpha \cdot a^2 \cdot B \cdot Ri}\right)^{3/2} \tag{2.18}$$

is discussed by *Lübken* (1993) and is found to be between 0.056 and 19. Therein, the values for B vary from 1 to 3 as already mentioned, Pr^{tur} vary from 1 to 5, Ri vary from 0.25 to 0.81, $a^2 = 2.8$ and $f_\alpha = 1$. Further, after *Lübken* (1999), N value in the mesosphere varies from 0.015 to 0.030. After substituting maximum and minimum values for the constants mentioned above into eq. 2.17 we obtain a theoretical limit for ε in terms of N_θ:

$$\varepsilon \in (10^4 : 10^7) \cdot N_\theta \tag{2.19}$$

The dependence of ε on N_θ obtained from experimental data in the frame of this thesis is given in App. E.

2.8. Mesospheric turbulence: main questions addressed in this work

There are still many open questions regarding turbulence in general. The intention of this work is to deduce the geophysical implications of the neutral air turbulence in the dynamics of the MLT region. In this work new turbulence climatologies are derived. Also extended turbulence statistics for the MLT region are made. This allows a qualitative scale analysis (i.e. statistics for turbulence layer's thickness), and makes a quantitative study of the MLT region's turbulence possible (i.e. statistics of turbulence variability with altitude). It also gives a better insight of the questions regarding morphology of the MLT turbulence (i.e. turbulence inhomogeneity).

In this work the following problems for the turbulence in the MLT region are addressed:

1. Turbulence climatologies for winter and summer periods based on in-situ data are derived

2. Turbulence layer thickness and turbulence inhomogeneity. With an improved vertical resolution of the wavelet turbulence analysis, it is possible to investigate these issues in more detail

3. Possibility of turbulence occurrence below 82 km in summer. In the climatologies shown by *Lübken et al.* (2002) for the summer period turbulence was never observed below this altitude

4. Turbulence connection to various phenomena in the MLT region, one of them are Mesospheric Inversion Layers (MIL), e.g., *Meriwether and Gerrard* (2004) and Chap. 3 of this work

5. Polar Mesospheric Summer Echoes (PMSE) occurrence rate is compared with turbulence occurrence rate for summer obtained using data set consisting of all the flights available until year 2014, and as well Polar Mesospheric Winter Echoes (PMWE) occurrence rate is compared with turbulence occurrence rate for winter

This manuscript contains an important set of in-situ measurements that consistently supports our current understanding of the significance of MLT region's turbulence in the atmospheric system. It has important geophysical implications that will be discussed in further sections.

Chapter 3.

Mesospheric Inversion Layers

Since first observed by *Schmidlin* (1976), Mesospheric Inversion Layers (MIL) have been routinely observed in the MLT region. A most recent review of both theory and observations has been provided by *Meriwether and Gerrard* (2004). These authors have pointed out that despite of the considerable progress that has been made in recent years, the formation mechanisms of the MIL remain poorly understood. Numerous observations show that temperature inversions are often associated with a near adiabatic lapse rates above the inversion layer (*Whiteway et al.*, 1995; *Duck et al.*, 2001), which is clearly indicative of turbulence activity in those regions. The numerical simulations showed that only vigorous turbulence revealing heating rates of ~ 10 K/h is capable of producing temperature inversions (*Liu et al.*, 2000). Such a strong turbulence, nonetheless, had rarely been observed (see, e.g., *Lübken*, 1997; *Lübken et al.*, 2002) before in contrast to MILs, which are common phenomena. However, re-analysis of all the turbulence rocket data with the wavelet technique, which is part of this work, shows that the MLT region does exhibit many turbulent layers with much higher turbulence dissipation rates, ε, than previously observed. Particularly, during the ECOMA09 flight strong turbulence accompanying a two layered MIL event was observed and described by *Szewczyk et al.* (2013). These results are described in Sec. 5.1. The small amount of high ε-values in the previous Fourier turbulence analysis is caused by the fact that the spatial resolution of this analysis was 1 km. As the turbulence is intermittent and inhomogeneous at scales much smaller than 1 km (e.g., *Hocking*, 1999), this caused smoothing of the highest ε-values.

In this chapter we review out current knowledge regarding Mesospheric Inversion Layers, its importance, the mechanism of its creation and its classification will be presented after *Meriwether and Gerrard* (2004).

3.1. Overview of MIL and its importance

The MIL is found as a layer ≈ 10 km vertically thick within the upper mesosphere with an amplitude of 30 - 50 K that is superimposed upon the characteristically decreasing temperatures of the upper mesosphere. This phenomenon occurs quite often, especially in the midlatitude winter hemisphere, is observed to have a broad horizontal distribution thousands of kilometers in scale, and may last for many days. Fig. 3.1 depicts a schematic showing a typical structure of a MIL profile as might be observed with a Rayleigh or Na lidar system capable of measuring vertical temperature profiles. There the temperature profile for the MLT region with (solid line) and without (dotted line) typical "upper" and "lower" MIL is shown. Almost always, on the topside of the MIL a lapse rate that is nearly as steep as the adiabatic lapse rate will exist. The MIL may appear in the MLT region at any time of the year. The discovery of the thermal feature, which was called an inversion layer, was first reported without explanation by *Schmidlin* (1976). The name "inversion layer" was given

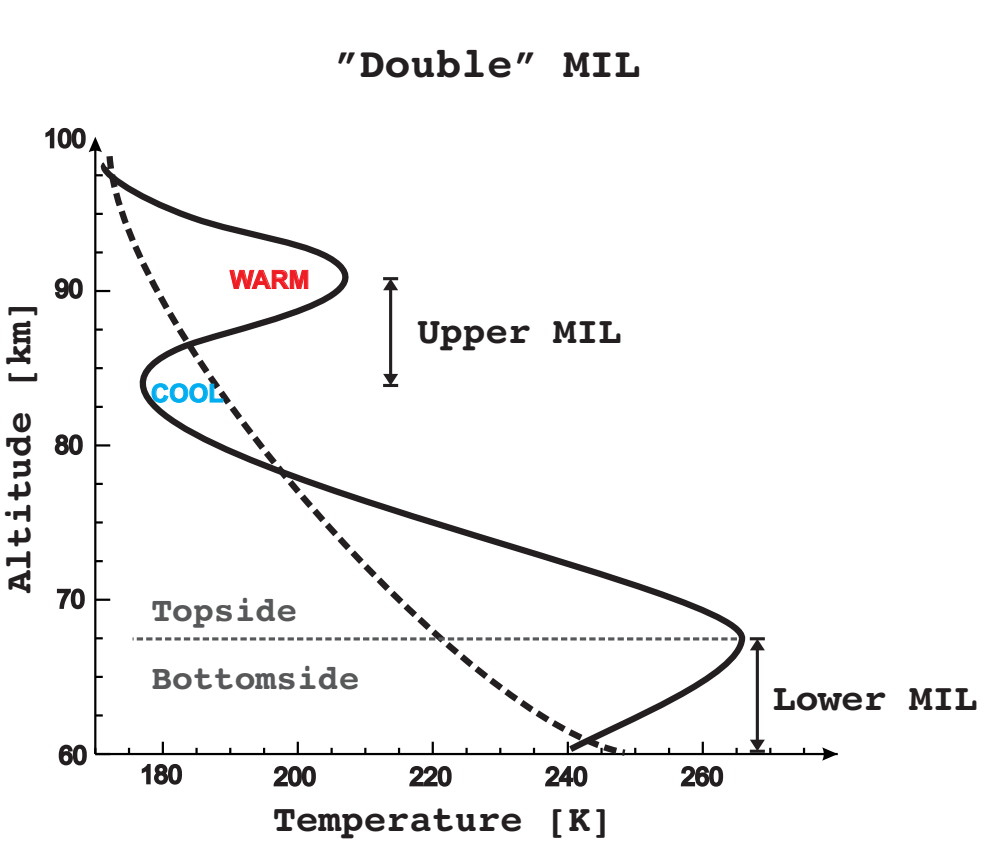

Figure 3.1 Illustration of the temperature profile for the MLT region with (solid line) and without (dotted line) typical "upper" and "lower" mesospheric inversion layers.

to the observed event because its appearance was so similar to that of the "inversion layers" seen in tropospheric profiles of temperature near the ground (*Meriwether and Gerrard*, 2004).

For the MILs, *Meriwether and Gerrard* (2004) reported about two well known MIL types. The first one, named "upper" MIL, tends to occur above 85 km. One of the hypothesis of its origin is that this MIL type originates from large-amplitude tidal waves propagating into the mesosphere and their subsequent nonlinear interactions with the gravity waves, which can often create the appearance of a "double MIL" separated by approximately one vertical tidal wavelength ($\approx$ 25 km). As other mechanism for the formation of this type of MIL strong turbulence is proposed (*Liu et al.*, 2000). The other subtype of MIL, named "lower MIL", is formed by a climatological planetary wave dissipation mechanism that occurs at a zero-wind line. The dissipation of the planetary wave tends to generate a mesoscale ($\approx$ 1000 km) inversion layer in the range of 65 - 80 km. These two formation mechanisms explain most of the observed characteristics, including reason behind the downward progression of some MILs and not others, the relative scarcity of MILs observations at high latitudes, and the different climatological nature of the two forms of MIL events.

Understanding MIL phenomena is important for the understanding of middle-atmosphere dynamics for two primary reasons: stability and energy transfer. Addressing the stability: at the bottom side of the thermal layers (where the temperature profile increases in altitude) the positive temperature gradient signifies an increase in atmospheric stability. In contrast, at the topside of the thermal layer the negative temperature gradient implies a reduction in

atmospheric stability to the point that the atmosphere may become convectively unstable. This can possibly support the development of turbulence (*Meriwether and Gerrard*, 2004). The MLT is a region of transition between the region of free molecular flow and a region where the hydrodynamical fluid equations apply. The physics of such a transition region is complicated even without the mechanisms like MIL, that makes this medium less stable on a mesoscale level and add a significant degree of complexity to the fluid dynamics of this region. Such instabilities are contributing to the production of atmospheric phenomena including that of atmospheric bores and mesospheric radar echoes. The vertical mixing associated with such disturbed circulation can suppress the otherwise downward ageostrophic flow, transport oxygen-containing species to ever higher altitudes, and potentially weaken the global polar vortex. Understanding the birth, evolution, and dissipation of MIL is a major modeling challenge, partly because the problem demands the modeling of the atmosphere's three-dimensional structure and also because it is very time-dependent (*Meriwether and Gerrard*, 2004).

It is known that the breaking of atmospheric waves represents the primary means by which energy is transferred from the lower atmosphere to the upper atmosphere. Such waves have horizontal wavelengths ranging from high wave numbers (several kilometers) to low wave numbers (3000 - 5000 km). The MLT region is the primary region where these waves break, and the amount of energy transferred into the mesosphere is known to be comparable with the amount of energy absorbed from the Sun there (e.g., *Lübken*, 1997). It had been believed for many years that the MIL phenomenon represents a marker of these breaking waves, but, in fact, recent research has shown that the MIL mechanism is far more complicated than this description implies (*Meriwether and Gerrard*, 2004). There are also several other reasons that provide additional motivation for achieving an understanding of MIL phenomenology. There is the question of the MIL influence upon the vertical profile distribution of airglow layer intensities for those emissions in which the chemical reaction rate constants are temperature-dependent. In addition, the study of MIL phenomenology gives insight into the possible effect of non-migrating tidal forcing upon the variability of tidal wave amplitudes and phase, and on how tidal waves variability depends upon gravity wave and planetary wave interactions, as well (*Meriwether and Gerrard*, 2004).

3.2. Processes responsible for MIL creation

The "upper" MIL

"Upper" MILs are those which are created in the upper part of the MLT region, above 85 km (e.g., *Meriwether and Gerrard*, 2004). Apart from the creation height the main features that distinguish them from the "lower" MILs are their creation mechanisms. The summary and examination of these mechanisms for the production of the "upper" MIL by *Meriwether and Gardner* (2000) concludes that the one of the formation mechanisms is a nonlinear interaction of gravity waves with tidal waves, as schematically shown in the left part of Fig. 3.2. There the solid black line represents relative zonal winds for equinox conditions (E), the dashed black line represents zonal winds for Northern Hemisphere winter solstice (W), and the gray line represents zonal winds for Northern Hemisphere summer solstice (S), based on values from *Roble* (2000). Gravity waves (indicated by thin phase lines with a thick arrow denoting the upward group velocity) reach a critical level via interaction with the background flow and/or tides. This initiates the onset of instability. The "upper" MIL often shows a downward phase propagation associated with 24 h tide. Also for a lot of

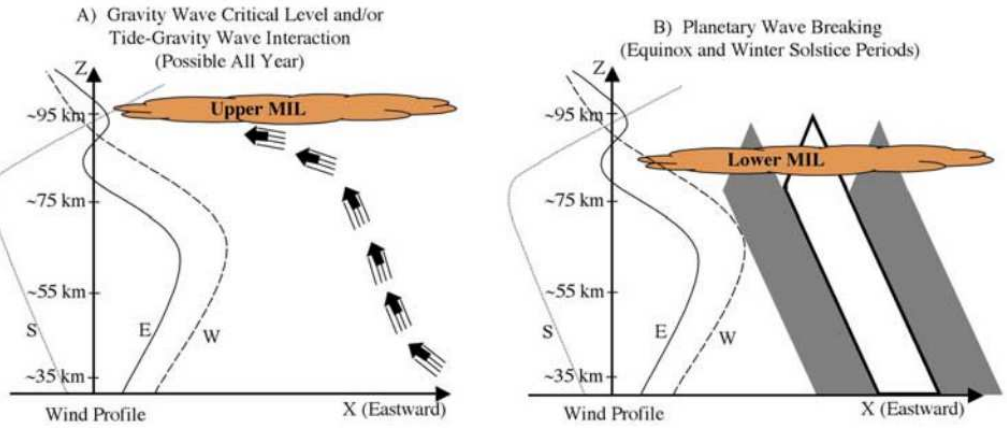

Figure 3.2 Schematic showing possible MIL formation mechanisms. Solid black line represents relative zonal winds for equinox conditions (E), dashed black line represents zonal winds for Northern Hemisphere winter solstice (W), and gray line represents zonal winds for Northern Hemisphere summer solstice (S), based on values from *Roble* (2000). (A) Gravity waves (indicated by thin phase lines with a thick arrow denoting the upward group velocity) reach a critical level via interaction with the background flow and/or tides. This initiates the onset of instability. (B) Planetary waves (indicated by westward tilting gray/white anomalies) can reach a zero-wind line in the middle mesosphere during equinox and winter solstice conditions, which, in turn, causes wave dissipation, thus creating a lower-altitude MIL. After *Brown et al.* (2004).

upper MIL events, it was found that when 24-hour observations of the MIL structure were averaged together, the MIL was no longer apparent. This point was also discussed in detail by *Meriwether and Gardner* (2000), where Na resonance lidar observations and subsequent analyses (*States and Gardner*, 2000) indicated that the "Upper" MIL did indeed "wash out". This MIL creation mechanism seems to be possible year-round, with gravity wave activity being spectrally filtered by the seasonally varying lower atmospheric winds.

Other mechanism, proposed by *Liu et al.* (2000), and based on the numerical simulations, showed that a vigorous turbulence revealing heating rates of ~ 10 K/h is capable of producing temperature inversions itself. Such strong turbulence, however, had rarely been observed (see, e.g., *Lübken*, 1997; *Lübken et al.*, 2002) before in contrast to the temperature inversion layers, which are common phenomena. The new turbulence analysis, which is part of this work, reveals many more strong turbulence layers in the data than previously observed, also with heating rates exceeding ~ 10 K/h (see Sec. 5.2).

Liu et al. (2000) demonstrated that large mean state changes in the thermal structure may indeed be introduced by the process of gravity wave breaking provided that the mean stability of the background atmosphere has been decreased by the propagation of the diurnal tidal wave through the region. This may mean, that two discussed mechanisms of the formation of "upper" MIL are connected, which also seem to be the case for the MIL observed during ECOMA09 flight (this MIL event was classified as the "upper" MIL).

The "lower" MIL

In addition to the tidally driven MILs discussed in previous subsection, it has become clear that there exists in all seasons a characteristic climatological feature of the mesosphere that is now identified as the "lower" MIL. *Meriwether and Gerrard* (2004) gathered studies characterizing the midlatitude climatology of the "lower" MILs. They are observed most often during the winter between 70 and 80 km with large amplitudes (typically 30 - 50 K), but with higher altitudes (typically 80 - 85 km) and weaker amplitudes in the summer (*Hauchecorne et al.*, 1987; *Gille et al.*, 1991; *Hauchecorne et al.*, 1991). In addition, *Hauchecorne et al.* (1987) also showed that the phenomenon is mesoscale in dimension with a cross section of many hundreds of kilometers. *Sassi et al.* (2002) has demonstrated that the simulation of the breaking of planetary waves in the mesosphere region would produce a MIL event with an amplitude of 10 - 50 K depending upon the strength of the planetary wave. These very rapid wave-breaking takes place when a critical line of zero wind in the upper mesosphere is encountered as these waves propagate vertically into the upper mesosphere. Existence of this critical line in the mesosphere is due to a deposition of easterly momentum by small-scale gravity waves (*Matsuno*, 1982; *Holton*, 1983; *Garcia and Solomon*, 1985). This is schematically shown in the right part of Fig. 3.2. There, planetary waves (indicated by westward tilting gray/white anomalies) can reach a zero-wind line in the middle mesosphere during equinox and winter solstice conditions, which in turn, causes wave dissipation, thus creating a lower-altitude MIL.

A study of the global distribution of "lower" MIL events as a function of latitude and season utilizing remote-sensing results from the UARS (Upper Atmosphere Research Satellite) platform (*Leblanc and Hauchecorne*, 1997) resulted in two interesting conclusions, namely, that these MIL events are rarely found at high latitudes and that they are most often observed at equatorial latitudes during equinoxes and at midlatitudes in the winter hemisphere. This morphological distribution was confirmed by *Siva Kumar et al.* (2001) for low-latitude MILs.

Also, the global distribution, seasonal, and interannual variations of the lower MILs using SABER (Sounding of the Atmosphere using Broadband Emission Radiometry) temperature data was shown by *Gan et al.* (2012). They showed that both the characteristics and the formation mechanisms of large spatiotemporal-scale lower MILs are latitude dependent. At low latitudes, the monthly zonal mean amplitude of the lower MILs exhibits a semi-annual cycle and reaches a maximum of 40 K in spring and a secondary maximum of 30 K in autumn. On the equator, the semi-annual oscillations in the background and diurnal-migrating-tide temperatures could contribute more than 12 and 25 K, respectively, suggesting they are the key causes of large spatiotemporal-scale lower MILs at low latitudes. At middle latitudes, the monthly zonal mean amplitude of the lower MILs exhibits an annual cycle with its maximum in the range 24 - 33 K in winter.

3.3. MIL observations

One of the problems that, in part, are responsible for the slow progress in reaching an understanding of the physics of the formation of MIL is that the MLT region, which lies above the reach of the radiosonde, is difficult to study with instrumentation, whether remote sensing or in-situ, that is capable of making the measurements of density, temperature, turbulence parameters, and winds. Without the constraints upon possible mechanisms that such measurements represent, gaining a detailed understanding of the basic physical processes that

enter into the production of MIL becomes rather difficult.

A common tool to study temperature inversion layers experimentally in the MLT region are lidar observations (e.g., *Hauchecorne and Chanin*, 1980, App. G.1). The advantage of the lidar measurements is that they yield continuous (or at least long duration) observation of the temperature field and allow to distinguish between signatures of (short-lived) strong gravity waves and (long-lived) temperature inversions layers that both create similar signatures in a single altitude-profile. However, this technique does not allow to measure turbulence parameters directly and must rely on indirect information (such as the lapse rate) or numerical simulations for this particular purpose (see e.g., *Whiteway et al.*, 1995; *Liu et al.*, 2000). Also, this technique is weather dependent.

By making use of in-situ measurements in the MLT region, i.e., employing sounding rockets, it is possible to directly measure both temperature and turbulence parameters simultaneously and in the same volume. This is the only possibility so far to directly measure and compare the turbulent energy dissipation rate, ε, profile with the temperature profile (App. C).

One of the other methods to investigate turbulence parameters with accompanying thermal structure is to use the radar echoes observations and SABER instrument temperature observations. *Sridharan et al.* (2013) compares the mesospheric echoes, observed with the MST radar at Gadanki (13.56^{o}N, 79.2^{o}E) with temperature information obtained by SABER instrument. They found the correlation between the echoes that arise due to change in refractive index associated with electron density fluctuations, and the thermal structure. The echoes are observed in the region exhibiting local temperature minimum caused probably by dynamical cooling due to turbulence at the height of wave breaking.

To study the spatial extension of the MIL satellite temperature measurements, as that of the Earth Observing System (EOS) Microwave Limb Sounder (MLS), onboard the National Aeronautics and Space Administration (NASA) Aura satellite are used (*Waters*, 1993, App. G.3). The advantage of MLS is a good spatial coverage of measurements in large altitude range (i.e. from 50 to 100 km). However, the vertical resolution of this technique, which is 3 to 6 km depending on the altitude, is only sufficient to detect larger MILs.

UARS and SABER measurements of the lower MILs were already mentioned in the previous subsection. *Ramesh et al.* (2013) used Rayleigh lidar temperature observations over Gadanki combined with SABER observation, and MF-radar at Tirunelveli (8.7^{o}N, 77.8^{o}E) observations to discuss the origin of the MILs at low latitudes. The conclusion they made is that the MILs are caused mainly due to the gravity wave breaking and the inversion amplitude may get modulated by the interaction between gravity waves and planetary waves. The eddy diffusion associated with gravity wave drag may also cause suppression in the planetary wave activity.

Ramesh et al. (2014) consider the triple layered MIL observed in SABER temperature profile. The origin of this MIL is also discussed with use of Rayleigh lidar temperature observations over Gadanki and MF-radar observations over Tirunelveli.

With the help of MF-radars, also a long time wind analyses are possible (App. G.2). This is helpful to detect periods with strong tidal activity and investigate them in terms of the accompanying MIL events.

Chapter 4.

New Statistical Turbulence Analysis

The statistical analysis of all the available, high resolution in-situ measurements of the mesospheric turbulence is presented in this work. The turbulence dissipation rate, ε, is obtained by fitting the theoretical model to the spectrum obtained after wavelet transform of the neutral density residuals measured during a rocket flight. In previous studies, these ε-values were obtained individually for each spectrum, either using the Fourier (e.g., *Lübken*, 1997; *Lübken et al.*, 2002, see App. D.1) or wavelet (e.g., *Strelnikov*, 2006, see App. D.2) analysis technique. In this work, data from 35 flights are analyzed, each in the altitude range from 60 to 100 km. Turbulence dissipation rate, ε, is obtained from the spectra given in the 100 m altitude bins, which gives 400 spectra for each flight and more than 10000 spectra in total. For each spectrum fitting ranges have to be set, the theoretical model has to be fitted and afterwards it has to be indicated whether the spectrum is turbulent or not (i.e. whether the measured spectrum satisfactorily reflects the theoretical model). To analyze this amount of spectra, a self-consistent technique of fitting of model to the measured data and to distinguish between the turbulent and non-turbulent spectra is implemented in this work and will be described in this section. This technique is referred to as the New Statistical Turbulence Analysis, or simply the new analysis henceforth.

In the following sections, a general algorithm for data treatment in the wavelet analysis technique is given. Afterwards the new features developed in this thesis for the use of the new analysis are described. The test its functionality, the new analysis is applied to a set of synthetic turbulent spectra.

4.1. General algorithm for data treatment in wavelet turbulence dissipation rate analysis

Before we apply the New Statistical Turbulence Analysis, the data from a rocket flight given in binary format have to be extracted and processed. This process taken together with the New Statistical Turbulence Analysis is done in the following steps, which we demonstrate on the data from LT-17 flight taken on October 3rd 1991:

1. The current as a function of time, $I(t)$, measured by ionization gauge is extracted from the binary data files (description of PCM formats used for binary data is given in App. B)

2. The liftoff point is detected in the data and subtracted from the data time vector. Current $I(t)$ is truncated to obtain only the part from the downleg of the rocket flight, because of the placement of the CONE sensor in the aft of the payload. As a result current $I(t)$ as a function of flight time t for the required altitudes during downleg of

the flight is obtained. The example current $I(t)$ is shown in Fig. 4.1. As shown in, e.g., *Lübken* (1993), $I(t)$ is directly proportional to atmospheric number density $n(t)$.

3. This current $I(t)$ is then converted to the relative density fluctuations, also called residuals, $r(t)$, which are determined as:

$$r(t) \equiv \frac{\Delta n}{< n >}(t) = \frac{n(t) - n_{ref}(t)}{n_{ref}(t)} = \frac{I(t) - I_{ref}(t)}{I_{ref}(t)} \tag{4.1}$$

   where the reference current $I_{ref}(t)$ is derived as a running average of the measured time series $I(t)$ (e.g., *Blix et al.*, 1990). The residuals $r(t)$ after subtracting the reference current $I_{ref}(t)$ are shown in Fig. 4.2.

4. Rocket spin is filtered out using band stop filtering. The residuals after spin filtering are shown in Fig. 4.3.

5. Wavelet analysis is applied to the resultant residuals (App.D.2). Wavelet PSD (Power Spectral Density) is shown in Fig. 4.4. With orange dashed-dotted vertical lines ranges for filtered spin frequencies are shown (two lines for each filtered spin frequency).

6. Global wavelet power spectra are derived for 100 m altitude bins. In Fig. 4.5 residuals from 100 m bin for the altitude range 89.7 - 89.8 km are shown. In Fig. 4.6 global PSD of this 100 m bin is shown. Measured global wavelet power spectrum, P_{EXP}, is shown as a black line. The blue dashed curve is fitted spectral model of *Heisenberg* (1948), P_{FIT}. Fitting ranges are shown as vertical orange dashed lines. Turbulence inner scale derived from the fit, l_0, is shown as black vertical dot-dashed line. With the yellow vertical dashed-dotted lines ranges for filtered spin frequencies are shown (two lines for each filtered spin frequency).

7. For each of the obtained 100 m altitude bins, mean noise level, L_{NS}, is derived, and afterwards fitting ranges, f_{MAX} and f_{MIN} are set (Sec. 4.4). Fitting ranges are shown with orange dashed lines in Fig. 4.6.

8. The *Heisenberg* (1948) model (eq. D.2 in App. D.1) is fitted to the spectrum in the obtained fitting ranges. The fitted model is shown with blue dashed curve in Fig. 4.6.

9. Turbulence dissipation rate, ε, and variability dissipation rate, N_θ, are derived from the best fit

10. Turbulence dissipation rate measurement error, ε_{ERR}, is derived using weights. Weights are derived during step 8. The process of deriving weights is described in Sec. 4.3.

11. The set of criteria developed in this work to distinguish between turbulent and non-turbulent spectra are applied (described in Sec. 4.5)

12. ε altitude profile is derived for analyzed flight with ε_{ERR} shown as error bars. ε altitude profile is shown in Fig. 4.7. The black crosses connected with the black line show the derived ε-values. ε_{ERR} values are shown as orange bars. Red and blue lines show the mean ε profiles obtained for winter (*Lübken*, 1997) and summer (*Lübken et al.*, 2002), respectively.

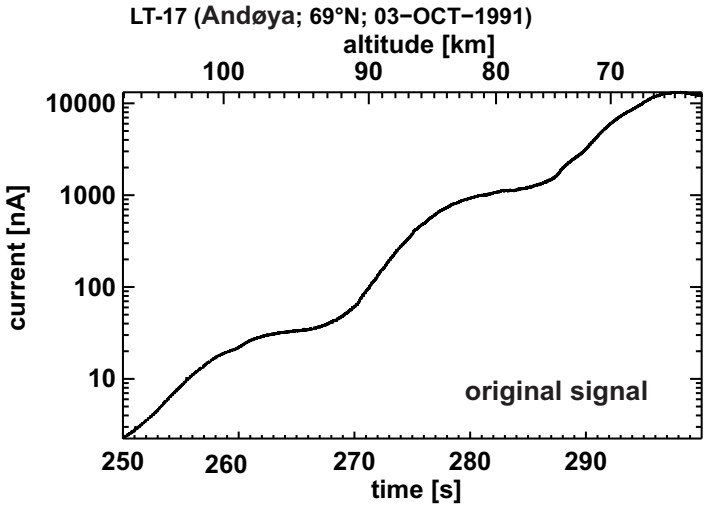

Figure 4.1 Current $I(t)$ obtained from the LT-17 flight taken on October 3rd 1991.

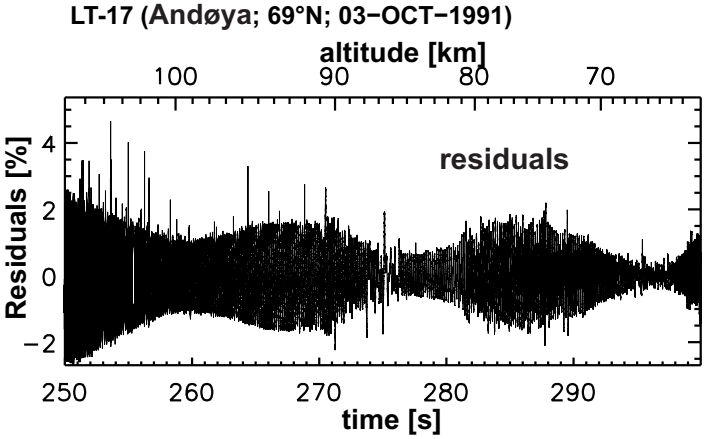

Figure 4.2 Residuals obtained from the LT-17 flight taken on October 3rd 1991. The high amplitude sinusoidal is due to the spin modulation. The lower amplitude sinusoidal is due to the rocket coning, which do not affect turbulence measurements.

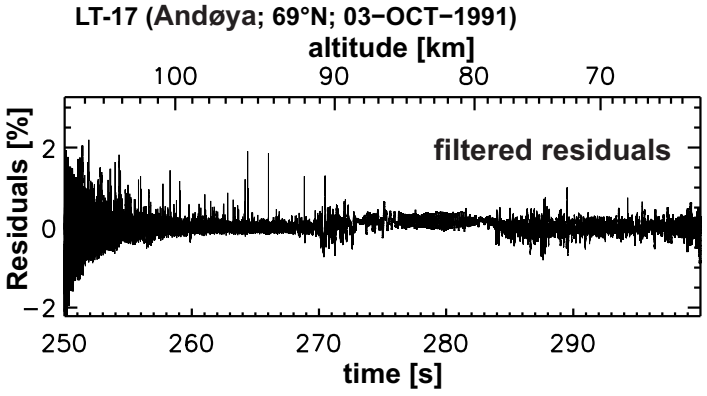

Figure 4.3 Residuals obtained from the LT-17 flight taken on October 3rd 1991 after spin filtering.

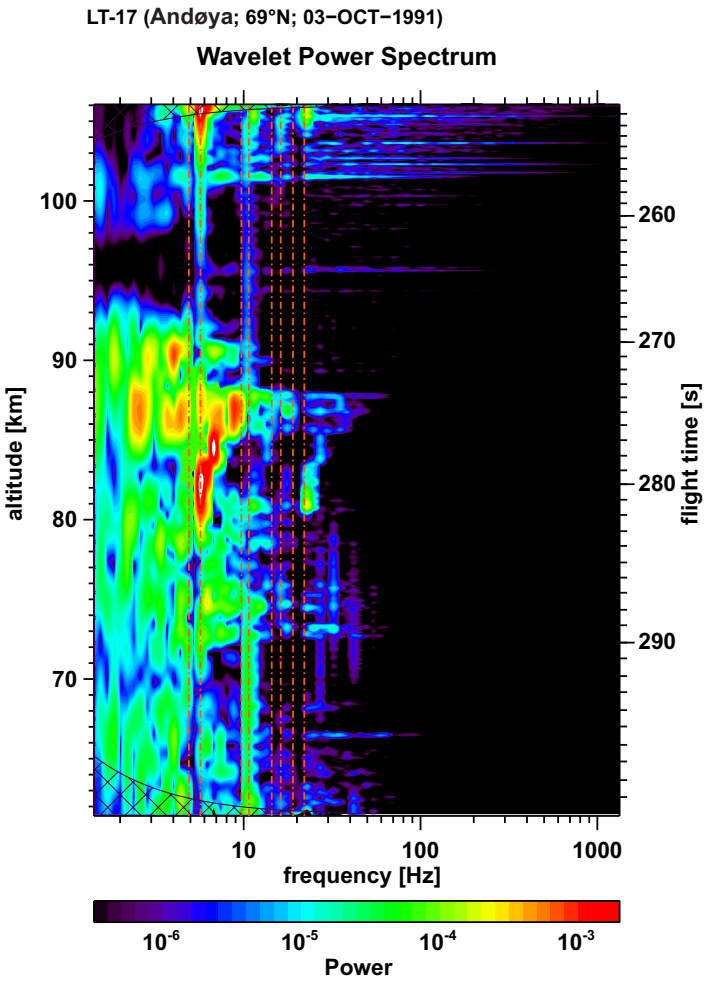

Figure 4.4 Wavelet PSD obtained from the LT-17 flight taken on October 3rd 1991. With orange dashed vertical lines the spin frequencies with harmonics are shown.

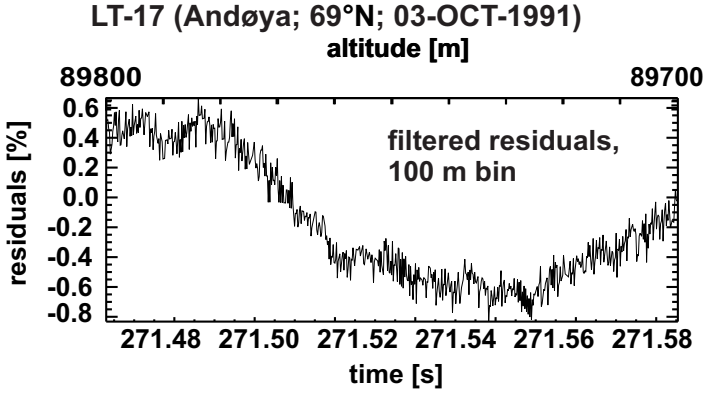

Figure 4.5 Residuals from 100 m altitude bin obtained from the LT-17 flight for the altitude range 89.7 - 89.8 km.

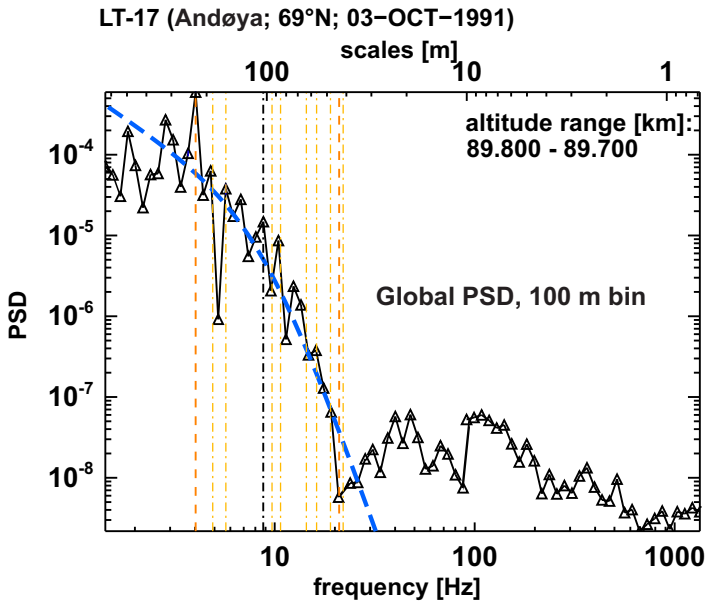

Figure 4.6 Global PSD of 100 m altitude bin obtained from the LT-17 flight for the altitude range 89.7 - 89.8 km. For the descriptions, see text.

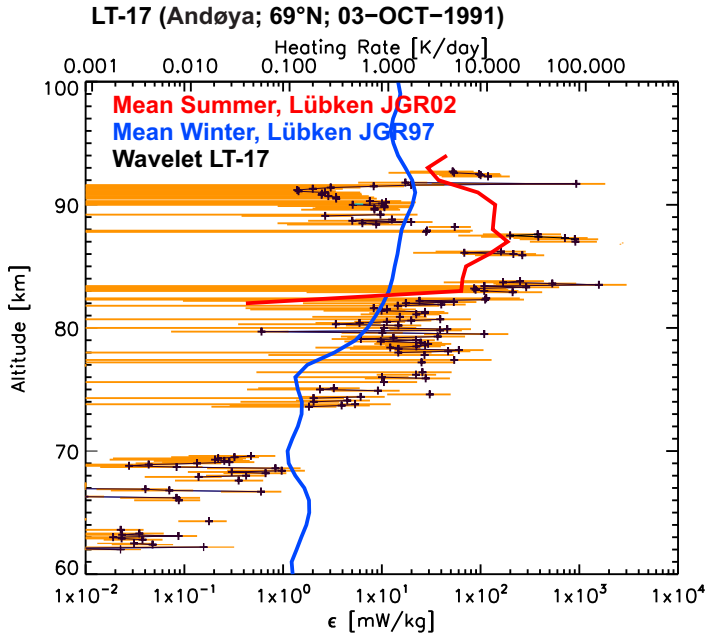

Figure 4.7 ε altitude profile obtained from the LT-17 flight taken on October 3rd 1991. For description please see text.

In the following sections, the new features in the ε derivation procedure developed for the use of the New Statistical Turbulence Analysis are described. First, the derivation of turbulence dissipation rate measurement error based on weights, ε_{ERR}, is described, which is one of the novelties of the presented analysis. Afterwards, the process of obtaining weights, w_i, used in the fitting process and error derivation, is explained. The procedure of setting noise level, L_{NS}, and fitting ranges, f_{MIN} and f_{MAX}, for each spectrum is described and the

criteria used to distinguished between turbulent and non-turbulent spectra are discussed. The New Statistical Turbulence Analysis technique is demonstrated on a set of synthetic turbulent spectra and its functionality is assessed.

4.2. Error treatment

In this section, the turbulence dissipation rate measurement error, ε_{ERR}, used in this work, will be derived and discussed. The error's formula will be given and each of its parts, as well as its meaning will be discussed. Also, the difference between ε_{ERR} used in this work and in the previous ones (e.g., *Lübken* (1997); *Lübken et al.* (2002); *Strelnikov* (2006)) will be debated.

The measurement error for turbulence dissipation rate, ε_{ERR}, has to account for:

- quality of fit: how well do experimental data fit the *Heisenberg* (1948) model
- CONE sensor measurement errors, and how they are transformed by the wavelet analysis technique into frequency domain
- less than infinite number of points used for a fit of the *Heisenberg* (1948) model
- number of fitted parameters

A typical turbulence spectrum obtained using wavelet technique is shown in Fig. 4.8. The plot shows global wavelet power spectral density (P_{EXP}) of the measured neutral density fluctuations obtained for 100 m bin of the rocket flight as black triangles connected with a black line. The lower x-axis shows frequency in the rocket domain, f, whereas the upper one shows spatial scales, obtained using rocket velocity as v_R/f. Fitted spectral *Heisenberg* (1948) model (P_{FIT}) is shown as a blue dashed line. With the orange dashed vertical lines minimum (f_{MIN}) and maximum (f_{MAX}) frequency ranges for the fitting are shown (i.e. fitting is made only inside these limits). The dashed-dotted black vertical line marks the turbulence inner scale, l_0, obtained from the fit. The variability dissipation rate, N_θ and the mean noise level, L_{NS}, are shown by dotted lines and marked on the plot.

Fig. 4.8 helps to explain the error derivation process which is described below. This derivation is done in the process of fitting of *Heisenberg* (1948) spectral model, P_{FIT}, to a measured global wavelet power spectrum, P_{EXP}. Fitting is done only inside of the fitting ranges, i.e. between f_{MIN} and f_{MAX}. The fit uses the Levenberg-Marquardt technique to solve the least-squares problem. This technique is explained in more details in e.g., *Wolberg* (2006). There are two free fitted parameters in the *Heisenberg* (1948) model, namely ε and N_θ. The other parameters are either measured in-situ using CONE sensor (temperature and density to derive kinematic viscosity, μ), or derived from the sounding rocket's trajectory (rocket velocity, v_R).

Measurement error for turbulence dissipation rate, ε_{ERR}, is calculated using formula (e.g., *Wolberg*, 2006):

$$\varepsilon_{ERR} = \sqrt{C_{kk}^{-1} \frac{\chi^2}{n-p}} \tag{4.2}$$

where χ^2 is a weighted chi-squared value, p is a number of fitted parameters (two in this case) and n is a number of data points used for the fitting process. Value of $n-p$ is also

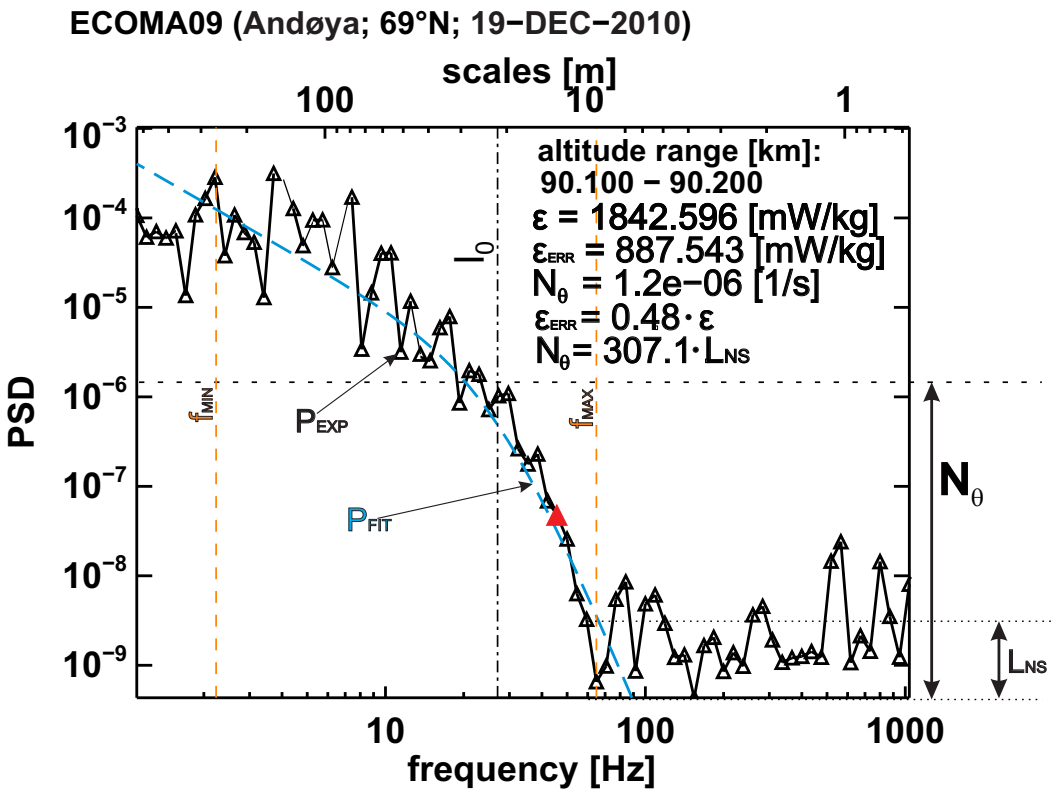

Figure 4.8 Typical measured global wavelet power spectrum, P_{EXP}, of the 100 m altitude bin in the region exhibiting turbulence (with $\varepsilon = 1843$ mW/kg) is shown as a black line with black triangles. The blue dashed curve shows the fitted spectral model of *Heisenberg* (1948) (P_{FIT}). Fitting ranges, upper (f_{MAX}) and lower (f_{MIN}), are shown as vertical orange dashed lines. Turbulence inner scale derived from the fit, l_0, is shown as a black vertical dot-dashed line. Average noise level, L_{NS}, and variability dissipation rate, N_θ, are shown as horizontal dotted black lines. The upper x-axis shows the spatial scales obtained from the frequency using rocket velocity as v_R/f.

known as number of degrees of freedom and is used to derive reduced chi-squared value, χ^2_{RDC}, described later in this section. C_{kk}^{-1} is the formal 1-sigma error in each parameter, computed from the covariance matrix C_{kk} (e.g., *Wolberg*, 2006):

$$C_{kk} = \sum_{i=1}^{n} w_i \frac{\partial^2 f}{\partial^2 a_k} \tag{4.3}$$

where f is the fitted function, a_k is k-th fitted parameter, w_i is the weight for i-th fitted point. Covariance matrix is the matrix used to find the least square values of parameters used in the fitting procedure, and subsequently, the chi square value, χ^2. More information on C_{kk} and how it is computed can be found in e.g., *Wolberg* (2006). χ^2, weighted chi-squared value, is derived using formula (e.g., *Wolberg* (2006)):

$$\chi^2 = \sum_{i=1}^{n} w_i \cdot (P_{EXPi} - P_{FITi})^2 \tag{4.4}$$

In this equation P_{EXPi} denotes the value of the i^{th} point of derived global wavelet spec-

trum, P_{EXP}, and P_{FITi} is the corresponding value on the curve P_{FIT}, obtained by fitting spectral *Heisenberg* (1948) model. The weights for each point, w_i, are necessary to account for the fact that different points of the measured wavelet spectra, P_{EXPi}, have different uncertainties. These weights estimate how the CONE sensor measurement error is transformed using wavelet technique. The weights derivation is described in the next section.

The chi-square value, χ^2, determines a "goodness of fit": it answers the question of how well the experimental data fit the model. The reduced chi-square value, χ^2_{RDC}, is calculated as (e.g., *Wolberg*, 2006):

$$\chi^2_{RDC} = \frac{\chi^2}{n-p} \tag{4.5}$$

The reduced chi-square value simultaneously estimates:

- The deviations between the measured data and the fitted model that occur because of the finite numbers of points being fitted
- The discrepancy between the experimental results and the predictions made by the fitted function
- The uncertainties originating from the number of fitted parameters, p, in the fitted model

In previous works, weights that were equal to $1/P_{EXP}$ were used (e.g., *Strelnikov*, 2006). Since the theoretical model was fitted in log-space, this resulted approximately in unit weighting, ($w_i = 1$). These weights, however, were not used for measurement error derivation, but only during the fitting process for the robust convergence of the fit. In this work the proper and precise turbulence dissipation rate measurement error, ε_{ERR}, is derived for the first time, using the new technique for the estimation of weights (described in the next section). This new technique derives weights that account for the fitting error that comes directly from the measurements and how it is transformed during the wavelet analysis.

4.3. Data weighting

In this section the new weight derivation technique which is used in the fitting process is discussed. The weights are used for a weighted least-squares regression where an additional scale factor (the weight) is included in the fitting process.

Regardless of the fitted function, a weight w_i should be specified for each point for a fitting process . The weight associated with i-th point of the spectra, P_{EXPi}, is based upon the relative uncertainties in x and y axis direction, σ_{xi} and σ_{yi} (errors associated with frequency and PSD uncertainties respectively), associated with this point. Clearly, one must place more weight on points that have smaller uncertainties, and less weight upon the points that have greater uncertainties. In other words we give less weight to the less precise measurements and more weight to the more precise measurements when estimating the unknown parameters in the fitting process.

The alternative to using w_i associated with the uncertainty of each data point is to simply use unit weighting (i.e. $w_i = 1$) for all points, (see e.g., *Wolberg*, 2006). This is a reasonable choice for w_i if the uncertainties for all points are approximately the same or if we have no idea regarding the values (actual or even relative) of the uncertainties for each point.

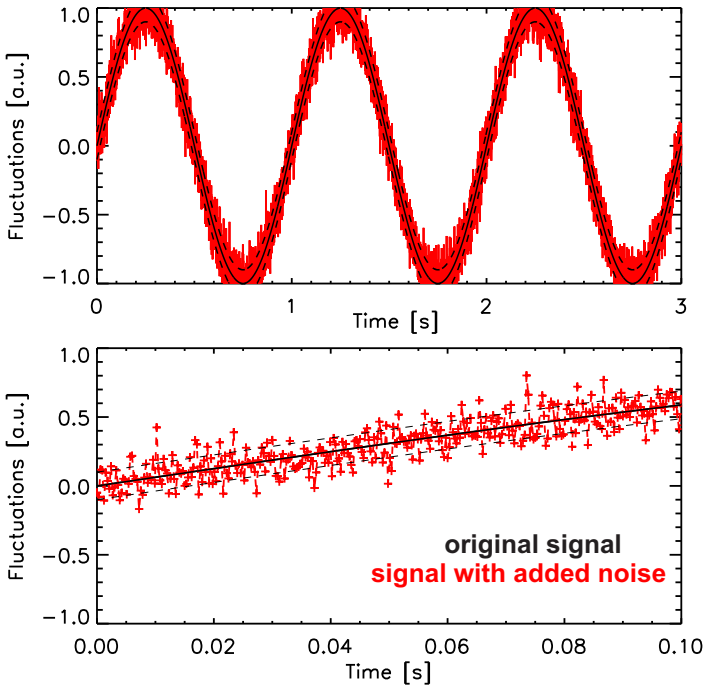

Figure 4.9 The black solid line shows an idealized sinusoidal signal with $f = 1$ Hz, amplitude $A = 1$ a.u., sampled with 3300 Hz, the frequency typical for the CONE instrument's electronics. The upper plot shows 3 s of the signal. The lower one focus on 0.1 s, for a 1000 m/s rocket velocity, v_R, it gives 100 m bin. Red line in the upper plot and red crosses in the lower plot show signal with added noise, with the standard deviation σ_{SD} = 0.1 a.u. (marked as black dashed lines in both plots).

However, when the differences in the uncertainties are significant, then using unit weighting can lead to poor results, (see e.g., *Wolberg*, 2006).

In our case the uncertainties associated with the measurements of frequency, σ_{xi}, are negligible due to the electronics' properties. Hence, the only objective is to derive the weights associated with the uncertainties in the power spectral density values, P_{EXP}, since the uncertainty for i-th point of the wavelet power spectra, P_{EXPi}, is not known. We assume that the current measured by the CONE instrument has the same measurement error for each point. Thus, by adding normally distributed noise to each point of the measured current, applying wavelet transform and repeating this procedure several times, we can derive the statistically measured weights for the obtained global wavelet power spectra.

The procedure of deriving weights is conducted as follows:

1. Since the measurement error of the CONE current is found to be 0.1% (e.g., *Strelnikov et al.*, 2013), a noise with a normal distribution and standard deviation $\sigma_{SD} = 0.1\%$ is added to the measured residuals

2. This is repeated n_{REP} times, so n_{REP} signals with added noise are obtained in the process

3. The wavelet transform is applied for each of the signals with added noise. This way for each measured time series (i.e. each flight) a n_{REP} wavelet PSD is obtained

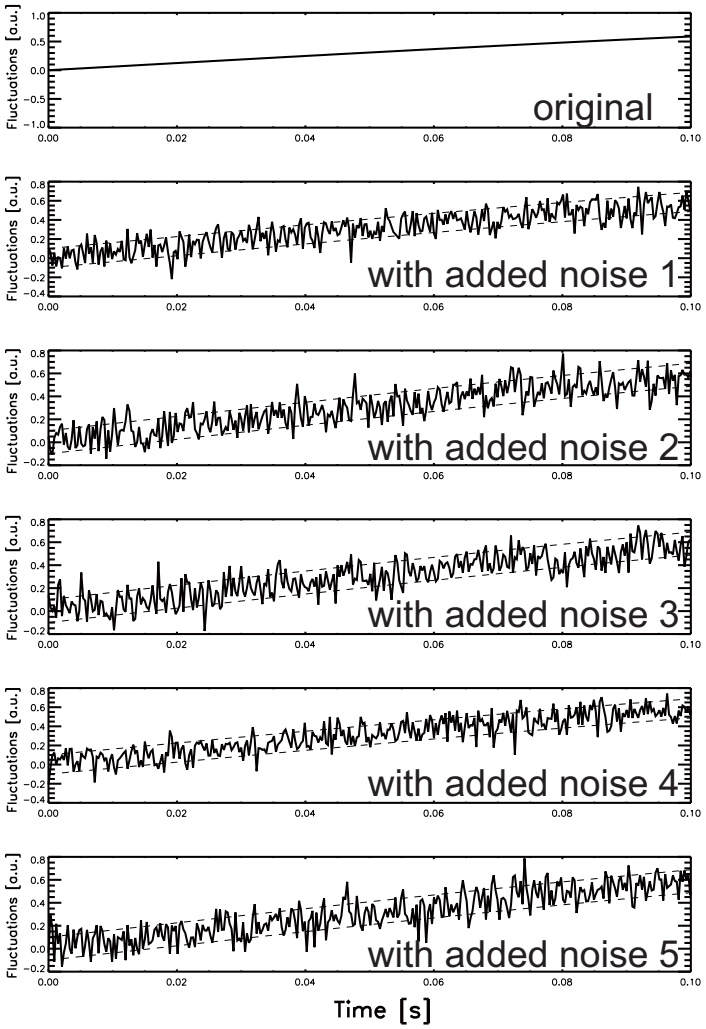

Figure 4.10 0.1 s of an idealized sinusoidal signal (uppermost panel) with frequency $f = 1$ Hz, amplitude $A = 1$ a.u., sampled with 3300 Hz. In the panels below the upper one, $n_{REP} = 5$ signals with added noise with standard deviation, $\sigma_{SD} = 0.1$, are shown. The standard deviation for each signal with added noise is shown with black, dashed lines.

4. Each of n_{REP} obtained wavelet PSDs is divided into 100 m altitude bins, as it is done for the original signal. As a result we get a set of n_{REP} global wavelet PSDs for every 100 m altitude bin. The difference between these global wavelet PSDs is that the time series have a different random "instrumental" noise

5. By taking i-th point of the n_{REP} global wavelet PSDs with noise, we construct the time series P_{yi}. From these time series, we derive the weights for the i-th point of original, i.e. without noise, global wavelet PSD as

$$w_i = 1/\sigma_{yi}^2 \tag{4.6}$$

(e.g., *Wolberg*, 2006), where σ_{yi} is the variance of P_{yi}. We do it for each point of PSD inside of the fitting ranges. This type of weight is called statistical weight and is used for our purposes, as we are using statistically distributed synthetic noise to derive ε_{ERR}.

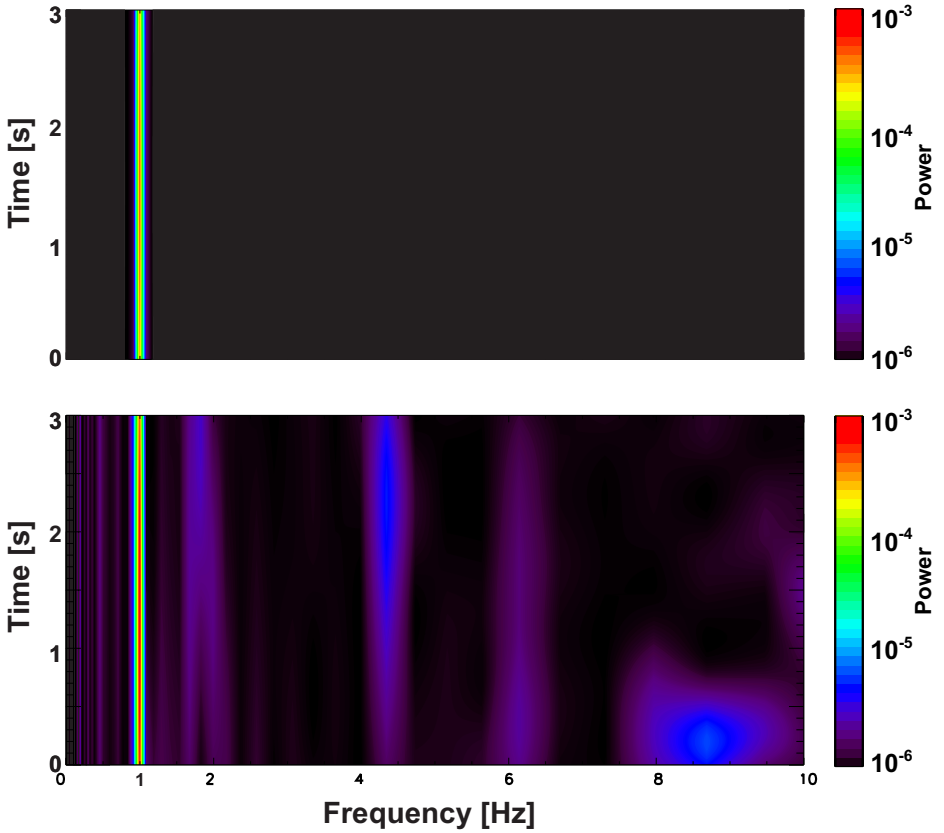

Figure 4.11 Wavelet power spectra obtained from the idealized sinusoidal signal (upper panel) and signal with added noise (lower panel).

The described procedure can be shown for an idealized signal. In Fig. 4.9 sinusoidal signal (f = 1 Hz) sampled with 3300 Hz (sampling rate of the CONE instrument's electronics) is shown with the black solid line. The upper plot shows 3 seconds of the signal, whereas the lower one focuses on 0.1 s, which for a rocket velocity of v_R= 1000 m/s gives a 100 m altitude bin. Normally distributed noise with standard deviation of $\sigma_{SD} = 0.1$ is added to this signal (red line in the upper plot and red crosses in the lower plot). The range of the standard deviation around the sinusoidal signal is shown as a black dashed line in both plots. In Fig. 4.10 0.1 s of the same sinusoidal signal is shown (uppermost line) and 5 signals with added noise are shown below (i.e. $n_{REP} = 5$). The black dashed lines around the signals with added, normally distributed noise denote standard deviation $\sigma_{SD} = 0.1$ of this normal distribution.

The original signal, and signals with added noise are then transformed using Morlet-24 function. The result is shown in Fig. 4.11. The upper plot shows the wavelet transformation of the original signal, whereas the lower one shows the wavelet transformation of one of the signals with added noise. The highest power is shown with a red stripe around 1 Hz, areas denoted with blue and violet colors represent the lowest power. The differences between the two plots are due to the noise.

Afterwards, global wavelet power spectra of the 0.1 s bins are obtained from the idealized wavelet PSD and from five wavelet PSDs with randomly added noise and are shown in Fig. 4.12. Here the lowermost black line represents the spectrum obtained from the original,

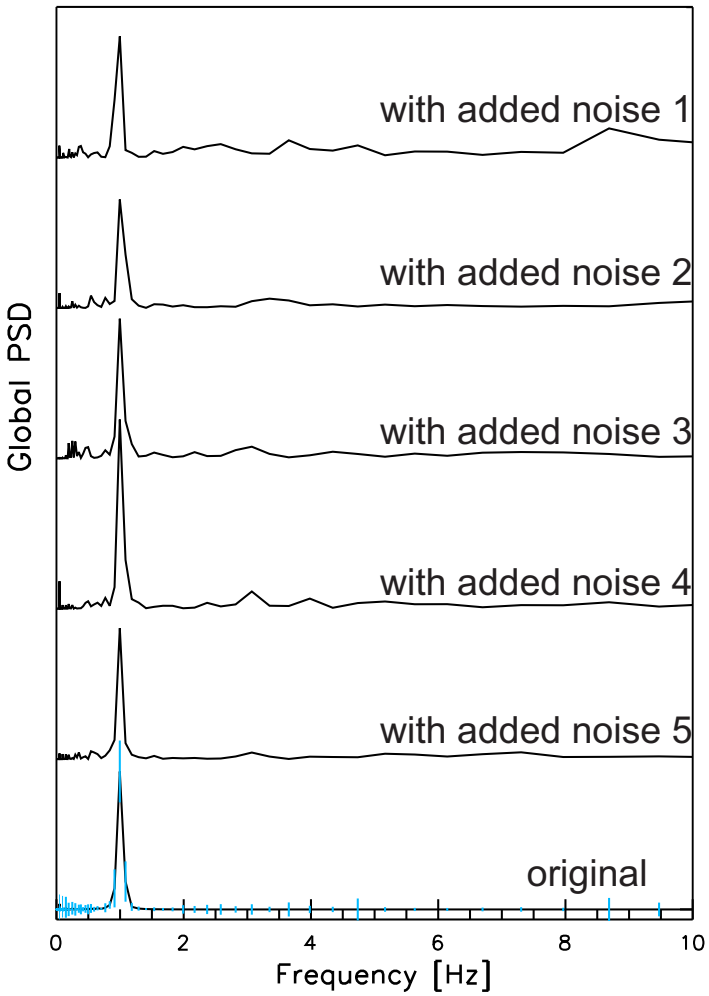

Figure 4.12 Global wavelet power spectra of the 0.1 s bins obtained from the idealized sinusoidal signal (the lowermost line) and from five sinusoidal signals with randomly added noise (the lines above). The standard deviation values, σ_{yi}^2, calculated from the five spectra with added noise at each frequency are shown as blue vertical lines on the idealized spectrum.

noise-free signal, whereas the five lines above it represent 5 spectra obtained from the signals with added noise. Weights are calculated for each frequency as $w_i = 1/\sigma_{yi}^2$ and obtained from values of 5 spectra with added noise as described above. In this example, the variance σ_{yi}^2 values are shown in Fig. 4.12 as blue vertical lines over the lowermost spectrum without noise. The frequencies with highest σ_{yi}^2 have the lowest weights. The same procedure is used for deriving weights in the fitting process of *Heisenberg* (1948) spectra in the New Statistical Turbulence Analysis.

After applying the described algorithm to several data sets, $n_{REP} = 10$ value was chosen for the process of obtaining weights. It had been tested that further repetitions, i.e. more randomly signals with added noise used in the weight derivation process, do not change the calculated weights significantly but notably extend the computational time needed for fitting process. The $n_{REP} < 10$ results in bad convergence of some spectra.

4.4. Noise level and fitting ranges

A typical turbulence spectrum obtained using wavelet technique is shown in Fig. 4.8. There minimum (f_{MIN}) and maximum (f_{MAX}) frequency ranges are shown as the orange dashed vertical lines (i.e. fitting is made only inside these limits). A few words need to be said on how the minimum and maximum frequency limits are derived. First, the frequency range where the instrumental noise dominates over P_{EXP} values is approximated using the typical Kolmogoroff microscale, η, values from *Lübken* (1993) for given altitude (Fig. 2.2) and rocket velocity, v_R. This frequency range changes with altitude, reaching lower values for higher altitudes. Then, the average noise level, L_{NS} (marked by the horizontal black dotted line in Fig. 4.8), is approximated as a mean of the P_{EXP} values in the noise frequency range. The highest frequency for which P_{EXP} value is larger than the L_{NS} by at least one order of magnitude is found (marked with a red triangle in Fig. 4.8). In the vicinity of this frequency (5 points in the spectrum to the left and 5 to the right from this frequency) the frequency with the lowest P_{EXP} value is found, for which the f_{MAX} is set.

The minimum frequency limit, f_{MIN}, is obtained by finding the frequency with the highest value of P_{EXP} in the frequency range from 0 to 4 Hz. Since the rocket spin frequency is normally set between 4 and 6 Hz, this ensures that artifacts do not affect the analysis at this stage due to spin of sounding rocket or due to filtering using band stop filter.

By choosing these fitting ranges we define the part of the measured spectrum which includes most of the inertial and viscous subranges, which are described by the *Heisenberg* (1948) model.

4.5. Criteria used to distinguish turbulent and non-turbulent spectra

After fitting the *Heisenberg* (1948) model to the measured spectra, turbulent energy dissipation rate, $\varepsilon(z)$, is automatically derived as a function of altitude. In this function not all the points have physical meaning. Thus, for example a value of $\varepsilon = 3 \cdot 10^{-3}$ mW/kg with the error of $\varepsilon_{ERR} = 5 \cdot 10^{4}$ mW/kg, or value of ε calculated from the inner scale, l_0, that is out of the fitting range can be considered by no means as a trusted measurement. Such points must be considered as derived from a non-turbulent spectrum and excluded from the $\varepsilon(z)$ profile. To automatize this process algorithm using five criteria was developed.

Nr	Criterion	Discarded [%]
1.	$f_{MAX} < f_{l_0}$	25
2.	$P_{FIT}(l_0) < L_{NS}$	2
3.	At least three points of P_{EXP} below the $0.1 \cdot PSD_{FIT}$	3
4.	$\varepsilon_{ERR} > 2 \cdot \varepsilon$	0.1
5.	$\varepsilon_{ERR} > \varepsilon \cap \frac{N_\theta}{L_{NS}} < 5 \cdot [1/s^2]$	6

Table 4.1 The table with all the criteria used to distinguish turbulent and non-turbulent spectra, and they occurrence (the part of the total spectra discarded exclusively using given criterion in percent).

These criteria are given and their physical meaning is discussed in this section. A list of the criteria is given in Tab. 4.1. If a spectrum fulfills at least one of these criteria it is

treated as a NON-TURBULENT spectrum. The part of the spectra discarded exclusively by each criterion after applying the New Statistical Turbulence Analysis is given in Tab. 4.1 as occurrence in percent. For each criterion an example non-turbulent spectrum, discarded by this criterion is shown in this section. A typical turbulent spectrum is shown in Fig. 4.8 and described in the previous subsection.

Crit. 1 $f_{MAX} < f_{l_0}$

This criterion discards spectra for which l_0 lies outside of the fitting range, that is the spectra for which the fitting frequency, f_{MAX}, is lower than the frequency for the turbulence inner scale, l_0. This is shown in Fig. 4.13 with key features highlighted in red.

Crit. 2 $P_{FIT}(l_0) < L_{NS}$

This criterion discards the spectra for which P_{FIT} value for the inner scale, l_0, is smaller than the averaged noise level, L_{NS}. This is shown in Fig. 4.14. The L_{NS} and l_0 are highlighted in red. The red dot on the blue curve denotes the fitted value, P_{FIT}, for the l_0, which is below the mean noise level, L_{NS}. This means that the l_0 is not resolved by the measurements.

Crit. 3 At least three points of the measured power spectrum, P_{EXP}, are one order of magnitude below the best-fit values, PSD_{FIT}, in the fitting range

This criterion discards the spectra with at least three points of the measured power spectrum, P_{EXP}, smaller by at least one order of magnitude than best-fit values, P_{FIT}. This is shown in Fig. 4.15. The fitted Heisenberg spectral model, P_{FIT}, is shown as a blue dashed line. This spectrum exhibits six points below $0.1 \cdot P_{EXP}$ level, marked with red triangles. This criterion discards the spectra which are non-continuous in the fitting range. According to the *Heisenberg* (1948) model, the turbulence spectrum should be continuous therein (i.e. should contain energy for each scale).

Crit. 4 $\varepsilon_{ERR} > 2 \cdot \varepsilon$

This criterion discards the spectra with a value of turbulence dissipation rate measurement error, ε_{ERR}, at least twice as large as the value of measured turbulence dissipation rate, ε. The ε_{ERR} value tells how well the experimental data fit the *Heisenberg* (1948) model . This criterion is illustrated in Fig. 4.16. It can clearly be seen that the P_{EXP} values (black triangles connected by black line) do not fit the *Heisenberg* (1948) model well (P_{FIT}, blue dashed line), although the fit did converge.

Crit. 5 $\varepsilon_{ERR} > \varepsilon \cap \dfrac{N_\theta}{L_{NS}} < 5 \cdot [1/s^2]$

This criterion considers the wavelet spectra with lower (than in **Crit. 4**), but still high ε_{ERR}. Additionally, variability dissipation rate, N_θ, and mean noise level, L_{NS}, are compared. N_θ value tends to move the spectrum along the y-axis, therefore it can be compared with the L_{NS} (this is demonstrated in Fig. 4.18). This criterion discards spectra with high ε_{ERR} values , which additionally exhibit low N_θ/L_{NS} ratio (i.e. L_{NS} value is of the order of N_θ). In Fig. 4.17 an example spectrum which does fulfil this criterion is shown, with the key features shown in red. In this spectra ε_{ERR} shows moderately high values (i.e. P_{EXP} and P_{FIT} differs considerably) and N_θ is only slightly above the mean noise level. It can be physically interpreted as the low N_θ/L_{NS} ratio results in a poorly resolved viscous subrange.

Finally, criteria to distinguish between turbulent and non-turbulent spectra discussed in this section are used for turbulence analysis. For each criterion an example spectrum was shown and its physical meaning was discussed. Without the use of these criteria it would be impossible to analyze the large amount of spectra analyzed in this work.

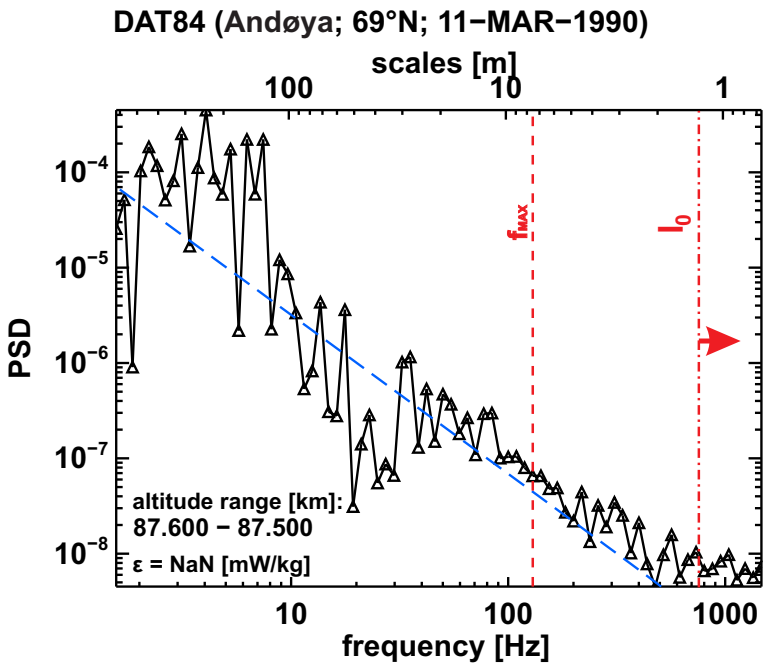

Figure 4.13 Global wavelet power spectrum that fulfills **Crit. 1**, with the key features highlighted in red color. For the description see Fig. 4.8. This spectrum comes from DAT84 flight taken on 11th of March 1990 during the DYANA campaign.

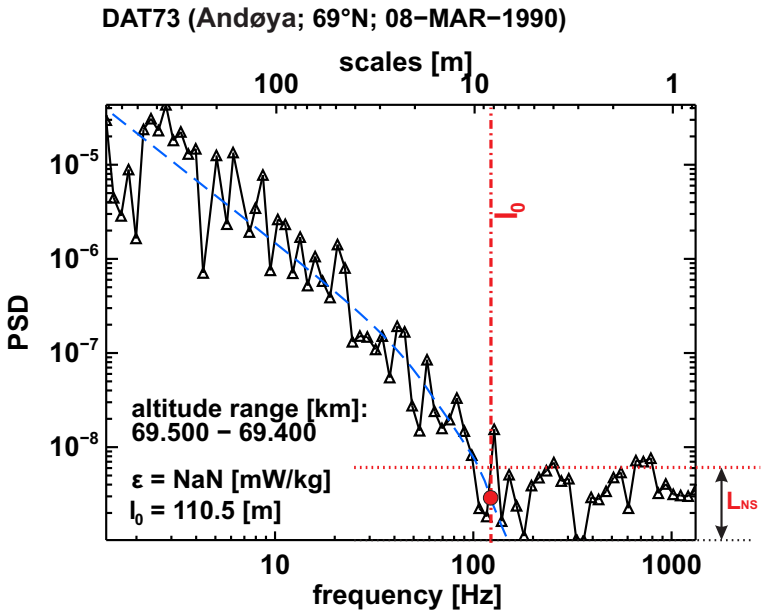

Figure 4.14 Global wavelet power spectrum that fulfills **Crit. 2**, with the key features highlighted in red color. The red dot on the blue curve denotes the P_{FIT} value for the l_0, which is below the mean noise level. For the other descriptions see Fig. 4.8. This spectrum comes from DAT73 flight taken on 8th of March 1990 during the DYANA campaign.

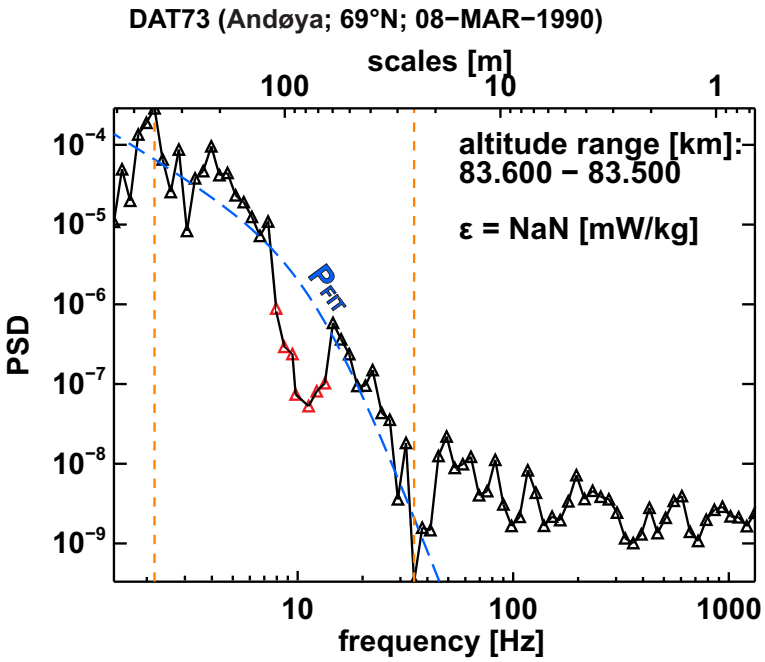

Figure 4.15 Global wavelet power spectrum that fulfills **Crit. 3**. P_{EXP} values below $0.1 \cdot P_{FIT}$ level are marked with the red triangles. For the description see Fig. 4.8. This spectrum comes from DAT73 flight taken on 8th of March 1990 during the DYANA campaign.

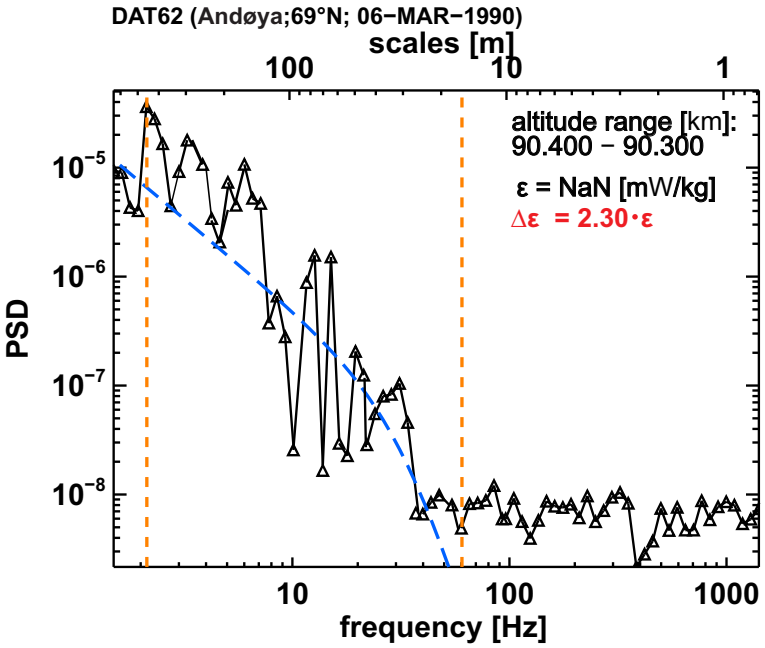

Figure 4.16 Global wavelet power spectrum that fulfills **Crit. 4**, with the key features highlighted in red color. For the description see Fig. 4.8. This spectrum comes from DAT62 flight taken on 6th of March 1990 during the DYANA campaign.

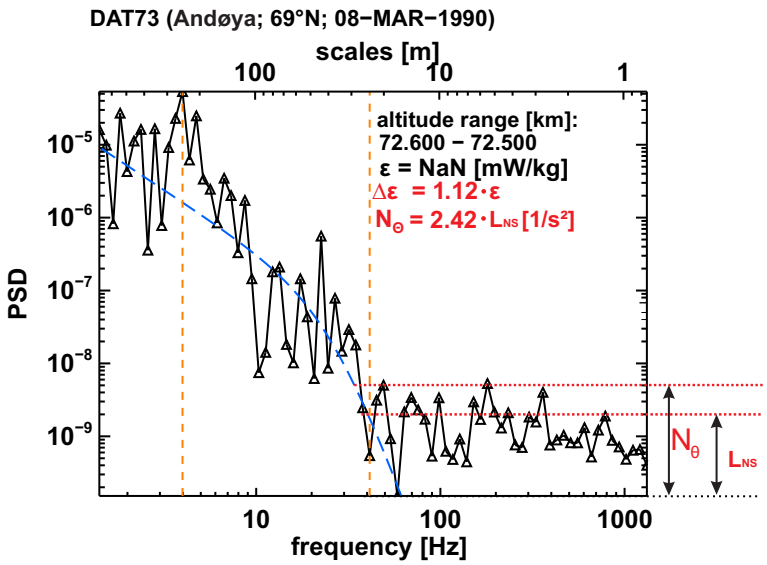

Figure 4.17 Global wavelet power spectrum that fulfills **Crit. 5**, with the key features highlighted in red color. For the description see Fig. 4.8. This spectrum comes from DAT73 flight taken on 8th of March 1990 during the DYANA campaign.

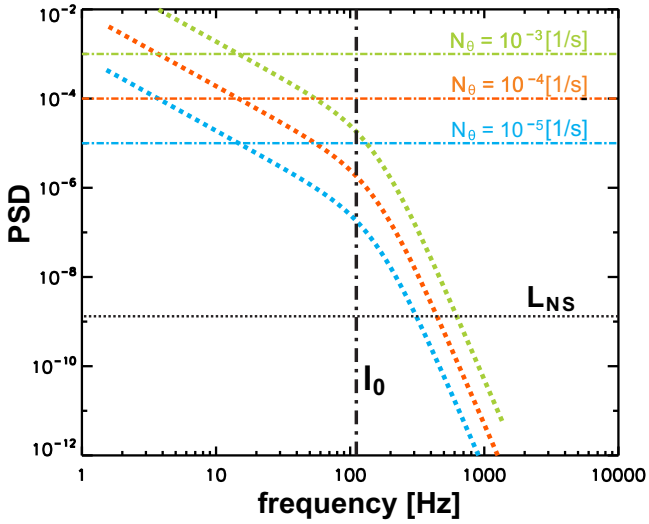

Figure 4.18 The ideal turbulence spectrum obtained from *Heisenberg* (1948) model for three values of N_θ (10^{-3} 1/s - green dashed line, 10^{-4} 1/s - red dashed line and 10^{-5} 1/s - blue dashed line). The other parameters in the model remain constant. Black dashed line shows l_0, which do not change for the different N_θ values. It can be seen that the changes in N_θ value will move the spectrum along the y-axis.

4.6. Demonstration of the functioning of the New Statistical Turbulence Analysis using synthetic signals

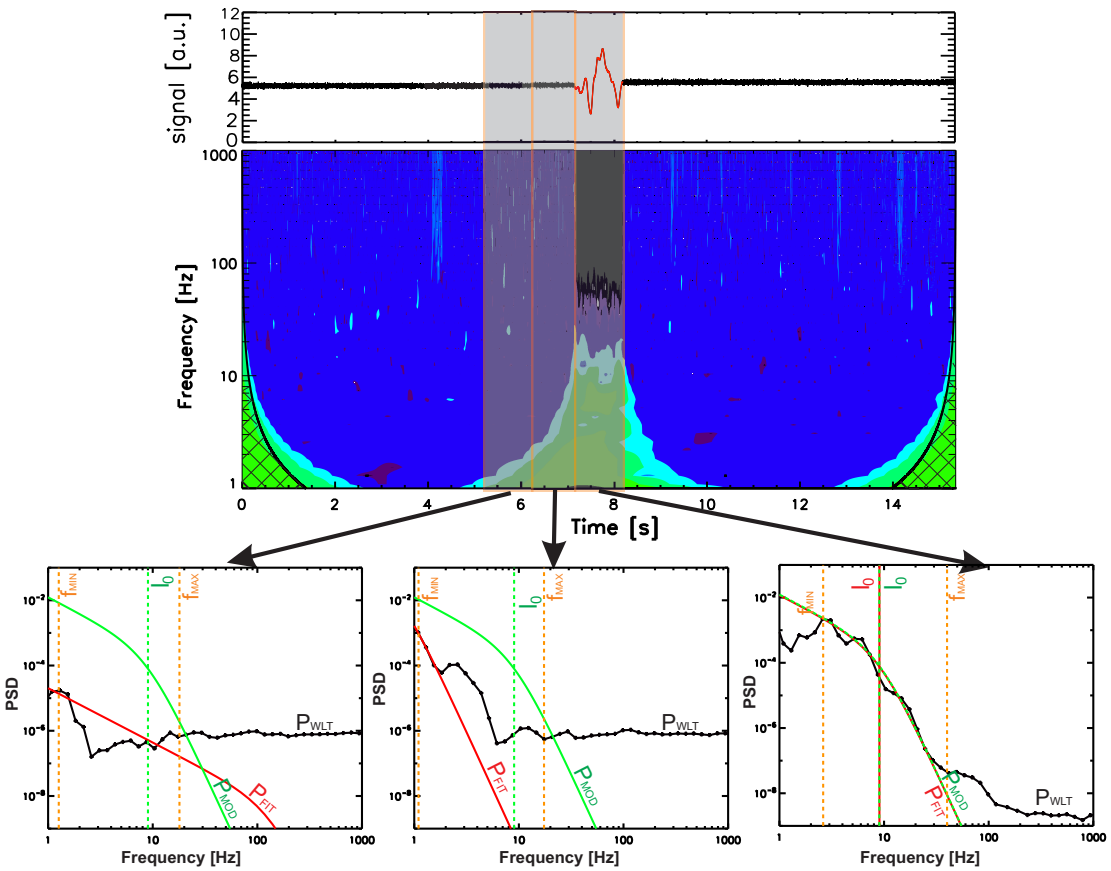

Figure 4.19 In the upper panel a signal consisting of non-turbulent (black line) and turbulent parts (red line) is shown. Wavelet PSD obtained from this signal using Morlet-24 function is shown in the middle panel, with the checkered area marking Cone Of Influence (COI). In the lower panels three global wavelet PSD obtained from parts of the signal marked with the shaded areas in the middle and upper panels are shown. These panels are connected with the corresponding parts of wavelet PSD with arrows. In the global PSD plots, green lines show the ideal turbulence spectrum, P_{MOD}, used to obtain the turbulent part of the signal. Black lines show the spectra obtained from the signal using wavelet transform, P_{WLT}. Red lines show the spectra obtained by applying the New Statistical Turbulence Analysis, that is the fitted spectra, P_{FIT}. For each spectrum fitting ranges are marked with orange vertical dashed lines. l_0 for P_{FIT} is shown as vertical red dashed line (only for the turbulent spectrum). l_0 for P_{MOD} is shown as vertical green dashed lines.

In this section the New Statistical Turbulence Analysis is tested on a synthetic signal. To demonstrate the function of the technique described in the previous section, it was applied to a signal that was synthetically constructed, and consisted of turbulent and non-turbulent parts. Finally, the ε_{ERR} derived using the new technique is compared with the true turbulence dissipation rate error, $\varepsilon_{ERR\ TRUE}$, used to construct the synthetic turbulence spectrum.

Application of the New Statistical Turbulence Analysis to a signal consisting of turbulent and non-turbulent parts

First, a signal consisting of a turbulent part and a non-turbulent part, i.e., with added noise, was constructed. The turbulent part of the signal was obtained by applying backward Fourier transform to the ideal turbulence spectrum obtained from the *Heisenberg* (1948) model. The parameters for the model used to obtain the ideal spectrum were: $\varepsilon = 10^0$ mW/kg and $N_\theta = 10^{-7}$ 1/s. These are typical values for the turbulence at the altitude of 80 km for northern polar latitudes. Density and temperature to obtain kinematic viscosity, μ, were taken from *Lübken* (1999) falling sphere experiments. Rocket velocity, v_R, was set to 800 m/s. The constructed signal is shown in Fig. 4.19 in the upper panel, the part with added noise is shown in black, whereas the turbulent part in red. In the middle panel wavelet PSD of the signal obtained with Morlet-24 function is shown. The Cone Of Influence (COI) is shown as checkered area. Three global wavelet PSDs for three bins, marked with shaded areas in the upper and middle panels, are shown in the lower panel. The selected bins are connected with the corresponding parts of wavelet PSD with arrows. The leftmost global PSD is obtained from the non-turbulent part of the signal separated from the turbulent signal. The middle global PSD is obtained from the non-turbulent part of the signal, adjacent to the turbulent signal. The rightmost global PSD is obtained from the turbulent part of the signal. In the global PSD plots the ideal turbulence spectrum, P_{MOD}, used to construct the turbulent part of the signal is shown with green lines. Spectra obtained using the wavelet analysis, P_{WLT}, are shown with black lines. Spectra resulting from applying the new analysis, that is the fitted spectra, are shown with red lines (P_{FIT}). For each spectrum fitting ranges are marked with orange vertical dashed lines. Inner scale, l_0, for P_{FIT} is marked with vertical red dashed line (only for the turbulent spectrum) and for P_{MOD} with vertical green dashed line. The global wavelet spectra of the turbulent signal exhibit noise at the level $L_{NS} \approx 10^{-8}$ [%^{2}/Hz], which agrees with typical noise levels obtained during calibrations of the CONE instrument in the vacuum chamber.

It can be seen, that the global wavelet PSD obtained for the turbulent part of the constructed signal represents the model very well (i.e. P_{FIT} coincides with P_{MOD}, l_0 values for P_{MOD} and P_{FIT} are almost identical). The two spectra obtained from the part of the signal with added noise are non-turbulent. In other words, for these spectra, the fit converged, but they are rejected by the criteria described in Sec. 4.5, namely Criteria 1, 2, 4, and 5. This means, that for these spectra e.g., the l_0 value lies outside the fitting ranges. When comparing the two non turbulent spectra it can be seen that the spectrum coming from part of the signal adjacent to the turbulent part is affected by the turbulence signatures in the low frequency range. This is caused by the fact that the applied wavelet function already covers part of the turbulent signal when shifted along the signal. Still, this spectrum is classified as a non-turbulent one.

To summarize, it was shown that the New Statistical Turbulence Analysis can detect the turbulent signal with the appropriate strength (i.e. turbulence dissipation rate, ε). For the signal with added noise adjacent to the turbulent signal no turbulence is detected.

How the atmospheric structures are reflected in the measured spectra

To investigate the influence of the real atmospheric turbulence on the measured spectra, a case study for two flights, namely ECOMA-09 conducted on 19th December 2010, and

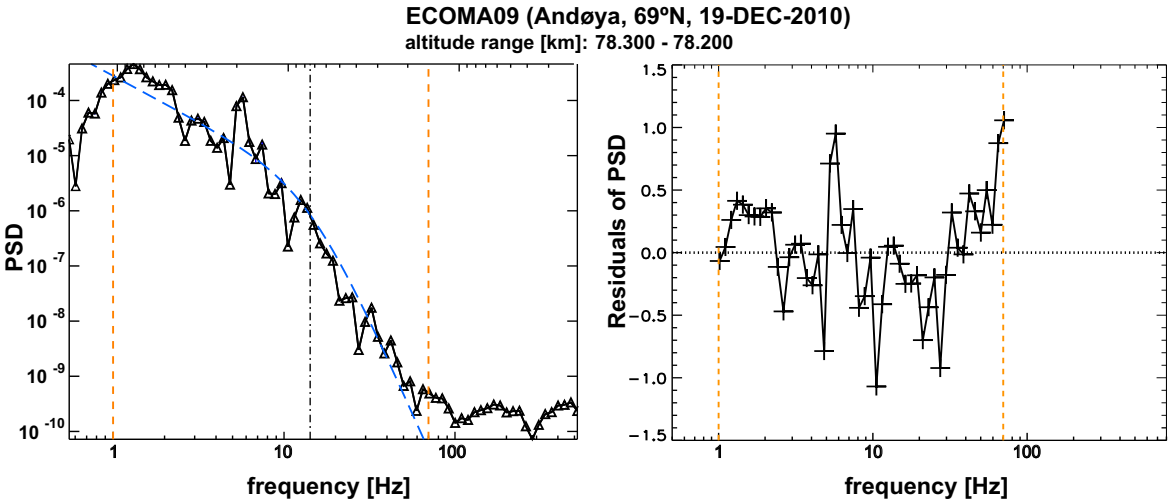

Figure 4.20 The left panel shows a typical global wavelet power spectrum of the 100 m altitude bin in the region exhibiting turbulence. This spectrum comes from measurements taken during ECOMA-09 flight in the altitude range 78.2 - 78.3 km. Black triangles connected with the black line show measured spectrum, P_{EXP}. The blue dashed curve shows the fitted spectral model of *Heisenberg* (1948), P_{FIT}. Fitting ranges, are shown as vertical orange dashed lines. Black vertical dot-dashed line shows turbulence inner scale, l_0. In the right panel residuals of this global PSD calculated in the log-space as $P_{EXP} - P_{FIT}$ are shown inside of the fitting ranges.

ECT-02 conducted on 28 July 1994, will be investigated. These flights were conducted in winter and summer respectively. The ECOMA-09 flight is described and the obtained $\varepsilon(z)$ profile is shown in *Szewczyk et al.* (2013). The ECT-02 flight is part of the ECHO campaign which was described in *Lübken et al.* (1996). Overall, 67 spectra in 100 m altitude bins, that were considered as turbulent spectra were obtained for ECOMA-09 flight and 26 spectra were obtained for ECT02 flight. The results agree with the general (climatological) turbulence occurrence rate. An example turbulent spectrum from ECOMA-09 flight is shown in Fig. 4.20, in the left panel. The plot shows global wavelet power spectrum (P_{EXP}) of the density residuals obtained for 100 m bin (78.2 - 78.3 km) as black connected triangles. The fitted spectral *Heisenberg* (1948) model (P_{FIT}) is shown as a blue dashed line. Fitting ranges are indicated with the orange dashed vertical lines. The turbulence inner scale, l_0, obtained from the fit is shown as dashed-dotted black vertical line. In the right panel of the figure, the residuals of the P_{EXP} are shown after subtraction of fitted model in the log-scale, using formula $P_{EXP} - P_{FIT}$. This is done only in the fitting ranges, shown as vertical orange dashed lines. This procedure was repeated for each turbulent spectrum from the ECOMA-09 flight and as well ECT-02 flight. The results are shown in Fig. 4.21, where the distribution of $P_{EXP} - P_{FIT}$, obtained from all the turbulent spectra from ECOMA-09 flight is shown with black crosses with a Gaussian fitting shown as a blue line. The same is shown for ECT-02 flight with orange crosses with Gaussian fitting shown as a red line. The standard deviation for Gaussian fit for the winter flight is $\sigma_{SD} = 0.55$ and for the summer flight, $\sigma_{SD} = 0.50$, and mean value for both flights $\mu \approx 0$. This shows that by adding randomly distributed noise with $\sigma_{SD} \approx 0.50$ to the ideal spectrum obtained from the *Heisenberg* (1948) model, one can obtain the synthetic turbulence spectrum, P_{TURB}, that imitates the turbulent global wavelet power spectra observed in the atmosphere. We use this result for further validation

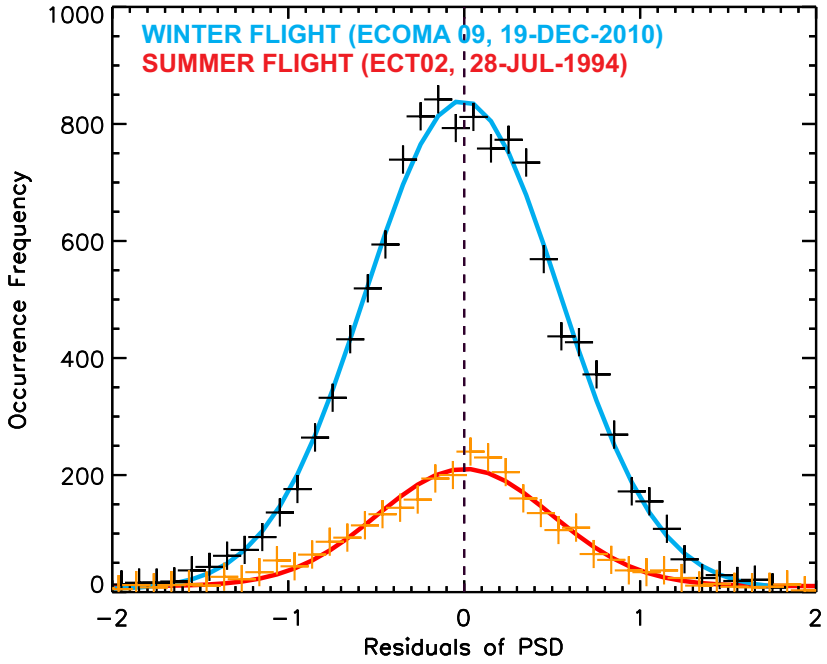

Figure 4.21 Plot showing the distribution of the residuals, $P_{EXP} - P_{FIT}$, obtained in log-space from all the turbulent spectra obtained during ECOMA-09 flight (black crosses) and ECT-02 flight (orange crosses). As a blue line Gaussian function with $\mu = 0.0091$ and $\sigma_{SD} = 0.55$ is fitted, as a red line Gaussian function with $\mu = 0.0067$ and $\sigma_{SD} = 0.50$ is fitted.

of the ε_{ERR} derived using the New Statistical Turbulence Analysis.

Validation of ε_{ERR} values using synthetic turbulence spectra

The next study aims to estimate the quality of the error derivation technique developed in this work. For this purpose, the ε_{ERR} obtained in the fitting process of the New Statistical Turbulence Analysis (i.e. calculated error) were compared with the true error, $\varepsilon_{ERR\ TRUE}$, derived as:

$$\varepsilon_{ERR\ TRUE} = |(\varepsilon_{MOD} - \varepsilon_{FIT})/\varepsilon_{MOD}| \tag{4.7}$$

where ε_{MOD} is the value used for the construction of the ideal turbulence spectrum, and ε_{FIT} value is obtained after fitting the *Heisenberg* (1948) model into synthetic turbulence spectra, P_{TURB}, obtained from this ideal spectrum. The synthetic turbulence spectra are produced by adding normally distributed noise, with $\sigma_{SD} = 0.50$ and mean value $\mu = 0$, to the ideal turbulence spectra in the log-scale. In Fig. 4.22 the ideal turbulence spectrum obtained from the *Heisenberg* (1948) model, P_{MOD}, is shown as a green line. With the black crosses, connected with the black line, the example synthetic turbulence spectrum, P_{TURB}, obtained from this ideal spectrum with added noise is shown. The fit obtained by applying the New Statistical Turbulence Analysis to P_{TURB} is shown as a red solid line (P_{FIT}). With the orange dashed vertical lines fitting ranges are shown. Turbulence inner scale, l_0, is shown with dashed-dotted vertical line for the ideal spectrum (green) and spectrum fitted with the New Statistical Turbulence Analysis (red).

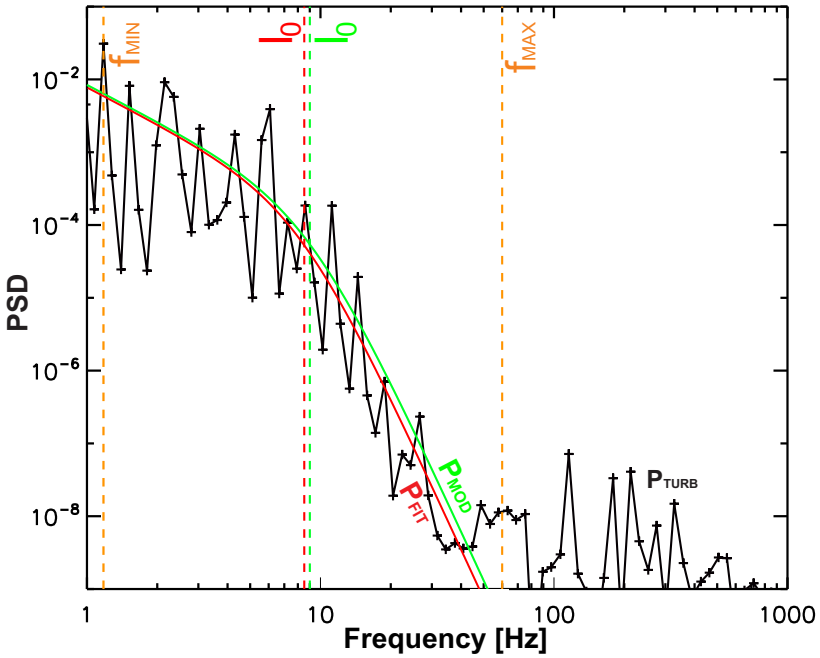

Figure 4.22 An example synthetic turbulence spectrum. Green line shows the ideal turbulence spectrum obtained from *Heisenberg* (1948) model, P_{MOD}. Black triangles, connected with black line show the synthetic turbulence spectrum, P_{TURB}. The red line shows the fit obtained using the New Statistical Turbulence Analysis, P_{FIT}. Orange dashed vertical lines show fitting ranges. Dashed vertical line shows the turbulence inner scale, l_0, for ideal spectrum (green) and for the spectrum obtained using New Statistical Turbulence Analysis (red).

Next, 10000 synthetic turbulence spectra, P_{TURB}, were constructed. The parameters for the ideal spectrum, P_{MOD}, for the construction of the synthetic turbulence spectra are: $\varepsilon_{MOD} = 10^0$ mW/kg, $N_{\theta MOD} = 10^{-7}$. These are typical values for the turbulence observed at the altitude of 80 km at northern polar latitudes. The kinematic viscosity is calculated using the density and temperature data obtained from *Lübken* (1999) falling sphere experiments. The added real turbulence noise has parameters of $\mu = 0$ and $\sigma_{SD} = 0.50$ as estimated above. For each spectrum New Statistical Turbulence Analysis was applied, and resultant turbulence dissipation rate value, ε_{FIT}, with error ε_{ERR} was calculated. The mean value obtained from 10000 spectra for $< \varepsilon_{FIT} >= 1.02 \cdot 10^0$ mW/kg , which is very close to the input value of $\varepsilon_{MOD} = 10^0$ mW/kg. The true error value for turbulence dissipation rate, $\varepsilon_{ERR\ TRUE}$, is obtained by comparing ε-values obtained from the ideal spectrum, P_{MOD}, and fitted spectrum, P_{FIT}, using Eq. 4.7.

The value for $\varepsilon_{ERR\ TRUE}$ was compared with the calculated ε_{ERR}, derived in the analysis for each of the 10000 spectra. The histogram of the $\varepsilon_{ERR}/\varepsilon_{ERR\ TRUE}$ values is shown in Fig. 4.23. Only for few spectra ($\approx 8\%$) the obtained $\varepsilon_{ERR\ TRUE}$ value is smaller than the calculated ε_{ERR} (i.e. values larger than one, marked with the orange dashed line in Fig. 4.23). This means that for 92% of the spectra ε_{ERR} represents the true dissipation rate error correctly. The rest of the ε_{ERR} values overestimates the $\varepsilon_{ERR\ TRUE}$ (up to 50%). The mean ε_{FIT} value was very close to the ε_{MOD} value. It has to be pointed out that the synthetic turbulence spectra used for this comparison (i.e. the exemplary one shown

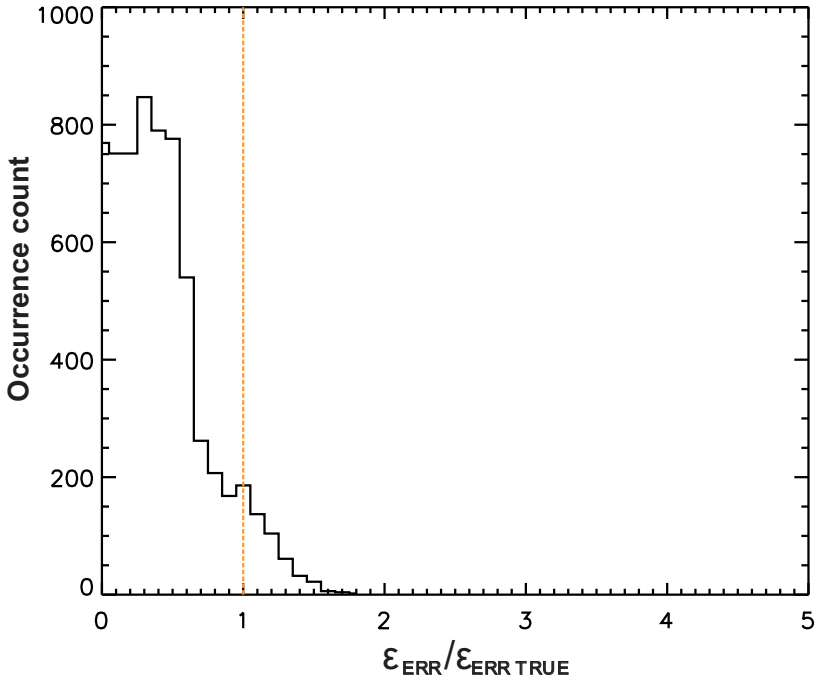

Figure 4.23 The histogram of the $\varepsilon_{ERR}/\varepsilon_{ERR\ TRUE}$ values.

in Fig. 4.22) looks more noisy than the actual spectra measured in the atmosphere. This influences the fit by increasing the ε_{ERR}.

Finally, using synthetic data constructed from turbulent and non-turbulent parts the ability of the New Statistical Turbulence Analysis to detect turbulence layers was demonstrated. In particular it was shown, that the analysis detects turbulence in the turbulent part of the signal with appropriate ε value, and does not detect turbulence in the adjacent, non-turbulent part of the signal. Afterwards, using the case study for winter and summer, the effect of the real atmospheric turbulence on the measured spectra was estimated. Using this estimation, set of 10000 synthetic turbulence spectra was created and the ε_{ERR} values were obtained using the New Statistical Turbulence Analysis. The result was compared to the true error value, $\varepsilon_{ERR\ TRUE}$, obtained from Eq. 4.7. A mean value of $\varepsilon_{FIT} = 1.02$ mW/kg derived from 10000 synthetic turbulence spectra was very close to the input value of $\varepsilon_{MOD} = 1$ mW/kg, and the ε_{ERR} values were properly calculated.

Chapter 5.

Geophysical results

In Chap. 3 main mechanisms for creation of MILs were described. One of these mechanisms, proposed by *Liu et al.* (2000) is that very vigorous turbulence, of at least 240 K/day, can create a MIL event by itself. Such high ε-values were detected during the ECOMA09 flight with an accompanying strong "upper" MIL. Results from this flight are described in the first part of this chapter.

These unusually high ε-values were never detected during flights analyzed using Fourier analysis in winter and very rarely in summer (e.g., *Lübken*, 1993, 1997; *Lübken et al.*, 2002). In Chap. 4 the New Statistical Turbulence Analysis is described which uses wavelet analysis technique to derive turbulent parameters, i.e. ε. Using this technique detects much higher ε-values in the mesosphere, mainly due to the superior vertical resolution of this new analysis approach. In the second section of this chapter, the turbulence dissipation rate's, ε, climatologies and statistics obtained using the New Statistical Turbulence Analysis from all the flights conducted between 1990 and 2014 are given. Also, the experimental results are compared with the results obtained using KMCM (Kühlungsborn Mechanistic Circulation Model).

Using the turbulence parameters obtained with the New Statistical Turbulence Analysis also dependence of ε on variability dissipation rate, N_θ, can be found. In Sec. 2.7 a theoretical limit for ε in terms of N_θ is derived. The experimental results for this dependence are given in App. E.

Finally, since the CONE/TOTAL sensors measure temperature and density in the same volume, in addition to the turbulence parameters, buoyancy frequency, N, mean profiles for summer and winter are derived and presented in App. F.

5.1. Simultaneous observations of a Mesospheric Inversion Layer and turbulence during the ECOMA-2010 rocket campaign

The Sec. 5.1 was published in Annales Geophysicae, number 31, pages 775 - 785, year 2013, under the title: "Simultaneous observations of a Mesospheric Inversion Layer and turbulence during the ECOMA-2010 rocket campaign" and is repeated in this thesis.

5.1.1. Campaign overview

The final sounding rocket campaign of the ECOMA project, ECOMA-2010, (see *Rapp*, 2009, for a project overview and payload description) took place from 19 November to 19 December 2010 at the north-Norwegian Andøya Rocket Range (69 ° N, 16° E). During this campaign three instrumented sounding rockets were launched, namely, ECOMA07 on

4 December 2010, ECOMA08 on 13 December 2010, and ECOMA09 that was launched on 19 December 2010 at 02:36 UTC.

Temperature and turbulence profiles were measured in situ using the CONE instrument onboard the ECOMA payload. Both temperature and turbulence parameters are derived from the same neutral density data. Also, the ALOMAR RMR- and Na-lidars were continuously operated whenever weather permitted, yielding among other things, continuous temperature measurements near the launch site and several hours before and after the flight. Additionally, the data from the Microwave Limb Sounder (MLS) experiment on the Aura satellite which overpassed the launch area around the rocket launch time was analyzed to investigate spatial variability of the temperature field.

In this section measurement results obtained during the last rocket launch labeled ECOMA09 are presented and discussed. These simultaneous and true common volume in-situ measurements of temperature and turbulence supported by ground-based lidar observations reveal two Mesospheric Inversion Layers (MIL) at heights between 71 and 73 km and between 86 and 89 km. Strong turbulence was measured in the region of the upper inversion layer, with the turbulent energy dissipation rates maximizing at 2 W/kg, corresponding to heating rate of $\approx$ 200 K/day. This upper MIL was observed by the ALOMAR Weber Na lidar over the period of several hours. The spatial extension of this MIL as observed by the MLS instrument on board AURA satellite was found to be more than two thousand kilometers. The presented analysis suggests that both observed MILs could possibly have been produced by local heating owing to neutral air turbulence.

The basic information about MIL, the mechanism of its creation and its classification are described in Chap. 3. The MIL described here is defined as the region in the mesosphere with continuous, positive temperature gradient. Therefore, it does not include the layer above it

5.1.2. Experimental results

In-situ temperature measurements

In-situ measurements performed during the downleg of the ECOMA09 flight provided simultaneous and high-resolution measurements of neutral air densities, temperatures and turbulence.

The temperature profile obtained using the CONE sensor between 70 and 110 km is shown in Fig. 5.1a in black. The lowest temperatures of $\sim$ 175 to 190 K appear at heights between 79 and 84 km. The measured temperature profile reveals two pronounced temperature perturbations at heights between 71 and 74 km and between 86 and 89 km, respectively. The amplitude of the upper perturbation, i.e., at 86 to 89 km, reaches values of 44 K and is 3 km thick. The lower perturbation is somewhat weaker, i.e., it has an amplitude of 20 K and a thickness of 3 km. The entire temperature profile, including regions with the temperature perturbations, also reveal clear signatures of gravity waves. These observed gravity waves, are also seen in the lidar data. They have likely been excited in the troposphere, and propagate upwards with increasing amplitude. Finally they break in the upper atmosphere, being one of the sources of the turbulence.

In Fig. 5.1a the CONE measurements are compared with temperatures obtained using the ground-based lidars. The results of temperature measurements with the RMR- and Na-lidars are shown as orange and blue profiles interrupted at $\sim$ 82 km height. That is, above $\sim$ 82 km the profiles represent Na-lidar measurements and below that height, the measurements by the RMR-lidar. The orange profile shows the data from the time of the ECOMA09 flight

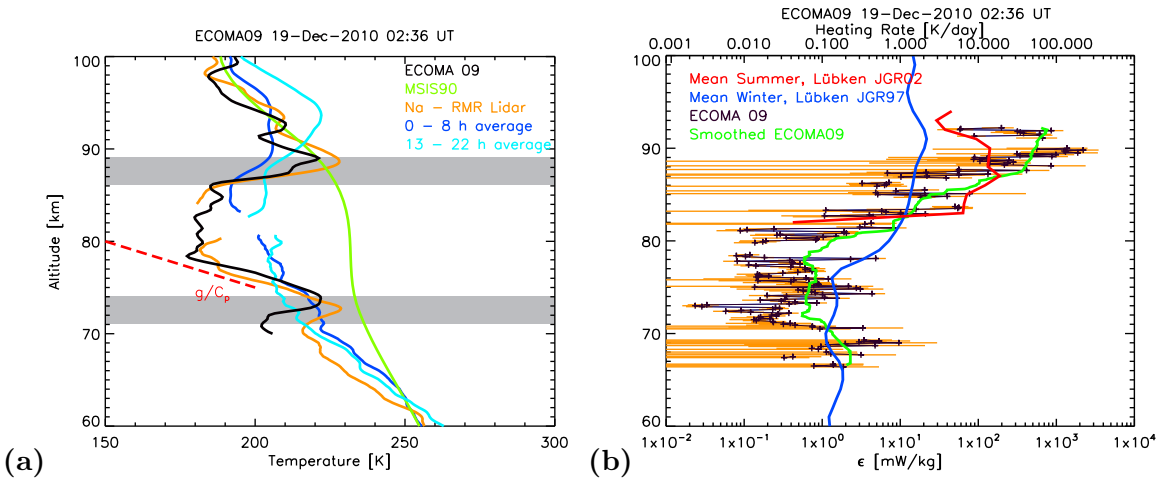

Figure 5.1 **(a)** Neutral temperatures measured during the ECOMA09 flight (black line). Climatologies MSISE-90 is shown as green line. ALOMAR RMR - Na lidar measurements are plotted with orange line, with a gap between 81 and 84 km where no measurements were available. The dashed red line shows the adiabatic lapse rate (see text for details). Altitude ranges where MIL where observed are shaded. **(b)** Turbulence energy dissipation rates (and corresponding heating rates on upper abscissa) measured in-situ during ECOMA09 flight (black crosses). Mean summer and winter profiles taken from *Lübken et al.* (2002) and *Lübken* (1997) are shown in red and blue, respectively. The high resolution ε-measurements were smoothed over 5 km to compare to the summer and winter "climatologies" (after *Szewczyk et al.*, 2013).

averaged over 30 min, whereas the blue profile shows an eight hour mean of the day of the rocket launch.

The lidar measurements reveal very similar wave structures to those measured with CONE. The small differences between the lidar and the in-situ temperature measurements can likely be attributed to horizontal distance of ~ 50 km between the lidar beam, that was pointing towards the direction of the rocket's ascent, and the volume probed by CONE on the descending part of the trajectory. Additionally, a reference profile from the MSISE-90 model (*Hedin*, 1991) is shown in Fig. 5.1a by the green line.

The two major temperature perturbations described above are clearly seen in both the in-situ measurements and the 30-min integrated lidar profile and are reminiscent of temperature inversion layers. However, it is not possible to qualify these temperature perturbations as inversion layers only based on single profiles. However, the 8-h mean profile obtained from the Na-lidar measurements, i.e., the upper part of the blue line, ultimately suggests that a mesospheric inversion layer (MIL) was caught by the in-situ measurements, because this temperature enhancement clearly persists even after averaging over eight hours. For this reason, hereafter the upper temperature enhancement is referred to as to the upper MIL. The time evolution of both temperature perturbations is further investigated in the next section utilizing the lidar measurements. The averaging of the lidar temperature over the whole day and over the second part of the day only was made (not shown here). They do not agree with the CONE data as well as the averaged temperature from the first part of the day, MIL exhibits there at higher altitudes. Assuming that the strong turbulence ceased in the second part of the day, this result agrees with our conclusions that the observed upper

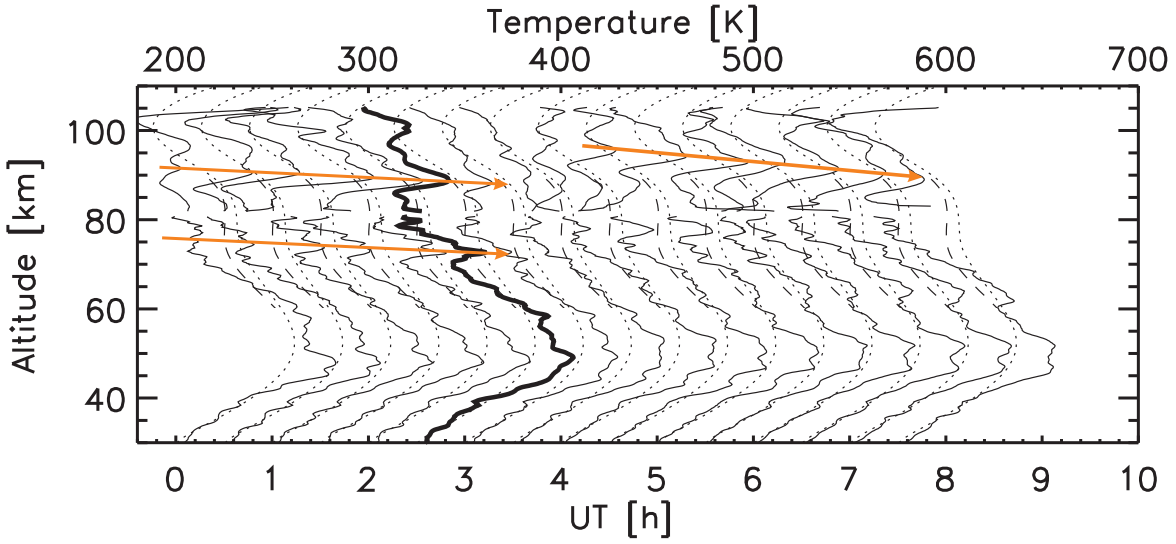

Figure 5.2 Combined RMR and sodium resonance lidar temperature profiles for first eight hours of 19 December 2010 obtained from ALOMAR observatory. The profiles are averaged over one hour periods. Please note the temperature perturbation downward progression denoted with the orange arrows (after *Szewczyk et al.*, 2013).

MIL was the local enhancement of the temperature caused by turbulence inside of the larger and long persisting MIL.

At heights between 74 and 79 km, i.e., right above the lower temperature enhancement and, at the same time below the upper MIL, the measured temperature profiles reveal an adiabatic to super-adiabatic lapse rate (compare with the adiabatic lapse rate shown by the red dashed line in Fig. 5.1a). Also, above the upper MIL, i.e., at heights between 89 and 95 km, the measured temperatures reveal an adiabatic gradient. These gradients are suggestive of turbulence activity in those regions and have repeatedly been observed at the topside of the inversion layers (*Whiteway et al.*, 1995; *Duck et al.*, 2001).

The lower MIL looks more similar to the many lidar observations and resembles much the temperature and turbulence structure and adiabatic layer reported in *Lehmacher and Lübken* (1995), although with even lower epsilon values.

Lidar temperature measurements

In this section, the time development of the temperature field is considered to see whether the in-situ observed temperature enhancements are indeed snapshots of inversion layers or simply represent large gravity wave amplitudes.

Figure 5.2 shows combined results of temperature measurements carried out simultaneously by the RMR- and sodium resonance lidars during the day of the ECOMA09 rocket launch. The upper abscissa shows temperature for the first profile and the other profiles are shifted by 25 K and represent subsequent measurements in 30 min intervals to allow to see the time evolution of the temperature enhancements. The lower abscissa shows time in UTC when the measurement was done. The bold profile represents the measurements done at $\sim$ 02:36 UT, that is at the time of the ECOMA09 launch. The integration time for each shown profile is 1 h. The dotted profiles shown in Fig. 5.2 represent the MSIS90 model and the dashed are the climatology by *Lübken* (1999) which is based on a large number of falling

sphere (FS) measurements (*Schmidlin*, 1991). As in Fig. 5.1a, the upper part of the profiles in Fig. 5.2 represents measurements done with the Na-lidar, whereas the lower part, i.e., below ∼ 82 km, shows the RMR-lidar observations.

As it is seen in Fig. 5.2, the upper MIL, i.e., between 86 and 89 km, was observed by the ALOMAR sodium resonance lidar for several hours around the rocket launch as it was already seen from the 8-h mean temperature profile in Fig. 5.1a. This MIL was already detected at ∼ 00:00 UT between ∼ 88 and 92 km and descended during the period of at least 4 h, however, afterwards its behavior is not clear due to larger uncertainties between ∼ 82 and ∼ 85 km. Then, at 05:00 UT there is already a new MIL formed at ∼ 95 km which propagates downward with the similar rate. The maximum amplitude of the MIL in the Na-lidar data was ∼ 50 K and thickness of 8 km.

The measurements in Fig. 5.2 also reveal that the lower temperature perturbation (i.e., between 74 and 79 km height), with amplitudes of up to 20 K and a few kilometers thickness, is observed for a few hours before and about an hour after the rocket launch. The RMR-lidar started to measure on 18 December at 23:37:30 UTC, that is three hours before the rocket launch and the lower temperature perturbation was already there as detected by the lidar. Based on this relatively long duration (∼ 3 h) this lower temperature enhancement was also qualified as a MIL. The measured temperature profiles also reveal oscillations with smaller amplitudes associated with short period gravity waves.

In Fig. 5.2 one can see a downward phase progression of both MILs which is marked by the arrows. Using simple analysis e.g., applied by *Dao et al.* (1995), that is by fitting a polynomial to the temperature profiles and looking on the temperature maxima, one can find that the upper MIL (86 to 89 km at the time of the rocket launch) descends approximately at a rate of 15 km per 12 h. The lower MIL descends with the same speed and is located ∼ 15 km below the upper one.

Satellite temperature measurements

Figure 5.3 shows temperature measurements obtained with the MLS over the rocket launch site close to the time of the ECOMA09 flight. Two temperature transects taken over Scandinavia were chosen. In the right panel of Fig. 5.3 transects geometries are shown by black arrows.

The red stars mark points where individual profiles were retrieved and revealed an inversion layer. The green diamond shows the location of the Andøya Rocket Range. The upper and the lower left panels show the temperature field as observed by the MLS along the tracks 1 and 2, respectively. The launch site is also denoted on the lower left panel by the vertical orange line.

From these observations it is clearly seen that the upper MIL detected by the rocket-borne instruments and the ground-based Na-lidar near the island of Andøya extents over at least 3000 km along the track 2. Since such a huge spatial extension of the temperature enhancement is a typical feature of the MILs (e.g., *Meriwether and Gerrard*, 2004), this ultimately confirms that the temperature inversion layer is observed between 86 and 89 km.

The MLS measurements reveal an amplitude of the upper MIL of about 20 K and a thickness of ∼ 10 km. It is already known from previous studies (e.g., *Wu et al.*, 2003), that the amplitude of the temperature inversion layers obtained from MLS measurements are significantly underestimated in comparison with e.g., lidar observations, due to its coarse altitude resolution. Also, due to poor resolution of MLS, the lower temperature perturbation observed both in-situ and by the RMR-lidar was not detected by the satellite borne

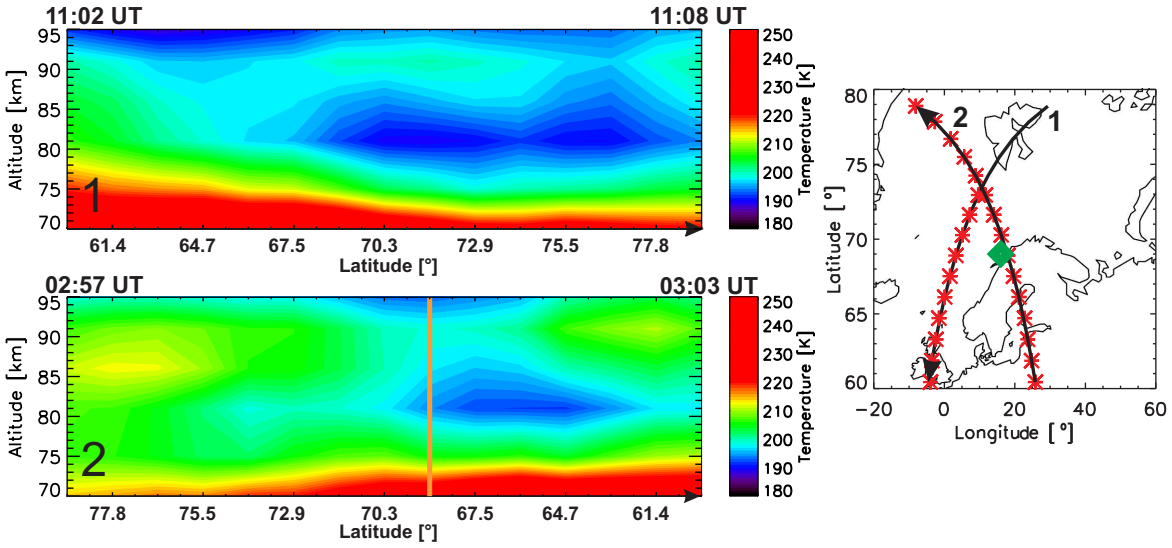

Figure 5.3 Two transects of satellite MLS temperature measurements taken on 19 December 2010 over Scandinavia. For convenience transects are numbered both on plots and in the inset map with their direction denoted with arrows. Launch area is marked as an orange line on the lower plots and as green rectangle in the inset map. On the inset map parts of the transects over which MIL is observed are marked with red stars. Over each transect its start and end time is shown (after *Szewczyk et al.*, 2013).

experiment.

In-situ turbulence measurements

The results of the turbulence measurements during the ECOMA09 flight are shown in Fig. 5.1b.

The turbulence energy dissipation rates, ε are shown in Fig. 5.1b as black crosses with orange error bars. Wavelet turbulence detection technique results in an effective altitude resolution of 100 m (*Strelnikov et al.*, 2003). Also, the derived ε-profile was smoothed to achieve the resolution of the available mean summer and winter climatologies by *Lübken et al.* (2002) and *Lübken* (1997), respectively, which is 5 km. The smoothed ε-profile is shown in Fig. 5.1b as the green line. The mean summer and winter turbulence energy dissipation rates are shown in Fig. 5.1b by red and blue profiles, respectively.

Energy dissipation rates are converted to heating rates (upper abscissa) using Eq. 2.8. The resultant heating rates are represented as upper abscissa in Fig. 5.1b.

As one can see, turbulence was observed over a broad altitude range from $\sim$ 65 to 93 km, which is typical for the winter polar mesosphere (*Lübken*, 1997). Also, the absolute values are close to the mean winter state at altitudes below 87 km. However, at altitudes around 90 km the energy dissipation rates measured during the ECOMA09 flight are extremely large and exceed even typical summer values.

It is interesting to compare the measured turbulence dissipation rates with the results of the temperature measurements shown in Fig. 5.1a. At heights of $\sim$ 75 and $\sim$ 90 km, i.e., on the topside of the two observed inversion layers, turbulence exhibits local maxima. Especially the upper MIL is accompanied by the extremely strong turbulence with a dissipation rate of $\sim$ 2 W/kg which is equivalent to a heating rate of 200 K/day. According to numerical

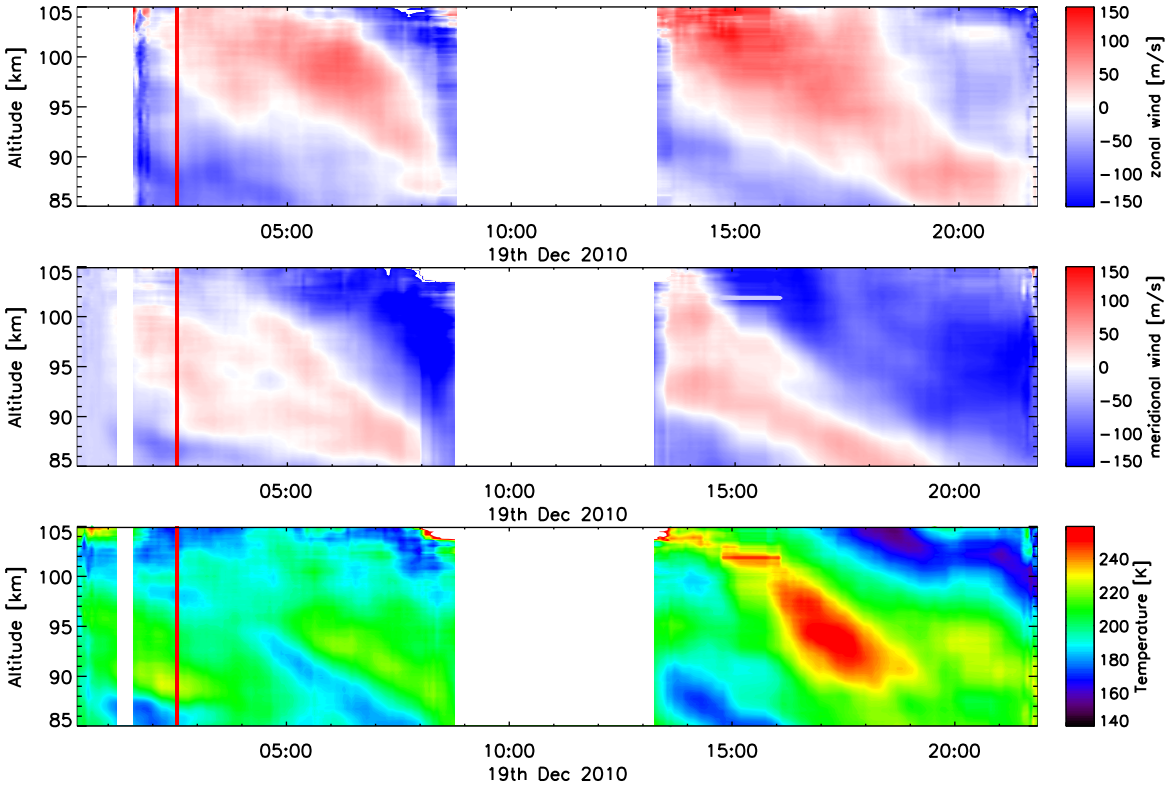

Figure 5.4 Zonal (upper panel) and meridional (middle panel) winds and temperatures (lower panel) as measured by the Alomar Na-lidar on 19 December 2010. The blank areas on the plots mark the periods where no data were available. With red vertical line launch time of the ECOMA09 rocket is marked (after *Szewczyk et al.*, 2013).

simulations by *Liu et al.* (2000), turbulence characterized by a heating rate of $\sim$ 10 K/h (i.e., 240 K/day) is sufficient for producing inversion layers alone. However, in the model of *Liu et al.* (2000) the dissipative heating rate itself is insignificant when compared with the rate of heating due to turbulent diffusion. In the simpler model by *Whiteway et al.* (1995) the dissipation heating rate is much larger, exceeding in the upper part of MIL heating due to turbulent diffusion. The turbulent heating and cooling were parameterized in this model in terms of the eddy diffusion coefficient for heat transport, K_{h}. For the region with MILs heating due to dissipation of 20 K/day occurred. This model is applied, however, in the region were lower MILs are occurring.

In the region around 69 km, it also exhibits peak in the turbulence data, with values exceeding those of the turbulence associated with the lower MIL. However, no MIL occurs at this altitude. The source of this turbulence is either wind shear or GW breaking. The wind data are not available for this altitude, hence it is not possible to investigate the latter.

It is also worth to note, that the used turbulence detection technique is not sensitive to turbulence in the regions where the temperature profile exhibits an adiabatic lapse rate (e.g., *Lehmacher and Lübken* (1995), Sec. 5.2.4 of this thesis) and, therefore, can underestimate the actual ε-values. This implies that the turbulence dissipation above the inversion layers could be even stronger than what is observed with the CONE instrument.

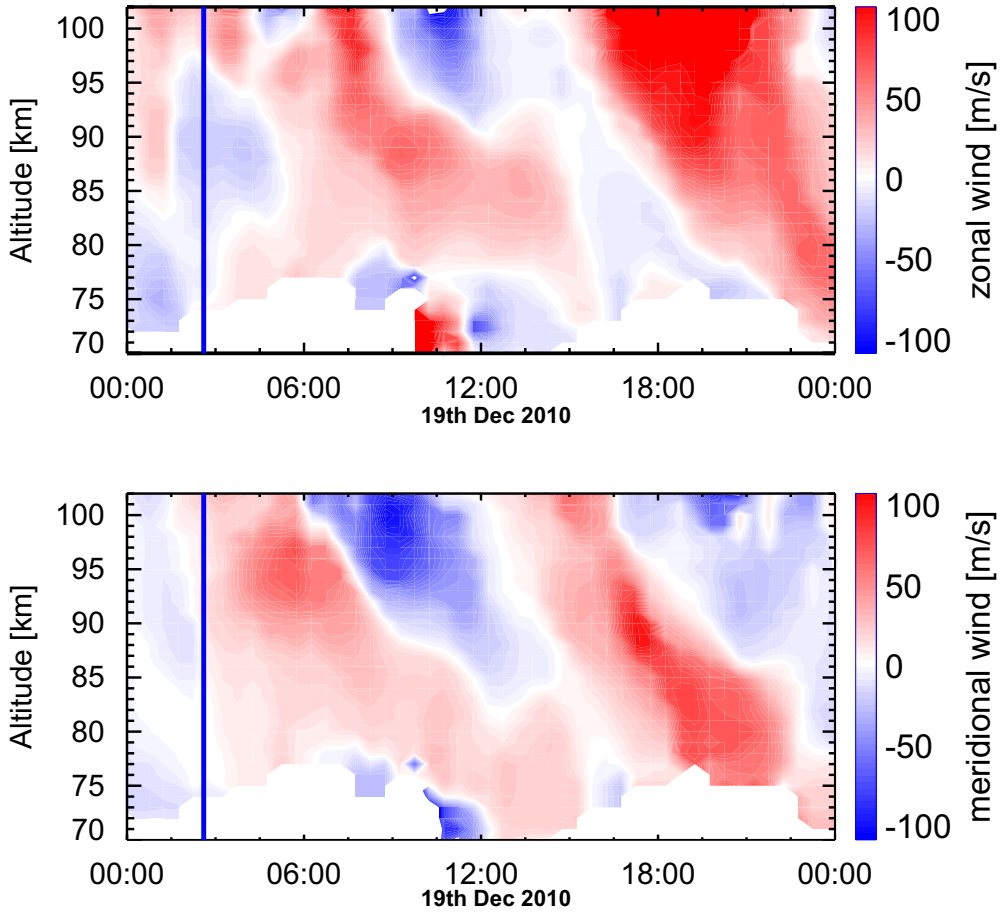

Figure 5.5 One day snapshot of wind measurements by Saura MF radar. Upper panel: zonal wind. Lower panel: meridional wind. The blue lines mark time of the ECOMA09 launch (after *Szewczyk et al.*, 2013).

Na-lidar and radar wind measurements

As described in App. G.1, the ALOMAR Na resonance lidar is capable of measuring horizontal winds. The results of the lidar wind measurements during the day of the rocket launch are shown in Fig. 5.4.

It shows measurements of zonal winds, meridional winds and temperatures in the top, middle and lower panels, respectively. These measurements reveal pronounced downward phase progression which is most probably associated with tides (*Hoffmann et al.*, 2008; *Stevens et al.*, 2010; *Hultgren et al.*, 2011). Since lidar measurements are weather dependent and there was no luck to have long enough measurements for proper tidal analysis, wind measurements done by the Saura MF radar which is located close to the launch site are further considered (see App. G.2).

The zonal and meridional wind measurements made by the Saura MF radar are shown in the upper and lower panel of Fig. 5.5, respectively. One can see the same downward phase progression as in the lidar observations (Fig. 5.4, two upper panels). The radar measurements cover a time period of several months around the rocket launch time which, in turn, makes it possible to perform deeper analysis with respect to tidal activity in the MLT region.

The wind measurements by SAURA MF radar during the entire month (December) were

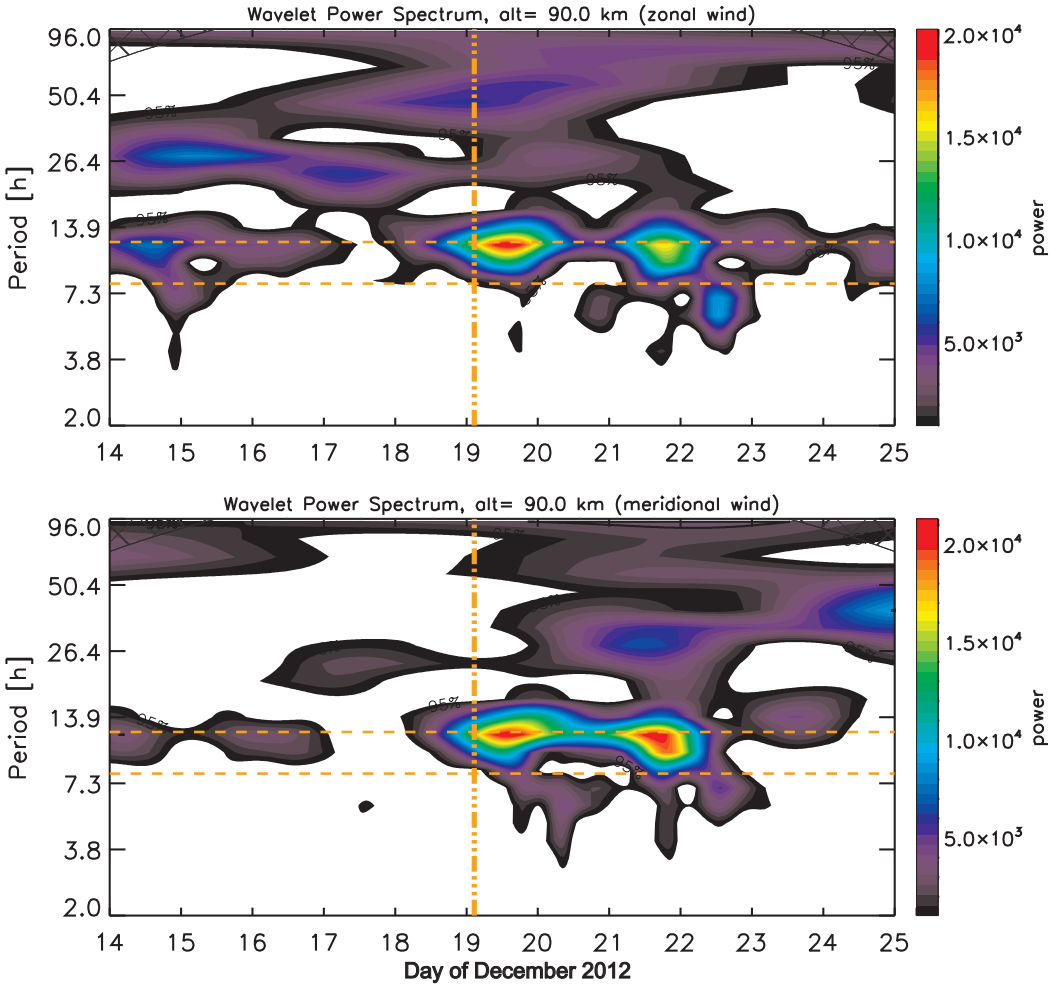

Figure 5.6 Wavelet spectra of the the wind measured by the SAURA MF radar during December 2010. Upper panel: zonal wind. Lower panel: meridional wind. Horizontal orange lines mark 12 and 8 h periods. Vertical lines mark launch time of ECOMA09 sounding rocket. Cross hatched areas mark cone of influence, i.e., uncertain part of the spectra affected by edge effects (after *Szewczyk et al.*, 2013).

analyzed with respect to the dominating wave activities at heights between 82 and ∼ 100 km. This analysis showed that a 12 h wave in both zonal and meridional wind measurements was dominating over the time period from 18 to 24 December. This is demonstrated by the wavelet power spectra shown in Fig. 5.6, where power spectrum for zonal and meridional wind components taken at 90 km height are shown in upper and lower panel, respectively. The horizontal dashed orange lines mark periods of 12 and 8 h and the vertical lines show time of the ECOMA09 launch. It can be seen that although a signature of the semidiurnal tide is present during the entire period from 18 to 24 December, the strongest activity of the 12 h wave was observed from 19 through 22 December.

5.1.3. Discussion

The discussion has to address two different formation mechanisms of the upper MIL. The first was initially proposed by *Whiteway et al.* (1995) and basically explains the formation of MIL by turbulent heating. The second goes back to *Dao et al.* (1995) and was summarized e.g., by *Meriwether and Gardner* (2000) and explains the formation of a MIL via the interaction of tides with gravity waves. Both these scenarios are discussed in detail e.g., in the review article by *Meriwether and Gerrard* (2004).

The adiabatic temperature gradient above both inversion layers detected in presented case has been repeatedly observed by lidars (e.g., *Whiteway et al.*, 1995; *Thomas et al.*, 1996; *Cutler et al.*, 2001; *Duck and Greene*, 2004; *Liu et al.*, 2004; *Collins et al.*, 2011) and has most often been the only argument regarding turbulence activity associated with temperature inversions. However, *Thomas et al.* (1996) performed simultaneous observations of MILs with Rayleigh lidar and mesospheric echoes by VHF radar and concluded that both dynamic and convective instabilities (and, therefore, the generated turbulence) are associated with these phenomena. Moreover, they found that the radar echoes occurred both above and below the temperature maxima of the MILs. Simultaneous in-situ measurements of both temperature and turbulence presented here do not only confirm that point, but also allow to investigate the morphology of the MLT turbulence in connection with the thermal structure.

The upper MIL observed in presented case by in-situ and Na-lidar soundings between 86 and 89 km was accompanied by extremely strong turbulence. The highest values of the energy dissipation rates, $\varepsilon \approx 2$ W/kg, were detected between 89 and 90 km height, that is on top of the MIL. Also, turbulence was detected almost continuously in the entire height range of this MIL (86 to 89 km). However, already at heights between 88 and 89 km the energy dissipation rate is an order of magnitude smaller than only 1 km above. Moreover, this gradient in the ε height-profile persists down to the bottom of the MIL, i.e., to 86 km altitude. So the energy dissipation rate increases by 3 orders of magnitude inside the inversion layer within only 3 km height range from 86 up to 89 km. The largest measured ε-values of 2 W/kg corresponds to a heating rate of $\sim$ 200 K/day is close to the model results by *Liu et al.* (2000) who showed that a heating rate of $\sim$ 10 K/h (240 K/day) is sufficient to produce a thermal structure in the mesosphere commonly associated with MIL. However, as mentioned before, heating rates described in *Liu et al.* (2000) are produced mainly with the turbulent diffusion, with the rate of heating due to dissipative heating (shown here), being insignificant. In the simpler model by *Whiteway et al.* (1995) the dissipative heating exceeds the heating rate due to turbulent diffusion in the upper part of MIL.

Whiteway et al. (1995) emphasized that it is not the high value of turbulence dissipation rates that plays the key role in creating MILs, but the rapid increase of the dissipation with height, i.e., the vertical gradient of the ε-profile. This point is consistent with our high resolution turbulence measurements.

There are two sources of turbulence relevant for presented study, namely wind shear and breaking of gravity waves. According to *Fritts et al.* (2003) shear instability causes turbulence confined to a narrow layer, whereas gravity-wave breaking causes turbulence progressing with the phase of the wave and can, therefore, spread over larger height range. Also, the effects of turbulence due to shear instability should be observed for longer time. On the other hand, numerical simulations by *Fritts et al.* (2003) show that turbulence layers produced by dynamical instabilities reveal maximum viscous dissipation rather in the middle of the layer, whereas thermal dissipation occurs at the edges. For a GW-breaking event such a spatial separation of the peak turbulent kinetic energy and thermal dissipation diminishes while the

event develops in time.

The vertical shear of the horizontal wind ($\sqrt{(du/dz)^2 + (dv/dz)^2}$) is calculated from the Na-lidar measurements for the time of the rocket launch and found a local maximum of 0.05 1/s close to 90 km height. This would imply low values of Richardson number, Ri, in this region, which is further confirmed by our stability analysis further below.

Presented turbulence measurements revealed that turbulent kinetic energy dissipation occurred in a broad altitude range which is typical for a GW-breaking event. The maximum of the dissipation measured with the CONE lies just on the top of the upper inversion layer. The adiabatic lapse rate between 89 and 91 km, i.e., above the upper MIL suggests that turbulence was active for some time before the rocket sounding. Also, lidar observations do not show any dominant GW-frequencies, but rather a broad spectrum of different frequencies that reveal large amplitudes (not shown here) and, therefore, can potentially break generating turbulence.

Thus, the morphology of the turbulent structures suggests that GW-breaking was an active source of turbulence. Also the wind shear was peaking around the upper part of the inversion layer. These results support the interpretation that turbulent heating was involved in the formation of the in-situ observed inversion layer.

Also, as noted by e.g., *Liu et al.* (2004), the net effect of turbulence activity on the thermal structure is heating below and cooling above. This should result in an inversion layer and an adiabatic temperature gradient on top similar to what is observed for the described case and what has been reported from a vast number of previous observations. So, associating the observed temperature enhancement between 86 and 89 km with turbulent heating, is consistent with the presented measurements.

This can further be investigated considering stability of the background atmosphere and by comparing it with the observed behavior of the MILs. The simultaneous measurements of horizontal winds and temperatures makes it possible to derive both the buoyancy frequency, N^2, which characterizes the convective or static stability of the background atmosphere and the Ri that can be used to identify dynamically unstable regions. The results are shown in Fig. 5.7 where the color red shows regions with $N^2 < 0$ and dark and light blue areas represent $Ri < 1/4$ and $Ri < 1$, respectively. The $Ri < 1/4$ is a favorable condition for instability to start, whereas $Ri < 1$ describes still favorable condition for instability to persist (*Woods*, 1969). The two downward progressing upper MILs are marked by the black arrows similar to what shown in Fig. 5.2. It is seen that both the convective ($N^2 < 0$) and dynamically ($Ri < 1/4$) unstable regions reveal downward phase progression similar to those observed in the temperature and wind fields and also the upper MIL (between 86 and 89 km).

There is, however, a zone in Fig. 5.7 marked with a black oval of a downward progressing unstable region which is not associated with a temperature enhancement, but rather with a near adiabatic laps rate below the inversion layer. The in-situ measurements show that there was also some turbulence activity below the inversion layer.

The lower panel of Fig. 5.4 shows the same measurements as shown in the upper part of Fig. 5.2, but during the entire day of the ECOMA09 launch. This plot reveals that the upper MIL observed by rocket-borne instrument, that descended during next ~ 3 h, appeared three times during that day. These upper MILs descended at a very similar rate, however, as shown by two upper arrows in Fig. 5.2, that speed was not exactly the same. Also it was shown in Sect. 5.1.2 that strong semi-diurnal tidal activity was observed during the day of lidar and rocket measurements.

The MIL observed during ECOMA09, is already inside of strong tidal activity, but seems to be increased even further by the strong turbulence during this time.

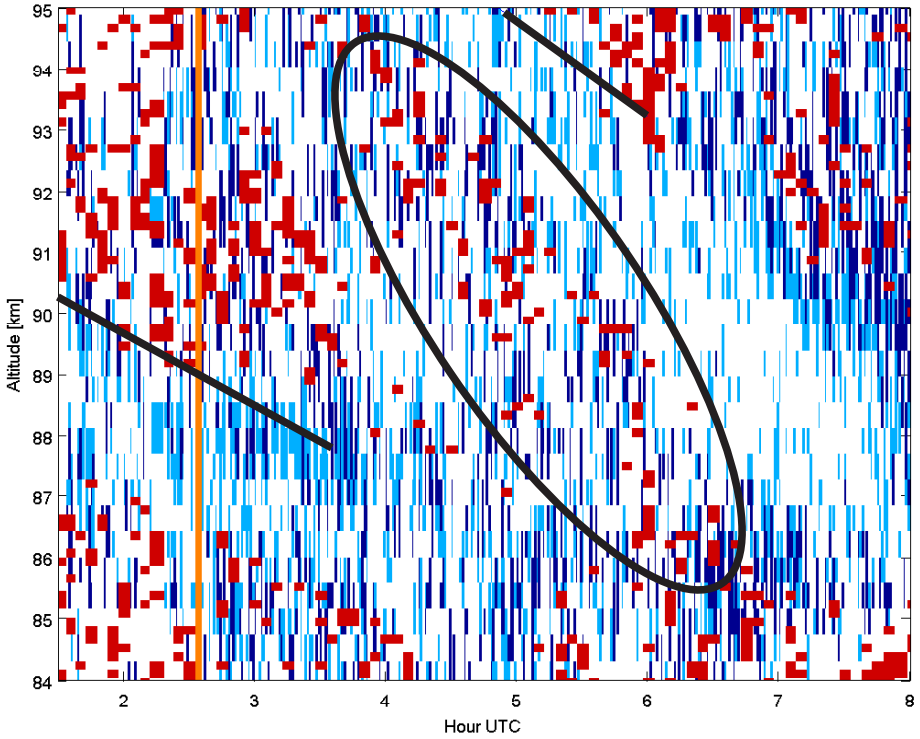

Figure 5.7 Stability analysis from ALOMAR Na-lidar measurements of winds and temperature for 19 December 2010. The color red represents regions that are convectively unstable (N^2 <0), dark blue points represent regions of dynamical instability ($0 < Ri < 1/4$), and the light blue areas are regions with $Ri < 1$. Orange vertical line marks time of the ECOMA09 launch (after *Szewczyk et al.*, 2013).

One of the arguments against turbulence heating as an important physical process (e.g., *Meriwether and Gardner*, 2000) in development of the inversion layers was based on the mean dissipation values published by *Lübken* (1997) and *Lübken et al.* (2002). However, there are two points that have to be taken into account. The first is that the profile of the mean ε-values for winter was smoothed over 5 km. Also each single point represents an average of "turbulent" cases with some very high ε-values and even "non-turbulent" cases. When at a given height there was no turbulence, ε was set to zero. The second point is that the vertical resolution of the analysis technique used for those turbulence "climatologies" had an altitude resolution of 1 km. As was later shown by *Strelnikov et al.* (2003), applying a new analysis technique (the wavelet analysis), the same measurements reveal a more structured ε-profile with regions of much higher ε-values, but in shorter than 1 km height ranges. In the frame of this thesis (see next section) all the available rocket turbulence data were re-analyzed using the wavelet analysis. This revealed much more high ε-values for the individual rocket flights. Final argument by e.g., *Duck and Greene* (2004) was that the adiabatic lapse rate associated with inversion layers was not reported from rocket measurements by e.g., *Lübken* (1997).

It is interesting to note that satellite measurements with MLS show that the upper MIL appears over Andøya, i.e., the launch site, on 18 December and disappears after 24 December (not shown here). This is in line with the occurrence of the 12 h wave activity as shown in Fig. 5.6.

The lower MIL observed by in-situ instrument and the RMR-lidar revealed the same descent rate as its upper counterpart and persisted for near the same time period (Fig. 5.2). The vertical separation of these layers was about 16 km which is too short for a vertical wavelength of tidal waves. The topside of this lower MIL is also accompanied by moderate local turbulence with relatively sharp gradients. Its morphology is very much reminiscent of GW-breaking event.

This analysis suggests that both MILs, i.e., between 71 and 73 km and between 86 and 89 km, observed in-situ were produced by strong turbulence which occurred in the region of non-linear interaction of gravity waves and tides.

Concluding, during the ECOMA09 sounding rocket flight in-situ temperature profile that revealed two temperature enhancements, between 71 and 73 km and between 86 and 89 km altitudes was measured. Simultaneously, the ALOMAR Weber Na- and RMR-lidars observed the same temperature perturbations. The long duration lidar observations showed that this temperature perturbations persisted for several hours such that they were qualified as inversion layers (MILs). Additionally, satellite-borne observations with MLS showed that the upper MIL extended over an extended mesoscale region and lasted for 7 days which again confirms that this was a MIL. On the other hand, the lidar observations show that this MIL repeatedly appeared and descended during several hours which is not captured by the satellite instruments.

Similarities in the morphology of the turbulent layers with theoretical expectations for GW-breaking events and, also the presence of the wind shear suggests that turbulent heating is a likely mechanism for the generation of the observed MILs.

However, presented analysis cannot exclude the influence of tides and that the observed MILs resulted from a nonlinear interaction of tides and gravity waves as described by (e.g., *Meriwether and Gerrard*, 2004; *Liu et al.*, 2000). However, the results ultimately show that if turbulence heating and downward heat transport were not the only mechanisms that generated the observed MIL, they at least significantly amplified the MIL.

Finally, it can be noted that a series of rocket flights should be conducted during the temporal development of an inversion layer in order to monitor and better understand the role of turbulence during these various stages.

5.2. New Statistical Turbulence Analysis - results

In the previous section we considered a case study based on only one flight, and present an ε profile obtained during this flight. Now let us see the MLT turbulence's picture on climatological scale by investigating data from all the available rocket flights. From 1990 to 2014 a series of 35 sounding rockets were launched from ARR (Andøya Rocket Range, 69^oN) and Esrange (68^oN) to investigate the dynamic state of the MLT region. From these flights 32 were conducted in ARR, and 3 were conducted in Esrange (list of all the flights is given in App. A). ARR was renamed to ASC (Andøya Space Center) on 25th April 2014. An ionization gauge, TOTAL until 1993 and CONE afterwards (App. C), mounted on board to these sounding rockets measured neutral density fluctuations down to very small spatial scales. The high resolution of these measurements makes it possible, using wavelet analysis, to unambiguously deduce turbulence parameters, i.e. turbulence dissipation rate, ε. The whole procedure of obtaining ε with its measurements errors, named in this work New Statistical Turbulence Analysis, is described in Chap. 4. *Lübken* (1997) and *Lübken et al.* (2002) published turbulence climatologies (mean ε profiles) for winter and summer

obtained from the flights taken before the year 2000. Their analysis was done based on 12 flights for winter and 8 flights for summer and using the Fourier analysis (App. D.1). In this section the turbulence climatologies for winter and summer from all the available flights obtained using the New Statistical Turbulence Analysis are presented and compared with the climatologies obtained by *Lübken* (1997) and *Lübken et al.* (2002). The discrepancies between the results obtained in the frame of this work and results obtained with the previous analysis are discussed. The turbulence layer's thickness, turbulence inhomogeneity, and turbulence measured in spite of the presence of the adiabatic temperature lapse rate are discussed. Finally, the extended statistics for turbulence variability, turbulence occurrence rate and turbulence layer thickness are shown.

The flights, for which results were published by *Lübken* (1997) and *Lübken et al.* (2002) are referred henceforth as the "old flights" (all the flights conducted before year 2000). The flights conducted starting from year 2000 are referred henceforth as the "new flights". It should also be noted that the New Statistical Turbulence Analysis uses wavelet analysis technique and is referred here also as the "new analysis", in contrary to Fourier analysis used by *Lübken* (1997) and *Lübken et al.* (2002) referred here as the "old analysis".

5.2.1. Comparison of ε mean profiles for winter and summer obtained using the new and old analyses

First, we start with the mean ε altitude profiles for winter and summer obtained from only the old flights using the new analysis. The new results are compared with the results obtained by *Lübken* (1997) and *Lübken et al.* (2002). The mean profiles obtained using the new analysis are determined by taking the mean of ε-values at a given altitude. For the altitudes where no turbulence was detected ε was set to 0. The mean profiles were afterwards smoothed over 5 km, for better comparison with *Lübken* (1997) and *Lübken et al.* (2002), which use the same smoothing. The mean profiles obtained using the new analysis are afterwards additionally smoothed over 2 km to exclude small scale variations.

In Fig. 5.8 ε climatology for winter obtained using the new analysis from only the old flights (light blue line) is compared with the climatology published by *Lübken* (1997) (dark blue line). General agreement between the new and old analysis can be seen, however the mean profile obtained using the new analysis has values lower up to two orders of magnitude below 70 km. The *Lübken* (1997) climatology exhibits a maximum around 91 km, whereas the new climatology exhibits a maximum around 89 km. The new ε mean profile is raising exponentially from 60 to 89 km, which was not observed for *Lübken* (1997) mean profile. Above 89 km the new mean ε profile is decreasing. Black dashed lines show minimum and maximum limits for the ε-values obtained using the new analysis, and smoothed over 5 km. The individual ε-values obtained using the new analysis shown as blue dots, and using the old analysis shown as green rectangles fall within approximately the same ε range. The difference is that the ε-values obtained using the new analysis occur with larger maximum and lower minimum values. This is caused by the fact, that the lower vertical resolution of the old analysis smooths the highest and lowest ε-values. The black dotted line shows the theoretical ε_{MIN} profile discussed in Sec. 2.6.

In Fig. 5.9 the ε climatology for summer obtained using the new analysis for only the old flights (red line) is compared with the climatology published by *Lübken et al.* (2002) (violet line). The mean profile obtained using the new analysis exhibits generally lower values. This is especially visible between 83 and 85 km, where one partially large value obtained by *Lübken et al.* (2002) at 85 km shifted the old mean profile to the right. The maximum

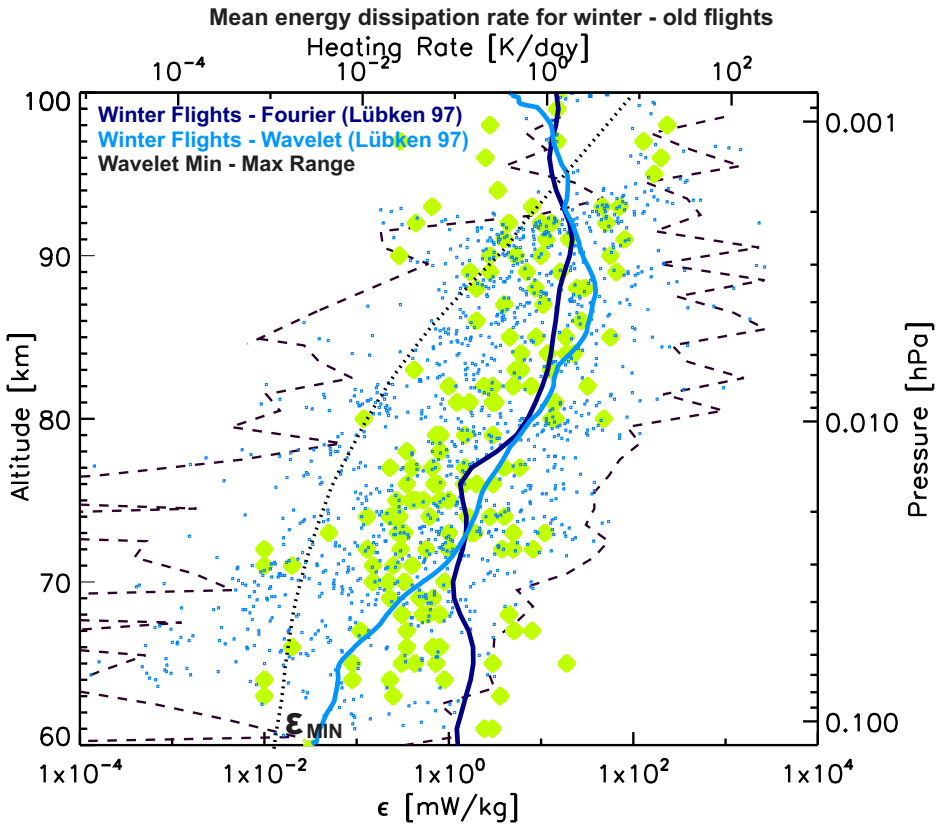

Figure 5.8 Mean profile of turbulent energy dissipation rate, ε, obtained using the new analysis (light blue line) from only the flights analyzed in *Lübken* (1997) paper (dark blue line for comparison). Heating rates on the top abscissa. On the right ordinate approximate atmospheric pressure is shown as a vertical coordinate. Blue dots: all the ε-values from the old flights detected using the wavelet analysis. Green rectangles: Fourier results from *Lübken* (1997). Black dashed lines show minimum and maximum limits for individual ε-values obtained using the new analysis, smoothed over 5 km. Black dotted line shows the theoretical ε_{MIN} profile.

ε-values in both climatologies lie between 87 and 90 km. Black dashed lines show minimum and maximum limits for the ε-values obtained using the new analysis, and smoothed over 5 km. The individual ε-values obtained using the new analysis shown as red dots, and using the old analysis shown as violet rectangles fall within approximately the same ε range. The difference is that the new analysis was able to detect several turbulent layers with small ε-values, and several turbulent layers below 82 km, which were not detected by the old analysis. Black dotted line shows the theoretical ε_{MIN} profile discussed in Sec. 2.6.

Despite general agreement between the mean profiles obtained using the new and old analysis, some differences are apparent. The origin of these discrepancies is discussed in the next subsection.

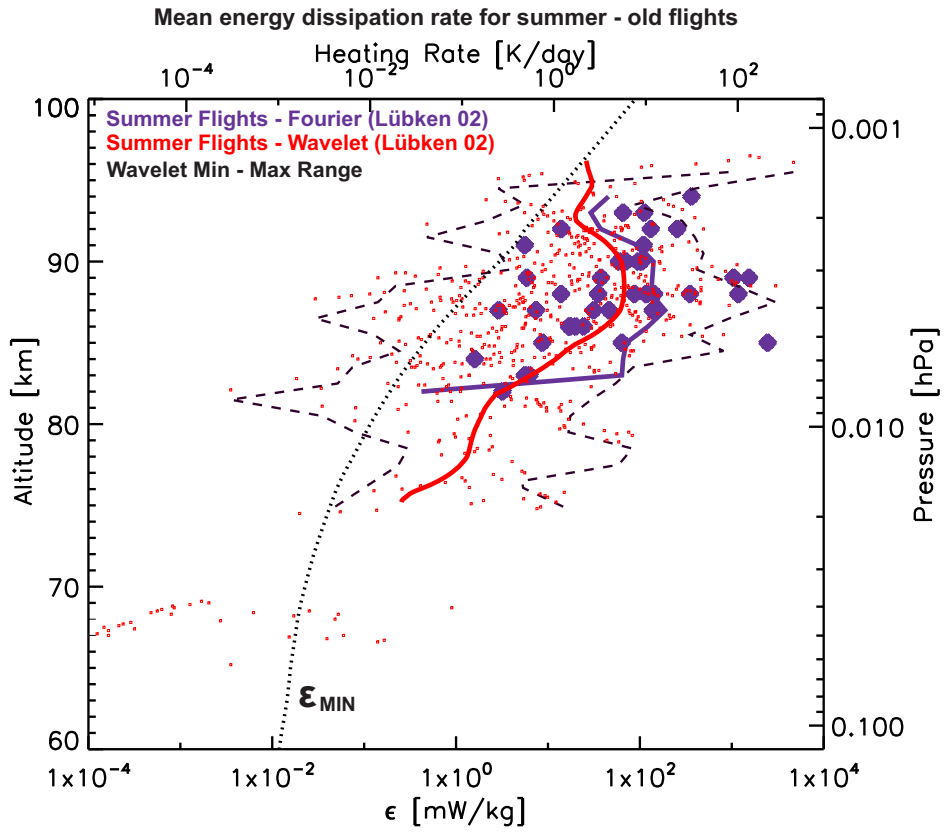

Figure 5.9 Mean profile of turbulent energy dissipation rate, ε, obtained using the new analysis (red line) from only the flights analyzed in *Lübken et al.* (2002) paper (violet line for comparison). Heating rates on the top abscissa. On the right ordinate approximate atmospheric pressure is shown as a vertical coordinate. Red dots: all the ε-values from the old flights detected using the wavelet analysis. Violet rectangles: Fourier results from *Lübken et al.* (2002). Black dashed lines show minimum and maximum limits for individual ε-values obtained using the new analysis, smoothed over 5 km. Black dotted line shows the theoretical ε_{MIN} profile.

5.2.2. Discrepancies between the ε-values obtained using Fourier and wavelet technique

The presented mean profiles, as well as the individual values, obtained from the old flights using the new and old analysis exhibit certain differences. For the winter profiles, these are the differences between the old and new profiles below 70 km. The main difference in summer are the turbulent layers detected with use of the new analysis below 82 km. We will now try to investigate the origin of these discrepancies.

The mean ε-profile for winter obtained using the new analysis below 70 km has values lower by as much as two orders of magnitude than the profile obtained using the old analysis (Fig. 5.8). For summer flights the mean ε-profile obtained using the new analysis has generally lower values than the profile obtained using the old analysis (Fig. 5.9). This is especially evident between 83 and 85 km. When analyzing the values obtained using the old analysis for winter and summer in the altitudes where these largest differences occur, large individual ε-values can be observed. Particularly, for winter flights it is the value of $\varepsilon = 20$ mW/kg

at 65 km and for summer flights it is the value of $\varepsilon = 2000$ mW/kg at 83 km. These two particularly high ε-values are higher by more than an order of magnitude than the mean profile at these altitudes. Since the mean profile is smoothed over 5 km, these high ε-values will significantly increase the mean profiles in the adjacent 5 km altitude range. These high ε-values were not observed in these altitudes using the new analysis. Since no detailed data about the flights and the Fourier analysis conducted by *Lübken* (1997) and *Lübken et al.* (2002) is available, it is hard to say where these unusually large values come from.

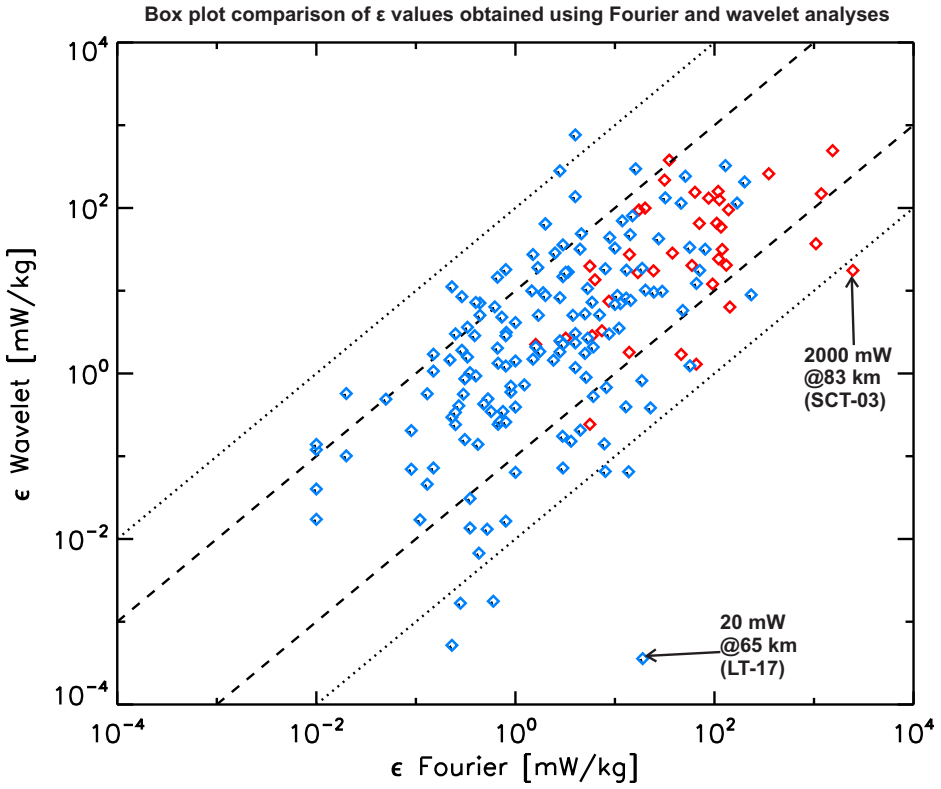

Figure 5.10 The differences in the individual values obtained using the wavelet and Fourier analysis for all the altitudes shown as a correlation plot, with blue rectangles for winter flights, and red rectangles for summer flights.

The differences in the individual values obtained using the wavelet and Fourier analysis are shown in Fig. 5.10 as a correlation plot, with blue rectangles for winter flights, and red rectangles for summer flights. For comparison the results obtained with the wavelet analysis were averaged over 1 km (e.g., as one rectangle the Fourier results at the altitude of 85 km is compared with the mean obtained from the wavelet results in the altitude range from 84.5 to 85.5 km for the same flight). It can be seen that most of the values show agreement within one order of magnitude (marked with dashed lines on the plot) and for very few values the disagreement is more than 2 orders of magnitude (marked as dotted lines). Values with the particularly large disagreement visible in the plot are the values that were discussed in the previous paragraph (i.e. summer value of $\varepsilon = 2000$ mW/kg at 83 km and winter value of $\varepsilon = 20$ mW/kg at 65 km).

To show the differences in the individual values obtained using the new and old analysis an example turbulent layer from DAT84 flight is shown in Fig. 5.11. In the left panel Fourier PSD from the altitude range 87.5 to 88.5 km is shown as a black line. In the right panels two

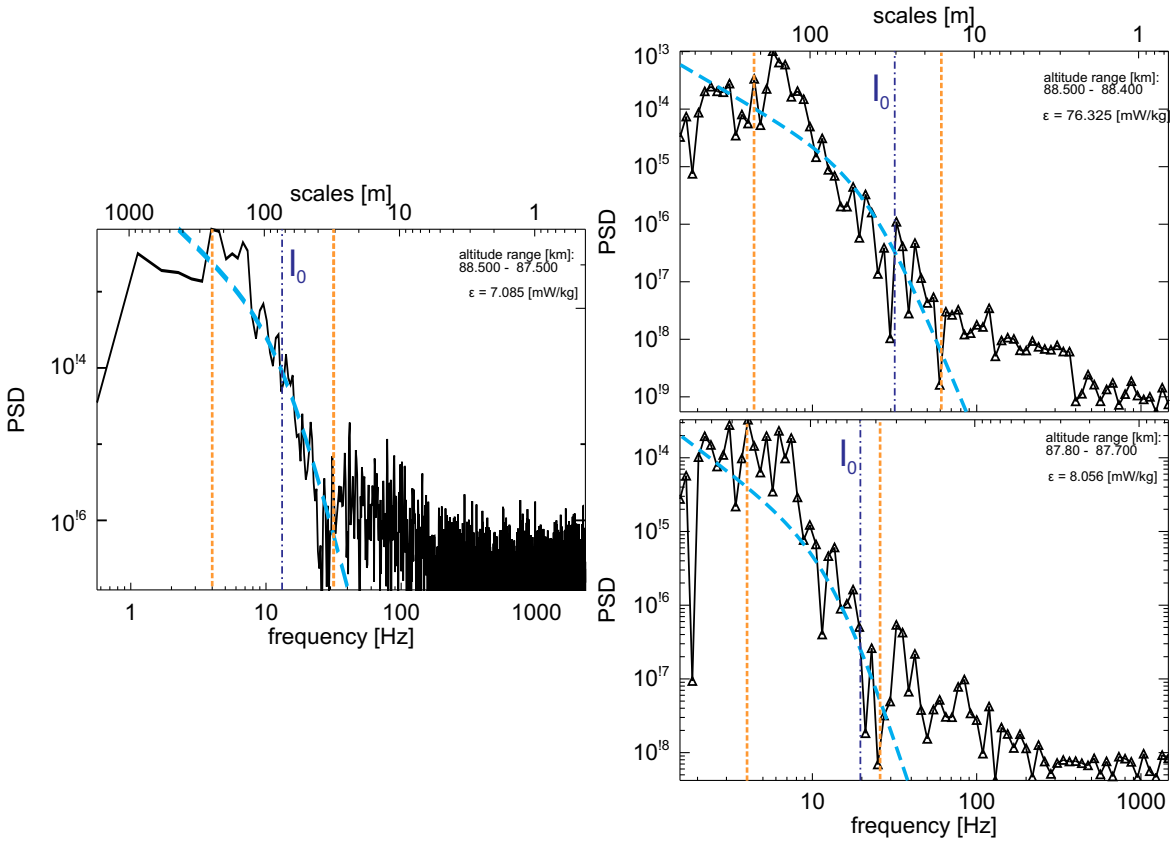

Figure 5.11 Example turbulent layer from DAT84 flight. In the left panel global Fourier PSD of 1 km altitude bin is shown as a black line. In the right panels global wavelet PSDs of the 100 m bins are shown as black triangles connected by the black lines. The fitted spectral *Heisenberg* (1948) model is shown as dashed blue lines. Fitting ranges are shown as dashed vertical orange lines. Inner scale, l_0, derived from the fit, is shown as vertical dashed black lines.

global wavelet PSD of the 100 m bins within this altitude range are shown as black triangles connected by the black lines. The fitted spectral *Heisenberg* (1948) model is shown as dashed blue lines. The inner scale, l_0, derived from the fit, is shown as vertical dashed black line. The ε-values obtained from l_0 are shown in the upper right corner of each plot. It can be seen that the lower wavelet spectrum exhibit similar ε value as the Fourier spectrum. The upper wavelet spectrum exhibits values of one order of magnitude higher. These differences come from the differences in the Fourier and wavelet analysis itself, namely the higher spatial resolution that the wavelet technique allows to achieve.

An example of a summer turbulence layer detected by the new analysis below 82 km is shown in the next subsection. In Fig. 5.13 the wavelet spectra of three 100 m altitude bins in the altitude range from 68 to 69 km are shown, one from inside the 500 m turbulence layer and two from the laminar atmosphere just above and below of this layer. In the Fourier spectrum of the 1 km bin of the same flight in the same altitude range no turbulence is detected. This shows that the wavelet analysis is able to detect thin turbulence layers, which are not detectable by the Fourier analysis.

In conclusion, the differences between the new and old analysis come from different sources.

The mean profiles both for winter and summer show general agreement. The differences in the mean profiles come from singular higher values found using the Fourier analysis at specific altitudes (i.e. summer value of $\varepsilon = 2000$ mW/kg at 83 km and winter value of $\varepsilon = 20$ mW/kg at 65 km). The differences in the individual values come from the differences between the Fourier and wavelet technique itself. Particularly the difference in the altitude resolution means, that we assume that inside of 1 km Fourier bin we have turbulence which is evenly distributed over this one kilometer. This is very rarely the case, as the turbulence is intermittent on scales smaller than 1 km, which is discussed in the next subsection. This means that measurements inside this 1 km bin with 100 m resolution technique will result in different results along this 1 km. It is also possible that inside this 1 km there may exist parts without turbulence. This means altogether, that the mean value of ten 100 m bins does not have to equal the value obtained from the 1 km bin.

5.2.3. Turbulent layer thickness and turbulence layer inhomogeneity

After comparing the ε profiles obtained from the old flights, and before presenting the new climatologies obtained from the full data set, let us consider turbulence layer thickness and turbulence layer inhomogeneity. These are topics of high interest in the MLT region's turbulence study. The old analysis (App. D.1) had 1 km vertical resolution, which obviously limited the minimum detected turbulence layer thickness to 1 km. In this section we show that the new analysis (e.g., *Strelnikov*, 2006, App. D.2), with its vertical resolution of 100 m, is superior over the Fourier turbulence analysis for investigation of the turbulence inhomogeneity and in detecting thin turbulence layers. First theoretical considerations regarding the turbulence layer thickness and turbulence inhomogeneity are presented. Then results obtained from DNS experiments are summarized. Afterwards experimental examples of turbulent layer thinner than 1 km isolated from other turbulent layers, and intermittent turbulent layers are presented. An intermittent turbulent layer is defined here as a region with two or more thin turbulent layers separated by thin laminar layer(s).

The clear air turbulence (CAT) is known to be intermittent and inhomogeneous. *Weinstock* (1978) states that vertical thickness of the intermittent patches of CAT is larger than the turbulence outer scale, L_B. He also states that the scales of inhomogeneity may likewise be larger than L_B. In other words, even intermittent patches of CAT may be approximately homogeneous on the scale of the inertial subrange. *Weinstock* (1978) also states that they were not aware, at that time, of any turbulence patches thinner than L_B. On the contrary, measurements available at that time had indicated that the thickness of CAT for the stratosphere varies from 300 to 800 m for intensities varying from very light to moderate. Some results for strong intensity CAT with thickness of 1.2 km were also mentioned. In works of *Lübken* (1997) and *Lübken et al.* (2002) maximum turbulence layer thickness found was 9 km. Mean outer scale value found using Eq. 2.5 with N, and l_0 values obtained in the frame of this thesis is $L_B \approx 500$ m, with the maximum observed L_B values being on the order of a few kilometers.

Hocking (1999) however states that turbulence can be even more intermittent both temporally and spatially, and very often occurs in thin layers in the middle atmosphere with layer thickness of a few tens of meters out to a kilometer. These thin layers are often separated by regions which are either only weakly turbulent or even laminar. The processes which induce diffusion can themselves be scale dependent. This spatial and temporal intermittency has been demonstrated in *Hocking* (1991, 1996), after adaptation from *Desaubies and Smith* (1982). These authors show how an ensemble of gravity waves can act together to produce

regions of instability separated in height by regions of stability. Examples of experimental studies of such layering are also discussed therein. One of their conclusions was that we must revisualize how large scale turbulent diffusion takes place to understand these problems in more detail.

Fritts and Alexander (2003) presented a review of dynamics of gravity waves in the atmosphere. These authors opined that the greatest advances in understanding of instability and turbulence dynamics accompanying gravity waves in recent years were made possible by the continuing evolution of high-performance computers, which are now capable of DNS of stratified and sheared flows. Such simulations are capable of describing both the transition to turbulence in a geophysical flow and the vorticity dynamics driving the turbulence cascade.

Based on such DNS-studies *Fritts et al.* (2013a) noticed that while there are instances where local instability dynamics appear to be driven by a single GW of large amplitude (and large vertical scale) in the absence of smaller-scale mean or GW structures, the frequent occurrence of turbulence in relatively thin layers suggests that instabilities and turbulence often arise because of superpositions of variable mean and GW motions that may span a range of spatial and temporal scales. In the MLT region superposed GWs arising from many sources, having disparate spatial scales and frequencies, and achieving larger vertical group velocities and amplitudes are often observed. In such environments, multiscale interactions can drive very different dynamics than arise owing to instabilities of individual and superposed GWs. These multiscale dynamics accompanying GW instability arise as a result of GW-fine structure (GW-FS) interactions. Multiscale GW-FS superpositions are ubiquitous throughout the atmosphere (*Fritts et al.*, 2013b).

GW-FS interactions are a subset of more general multiscale interactions among GWs, planetary waves, tides at higher altitudes, and mean wind and stability fields that encompass the mutual influences and evolutions of motions spanning a wide range of spatial and temporal scales. GW-FS interactions arguably occur to varying degrees at essentially all altitudes all of the time. Evidence for potential multiscale influences on GW instability dynamics has increased dramatically as high-resolution profiling capabilities for winds, temperatures, and other dynamical parameters have advanced (*Fritts et al.*, 2013b).

Fritts et al. (2009a) have done an initial DNS of GW-FS dynamics. They employed a number of idealizations of the GW-FS flow. Despite its simplicity, the results of this DNS provide a number of interesting insights into GW-FS interactions that may be relevant to more general superpositions of larger- and smaller-scale, and higher- and lower-frequency, motions throughout the atmosphere. The conclusions *Fritts et al.* (2009a) made and which are particularly interesting for us are the following:

1. instabilities and turbulence occur at vertical scales defined more by the FSs than by the GWs

2. turbulence generation is intermittent and spatially localized following instability onset

3. layered turbulence accompanying various turbulence events leads to sheet and layer structures that closely resemble observations in the atmosphere.

The multiscale dynamics accompanying GW instability arising as a result of GW-FS interactions are also the subject of *Fritts et al.* (2013a) paper. They use DNS to examine the dynamics and energetics of idealized GW-FS interactions. *Fritts et al.* (2013a) confirmed both the roles of small-scale shears and overturning in driving turbulence generation and

the strong departures of such evolutions from GW instability dynamics occurring without FS influences (*Fritts et al.*, 2009b,c). *Fritts et al.* (2013a) further identified "intrusions" comprising superposed GW and FS flows as a principle driver of turbulence events.

Fritts et al. (2013a) also provide indications and/or confirmation of the environments in which GW-FS interactions are most likely to be strong - for example, accompanying large increases in N with altitude, yielding large increases in ε in crossing the polar summer mesopause (*Lübken et al.*, 2002; *Rapp and Lübken*, 2004), as was predicted by *Van Zandt and Fritts* (1989).

The purpose of *Fritts et al.* (2013b) was to examine the characteristics and statistics of ε within the turbulence fields arising in the DNS described in *Fritts et al.* (2013a). Specifically, they defined the dependence of turbulence dissipation morphologies on the turbulence sources and evolutions, quantified the dissipation statistics and their evolutions and correlations in space and time, and discussed the implications of these dissipation fields for measurements of turbulence parameters.

The findings of *Fritts et al.* (2013b) include:

1. dissipation that tends to be much more localized and variable than that due to GW instability in the absence of FS

2. strong influences of FS shears on instability occurrence and turbulence intensities and statistics

3. significant differences between mechanical and thermal dissipation rate fields having potentially important implications for measurements of these flows

4. turbulent dissipation events that are strongly layered in the vertical and lead to sheet-and-layer u structures, owing to stable stratification and velocity FS

To investigate these theoretical statements and DNS experiments results, two examples from the real rocket data are shown, first with a larger, intermittent turbulent layer (with intermittency on the order of hundreds of meters) and a second one with an isolated turbulence layer with thickness of 500 m separated from other turbulence layers by more than 1 km. Two things have to be addressed here: theoretically our turbulence detection technique is not sensitive to turbulence exhibiting on the adiabatic temperature lapse rate (see next Subsection). To avoid this issue, the examples shown are taken from the sections of flights exhibiting a non-adiabatic temperature lapse rates. The other issue is discussed in Sec. 4.6. There it was shown, using a synthetic signal, that wavelet analysis can distinguish turbulent and laminar parts of the signal, i.e. even for the laminar part of the signal, which is adjacent to the turbulent part, no turbulence is detected. Hence the new analysis should be appropriate to investigate turbulence inhomogeneities on the scales of hundreds of meters and to detect isolated turbulence layers smaller than 1 km with proper accuracy.

In Fig. 5.12 an example of an intermittent turbulence layer is shown. This layer was detected during the SCT-06 flight on August 1st 1993 in ARR. The turbulence layer appears from 78.1 to 79.6 km, above and below of these altitudes no turbulence is detected for more than 1 km. A laminar patch inside of this turbulence layer exhibits from 78.4 to 78.8 km. Six wavelet spectra from inside of this turbulence layer and just outside of it are shown in this figure. In these spectra, global wavelet PSD of the 100 m altitude bins are shown as black triangles connected with black lines. The fitted spectral *Heisenberg* (1948) model is shown as dashed blue lines. Fitting ranges are shown as dashed vertical orange lines. The inner scale, l_0, is indicated as vertical dashed black lines only for the turbulent spectra. Spectra

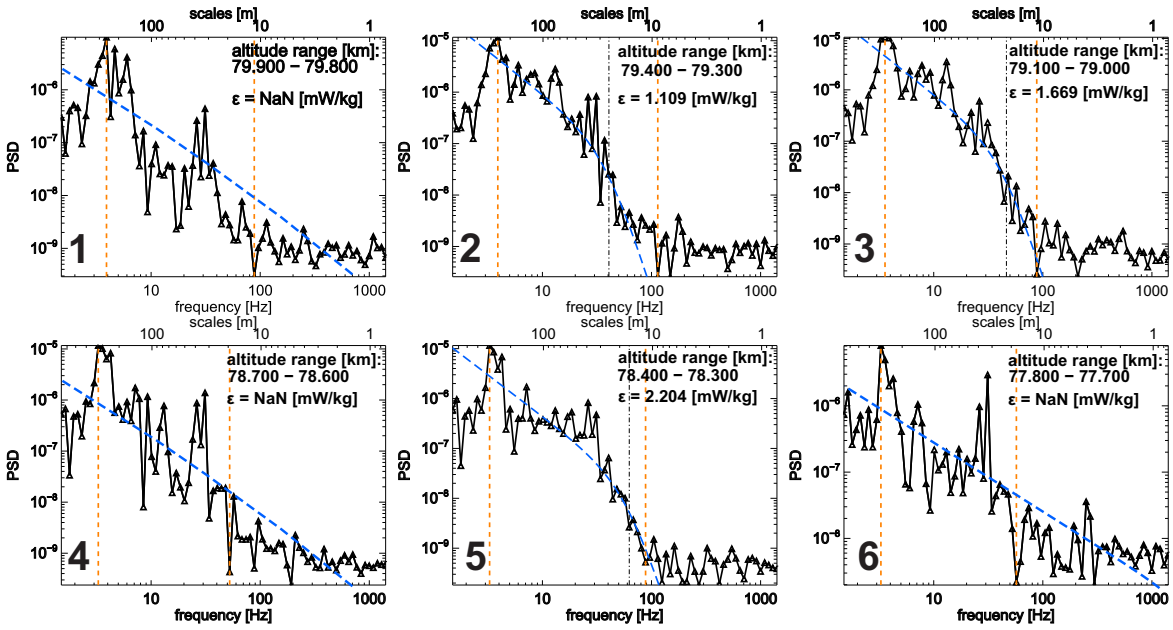

Figure 5.12 Wavelet spectra from an intermittent turbulence layer detected during the SOMI-06 flight of 1st August 1993 in ARR in the altitude range from 78.1 to 79.6 km. Global wavelet PSD of the 100 m bins are shown as black triangles connected with black lines. The fitted spectral *Heisenberg* (1948) model is shown as dashed blue lines. Fitting ranges are shown as dashed vertical orange lines, and inner scale, l_0, as a vertical dashed black line only for the turbulent spectra. Above 79.6 and below 78.1 km no turbulence is detected for more than 1 km.

are numbered 1 to 6. Spectra number 1 and 6 are taken from the non-turbulent part of the atmosphere just above and below the turbulence layer, respectively. Spectra 2, 3, and 5 are taken from the turbulent parts of the layer. Between these turbulent parts there is a laminar patch, which is shown as a spectrum number 4. This demonstrates that the new analysis can investigate the turbulence inhomogeneity on scales as small as 100 m.

In Fig. 5.13 an example of an isolated turbulence layer of 500 m thickness is shown. This layer was detected during the MDMI05 flight on 6th July 1997 in ARR in the altitude range from 68.2 to 68.7 km. Outside of this turbulence layer no turbulence is detected for at least 1 km above and below. Markings are the same as in Fig. 5.12. Global wavelet PSD from 100 m of this turbulence layer is given in the upper right panel. Above and below this layer no turbulence was detected for more than 1 km. Global wavelet PSD from these non-turbulent parts of the flight are given in the upper-left and lower-left panels. It can be seen that using Fourier analysis, i.e. as shown in the lower-right panel of Fig. 5.13, no turbulence is detected between 68 and 69 km. This shows that the wavelet analysis is able to detect thin isolated turbulence layers, which are not detectable for the Fourier analysis.

In conclusion, theoretical considerations show that turbulence can occur in the intermittent layers on the scales down to tens of meters or down to the turbulence outer scale L_B. Mean outer scale value found using Eq. 2.5 with l_0 and N values obtained in the frame of this thesis is $L_B \approx 500$ m, with the maximum observed L_B values being on the order of a few kilometers, and minimum values on the order of tens of meters, which agrees with the former

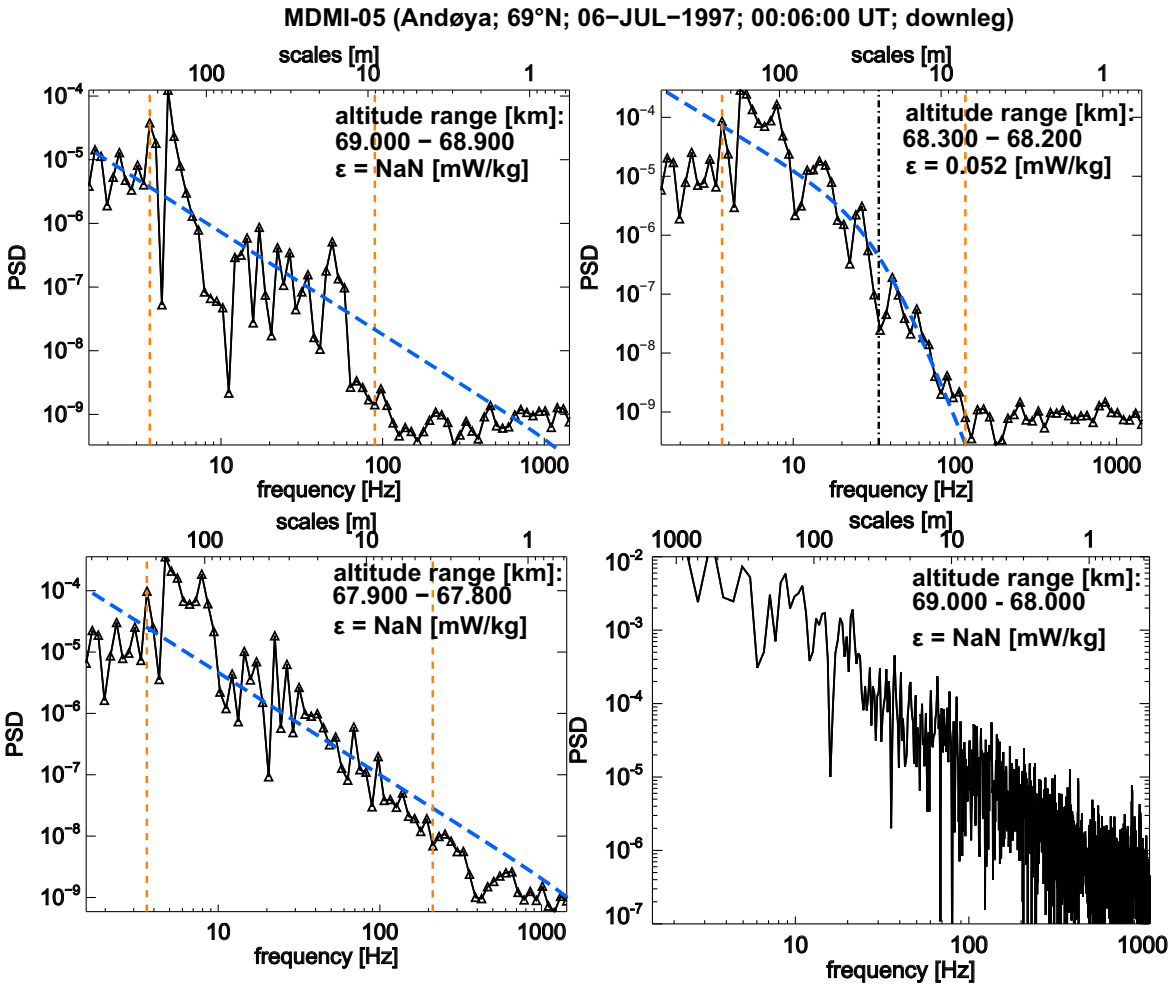

Figure 5.13 An isolated turbulence layer detected during the MDMI05 flight taken on 6th July 1997 in ARR in the altitude range from 68.2 to 68.7 km. Global wavelet PSD from 100 m of this turbulence layer is given in the upper right panel. Above and below this layer no turbulence was detected for more than 1 km. Global wavelet PSD from these non-turbulent parts of the flight are given in the upper-left and lower-left panels. The lower-right panel shows the Fourier PSD obtained during this flight in the altitude range from 68 to 69 km. Markings in the figure are the same as in Fig. 5.12.

statement. Also multiple DNS experiments show that dissipation tends to be very localized and variable, and turbulence generation is intermittent. This altogether suggests that turbulent layers can have thickness below 1 km. Two example turbulence layers are presented in the real rocket data analyzed using wavelet technique. One isolated from other turbulence layers, with a thickness of 500 m, and one thicker, which exhibits intermittency on the orders of hundreds of meters. This examples confirm that it is possible to detect isolated turbulence layers thinner than 1 km and to investigate turbulence intermittency/inhomogeneity on the order of hundreds of meters using wavelet analysis technique. Better vertical resolution would probably be needed to investigate the thinnest turbulence layers and smallest scale inhomogeneities in the MLT region. We conclude, stating that further investigations, both theoretical, DNS, and in-situ need to be performed to investigate topics of turbulence

inhomogeneity and turbulence layer's thickness in more detail.

The statistics on the turbulence layer's thickness obtained from all the available flights using the New Statistical Turbulence Analysis are shown in Fig. 5.21 in Sec. 5.2.

5.2.4. Turbulence found in the regions with adiabatic temperature lapse rate

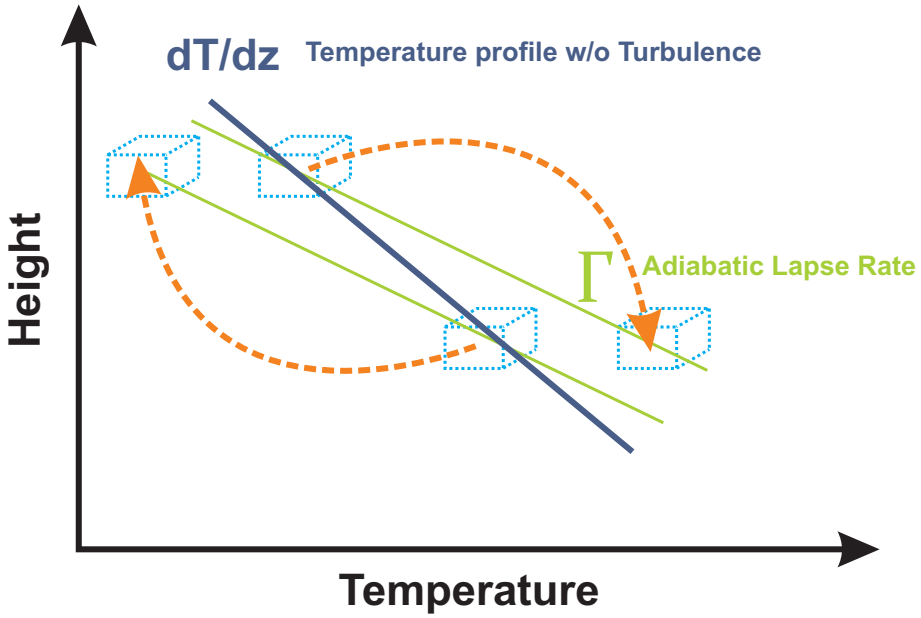

Figure 5.14 Turbulent eddies move adiabatically an air parcel to a different height. This creates fluctuations of quantities like temperature or density. Dark blue line: background temperature profile, dT/dz- Green line: adiabatic lapse rate, Γ.

Other problem that should be addressed before presenting the new climatologies, is the existence of turbulence in the regions with adiabatic temperature lapse rate. Theoretically, the CONE instrument is insensitive to the turbulence found in the altitude regions where the temperature exhibits adiabatic lapse rate (e.g., *Lübken*, 1993; *Strelnikov*, 2006). This situation is presented schematically in Fig. 5.14. A turbulent eddy moves an air parcel to a different height mechanically. The time of collisional relaxation inside the air parcel is large compared to the time of the mechanical transport by the turbulent motion, so this process can be considered as adiabatic. As a result, the temperature (or density) at that new location will deviate from the background temperature (density) profile. Where the profile of background temperature is adiabatic, i.e. $dT/dz = \Gamma$, the air parcel's temperature at the new location will not differ from the background air temperature, and the turbulence will not be detected by the CONE sensor.

However, after re-analysis of the turbulence rocket data with the wavelet technique, several turbulent layers were found in the altitude ranges where the temperature exhibits quasi adiabatic lapse rate (by quasi adiabatic lapse rate in this work we mean $-dT/dz$ between 8.8 and 10.8 K/km). Occurrence rate of 100 m altitude bins of turbulence for different lapse rates from all the flights is given in Fig. 5.15. In the left panel for 1 K/km step, in the right panel zoomed to 0.1 K/km step. With red-dotted lines dry adiabatic lapse rate of

−9.8 K/km is given. The problem of turbulence found in the altitude bins with adiabatic temperature lapse rate is discussed in this Subsection.

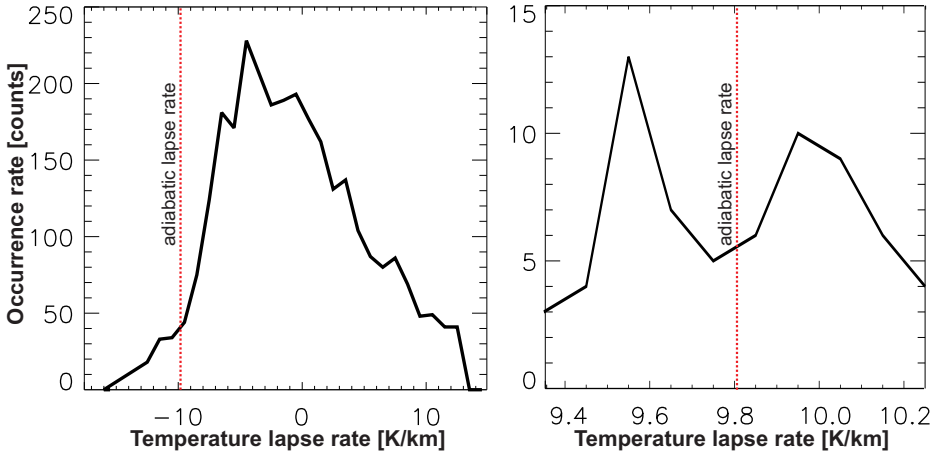

Figure 5.15 Occurrence rate of 100 m altitude bins of turbulence for different lapse rates from all the flights. In the left panel for 1 K/km step, in the right panel zoomed to 0.1 K/km step. With red-dotted lines dry adiabatic lapse rate of −9.8 K/km is given.

To remove the modulation due to rocket spin, the temperature has been smoothed to approx. 200 m resolution (*Rapp et al.* (2001) and App. C). The measurement resolution of the turbulence dissipation rate, ε, derived using wavelet technique is 100 m. Two things have to be accounted for: even if we measure adiabatic lapse rates, we are not able to say if inside of the 200 m bin the lapse rate is steadily adiabatic. Other important point is that, the total density derivations (from which the temperature is subsequently derived (App. C)) are disturbed by aerodynamic disturbances leading to enhancement of the densities inside the sensor compared to atmospheric values. To account for this *Rapp et al.* (2001) introduced ram correction factor for the CONE density measurements. This factor was derived using the Direct Simulation Monte Carlo (DSMC) method for apogees of 105 and 130 km. The apogees for flights investigated in this work vary from from 102 km (MSMI05 and MDMI05 flights) to 138 km (ECOMA-08). It is possible that a slight error in estimation of RAM correction factor for different apogees would be enough to draw the measured lapse rate from the real lapse rate slightly, i.e. by 0.1 K/km. This possibility makes it even harder to pinpoint where the measured adiabatic lapse rate is exactly true atmospheric adiabatic lapse rate, i.e. 9.8 K/km. To clarify this point, extensive sensitivity studies need to be conducted.

In conclusion, from theoretical investigations available (e.g., *Lübken*, 1993; *Strelnikov*, 2006) the CONE sensor is not, in fact, sensitive to the turbulence found on the adiabatic lapse rate, but it is difficult to measure the altitude regions where this lapse rates occur with high reliability. Additionally, after reviewing all the flights, there is no turbulence found in the 200 m bins with the adiabatic temperature lapse rate between 9.7 and 9.9 K/km.

5.2.5. ε climatologies for winter and summer

Having compared the results obtained from the old flights using the old and new analyses, and discussed the discrepancies between these two analyses, we are ready to present the climatologies obtained using the new analysis from all the available flights. Presented cli-

matologies use a data set consisting of 16 winter and 19 summer flights (a list of all flights is given in App. A).

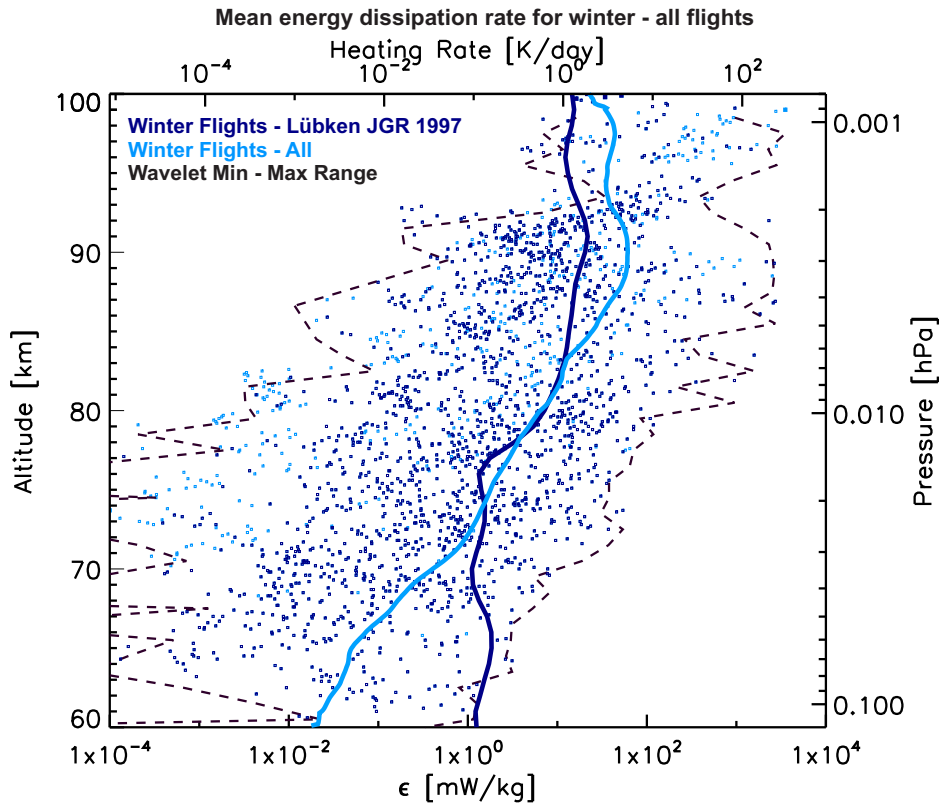

Figure 5.16 Comparison of the turbulent energy dissipation rate, ε, mean profiles obtained from all the winter flights using the new analysis (light blue line) with the results obtained by *Lübken* (1997) (dark blue line). Heating rates on the top abscissa. On the right ordinate approximate atmospheric pressure is shown as a vertical coordinate. Dark blue dots: results obtained using the new analysis from the old flights. Light blue dots: results obtained using the new analysis from the new flights. Black dashed lines show minimum and maximum limits for individual ε-values obtained using the new analysis, smoothed over 5 km.

In Fig. 5.16 ε climatology for winter obtained using the new analysis for all winter flights (light blue line) is compared with the climatology published by *Lübken* (1997) (dark blue line). The dark blue dots show ε-values detected for the old flights. The light blue dots show ε-values from the new flights. The mean profile obtained by the new analysis is raising exponentially from 60 to 89 km. The maximum of $\varepsilon \approx 60$ mW/kg is obtained in the altitude range between 89 and 91 km. This value corresponds to a heating rate of ≈ 5 K/day, which is comparable to that of other contributions to the energy budget in the MLT region (e.g., *Lübken*, 1993). The mean ε profile is gradually decreasing above 91 km. The mean ε profiles obtained using the new analysis and by *Lübken* (1997) show general agreement. The differences are similar as the differences obtained from only the old flights and discussed below Fig. 5.8. The minimum and maximum limits for ε-values shown as black dashed lines in Fig. 5.16 show approximately general exponential increase with the altitude. Variability of the ε-values with altitude in winter is shown in Fig. 5.19 and is discussed in the next

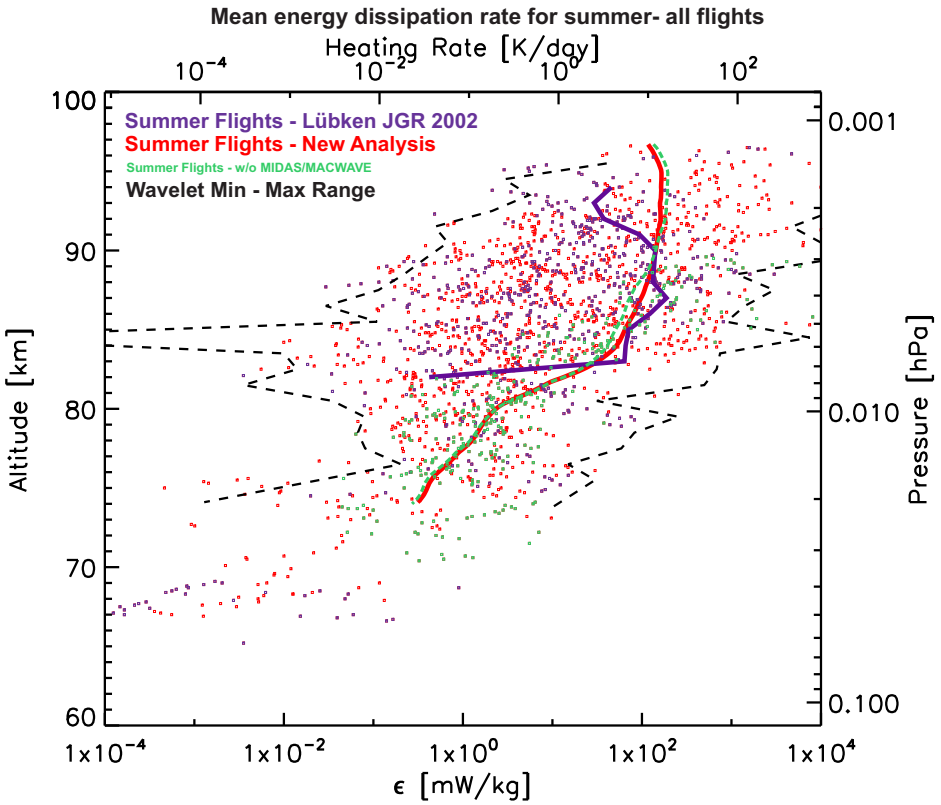

Figure 5.17 Comparison of the turbulent energy dissipation rate, ε, mean profiles obtained from all the summer flights using the new analysis (red line) with the results obtained by *Lübken et al.* (2002) (violet line). Green dashed line shows the mean profile obtained using the new analysis after excluding flights from the MIDAS/MACWAVE campaign. Heating rates on the top abscissa. On the right ordinate approximate atmospheric pressure is shown as a vertical coordinate. Violet dots: results obtained using the new analysis from the old flights. Red dots: results obtained using the new analysis from the new flights. Green dots: values from MIDAS/MACWAVE campaign. Black dashed lines show minimum and maximum limits for individual ε-values obtained using the new analysis, smoothed over 5 km.

subsection.

In Fig. 5.17 ε climatology for summer obtained using the new analysis from all the summer flights (red line) is compared with the climatology published by *Lübken et al.* (2002) (violet line). The violet dots show ε-values detected for the old flights. The red dots show ε-values from the new flights. The green dots show values from the MIDAS/MACWAVE campaign. During the MIDAS/MACWAVE campaign (3 flights: MMMI12, MMMI24 and MMMI25) very specific atmospheric conditions exhibited, leading to extreme temperature and wind gradients near the summer mesopause. These specific atmospheric conditions caused e.g., turbulence occurrence below 82 km (e.g., *Rapp et al.*, 2004; *Fritts et al.*, 2004; *Becker et al.*, 2004). However, because of the limited data set and the fact that the ε-values from this campaign change the mean summer profile only slightly, they are not excluded from the mean ε profile. The mean profile obtained after excluding flights from the MIDAS/MACWAVE campaign is plotted over with a green dashed line. Turbulence in summer occurs in the

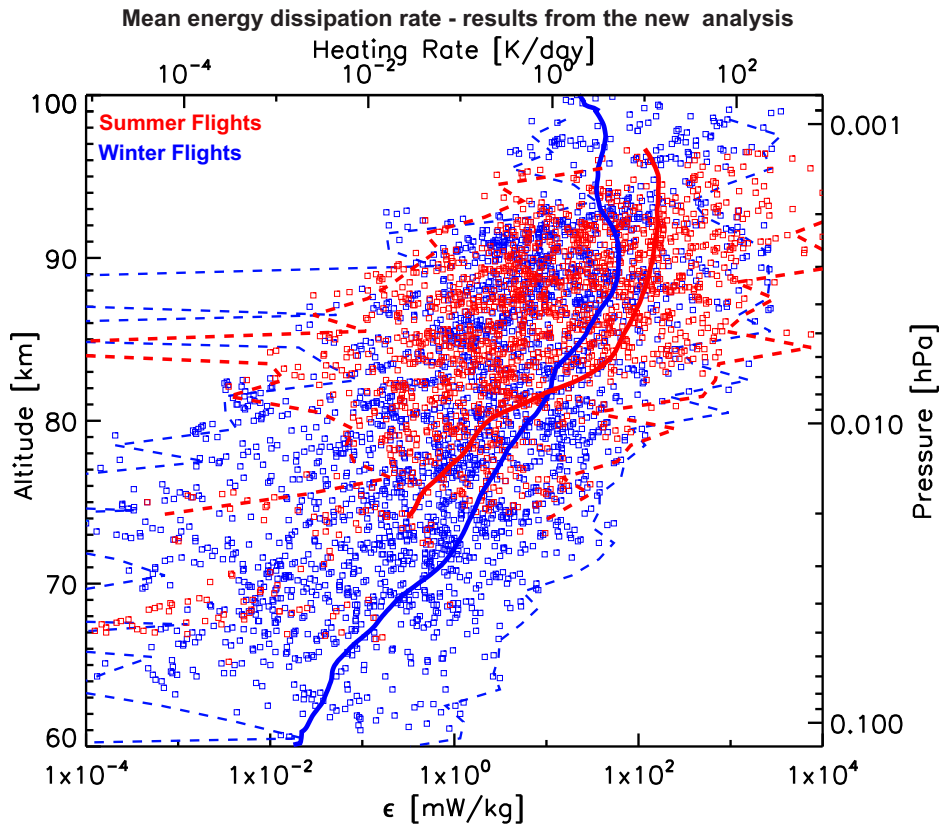

Figure 5.18 Comparison of mean profiles of turbulent energy dissipation rate, ε, obtained using the new analysis from all the winter flights (blue line) and all the summer flights (red line). Heating rates on the top abscissa. On the right ordinate approximate atmospheric pressure is shown as a vertical coordinate. Blue squares: results obtained from winter flights. Red squares: results obtained from summer flights. Minimum and maximum limits for individual ε-values obtained using the new analysis are shown with blue (winter) and red (summer) dashed lines.

altitude range from 74 to 97 km, with turbulence occurrence rate dropping down to less than 10 % below 74 km, and the mean profile below this altitude is not shown. The mean profile obtained by the new analysis exhibits a maximum $\varepsilon \approx 170$ mW/kg obtained for the altitude range between 92 and 95 km. This value corresponds to a heating rate ≈ 15 K/day, which is again comparable to that of other contributions to the energy budget in the MLT region (e.g., *Lübken*, 1993). The mean ε profiles obtained for summer in the frame of this work and by *Lübken et al.* (2002) show agreement in the altitude range from 83 to 91 km. The main difference is the existence of turbulent layers below 82 km. However, only four layers thicker than 1 km (Fourier analysis vertical resolution) are found below this altitude using the new analysis. An example turbulence layer detected below 82 km using the new analysis and not detected using Fourier analysis is shown in Fig. 5.13. The minimum and maximum limits for ε-values shown as black dashed lines in Fig. 5.17 show approximately general exponential increase with the altitude.

In Fig. 5.18 mean profiles of turbulent energy dissipation rate, ε, obtained using the new analysis from all the winter (blue line) and all the summer flights (red line) are shown. Turbulence in summer exhibits higher values above 82 km and lower below that height than

turbulence in winter. The maximum $\varepsilon \approx 150$ mW/kg in summer is obtained for the altitude range between 92 and 95 km. This is three times the maximum of ε for winter obtained for the altitude range between 89 and 91 km. ε-values are shown as blue and red squares for winter and summer, respectively. Turbulence in winter occurs in a broad altitude range, whereas in summer it is confined to altitude range from 74 to 97 km, with turbulence being observed sporadically below 74 km (see Fig. 5.20 in the next subsection). From the minimum and maximum limits for the ε-values shown as the blue dashed lines for winter and red dashed lines for summer general exponential increase of ε with altitude can be observed.

5.2.6. Turbulence statistics

After presenting the climatologies for summer and winter, we will present statistics on turbulence variability, turbulence occurrence rate and turbulence layer thickness, also obtained using the new analysis. In contrast to the climatologies, the three flights from MIDAS/MACWAVE campaign were not included in the turbulence statistics. These flights affect turbulence occurrence rate and turbulence variability statistics significantly, e.g., increasing turbulence occurrence below 80 km. Statistics for ε variability and occurrence rate for this campaign are shown in App. I.

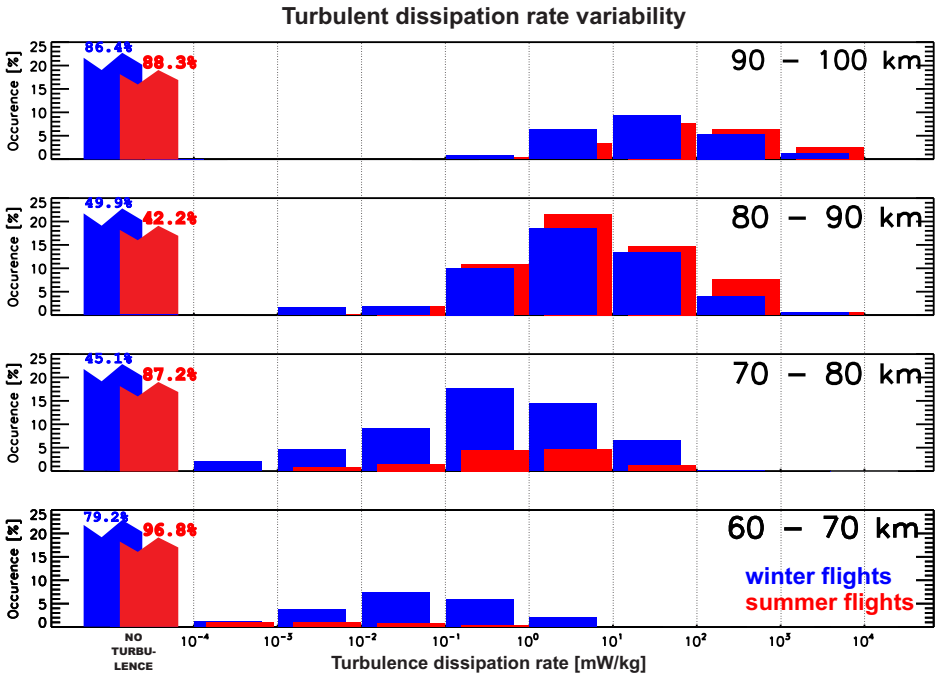

Figure 5.19 Turbulence dissipation rate, ε, variability for winter (blue bars) and summer (red bars) seasons. Different panels show the results in different altitude ranges, given as text in the right-upper corner of each panel. As text over leftmost unscaled bars bins where no turbulence was detected are shown for each altitude range.

In Fig. 5.19 statistics for ε variability with altitude for winter (blue bars) and summer (red bars) is shown. Different panels show statistics in different altitude ranges, given as text in the upper-right corner of each panel. As colored text over leftmost unscaled bars bins where no turbulence was detected are shown for each altitude range. General increase of ε-values with altitude is visible for both summer and winter, which was already shown

in Figs. 5.16 and 5.17. Most winter ε-values found between 90 and 100 km lie between 10^1 and 10^2 mW/kg, between 80 and 90 km lie between 10^0 and 10^1 mW/kg, between 70 and 80 km lie between 10^{-1} and 10^0 mW/kg, and between 60 and 70 km lie between 10^{-2} and 10^{-1} mW/kg, and thereby exhibit an exponential gradient. Most summer ε-values for turbulence found between 90 and 100 km lie between 10^1 and 10^2 mW/kg, between 80 and 90 km lie between 10^0 and 10^1 mW/kg, and between 70 and 80 km between 10^{-1} and 10^1 mW/kg. Turbulence occurs very sporadically in summer at altitudes 60 to 70 km.

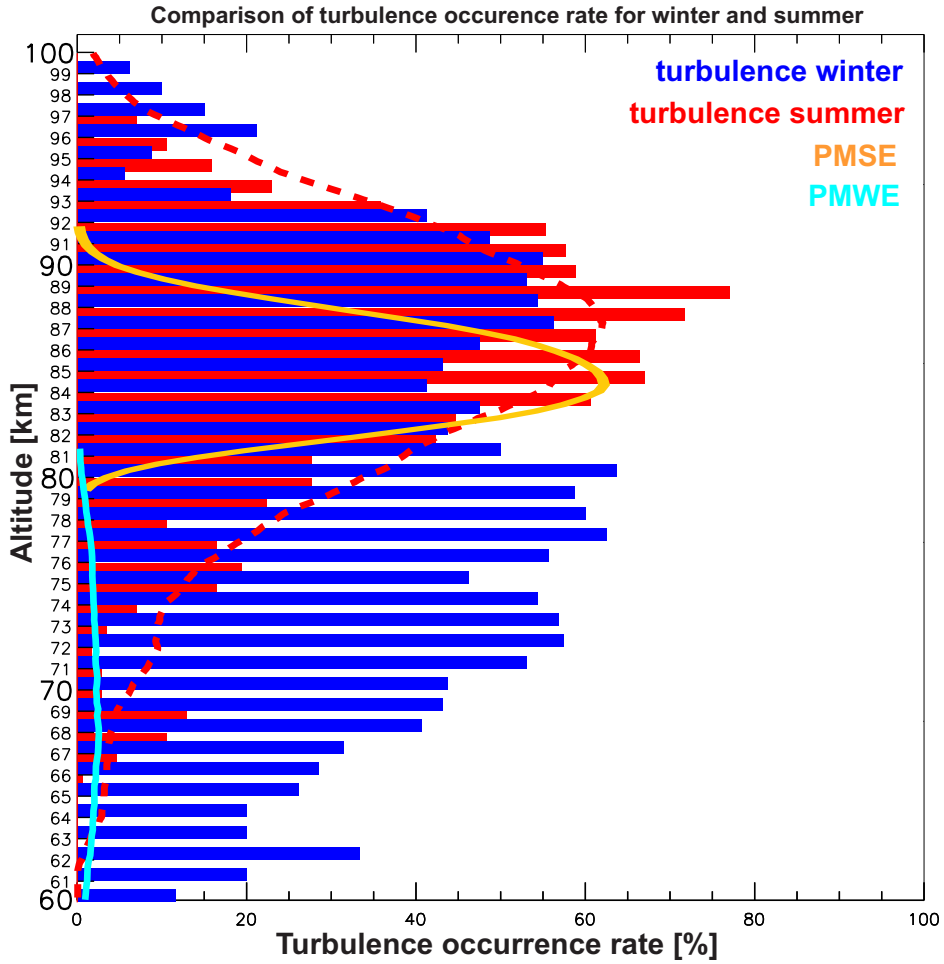

Figure 5.20 Turbulence occurrence rate with altitude for winter (blue bars) and summer (red bars and red dashed line). The occurrence rates of Polar Mesospheric Summer Echoes (PMSE) (*Rapp and Lübken*, 2004) and Polar Mesospheric Winter Echoes (PMWE) are shown as orange and light blue lines respectively (courtesy of Ralph Latteck).

In Fig. 5.20 statistics for turbulence occurrence rates with altitude for winter (blue bars) and summer (red bars and red dashed line) is shown. As light blue and orange lines the occurrence rates of PMSE, Polar Mesospheric Summer Echoes (*Rapp and Lübken*, 2004), and PMWE, Polar Mesospheric Winter Echoes (courtesy of Ralph Latteck) are shown for comparison. PMSE statistics were obtained from measurements made from 1999 to 2013 using both the ALWIN and the MAARSY radar. The PMWE statistics was obtained from measurements made from 2010 to 2013 using MAARSY radar. It can be seen that in winter turbulence is observed with typical occurrence rate between 30 and 65% between 70 and

90 km. A decrease in occurrence rate above 90 km (turbopause) and below 70 km is observed. Below 74 km in summer, turbulence is observed with occurrence rates staying mostly below 10 %. It can be seen that maximum summer turbulence occurrence rate occurs at ≈ 87.5 km, whereas the maximum PMSE occurrence rate occurs at ≈ 85 km. This shift in maxima of occurrence of neutral turbulence and PMSE agrees with results published by *Rapp and Lübken* (2004). In a climatological sense neutral air turbulence occurs in the entire altitude range where PMSE is observed. Neutral air turbulence is known to be producing structures in the refractive index necessary for the PMSE existence (e.g., *Rapp and Lübken*, 2004). The PMWE occur only below 80 km, whereas the turbulence in winter occurs in a broader altitude range. The mechanism of the creation of PMWE is still an open question (*Rapp et al.*, 2011). Combined in-situ rocket sounding and radar measurements provided evidence that at least some of these echoes can be attributed to Bragg scattering from fluctuations that are due to neutral air turbulence (*Lübken et al.*, 2006). *Stebel et al.* (2004); *Kavanagh et al.* (2006); *Belova et al.* (2008); *Kero et al.* (2008); *Havnes and Kassa* (2009); *Havnes et al.* (2011); *La Hoz and Havnes* (2008) presented results which suggest that the charged nanometer-scale particles, much like ice in the case of PMSE, take part in the creation of PMWE. The obtained broad range of turbulence occurrence in winter combined with narrow range of PMWE occurrence can imply that these charged nanometer-scale particles number densities are higher from 60 to 80 km than in the upper parts of the mesosphere.

Statistics for the turbulence layer's thickness obtained from all the available flights is shown in Fig. 5.21. The thickness of the layers measured with the resolution of 100 m is given with red bars. The thickness of the layers with excluded small scale inhomogeneities are shown with blue and green bars on the plot. This study was conducted as follows: turbulent layers with a thin, non-turbulent layer in between are treated as one thicker inhomogenous turbulent layer. In this study inhomogeneities thinner than 500 m (green bars in the plot), and thinner than 1000 m (blue bars in the plot) were excluded. This inhomogeneity's thickness was chosen according to discussion in Subsec. 5.2.3, where it was stated that turbulence may exhibit inhomogeneties from tens of meters up to a kilometer. On the x-axis turbulent layer's thickness in km is shown, whereas on the y-axis the number of layers with given thickness is shown. It can be seen, that without excluding the small scale inhomogeneities, most layers exhibit thickness of 100 m (or below, since 100 m is the limit due to the analysis' technique/instrument). After excluding small scale inhomogeneities most of the turbulence layers exhibit thickness of a few kilometers.

It is interesting to compare the statistical turbulent layer thickness (excluding intermittencies of up to 500 m) for summer below and above 82 km. This is the altitude below which no turbulence was detected by *Lübken et al.* (2002) analysis. The reason for lack of turbulence below 82 km in summer was associated with lack of gravity wave breaking events there (which is associated with the fact that weaker gravity waves in summer are filtered by mean winds (e.g., *Lindzen*, 1981)). This comparison reveals that statistical turbulent layer below 82 km is thinner than the one above 82 km. Below 82 km more than 50% of layers are thinner than 1 km, whereas above this altitude only 30%.

According to *Fritts et al.* (2003) shear instability causes turbulence confined to a narrow layer, whereas gravity wave breaking causes turbulence that spreads over a larger height range. Therefore, the presented statistics may imply that the turbulence detected below 82 km is created to greater extent by wind shear than the turbulence above 82 km (and to lesser extent by gravity wave breaking). The mean daily profiles for wind shear obtained with Saura MF-radar, which are not shown here, do in fact show that there exists individual strong wind shear events in summer below 82 km, which can be associated with turbulence.

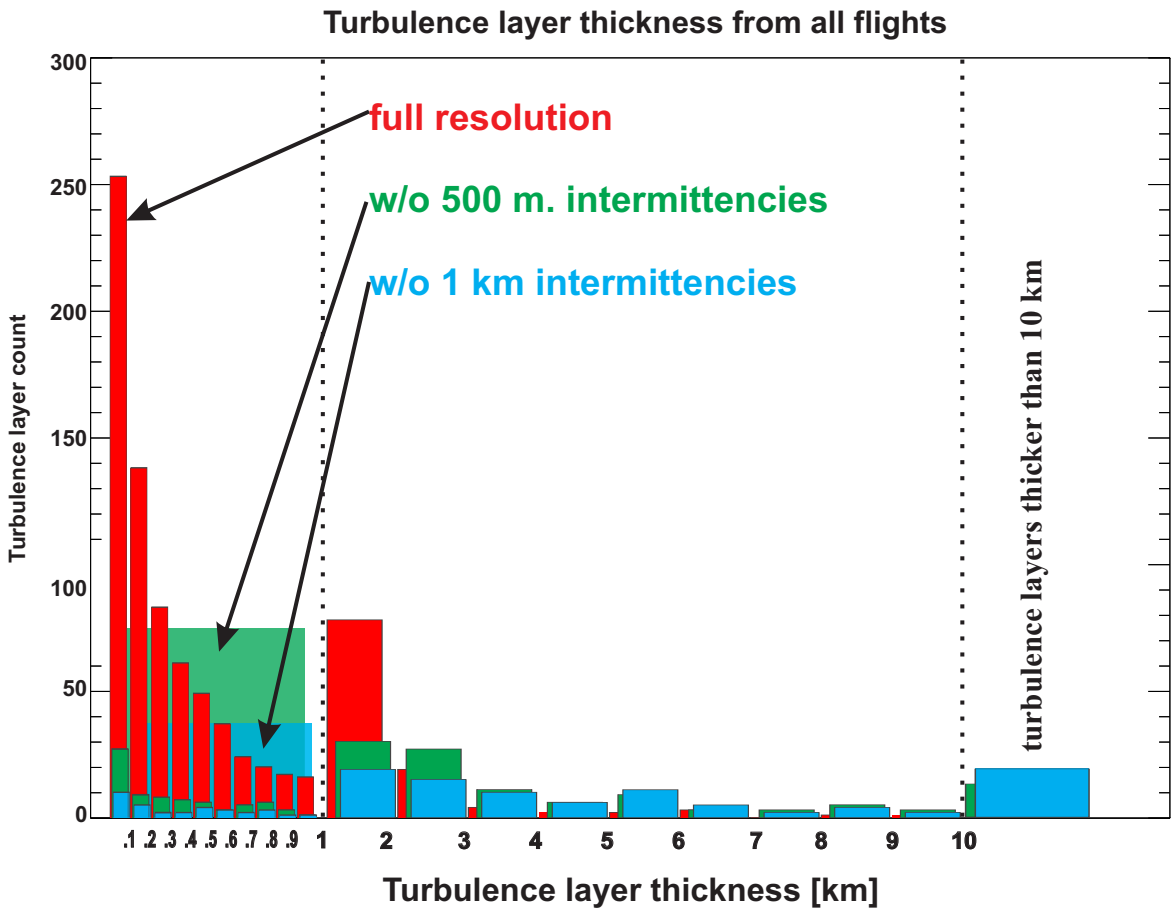

Figure 5.21 Statistics of the turbulence layer's thickness are shown as red bars. On the x-axis turbulent layer's thickness in km is shown (below 1 km with 100 m resolution, above with 1 km resolution), whereas on the y-axis the number of layers with given thickness detected in all the available flights is shown. Turbulence layer's thickness statistics after excluding small scale intermittencies, of 500 m thickness and thinner (green bars) or 1 km and thinner (blue bars), are shown for comparison. Total amount of turbulent layers thinner than 1 km after excluding these intermittencies is shown as background transparent green and blue bars.

5.2.7. Summary

Now we are ready to summarize the results for MLT region's turbulence obtained in the frame of this work. First, the results obtained from the old flights using the new analysis for winter and summer are presented and compared with the results published by *Lübken* (1997) and *Lübken et al.* (2002). General agreement between these mean profiles is found, however some differences are evident. These differences are discussed later. Also turbulence layer's thickness, turbulence inhomogeneity, and turbulence found on the adiabatic temperature lapse rate is discussed.

Then the mean profiles obtained using the new analysis from all the winter and all the summer flights are presented and discussed. The mean ε value for winter increases exponentially from 60 to 89 km. The maximum $\varepsilon \approx 60$ mW/kg is obtained for the altitude range between 89 and 91 km. This value corresponds to a heating rate of ≈ 5 K/day, which is

comparable to that of other contributions to the energy budget in the MLT region (e.g., *Lübken*, 1993). Above 91 km the mean profile is decreasing. Minimum and maximum limits of the ε occurrence in winter show exponential increase with altitude.

The mean ε profile for summer reveals the maximum $\varepsilon \approx 170$ mW/kg in the altitude range between 92 and 95 km. This value corresponds to a heating rate of ≈ 15 K/day, which is also comparable to that of other contributions to the energy budget in the MLT region (e.g., *Lübken*, 1993). Minimum and maximum limits of the ε occurrence in summer show exponential increase with altitude. Turbulence in summer occurs in the narrower altitude range from 74 to 97 km, with turbulence occurrence rate below 74 km dropping below 10 %. Strong wind shear events are proposed to be the main source of the turbulence found below 82 km.

When comparing the mean ε profiles for winter and summer obtained using the new analysis it can be seen that turbulence in summer exhibits higher ε-values above 82 km and lower below 82 km than turbulence in winter. The maximum mean ε value for summer is about three times the maximum value for winter. The summer maximum also occurs at a slightly higher altitude. The mean profiles published by *Lübken* (1997) for winter and by *Lübken et al.* (2002) for summer show a similar altitude dependence, however the differences between summer and winter were more pronounced.

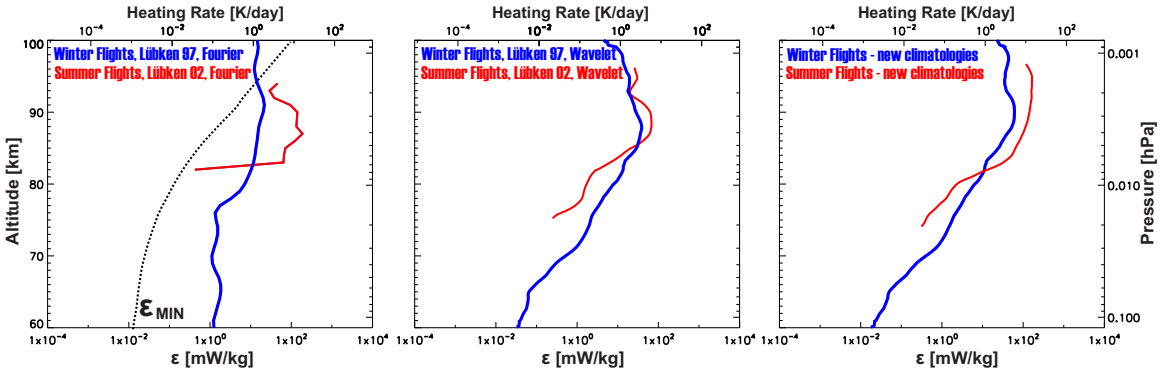

Figure 5.22 The comparison of different ε climatologies. In the left panel ε climatologies obtained by *Lübken* (1997) and *Lübken et al.* (2002) (the theoretical ε_{MIN} obtained by *Lübken* (1993) is marked with dotted line). In the middle panel the ε results obtained using the new analysis for only the old flights. In the right panel the ε results obtained using the new analysis for all flights (i.e. new climatologies). Blue lines denote winter flights, red lines denote summer flights. Heating rates on the top abscissa. On the right ordinate approximate atmospheric pressure is shown as a vertical coordinate.

The comparison of different ε climatologies is given in Fig. 5.22 with the blue lines for winter flights and the red lines for summer flights. The left panel shows ε climatologies obtained by *Lübken* (1997) and *Lübken et al.* (2002). The theoretical ε_{MIN} obtained by *Lübken* (1993) is marked with a dotted line. The middle panel shows the ε results obtained using the new analysis for only the old flights. The right panel shows the ε results obtained using the new analysis for all flights (i.e. new climatologies).

Besides turbulence climatologies, extended turbulence statistics are also shown. Turbulence variability as a function of altitude, both in winter and summer, shows a general tendency for increase of ε-values with altitude, which was already seen in the mean profiles. Using the variability statistics, however, this trend is quantified for the ε-values in given

altitude ranges. Statistics for turbulence occurrence rate with altitude for winter and summer are compared with the occurrence rate of PMWE and PMSE, respectively. It can be seen that winter turbulence occurs in a broad altitude range. Between 70 and 90 km the typical occurrence rate lies between 30 and 65 %. Decrease in occurrence rate above 90 km (turbopause) and below 70 km can be observed. In summer turbulence occurs in a narrower altitude range with maximum occurrence of up to $\approx$ 80 % at $\approx$ 87.5 km, which is above the maximum altitude for PMSE occurrence found at $\approx$ 85 km.

Afterwards, statistics for the turbulence layer's thickness were shown. It can be seen that most layers exhibit thickness of 100 m (or below since 100 m is the limit coming from the instrument). To account for the turbulent layer inhomogeneity, statistics after excluding small scale intermittencies are presented. This statistics can imply that majority of the turbulent layers are actually thicker than 1 km and exhibit inhomogeneities on order of few hundreds of meters or below. Results for turbulence layer inhomogeneities and turbulence layer thickness agree with presented theoretical results, and as well DNS experiments (e.g., *Fritts et al.*, 2013b).

5.3. Comparison of the experimental and model results

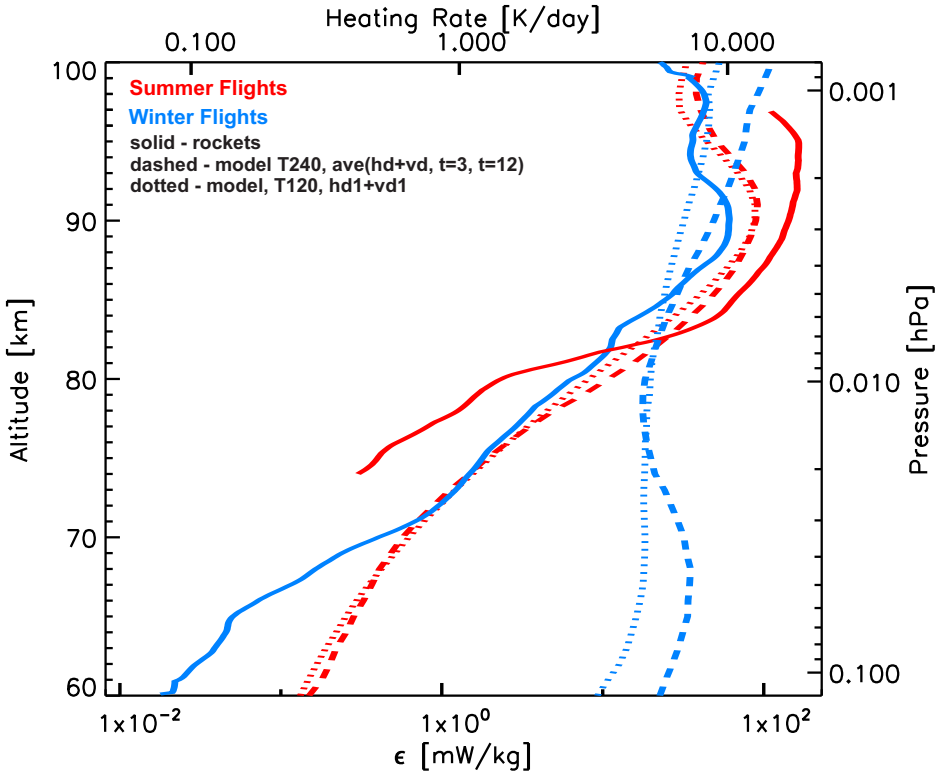

Figure 5.23 Comparison of ε mean profiles obtained using the new analysis (solid lines) with ε profiles obtained with the model with resolutions T = 240 (dashed lines) and T = 120 (dotted lines). Summer profiles are denoted with red color, whereas the winter profiles are denoted with blue color. On the right ordinate approximate atmospheric pressure is shown as a vertical coordinate.

In this section the mean ε-profiles obtained using the new analysis are compared with

ε-profiles obtained with Kühlungsborn Mechanistic Circulation Model (KMCM) (*Becker*, 2009). The concept of this mechanistic general circulation model is that it simulates the gravity wave drag in the upper mesosphere in a self-consistent fashion. The model reproduces various mean and variable features of the wave-driven general circulation from the boundary layer to the mesopause region (*Becker*, 2009). In comparison to many other models, which derive turbulent diffusion coefficient, K, KMCM derives ε directly, which can be easily compared with the results obtained from the in-situ rocket measurements.

In Fig. 5.23 mean ε-profiles obtained using the new analysis (solid lines) and ε-profiles obtained with KMCM with resolutions T = 240 (dashed lines) and T = 120 (dotted lines) are shown. Summer profiles are plotted in red, whereas winter profiles are plotted in blue. Profiles obtained with the model exhibit higher ε-values above 82 km in summer than in winter, which agrees with the experimental results. When comparing summer experimental and the model results directly, it can be seen that the model slightly underestimates ε-values below 82 km and slightly overestimates them above 82 km (this is the same for both model's resolutions). However, general agreement can be observed. In winter experimental and model results generally agree above 82 km, whereas below 82 km the model overestimates ε-values by up to 3 orders of magnitude. Also exponential increase observed in the experimental results is not observed in model results. The differences between the model and new climatologies, especially below 82 km, may suggest that the model should be revised to fit the new climatologies, obtained from the larger data set than the previous ones.

In their paper *Rapp et al.* (2006) noted that the most striking difference between the model and experimental results is that there are no cases with "zero" dissipation rates, i.e. very small dissipation rates are much less probable than in the real atmosphere. This "non-turbulent" altitude bins are shown for experimental results in Fig. 5.19, leftmost column. They are not shown for model results in the frame of this work. Concerning the inability of the model to produce a large number of "non-turbulent" altitude bins, we need to consider that the modeled heating rates are actually average values representative of volumes with typical dimensions of a few hundred kilometers in the horizontal direction, a few kilometers in the vertical direction, and about 30 min in time. This needs to be compared to the measurements which are snapshots in both horizontal and temporal dimensions (i.e., a few centimeters and 0.1 s of flight-time) and are only averaged over a vertical scale of 100 m. This means that a single model value should actually be considered representative of the mean of a few thousand "real" values. Hence, if e.g., 70% of these values are zero and 30% do show significant heating rates (the actual numbers are 65 % of non-turbulent bins for winter and 78 % for summer), then the average of thousands of values should actually be non-zero - as seen in the model. Hence, the missing zero heating rates in the model are not necessarily in contradiction to our observations but can likely be explained by the very different sampling statistics of observations and model.

Chapter 6.

Summary and outlook

6.1. Summary

The main topic of this thesis was to investigate turbulence in the MLT region, particularly its role in creating mesospheric inversion layers. Up to now, the only available statistical analysis of turbulence measurements in the MLT region were the works of *Lübken* (1997) and *Lübken et al.* (2002), where ε-climatologies for winter and summer were presented based on the set of 20 sounding rocket flights. These authors used Fourier turbulence analysis technique with 1 km vertical resolution. In this thesis new analysis is presented, based on the wavelet analysis technique developed by *Strelnikov* (2006), with increased vertical resolution of 100 m. This new analysis, with database extended to 35 flights, is referred here as the New Statistical Turbulence Analysis, or simply the new analysis. Vertical resolution of 1 km is good enough for quantitative description of turbulence in the mesosphere, however theoretical studies, e.g., by *Weinstock* (1978) and *Hocking* (1999), and direct numerical simulations made by *Fritts et al.* (2003, 2009a, 2013a,b), show that turbulence generation is intermittent, and turbulence in the mesosphere exhibits inhomogeneity on the order down to tens of meters. These scales cannot be investigated in sufficient details with Fourier analysis technique. Also it was shown in the frame of this thesis that Fourier technique is "blind" to thin turbulent layers (i.e. significantly thinner than 1 km). Another thing that has to be accounted for, is that measurements with 1 km resolution will smooth the high ε-values obtained on the smaller (i.e. 100 m) scales. High enough ε-values, that are suggested to create phenomena of MIL (*Liu et al.*, 2000), will not be detected by Fourier technique.

The new analysis introduced several improvements to the turbulence derivation technique. The turbulence dissipation rate, ε, is obtained by fitting theoretical model to the spectrum obtained after wavelet transform of the residuals of neutral density fluctuations measured during a rocket flight. Since the new data set is very extensive (35 flights in the altitude range from 60 to 100 km divided into 100 m altitude bins gives more than 10000 individual spectra to analyze) automatization of the fitting process and derivation of ε-values from the fit was made. The whole procedure of deriving turbulence parameters, including the new analysis, is presented in Chap. 4. Therein procedures of automatically setting fitting ranges, derivation of ε measurements error based on weights, ε_{ERR}, and set of criteria to distinguish between turbulent and non-turbulent spectra are given. Procedures listed above were newly developed in the frame of this thesis. Also, using signal consisting of turbulent and non-turbulent parts the ability of the new analysis to detect turbulence layers was demonstrated. In particular it was shown, that the analysis detects the turbulence in the turbulent part of the signal with appropriate ε value, and does not detect turbulence in the adjacent, non-turbulent part of the signal.

In Chap. 5 geophysical results are shown. First results obtained during ECOMA09 flight conducted on 19th December 2010 in ARR are given, where a MIL with accompanying strong

turbulence was detected and investigated. As it was already mentioned turbulence can be involved in the creation of MIL. Specifically *Liu et al.* (2000) suggested that the strong turbulence with heating rates exhibiting ≈ 240 K/day can create MIL even in the absence of gravity waves and tides activity. This high ε-values were measured during ECOMA09 rocket flight, and are compared with temperature measurements made in the same volume. The comparison shows that the maximum for the turbulence dissipation rate, ε, and temperature exhibit in the same altitude range. Further investigations were conducted, using lidars, radar and satellite. It was shown that this strong turbulence was at least significantly amplifying MIL, and was possibly the only mechanism responsible for this MIL creation. It must again be stressed that only by using in-situ measurements and spectral analysis with high enough vertical resolution (wavelet analysis in our case) was it possible to detect such a high ε-values, and they were never observed with the Fourier analysis technique during winter period.

Afterwards the turbulence results obtained using the new analysis are presented. First the mean ε profiles obtained using the new analysis from only the old flights are shown and compared with the mean ε profiles obtained by *Lübken* (1997) and *Lübken et al.* (2002). General agreement exists, with the differences being discussed in Subsec. 5.2.2. The main differences between the results obtained using the old and new analysis is existence of turbulence layers in summer below 82 km, existence of turbulence inhomogeneities on scales of below 1 km, and as well the clear exponential increase of winter ε profile with altitude until the turbopause. Then the ε-climatologies obtained using the new analysis are presented for winter and summer periods.

The new mean profile for winter is raising exponentially from 60 to 89 km. The maximum $\varepsilon \approx 100$ mW/kg is obtained for the altitude range between 89 and 91 km. This value corresponds to a heating rate of ≈ 10 K/day. Above 91 km the mean ε profile is gradually decreasing. The new mean profile for summer exhibits maximum $\varepsilon \approx 200$ mW/kg obtained for the altitude range between 92 and 95 km. This value corresponds to a heating rates of ≈ 20 K/day. Maximum mean heating rates, both for winter and summer, are of magnitude comparable to that of other contribution to the energy budget in the MLT region (e.g., *Lübken*, 1993). Turbulence in summer exhibits in the narrow altitude range from 74 to 97 km, with turbulence occurrence rate below 74 km dropping below 10 %. As already mentioned, several thin turbulence layers were observed using the new analysis below 82 km, which were not observed by *Lübken et al.* (2002).

This work also presents extended turbulence statistics in addition to the turbulence climatologies. These extended statistics are helpful for investigating various phenomena in the MLT region. From the variability of individual ε-values with altitude a general tendency for exponential increase can be seen. Turbulence occurrence rate statistics are presented and compared with PMSE and PMWE occurrence rate. In the summer turbulence exhibits in the narrower altitude range from 74 to 97 km with the maximal occurrence of up to ≈ 80 % exhibiting ≈ 87.5 km, which is above the maximum altitude for PMSE occurrence found at ≈ 85 km. Work of *Rapp and Lübken* (2004) shows similar dependence. The PMWE occur only from 50 to 80 km, whereas the turbulence in winter occurs in broader altitude range. The mechanism of creation of PMWE is still an open question (*Rapp et al.*, 2011). The presented turbulence occurrence rate can help to understand the phenomena of PMWE in more detail.

Afterwards the statistics for turbulence thickness were shown, for individual turbulence layers and for the layers with small scale intermittencies excluded. These statistics imply that turbulence in the mesosphere is intermittent, and exhibits in thicker layers, which are often separated by regions which are either only weakly turbulent or even laminar. This

agrees with theoretical results, and DNS experiments (e.g., *Fritts et al.*, 2013b).

Finally comparison of ε mean profiles obtained using the new analysis with the ε profiles obtained with KMCM model is conducted. The main difference was the fact that the model does not yield a large part of samples with no turbulence at all, as it was already noticed by *Rapp et al.* (2006). It appears most likely that the very different sampling statistics of model and observations create this difference. This issue will require our attention in the future. Also, comparison between the ε/N_θ values obtained experimentally and from theoretical considerations is presented in App. E. Buoyancy frequency, N, climatologies obtained from the available rocket data for winter and summer are presented in App. F.

Taking all these results together we summarize the new significant findings of this thesis as follows:

- the new analysis was developed, the new features included in this analysis are:
  - automatization of the fitting process, with fitting ranges based on the noise level
  - new error treatment based on weights
  - set of criteria to distinguish between turbulent and non-turbulent spectra

  The functionality of this technique was approved on synthetic signal
- MIL with accompanying strong turbulence (above 240 K/day) was detected and investigated. In particular it was shown, that the turbulence was involved in the formation of MIL, or even was the only mechanism of MIL creation
- new ε-climatologies for winter and summer were presented, winter climatology shows exponential increase with an altitude which was not observed before
- it was shown that wavelet technique is able to discover turbulent layers thinner than 1 km and is able to investigate turbulence inhomogeneity on the scales of a few hundreds of meters
- several thin turbulent layers were discovered in summer below 82 km
- extensive set of statistics for the MLT region's turbulence was shown, including turbulence variability with altitude, turbulence occurrence rate, and turbulence layer's thickness

6.2. Outlook

Results presented in this thesis motivate us for further investigations. The next short term plan that naturally arises from the presented studies is to compare MILs with accompanying turbulence obtained using the new analysis for individual flights (additional tidal and gravity wave analysis, where available, can help to distinguish the origin of the observed MIL events). Also comparison of turbulence statistics with PMSE and PMWE can be conducted more extensively. The forthcoming sounding rocket project PMWE is aimed to investigate the PMWE phenomenon and the role of turbulence in its creation in more detail.

The next open question is turbulence inhomogeneity. More theoretical investigations and more detailed insight into available data can help here, as well as development of new measurement/analysis technique with higher vertical resolution.

The open question about turbulence that can also be addressed in the future is that of its three dimensional structure. The WADIS 1 campaign was the first rocket campaign where

turbulence parameters were measured on both upleg and downleg of the flight and revealed significant differences. The next step is the forthcoming sounding rocket campaign TURB3D, where three ionization gauges for each payload will be used, which can help to address this problem in more detail. MAARSY radar 3D observation can be helpful for observation of time development of the turbulence.

Finally, although many of sounding rocket campaigns investigating the MLT region's turbulence were conducted at polar latitudes, up to now only one successful measurement was conducted at equatorial latitudes. This measurement using CONE instrument was conducted during NASA EQUIS II campaign conducted at Kwajalein Atoll, Marshall Islands (8^oN). Interestingly, during this flight also a strong MIL event was also detected and compared with accompanying turbulence (*Lehmacher et al.*, 2006). To obtain the statistical picture of turbulence at equatorial latitudes in the MLT region more flights should be conducted there using CONE ionization gauge, or new generation ionization gauges developed for TURB3D campaign.

Appendices

Appendix A.

Flights list

In Tab. A.1 on the next page a list of all the flights conducted between 1990 and 2014 is given. Information included in columns from left to right: flight label, campaign name, used gauge (see Sec. C), date of flight (with labels W for the winter period and S for the summer period), if temperature measurements from this flight are available (with * the upleg of WADIS 1 flight that was not included into buoyancy frequency climatology is denoted), and used PCM format (see Sec. B). The flights labeled NBT05, NAT13 and PHOCUS were conducted in Esrange, Sweden (68^{o}N), all the other flights were conducted in ARR, Norway (69^{o}N). For all the flights the measurements using CONE/TOTAL sensors were conducted during the downleg of flight, only during WADIS 1 campaign the measurements were conducted both during up- and downleg of flight. In his paper *Lübken* (1997) made turbulence dissipation rate, ε, climatologies for winter period using flights from DYANA and METAL campaigns (12 flights in total). Likewise, in *Lübken et al.* (2002) summer ε climatologies were published using flights from campaigns NLC91, SCALE, ECHO and MIDAS/DROPPS (8 flights in total). It should be noted that during MaCWAVE/MIDAS campaign very specific conditions exhibited of extreme temperature and wind gradients near the summer mesopause (e.g., *Rapp et al.*, 2004; *Fritts et al.*, 2004; *Becker et al.*, 2004).

Table A.1 List of all the flights conducted between 1990 and 2014. Information included in columns from left to right: flight label, campaign name, used gauge, date of flight, if temperature measurements from this flight are available, used PCM format.

Flight	Campaign	Gauge	Date	Temp. Data	PCM format
DAT13	DYANA	TOTAL	22/01/1990 (W)	yes	OLD
DAT50	DYANA	TOTAL	25/02/1990 (W)	yes	OLD
DAT62	DYANA	TOTAL	06/03/1990 (W)	yes	OLD
DAT73	DYANA	TOTAL	08/03/1990 (W)	yes	OLD
DAT76	DYANA	TOTAL	09/03/1990 (W)	no	OLD
DAT84	DYANA	TOTAL	11/03/1990 (W)	no	OLD
NBT05	NLC91 (salvo B)	TOTAL	01/08/1991 (S)	yes	OLD
NAT13	NLC91 (salvo A)	TOTAL	09/08/1991 (S)	yes	OLD
LT01	METAL	TOTAL	17/09/1991 (W)	yes	OLD
LT06	METAL	TOTAL	20/09/1991 (W)	yes	OLD
LI09	METAL	TOTAL	20/09/1991 (W)	yes	OLD
LT13	METAL	TOTAL	30/09/1991 (W)	yes	OLD
LT17	METAL	TOTAL	03/10/1991 (W)	yes	OLD
LT21	METAL	TOTAL	03/10/1991 (W)	yes	OLD
SCT03	SCALE	CONE	28/07/1993 (S)	yes	OLD
SCT06	SCALE	CONE	01/08/1993 (S)	yes	OLD
ECT02	ECHO	CONE	28/07/1994 (S)	yes	OLD
ECT07	ECHO	CONE	31/07/1994 (S)	yes	OLD
ECT12	ECHO	CONE	12/08/1994 (S)	yes	OLD
MDMI05	MIDAS/DROPPS	CONE	06/07/1999 (S)	no	OLD
MSMI03	MIDAS/SPRING	CONE	06/05/2000 (W)	yes	NEW
MSMI05	MIDAS/SPRING	CONE	15/05/2000 (S)	yes	NEW
SOMI05	MIDAS/SOLSTICE	CONE	17/06/2001 (S)	yes	NEW
SOMI11	MIDAS/SOLSTICE	CONE	24/06/2001 (S)	yes	NEW
MMMI12	MIDAS/MACWAVE	CONE	02/07/2002 (S)	yes	NEW
MMMI24	MIDAS/MACWAVE	CONE	05/07/2002 (S)	no	NEW
MMMI25	MIDAS/MACWAVE	CONE	05/07/2002 (S)	yes	NEW
ECOMA01	ECOMA2006	CONE	08/09/2006 (W)	yes	NEW
ECOMA02	ECOMA2006	CONE	17/09/2006 (W)	yes	NEW
ECOMA03	ECOMA2007	CONE	03/08/2007 (S)	yes	NEW
ECOMA04	ECOMA2008	CONE	30/06/2008 (S)	yes	NEW
ECOMA06	ECOMA2008	CONE	12/06/2008 (S)	yes	NEW
ECOMA09	ECOMA2010	CONE	19/12/2010 (W)	yes	NEW
PHOCUS	PHOCUS	CONE	21/07/2011 (S)	yes	NEW
WADIS1-up	WADIS I	CONE	27/06/2013 (S)	yes	WADIS
WADIS1-down	WADIS I	CONE	27/06/2013 (S)	yes*	WADIS

Appendix B.

PCM formats description

In this section PCM formats used for telemetry during sounding rocket campaigns (see Tab. A.1 in App. A) are described. The PCM format used until MIDAS/DROPPS campign is labeled as the old format, PCM format used starting from MIDAS/SPRING campaign until WADIS 1 campaign is labeled as the new format. For WADIS 1 campaign new PCM format was modified and is labeled here as the WADIS format. For each PCM format tables with the main frame channel assignments and housekeeping assignments are given. Additionally for the old format the division of bits inside of ElectroMeter Mantissa (EMM) and ElectroMeter Range (EMR) words are given. For each format its bit rate, words per frame and frames per format values are given. The main difference between the old and new formats, beside the change in assignment of words inside of the frame, is the bit rate and size of the cell where EMM is saved. Old format was using 13 bits for this purpose, which gives $2^{13} = 8192$ possibilities of different EMM values. The new and WADIS formats are using 16 bits which gives $2^{16} = 65536$ possibilities of different EMM values. This gives the possibility for the higher EMM measurements accuracy, assuming that there are no other restrictions, like sensor sensitivity etc. (i.e. assuming sufficiently high sensor sensitivity, with the new and WADIS PCM formats one can get more accurate EMM values than with the old format). This improvement of EMM accuracy was possible with improvement of telemetry bandwidth.

B.1. Old PCM Format

- Bit rate: 312.50 kbits/s
- 8 bit words/frame: 32
- Frames/format: 32

Table B.1 Main frame channel assignments used in the old PCM format

Word	Assignment	Commutation
00	Sync Word (11101011) (EB)	1:1
01	Sync Word (10010000) (90)	1:1
02	Frame Counter/Events	1:1
03	ElectroMeter Range (EMR)/EMM	4:1
04	ElectroMeter Mantissa (EMM)	4:1
11	ElectroMeter Range (EMR)/EMM	4:1
12	ElectroMeter Mantissa (EMM)	4:1
16	Format Counter MSB	1:1
17	Format Counter LSB	1:1
19	ElectroMeter Range (EMR)/EMM	4:1
20	ElectroMeter Mantissa (EMM)	4:1
27	ElectroMeter Range (EMR)/EMM	4:1
28	ElectroMeter Mantissa (EMM)	4:1
29	HouseKeeping Data (HKD)	1:16

Table B.2 Housekeeping assignments used in the old PCM format

Frame	Assignment
00	Battery Voltage (+28 V)
01	Total Current
02	Emmision Current (IEM)
03	IGP voltage
04	IGP current
05	Temperature Sensor
06	Temperature Electronics 1
07	Temperature Electronics 2
08	Internal Voltage (+5 V)
09	Total Current
10	Emmision Current (IEM)
11	Internal Voltage (+10 V)
12	Internal Voltage (+15 V)
13	Internal Voltage (+100 V)
14	Internal Voltage (-10 V)
15	Internal Voltage (-15 V)

Table B.3 ElectroMeter Mantissa (EMM) and ElectroMeter Range (EMR) words division used in the old PCM format

Words 3/11/19/27	EMR	EMR	EMR	EMM	EMM	EMM	EMM	EMM
Words 4/12/20/28	EMM	EMM	EMM	EMM	EMM	EMM	EMM	EMM

B.2. New PCM format

- Bit rate: 833.00 kbits/s
- 8 bit words/frame: 96
- Frames/format: 64

Table B.4 Main frame channel assignments used in the new PCM format

Word	Assignment	Commutation
00	Sync Word (11101011) (EB)	1:1
01	Sync Word (10010000) (90)	1:1
02	Frame Counter/Events	1:1
04	ElectroMeter Mantissa (EMM) MSB	3:1
05	ElectroMeter Mantissa (EMM) LSB	3:1
06	ElectroMeter Range (EMR)	3:1
07	HouseKeeping Data (HKD)	1:16
08	Emission Current (IEM) MSB	3:1
09	Emission Current (IEM) LSB	3:1
34	Format Counter MSB	1:1
35	Format Counter LSB	1:1
36	ElectroMeter Mantissa (EMM) MSB	3:1
37	ElectroMeter Mantissa (EMM) LSB	3:1
38	ElectroMeter Range (EMR)	3:1
39	HouseKeeping Data (HKD)	1:16
40	Emission Current (IEM) MSB	3:1
41	Emission Current (IEM) LSB	3:1
64	Timer	1:1
65	Timer	1:1
68	ElectroMeter Mantissa (EMM) MSB	3:1
69	ElectroMeter Mantissa (EMM) LSB	3:1
70	ElectroMeter Range (EMR)	3:1
71	HouseKeeping Data (HKD)	1:16
72	Emission Current (IEM) MSB	3:1
73	Emission Current (IEM) LSB	3:1

Table B.5 Housekeeping assignments used in the new PCM format

Frame	Assignment
00	Battery Voltage (+28 V)
01	Total Current
02	IGP voltage
03	IGP current
04	Internal Voltage (+5 V)
05	Internal Voltage (+12 V)
06	Internal Voltage (+15 V)
07	Internal Voltage (-12 V)
08	Internal Voltage (-15 V)
09	Anode Voltage
10	Offset Voltage
11	Shield Voltage
12	Temperature 1
13	Temperature 2
14	Temperature 3
15	Temperature 4

B.3. Wadis PCM format

- Bit rate: 3333.33 kbits/s
- 8 bit words/frame: 29
- Frames/format: 64

Table B.6 Main frame channel assignments used in the WADIS PCM format.

Word	Assignment	Commutation
00	Sync Word (11101011) (EB)	1:1
01	Sync Word (10010000) (90)	1:1
05	Frame Counter	1:1
06	Frame Counter	1:1
07	Frame Counter	1:1
08	Frame Counter	1:1
09	ElectroMeter Mantissa (EMM) MSB	3:1
10	ElectroMeter Mantissa (EMM) LSB	3:1
11	ElectroMeter Range (EMR)	3:1
12	HouseKeeping Address/Frame Cnt	1:16
13	Emission Current (IEM) MSB	3:1
14	Emission Current (IEM) LSB	3:1
15	ElectroMeter Mantissa (EMM) MSB	3:1
16	ElectroMeter Mantissa (EMM) LSB	3:1
17	ElectroMeter Range (EMR)	3:1
18	Empty	
19	Emission Current (IEM) MSB	3:1
20	Emission Current (IEM) LSB	3:1
21	ElectroMeter Mantissa (EMM) MSB	3:1
22	ElectroMeter Mantissa (EMM) LSB	3:1
23	ElectroMeter Range (EMR)	3:1
24	HouseKeeping Data (HKD)	1:16
25	Emission Current (IEM) MSB	3:1
26	Emission Current (IEM) LSB	3:1

Table B.7 Housekeeping assignments used in the WADIS PCM format

Frame	Assignment
00	Temperature 4
01	Battery Voltage (+28 V)
02	Total Current
03	IGP voltage
04	IGP current
05	Internal Voltage (+5 V)
06	Internal Voltage (+12 V)
07	Internal Voltage (+15 V)
08	Internal Voltage (-12 V)
09	Internal Voltage (-15 V)
10	Anode Voltage
11	Offset Voltage
12	Shield Voltage
13	Temperature 1
14	Temperature 2
15	Temperature 3

Appendix C.

The ionization gauges TOTAL and CONE

There are some obvious requirements for the instruments operating onboard the sounding rockets. One is that the time constant of the instrument must be small enough to allow a good altitude resolution. Usually, a sounding rocket passes through the mesosphere with a velocity of about 1000 m/s. This means that one need a time resolution of 1 ms in order to measure with 1 m altitude resolution.

Since 1990 sounding rocket campaigns were conducted with use of TOTAL (as it measures total densities) and improved version of TOTAL, the CONE (COmbined sensor for Neutral and Electrons) sensors to investigate neutral air turbulence, and as well neutral densities and temperatures in the MLT region. These sensors were mounted in the rear of the payload so that they look along the rocket velocity vector during downleg. During WADIS 1 campaign CONE sensor was mounted both in the rear and in the front of the payload. A list of all sounding rocket campaigns conducted in polar latitudes with use of TOTAL or CONE sensors is given in App. A.

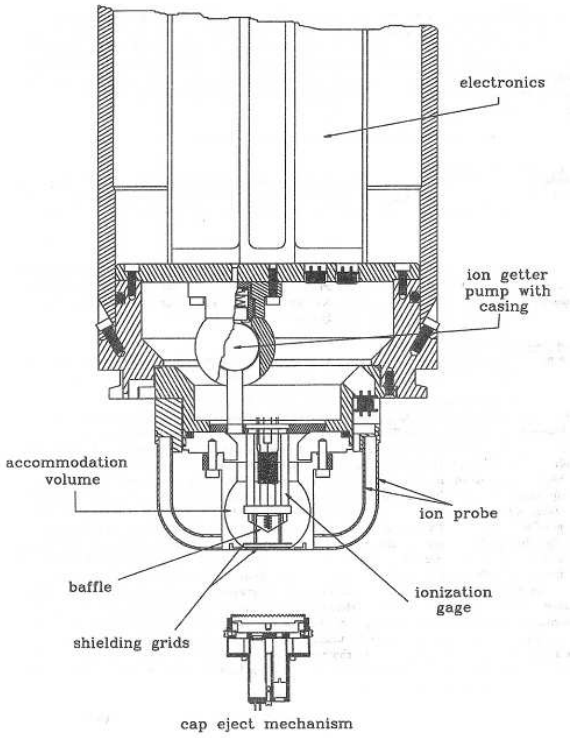

Figure C.1 Schematic of the TOTAL instrument.

Both TOTAL and CONE are ionization gauges optimized for a pressure range between

10^{-5} and 1 mbar., thus suitable to investigate turbulence at atmospheric altitudes between 60 and 100 km. The main difference between the two ionization gauges is their geometrical design. TOTAL was a 'closed' gauge where the triode system was placed inside a cylindrical tube (*Hillert et al.*, 1994). A schematic picture of TOTAL sensor and part of the TOTAL rocket section is presented in Fig. C.1. Ambient air molecules can enter the gauge only through a small orifice which is covered by the entrance grid. Having passed the shielding grid, which in addition protects the ionization gauge from the disturbing influence of atmospheric plasma, the molecules first hits the baffle. This is mounted in such a way that at least two collisions with the walls of the accommodation chamber have to take place before the molecules can enter the gauge itself. The major drawbacks of such a design is relatively large time constant of $\approx$ 5 ms limiting spatial resolution of the gauge to 5 m for a rocket velocity of 1000 m/s (*Hillert et al.*, 1994).

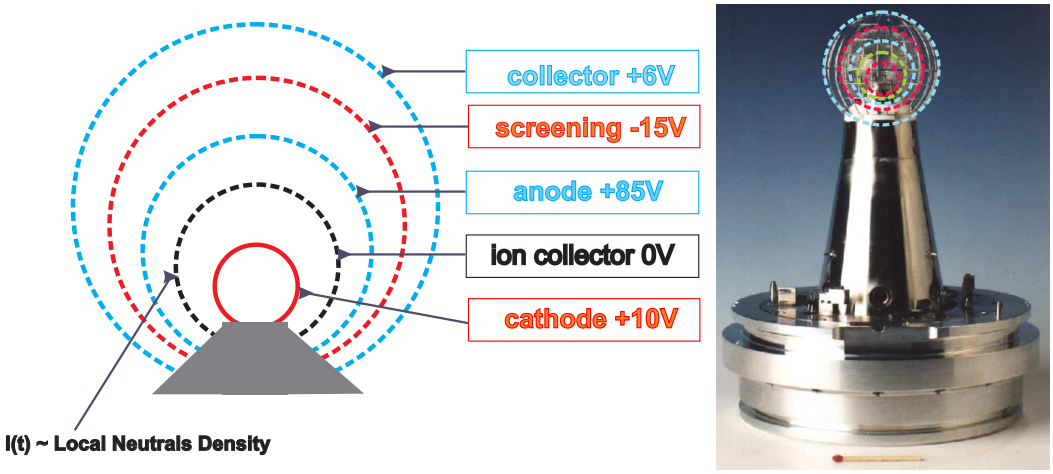

Figure C.2 Schematic and photo of the CONE instrument.

To improve the time constant of the system, a new ionization gauge, namely CONE, was developed, realizing an 'open design' (*Giebeler et al.*, 1993). The CONE is a combination of an ionization gauge and a fixed biased Langmuir probe. A schematic of the CONE instrument is shown in Fig. C.2. Briefly, this instrument functions as follows. The outermost grid of the CONE instrument is positively biased: therefore, it attracts negatively charged atmospheric constituents. Obviously, this grid also works as a shield for positive ions. The next grid is negatively biased, and hence, it shields the ionization gauge against the rest of the ambient plasma. The innermost cathode, ion collecting electrode, and anode form the ionization gauge itself.

The outermost grid of CONE (electron collector) and the inner grid of the ionization gauge (ion collector) are connected to sensitive electrometers. Thus, the currents measured by them are proportional to the number of the collected elements: i.e., to the local electron and neutral number density, respectively.

The time constant of both the electron and neutral density measurements is less than 1 ms. For a typical rocket flight this implies an altitude resolution of tens of centimeters. The precision of the measurements with the CONE instrument is better than 0.1 %.

The high precision and small time constant of both TOTAL and CONE instruments make it possible to detect small-scale neutral density fluctuations that arise due to processes like neutral air turbulence (*Lübken et al.*, 2002).

The technical parameters of TOTAL and CONE sensors are given in Tab. C.1.

Table C.1 Technical data of the TOTAL and CONE ionization gauges (after *Rapp*, 1999)

	TOTAL	CONE
Cathode	0.1×1.0 mm, $U_c = +10$ V	$\oslash$6.0 mm, $U_c = +10$ V
Ion collector	$\oslash$6.6 mm, $U_{ic} = 0$ V	$\oslash$20.0 mm, $U_{ic} = 0$ V
Anode	$\oslash$14.5 mm, $U_a = +100$ V	$\oslash$30.0 mm, $U_a = +85$ V
Emission current	16 μA	14 μA
Vacuum meter constant	0.4 mbar^{-1}	1.5 mbar^{-1}
Time constant @ 10^{-2} mbar)	4.5 ms	0.3 ms
altitude resolution @ $v_R = 1000\ m/s$	$\approx$ 4.5 m	$\approx$ 0.3 m

C.1. Background parameters

For the derivation of the turbulent parameters one need to know the atmospheric temperature, T, and density, ρ, measured in the same volume. These parameters, however, must not include small-scale variation but must be smoothed over spatial distance of the size of largest eddy. These mean values are called the background parameters, also referred to as the *background atmosphere*. For background temperatures and densities the smoothed altitude profiles are used, derived either from the TOTAL or CONE measurements. Making use of an absolute laboratory calibration for the CONE/TOTAL instrument allows to derive an absolute neutral air density altitude profile (*Lübken*, 1993; *Rapp et al.*, 2001). Also, because of the disturbed density field due to the shock front, for the absolute density derivation aerodynamical calculations must be used to correct the measurements (so called RAM factor *Rapp et al.*, 2001). This, however, does not affect the measurements of the small-scale density fluctuations, which are used in the turbulence detection technique. Afterwards, the altitude profile of neutral number densities is integrated assuming hydrostatic equilibrium to yield a temperature profile at ∼200 m altitude resolution and an accuracy of ∼3 K (*Rapp et al.*, 2001, 2002).

Appendix D.

Analysis techniques

In this appendix a description of the Fourier analysis technique based on the Fourier spectral analysis and wavelet analysis technique based on the wavelet spectral analysis are described. This is copied from the work of *Strelnikov* (2006), with minor changes made by the author.

D.1. Fourier

Fourier technique to analyze neutral air density fluctuations with respect to turbulence has been described in detail in *Lübken* (1992, 1993); *Lübken et al.* (1993); *Lübken* (1997). Here this technique is shortly summarized. The procedure of applying Fourier analysis to rocket data is similar to the one used in the New Statistical Turbulence Analysis which uses wavelet analysis technique and is described in Chap. 4.

Using rocket trajectory, the measured currents are subdivided into altitude bins, typically of 1−5 km extent. Then the residuals, $r(t)$, for each altitude bin are derived. The Fourier power spectrum of the derived residuals, $r(t)$, applying the Hanning-windowed Fast Fourier Transform (FFT) is then calculated. The power spectrum is normalized to yield the variance, σ, of the observed relative fluctuations:

$$\int_{-\infty}^{\infty} W(w)dw = \sigma^2 \tag{D.1}$$

Subsequently, the power spectrum of each bin is fitted by a spectral turbulence model (e.g., *Heisenberg*, 1948), where the main free fitting parameter is the turbulent energy dissipation rate, ε:

$$\mathbf{W}(2\pi\boldsymbol{f}) = \frac{\Gamma(5/3)\sin(\pi/3)}{2\pi\boldsymbol{v_R}}\, a^2 \frac{N_\vartheta}{\varepsilon^{1/3}} f_a \frac{(2\pi\boldsymbol{f}/\boldsymbol{v_R})^{-5/3}}{\left(1+\left[\left(2\pi\boldsymbol{f}/\boldsymbol{v_R}\right)/\left(2\cdot 9.90\pi\left(\boldsymbol{\nu}^3/\varepsilon\right)^{1/4}\right)\right]^{8/3}\right)^2} \tag{D.2}$$

The final result of Fourier technique is an ε-profile with a typical altitude resolution of 1 km.

D.2. Wavelet

In contrast to the Fourier analysis, which decomposes time series into a sum of the infinite in-time harmonic functions, namely sine and cosine, the wavelet analysis decomposes the signal into the time-frequency domain, also referred to as the phase space (e.g., *Holschneider*, 1993). That is, it allows the detection of the time intervals where detected frequencies appear in the time series. For the description of the basic principles, mathematical details, and different applications of the wavelet analysis the reader is referred to the numerous and continuously appearing publications and Web resources. Some of them are cited in this Appendix.

D.2.1. Wavelet analysis: Definitions

The wavelet transform of a time series $x(t)$ is defined as (e.g., *Daubechies*, 1992; *Kumar and Foufoula-Georgiou*, 1997):

$$(\mathbb{W}x)(\tau, s) = \int x(t)\ \psi^*_{\tau,s}(t)\ dt \tag{D.3}$$

The function ψ is called *"mother wavelet"* (equally *"wavelet function"*) and * indicates the complex conjugate. Each function from the family

$$\psi_{\tau,s}(t) = \frac{1}{\sqrt{s}}\psi\left(-\frac{t-\tau}{s}\right) \tag{D.4}$$

is called *"daughter wavelet,"* where τ and s are parameters.

To be a wavelet, a function $\psi(t)$ must be well localized in both time and frequency space (e.g., *Daubechies*, 1992; *Lewalle*, 1995; *Farge et al.*, 1999): That is, it must have a finite energy and zero mean. The latter condition is also known as admissibility condition:

$$\int_{-\infty}^{\infty} \psi(t)dt = 0 \tag{D.5}$$

There are many different wavelet functions, but generally they can be divided into orthogonal and nonorthogonal (e.g., *Daubechies*, 1992; *Lewalle*, 1995; *Torrence and Compo*, 1998). There are two sorts of the wavelet transform: continuous and discrete (e.g., *Daubechies*, 1992; *Lewalle*, 1995; *Torrence and Compo*, 1998). In the continuous case parameters s and τ can change continuously. In the discrete wavelet transform s and τ can only take on discrete values. Each wavelet function is only applicable either for the continuous (nonorthogonal) or discrete (orthogonal) analysis algorithm. One can also try to construct a new wavelet that can be more suitable for the particular problem (e.g., *Sweldens and Schröder*, 1996).

Here only the *Morlet* wavelet function is futher considered. It is defined as (*Grossmann and Morlet*, 1984)

$$\psi(\eta) = \sqrt[4]{\frac{1}{\pi}} exp\left(i\omega_0\eta\right) exp\left(-\frac{\eta^2}{2}\right), \qquad \eta = \frac{t-\tau}{s} \tag{D.6}$$

where ω_0 is a non-dimensional frequency parameter of the wavelet function and η is a non-dimensional time parameter. The Morlet wavelet is a nonorthogonal complex-valued function and. Therefore, we only consider the continuous wavelet transform here.

The Morlet wavelet consists of a plane wave modulated by a Gaussian envelope of width ω_0/π (*Lewalle et al.*, 2005). The envelope factor ω_0 controls the number of oscillations of the wavelet (the higher ω_0-value, the more oscillations). Fig. D.1 shows an example of two Morlet wavelets with $\omega_0 = 6$ (left panel) and $\omega_0 = 12$ (right panel), and η is arbitrary but the same for both cases. The upper panel shows these functions in the time space: the solid line displays the real part, and the dashed line displays the imaginary part. The lower panel shows the same functions in the frequency space.

One sees that the higher order Morlet function (larger ω_0-value) has larger time and smaller frequency support (or the widths σ^t and σ^ω). This is the direct consequence of Heisenberg's uncertainty principle, which can be written as:

$$\sigma^t\sigma^\omega = \sigma^t\ 2\pi\sigma^f \geq \frac{1}{2} \tag{D.7}$$

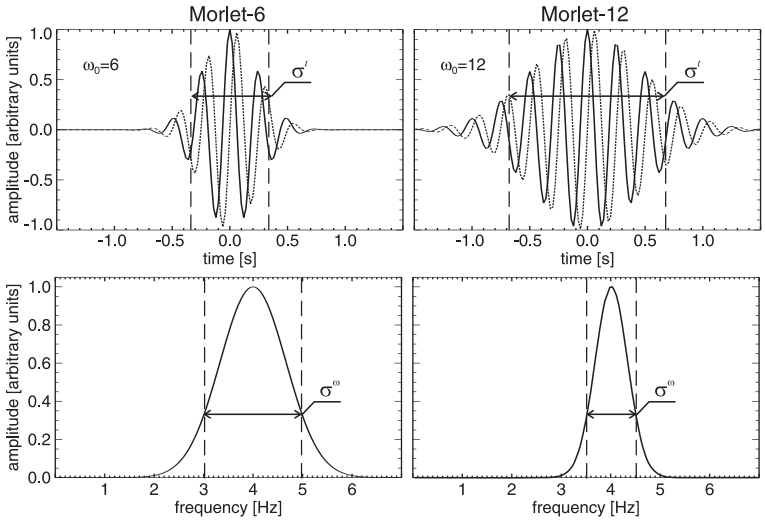

Figure D.1 Upper panel: Real (solid line) and imaginary part (dashed line) of a Morlet wavelet in the time space with ω_0=6 (left) and ω_0=12 (right). Lower panel: The same wavelet functions in the Fourier space. Dashed lines mark the width of the function, which is denoted by σ^t and σ^ω for the time and frequency space, respectively (after *Strelnikov*, 2006).

where σ^t and σ^ω are the width of the wavelet function in time (time support) and frequency space (frequency support), respectively.

By changing parameter τ of a wavelet function $\psi_{\tau,s}$, one changes the time localization of the wavelet:

$$\psi_{\tau,s}(t)\Big|_{s=const} = \frac{1}{\sqrt{s}}\psi\left(-\frac{t-\tau}{s}\right), \qquad \tau = \tau_1, \tau_2, ... \tag{D.8}$$

This operation is called *translation* of the mother wavelet. Each function $\psi_{\tau,s}(t)$ is localized around the time point $t = \tau$. Changing parameter τ, one shifts the localization point of the function $\psi_{\tau,s}(t)$ along the time axis t (translates). The translation of the Morlet-12 wavelet is demonstrated in Fig. D.2, where the upper panel shows the signal to be analyzed in the time space. The lower panels show two translated versions of the wavelet function in the same (as for the signal) time domain. The wavelet function must have the same number of points as the investigated signal, but its energy is concentrated around the time point $t = \tau$.

Changing parameter s, also called *wavelet scale*, one changes the frequency of the function:

$$\psi_{\tau,s}(t)\Big|_{\tau=const} = \frac{1}{\sqrt{s}}\psi\left(-\frac{t-\tau}{s}\right), \qquad s = s_1, s_2, ... \tag{D.9}$$

This operation is called *scaling* of the mother wavelet. Large values of the scaling parameter s correspond to the low frequencies or the large scales of the function $\psi_{\tau,s}$. Small s-values correspond to the high frequencies or the small scales of $\psi_{\tau,s}$. Fig. D.3 demonstrates the scaling of the Morlet wavelet function. The left panels in Fig. D.3 show the Morlet-12 wavelet (ω_0=12) at the scale s_1, which corresponds to the frequency of 4 Hz. The right panels in Fig. D.3 show the same Morlet-12 wavelet but at the scale $s_2 > s_1$, which corresponds to the frequency of 2 Hz.

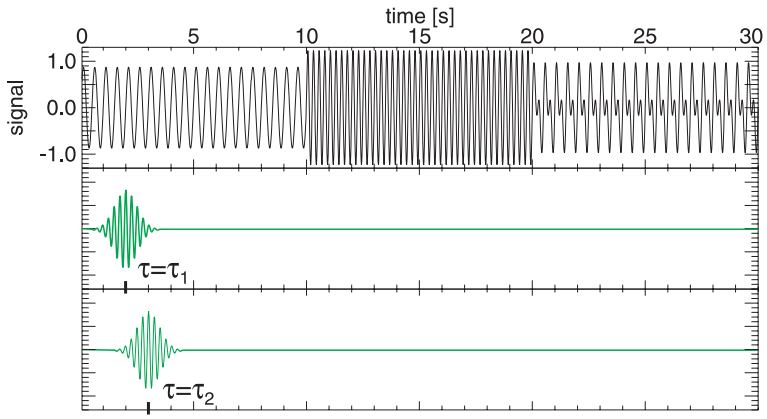

Figure D.2 Translation of the wavelet function. The upper panel shows the signal to be analyzed. The lower panels show two translated Morlet-12 wavelet functions at a fixed scale (after *Strelnikov*, 2006).

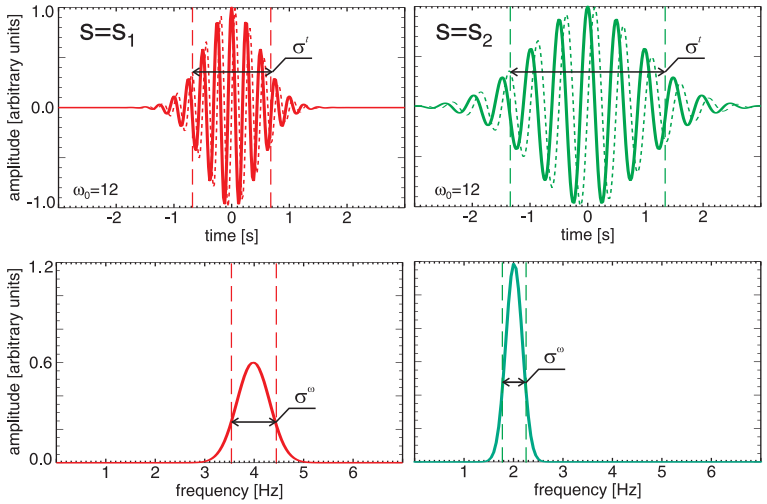

Figure D.3 Scaling of the wavelet function. Upper plots show the Morlet-12 wavelet function (complex valued) in the time domain. The solid line is the real part, and the dashed line is the imaginary part. The lower plots show the same functions in the Fourier domain. Left panel: The scale of the Morlet function corresponds to the frequency of 4 Hz. Right panel: The scale of the Morlet function corresponds to the frequency of 2 Hz. The larger scales correspond to the lower frequency (after *Strelnikov*, 2006).

Simply speaking, the wavelet transform correlates the signal with the wavelet function in the following sequence:

1. Moving the wavelet of a fixed scale (frequency) along the time axis (translation) find the time regions where the correlation is high.
2. Change the scale (frequency) of the wavelet function (scaling).
3. Repeat the steps 1 and 2 until we fill up the scale (frequency) range we are interested in.

Properties of wavelet analysis are described in *Strelnikov* (2006). The comparison of

Fourier and wavelet technique is also conducted therein. In summary, among the other advantages of the wavelet technique, the most important is the frequency-dependent time resolution of the analysis. Applied to the turbulence analysis, it means that in time the wavelet analysis resolves the small scales (high frequencies) better than the large scales.

Appendix E.

Experimental relation between turbulence dissipation rate and variability dissipation rate

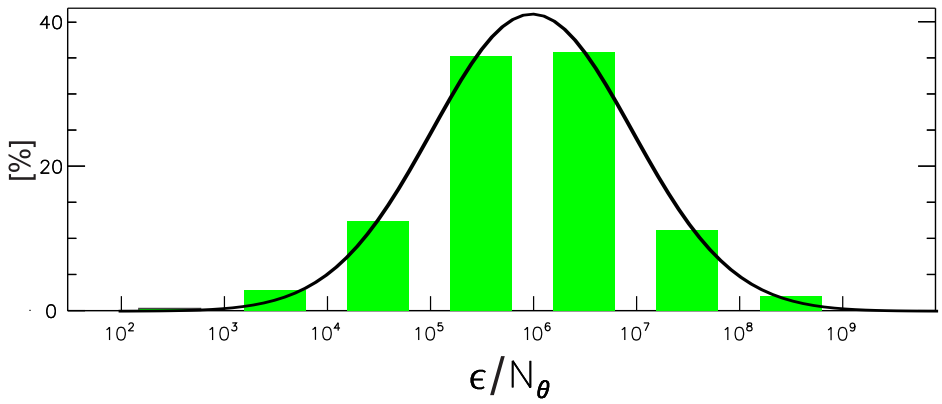

Figure E.1 Histogram of ε/N_θ values is given as green bars. The black line is a fitted Gaussian.

It is interesting to compare the ε and N_θ values obtained using the new analysis. Theoretical relation between turbulence dissipation rate ε and variability dissipation rate N_θ was derived in Sec. 2.7 to be:

$$\varepsilon \in (10^4 : \cdot 10^7) \cdot N_\theta \tag{E.1}$$

This derivation was made by substituting different constants/parameters values available in the literature to Eq. 2.17. Here, the dependence derived using experimental values of ε and N_θ obtained using the new analysis is derived and presented. In Fig. E.1. As green bars a histogram of measured ε/N_θ values is shown. As a black line Gaussian function with $\mu \approx 10^6$ and $\sigma \approx (10^5 : 10^7)$ is fitted in the log scale. It can be seen that ε/N_θ values exhibit in the range from 10^2 to 10^9 with majority ($\approx 80\%$) exhibiting in the obtained theoretical range from 10^4 to 10^7. Unfortunately this results cannot help us to narrow the values of the constants used in Eq. 2.17, but they do confirm that the theoretical assumptions used for derivation of these constants were valid.

Appendix F.

Buoyancy frequency climatology from rocket temperature data

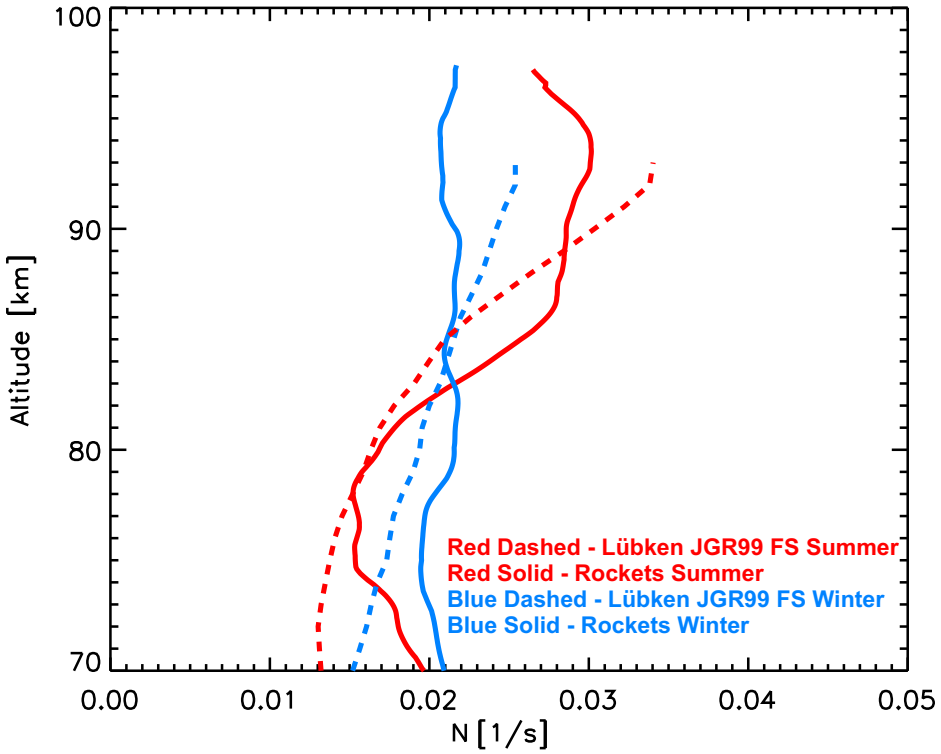

Figure F.1 Buoyancy frequency obtained by *Lübken* (1999) from falling sphere measurements (dashed lines) and in the frame of this work from the rocket measurements (solid lines) for winter and summer (blue and red lines respectively).

Finally, since the CONE instrument measures, besides the turbulence parameters, also temperature and density, it is interesting to use these data to derive buoyancy frequency, N, profiles for winter and summer. Buoyancy frequency, N, can be determined using following equation:

$$N = \sqrt{\left(\frac{dT}{dz} + \frac{g}{C_P}\right) \cdot \frac{g}{T}} \tag{F.1}$$

in which g is the acceleration due to gravity and C_P is the specific heat of dry air at constant pressure.

In the frame of this work the buoyancy frequency mean profiles for winter and summer were obtained using temperature data for winter (14 flights) and summer (15 flights). The flights used for this statistics are given in App. A. These are the flights in which successful temperature measurements were conducted. In Fig. F.1 the mean N profiles are shown as solid lines with blue color for winter and red color for summer. For comparison results obtained by *Lübken* (1999) using falling sphere measurements are shown with dashed lines with the same color labeling. The profiles for summer show general agreement. In winter, the N values obtained using the falling sphere experiments increase with altitude. The profile obtained using the rocket data, however, do not change significantly with altitude. It has to be taken into account that the falling sphere experiments were conducted only between April and September, whereas the rocket flights were conducted all year long. Therefore the mean winter profile from falling sphere measurements shown in Fig. F.1 is obtained as a mean from months of April until middle of May, and middle of August until middle of October, whereas the mean winter profile from rocket measurements is obtained from all the flights conducted between middle of August and middle of May. Also for *Lübken* (1999) climatologies a larger number of 89 falling sphere experiments were available. The smallest scales detected by the falling sphere experiments are typically 8, 3, and 0.8 km at 85, 60, and 40 km, respectively. The rocket temperature measurements have higher altitude resolution of 200 m (App. C). Also rocket temperature measurements are conducted in the 70 - 110 km altitude range, whereas the falling sphere experiments in 35 -95 km altitude range.

The N results obtained from the rocket measurements do agree with the results obtained by *Hall et al.* (2007) for Svalbard (78 ^{o} N). They obtained values only for the altitude of 90 km. For the temperature measurements they used a meteor wind radar. Their result for summer months is $N \approx 0.03$ and for winter months $N \approx 0.02$

Concluding, the buoyancy frequency, N, summer profile obtained from the rocket data shows general agreement with summer profile obtained by *Lübken* (1999). The winter profile, however, obtained using rocket data differs from the one obtained by *Lübken* (1999). Profile obtained from rocket data shows only roughly dependence on altitude, which is often assumed by theoreticians (e.g., *Holton*, 1992). Winter profile obtained by *Lübken* (1999) increases with altitude.

Appendix G.

Overview of remote atmosphere measurements

In situ measurements of turbulence in the MLT region can be accompanied by remote sensing using radars, lidars and satellites. In this appendix short description of the remote sensing techniques used in the frame of this work (e.g., to investigate MIL detected during ECOMA09 campaign, Sec. 5.1) is given.

G.1. Radar technique

Over the past decades mesosphere-stratosphere-troposphere (MST) radars have proven to be a powerful technique for the investigation of atmospheric dynamics from the troposphere up to the mesosphere (e.g., *Hocking*, 2011). In the frame of this work, the wind measurements from the Saura MF-radar were used. Saura MF-radar is a Doppler radar that runs at 3.17 MHz and is installed close to the Andøya Rocket Range as part of the ALOMAR observatory in Andenes. Among other things, Saura MF radar measures mesospheric winds using the Doppler beam steering (DBS) technique (e.g., *Stober et al.*, 2012). For the described experiment, a total of 4 off-vertical beam directions are chosen, each at an angle of 6.8° to the zenith and directed towards the north-east, south-east, south-west and north-west.

The main feature of this radar is the antenna which is formed by 29 crossed half-wave dipoles arranged as a Mills-Cross. The spacing of the crossed dipoles is 0.7 wave lengths resulting in a minimum beam width of 6.4°. Each dipole is fed by its own transceiver unit with a peak power of 2 kW (phase controlled on transmission and reception) providing high flexibility in beam forming and pointing as well as o- and x-mode operation for differential absorption and phase measurements (*Singer et al.*; *Singer et al.*, 2008, 2011).

G.2. ALOMAR RMR-Na lidar

Two ground based lidars are operating at the Arctic Lidar Observatory for Middle Atmosphere Research (ALOMAR) located on the northern Norwegian island Andøya. The ALOMAR Weber sodium (Na) lidar is a resonance fluorescence lidar (69^oN, 16^oE). *She et al.* (2002) and *Arnold and She* (2003) have described this Na lidar in detail. The set-up and status of the Na Lidar during December 2010 is described in more detail by *Dunker et al.* (2012). The Na lidar measures sodium number density, line-of-sight wind speed and temperature in the altitude range between about 80 and 110 km with uncertainties better than 10^8 m^{-3}, 2 m/s and 2 K, respectively. A cycle of three frequencies is emitted by the lidar, one at the D_{2a} frequency of sodium (589.189 nm) and the other two at +630 (±50) and -630 (±50) MHz, relative to the D_{2a} frequency. The emitted photons are resonantly scattered by the mesospheric sodium atoms, and the backscattered photons are collected

with two telescopes (ø = 1.8 m) that belong to the ALOMAR Rayleigh/Mie/Raman lidar. The geophysical variables can be calculated from the recorded photon count profiles after integrating for one hour for each profile. The lidar emits pulses of amplified 589 nm light. At first, continuous-wave (cw) 589 nm light is created through sum-frequency generation of a cw Nd:YAG beam at 1319 nm and 1064 nm. This 589 nm beam is frequency-locked at the Na D2a resonance frequency using Doppler-free spectroscopy. An acousto-optic modulator generates the two additional frequencies at 630 MHz. This cw light then enters a Spectra-Physics Quanta-Ray Pulsed Dye Amplifier 1, consisting of three dye cells (i.e. amplification stages). This dye amplifier is pumped by a pulsed, frequency-doubled Spectra-Physics Quanta-Ray PRO 230 Nd:YAG, producing the pulsed 589 nm beam.

The ALOMAR Rayleigh-/Mie-/Raman (RMR) lidar uses two Nd:YAG lasers with a repetition frequency of 30 Hz and an energy of 400 mJ/pulse at 532 nm (*von Zahn et al.*, 2000). The emitted wavelengths are at 1064 nm, 532 nm and 355 nm. The atmospheric backscatter is recorded with two 1.8 m diameter Cassegrain telescopes that can be tilted up to 30 deg off-zenith. Hydrostatic temperature profiles are calculated from relative density profiles obtained at 532 nm (*Hauchecorne and Chanin*, 1980). Densities are smoothed by a 1 h, 600 m window before temperature integration. Seed temperatures are taken from the MSIS model at an altitude of 90 km. Seasonal temperature variations measured with the ALOMAR Rayleigh-/Mie-/Raman lidar along with a description of the analysis method can be found in *Schöch et al.* (2008).

G.3. MLS instrument onoard NASA EOS satellite

The Earth Observing System (EOS) Microwave Limb Sounder (MLS), onboard the National Aeronautics and Space Administration (NASA) Aura satellite uses the microwave limb sounding technique (*Waters*, 1993) to provide information on Earth's upper stratosphere and mesosphere. The satellite rounds the Earth 15 times per day. For purposes of the ECOMA09 campaign the temperature data in the vicinity of the launch area for the 19th of December 2010 were investigated. This was made to investigate spatial extension of MIL event. The advantage of MLS measurements is a good spatial coverage of measurements in large height range (i.e. from 50 to 100 km). The vertical resolution of this technique is 3 to 6 km depending on altitude (*Livesey et al.*, 2007; *Wu et al.*, 2003) which is enough to detect large-scale MILs.

Appendix H.

Results from PHOCUS campaign in June/July 2011

H.1. Campaign overview

From the 28th of June to the 22nd of July 2011 the PHOCUS rocket campaign was conducted at Esrange (68 °N, 21 °E) in northern Sweden. One sounding rocket was launched to study the particle layers in the mesosphere, i.e. the nucleation and evolution of ice particles, the properties of meteoric smoke, and the possible influence of these particle populations on mesospheric chemistry. The launch took place during strong PMSE with occurring NLC. The PHOCUS rocket consisted of 18 different instruments, one of which was CONE to measure neutral air density, temperature and turbulence with very high altitude resolution and precision. These measurements were done during the downleg of the rocket flight. In addition data from ESRAD in Esrange and MAARSY in Andøya Rocket Range were available.

In this Appendix experimental results obtained during the rocket flight of the PHOCUS campaign are presented. First, density and temperature measurements obtained with the CONE instrument, which describe the background atmosphere, are shown. Then in situ measurements of small-scale structures in neutral air are discussed and compared with the temperature profile, PMSE and NLC.

H.2. Measurements

In situ measurements performed during downleg of the PHOCUS flight provided simultaneous and high-resolution measurements of neutral air density, temperatures, and turbulence parameters.

H.2.1. Background atmosphere

The results of the neutral density measurements at heights between 70 and 100 km are shown in the Fig. H.1 as the black profile. The measured densities are comparable to the *Lübken* (1999) falling spheres measurements (red line). Above 80 km CONE density measurements are slightly lower than falling sphere measurements.

The temperature profile obtained using the CONE sensor between 70 and 100 km is shown in the Fig. H.2 as a black line. The lowest temperatures of $\sim$ 120 K appear at the altitude of 91 km. The measured temperature profile reveals pronounced mesospheric inversion layer (MIL) at altitudes between 81 and 84 km. The amplitude of the inversion layer reaches values of about 15 K. The temperature gradient above the inversion layer is close to the adiabatic lapse rate (please compare with dashed orange line), which is typical feature of

the MIL and coincides often with high turbulence regions. The entire temperature profile, including region with the inversion layer, reveals signatures of gravity waves.

Results from falling sphere measurements made by *Lübken* (1999) are shown in Fig. H.2 as red line. Additionally, results from IAP impact detector are overplotted. The latter is shown as the dark blue profile in Fig. H.2. This result is the netto current of the measured aerosols (lighter particles are not measured here). To the current understanding, the strong negative peak around the occurrence of the NLC is due to negatively charged ice particles.

At the altitudes from 78 to 84 km and 86 to 91 km the temperature drops below the frost point. This is marked as the two light blue, dashed lines in Fig. H.2. These lines are shown for two typical, measured values of water content at these altitudes. The PMSE were observed by ESRAD between 80 and 83 km, were as NLC were observed by photometer on board of the PHOCUS rocket at around 81.5 km. These altitudes are below the frost point observed at the temperature profile obtained using CONE sensor. Please compare also with Fig. H.3.

H.2.2. Turbulence

Next, in Fig. H.3 the results of measurements of the turbulence energy dissipation rates, ε in the altitude range from 60 to 100 km are presented and compared with the temperature profile obtained with the CONE sensor. The derived ε-values are shown by dark blue crosses with error bars in orange. Whenever a continuous turbulence layer was detected, the single crosses are connected by a dark blue line. Energy dissipation rates are converted to heating rates (upper abscissa) using Eq. 2.8

The measured dissipation rates reveal typical summer-values and are not continuous but

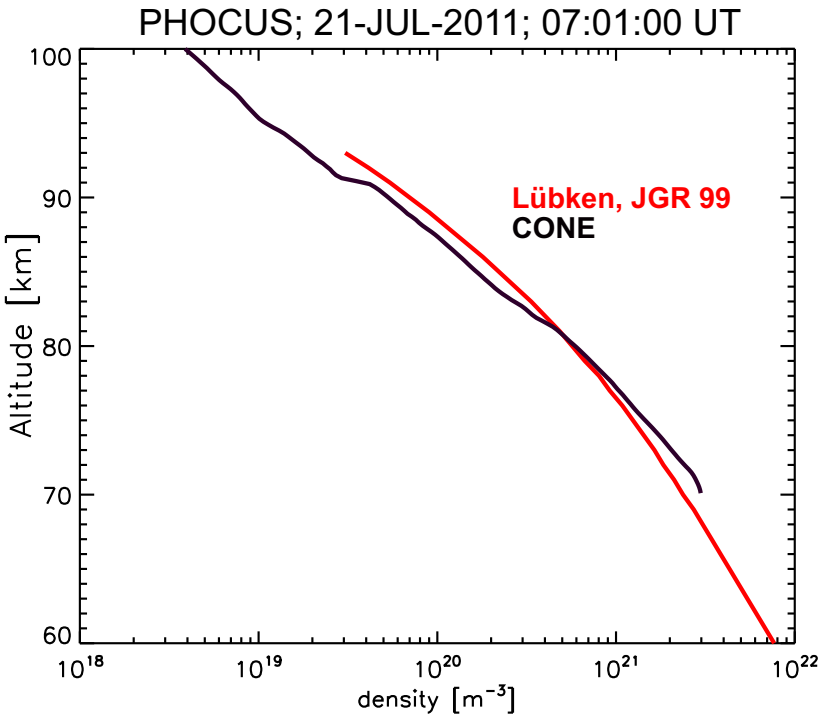

Figure H.1 Neutral densities measured during PHOCUS flight (black line). Falling sphere measurements from *Lübken* (1999) are shown with the red line.

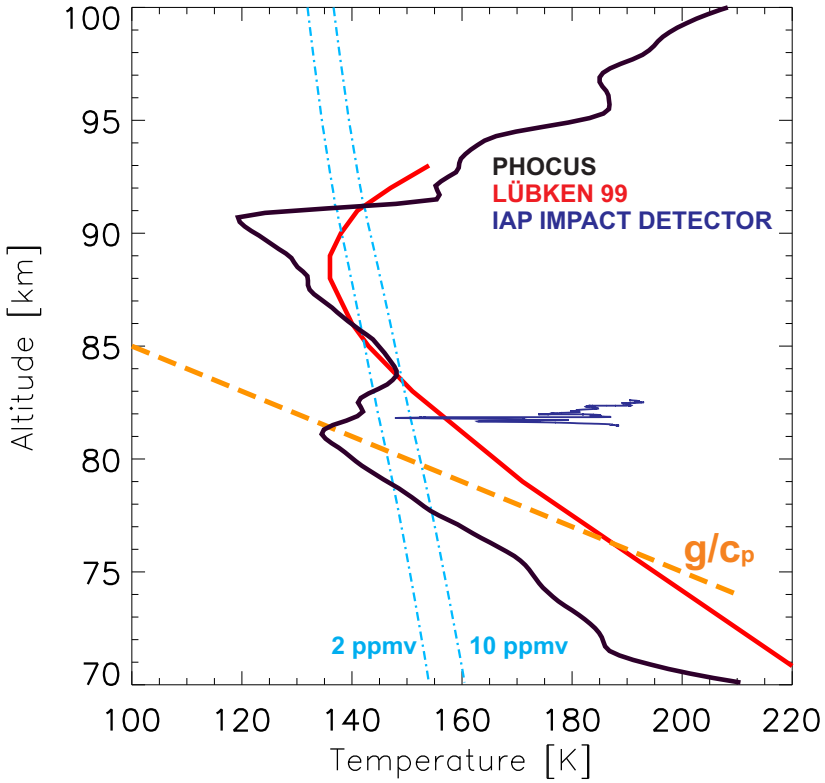

Figure H.2 Neutral temperatures measured during the PHOCUS flight (black line). Falling sphere measurements from *Lübken* (1999) are shown as red line. Adiabatic lapse rate is shown as dashed orange line. Additionally, IAP Particle Detector is shown as a dark blue line. Two dashed, light blue lines show the frost point values for typical measured values of water content for these altitudes between 2 and 10 ppmv (please see the text for more details).

rather exhibit in narrow layers, which is also typical for summer period. The highest dissipation rate are observed above 90 km, with the heating rates reaching up to 1000 K/day. Also, the measured energy dissipation rates exhibit large gradients. The ε-value often changes by an order of magnitude within one kilometer. Above 93 km the turbopause is observed, that is above this height molecular diffusion dominates over viscosity and no more turbulence was detected

It is interesting to compare the measured dissipation rate profile with the temperature profile. At the altitudes from 80 to 84 km MIL is observed in the temperature profile, which coincides with the high dissipation rate values, with heating rate of up to 100 K/day. This is typical for many MIL phenomena and was described, e.g., by *Szewczyk et al.* (2013). According to numerical simulations by *Liu et al.* (2000), a heating rate of $\sim$10 K/day is sufficient for producing inversion layers. In our case dissipation rates is smaller, additional analysis of gravity waves and tidal activity in the region should be made to investigate the MIL creation mechanism.

It is also worth to note, that used turbulence detection technique is not sensitive to turbulence in the regions where the temperature profile exhibits an adiabatic lapse rate (e.g., *Lehmacher and Lübken* (1995), Sec. 5.2.4 of this thesis) and, therefore, can underestimate the actual ε-values. This implies that the turbulence dissipation above the inversion layers

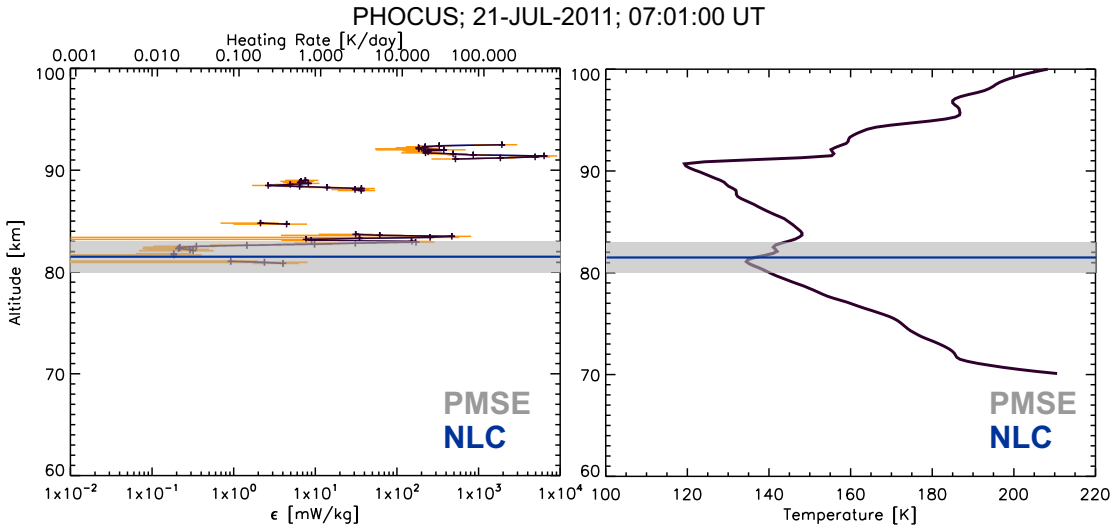

Figure H.3 Turbulence energy dissipation rates measured in-situ during the PHOCUS flight shown with dark blue crosses in the left panel. The single crosses are connected whenever continuous turbulence layer was detected. The error bars for each point shown by orange line. The corresponding heating rate is shown on the upper axis. In the right panel temperature profile obtained in the same volume is shown with the black line. Shaded grey area marks the region with the PMSE observed by Esrad during rocket launch, whereas the blue horizontal line marks the altitude at which the NLC were observed by photometer on board PHOCUS rocket.

could be even stronger than what is observed with the CONE instrument.

If turbulent dissipation rate is compared with the height of the occurrence of the PMSE (gray shaded area in Fig. H.3) and NLC (blue horizontal line in the same Figure) it can be seen that they coincide with turbulent activity. The current understanding of the phenomena of PMSE is that it needs turbulence to be created, which is confirmed by described measurements.

H.3. Summary

The PHOCUS flight provided real common volume in-situ measurements of neutral densities, temperatures and turbulence. The measured neutral densities are comparable with the falling sphere results from *Lübken* (1999). The neutral temperature profile when compared to *Lübken* (1999) falling sphere measurements shows a relatively cold atmosphere. In the regions from 78 to 84 km and 86 to 91 km the temperature drops below the frost point. In the lower regions, from 80 to 83 km these low temperatures coincides with PMSE and around 81.5 km with NLC. Also IAP Particle Detector shows a negative peak in the current around these altitudes. Regions with PMSE were also connected with turbulent activity there, which agrees with the current understanding of the PMSE phenomena. In the temperature profile MIL exhibits from 81 to 84 km, with coincides with strong turbulence in this region.

Appendix I.

Turbulence occurrence rate and variability during MIDAS/MACWAVE campaign

I.1. Turbulence dissipation rate variability

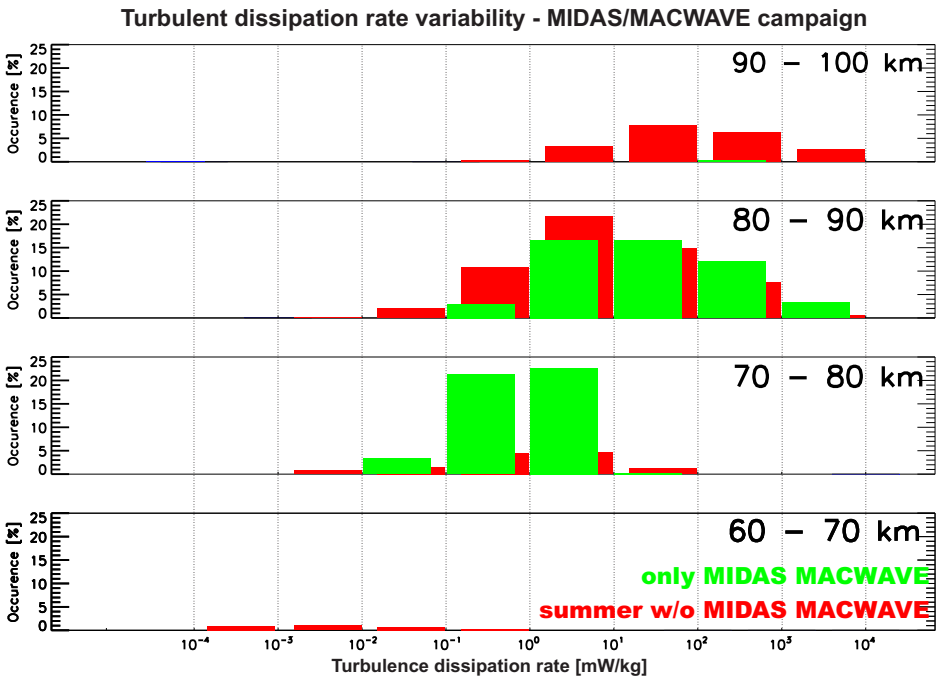

Figure I.1 Turbulence dissipation rate, ε, variability during MIDAS/MACWAVE campaign (green bars) and during remaining summer flights (red bars). In the uppermost row for the altitude range from 90 to 100 km, in the upper middle row from 80 to 90 km, in the lower middle row from 70 to 80 km, and in the lowermost row from 60 to 70 km.

I.2. Turbulence occurrence rate

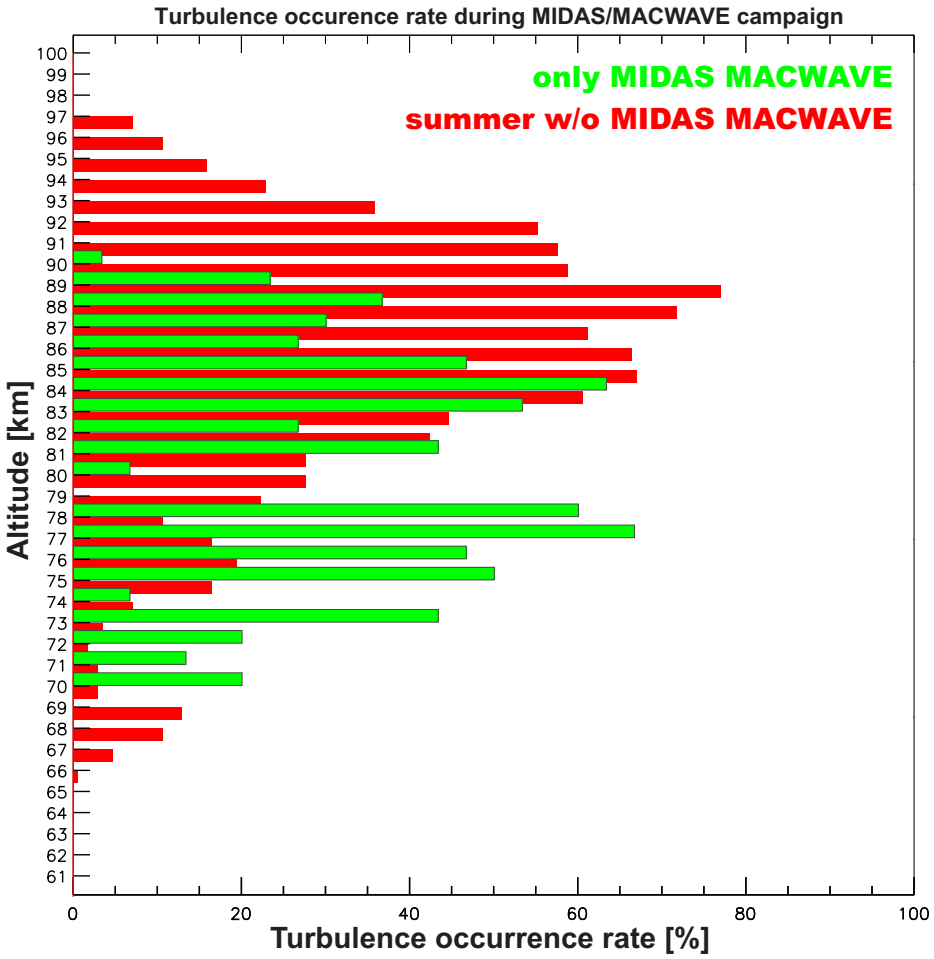

Figure I.2 Turbulence occurrence rate with altitude during MIDAS/MACWAVE campaign (green bars) and during remaining summer flights (red bars).

Appendix J.

ε and temperature profiles for individual flights.

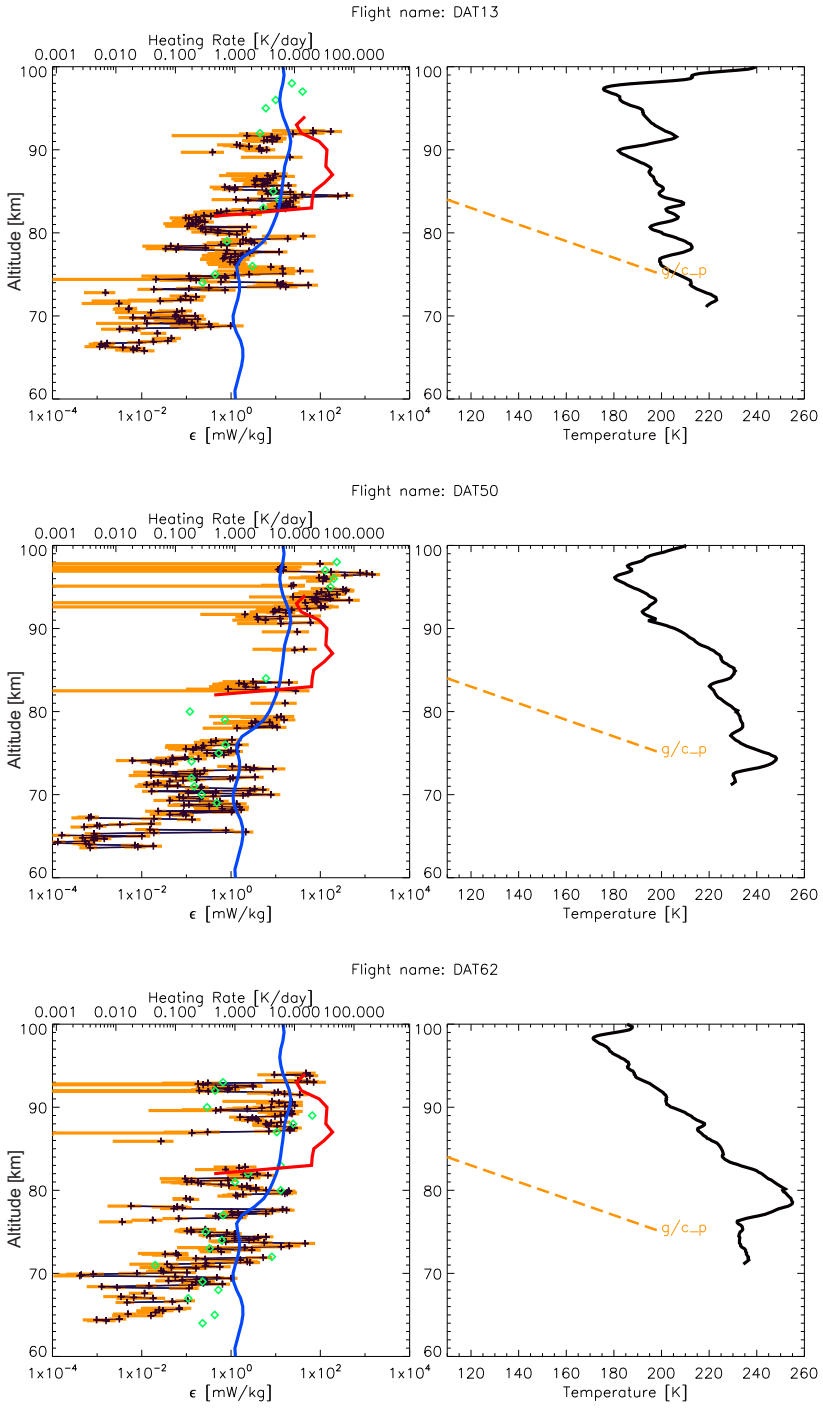

Figure J.1 Individual ε (left column) and temperature (right column) profiles for DAT13 (upper row), DAT50 (middle row) and DAT62 (lower row) flights. In the left panels with black crosses connected with the black lines ε-values are given, with ε_{ERR} given as orange bars. As green rectangles ε-values obtained by *Lübken* (1997) are shown for comparison. As blue and red lines mean ε profiles for winter (*Lübken*, 1997) and summer (*Lübken et al.*, 2002) are given respectively. In the right panels temperature profiles are given as black lines, with adiabatic lapse rate (orange dashed lines) given for comparison.

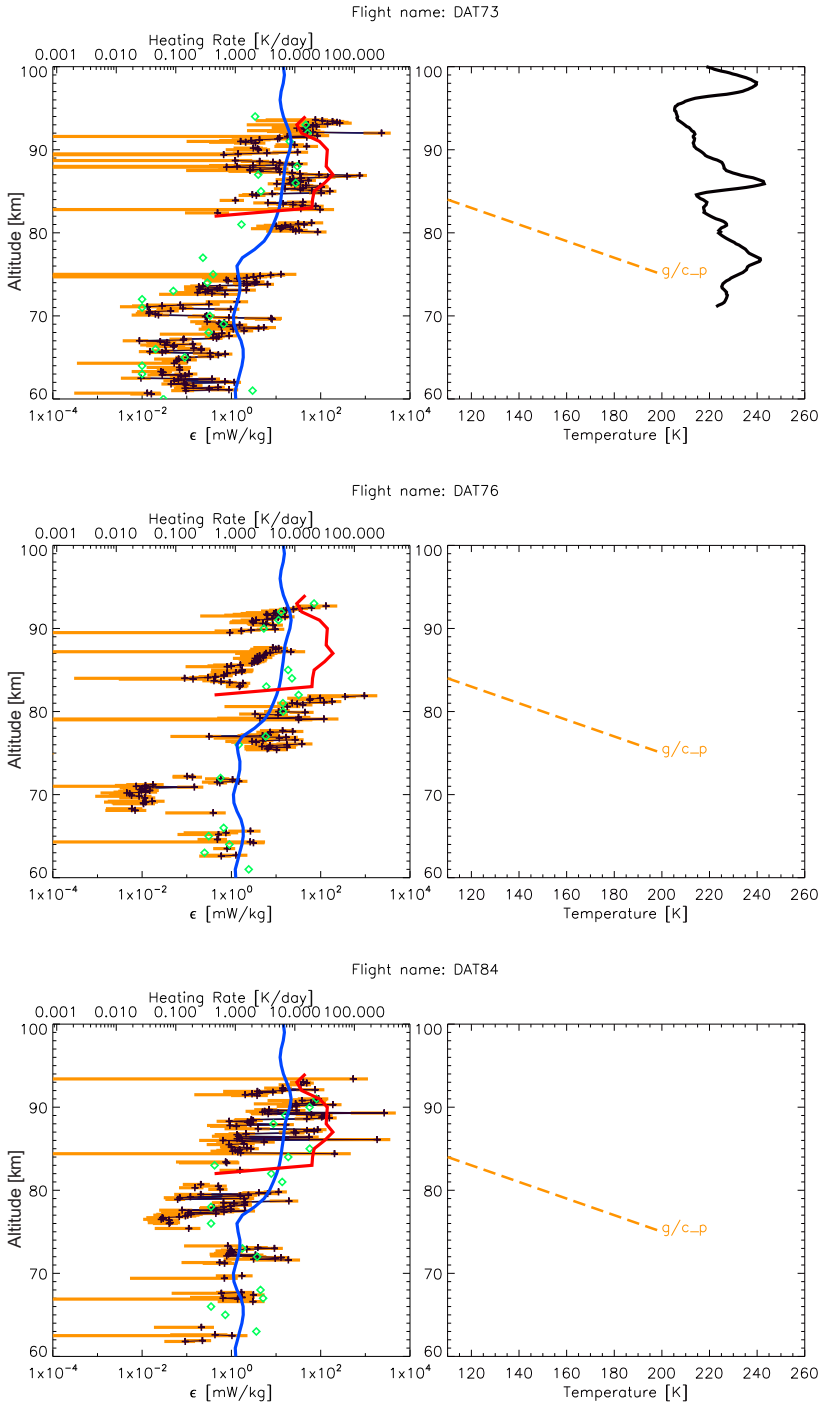

Figure J.2 Individual ε (left column) and temperature (right column) profiles for DAT73 (upper row), DAT76 (middle row, no temperature data) and DAT84 (lower row, no temperature data) flights. In the left panels with black crosses connected with black lines ε-values are given, with ε_{ERR} given as orange bars. As green rectangles ε-values obtained by *Lübken* (1997) are shown for comparison. As blue and red lines mean ε profiles for winter (*Lübken*, 1997) and summer (*Lübken et al.*, 2002) are given respectively. In the right panels temperature profiles are given as black lines, with adiabatic lapse rate (orange dashed lines) given for comparison.

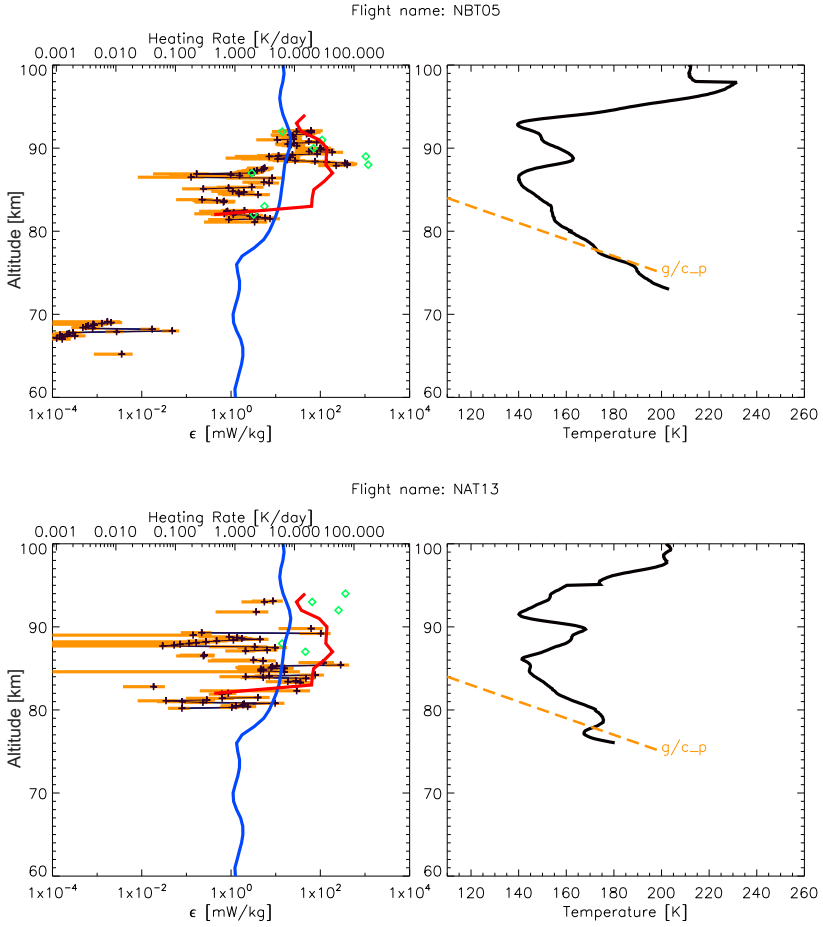

Figure J.3 Individual ε (left column) and temperature (right column) profiles for NBT05 (upper row) and NAT13 (lower row) flights. In the left panels with black crosses connected with black lines ε-values are given, with ε_{ERR} given as orange bars. As green rectangles ε-values obtained by *Lübken et al.* (2002) are shown for comparison. As blue and red lines mean ε profiles for winter (*Lübken*, 1997) and summer (*Lübken et al.*, 2002) are given respectively. In the right panels temperature profiles are given as black lines, with adiabatic lapse rate (orange dashed lines) given for comparison.

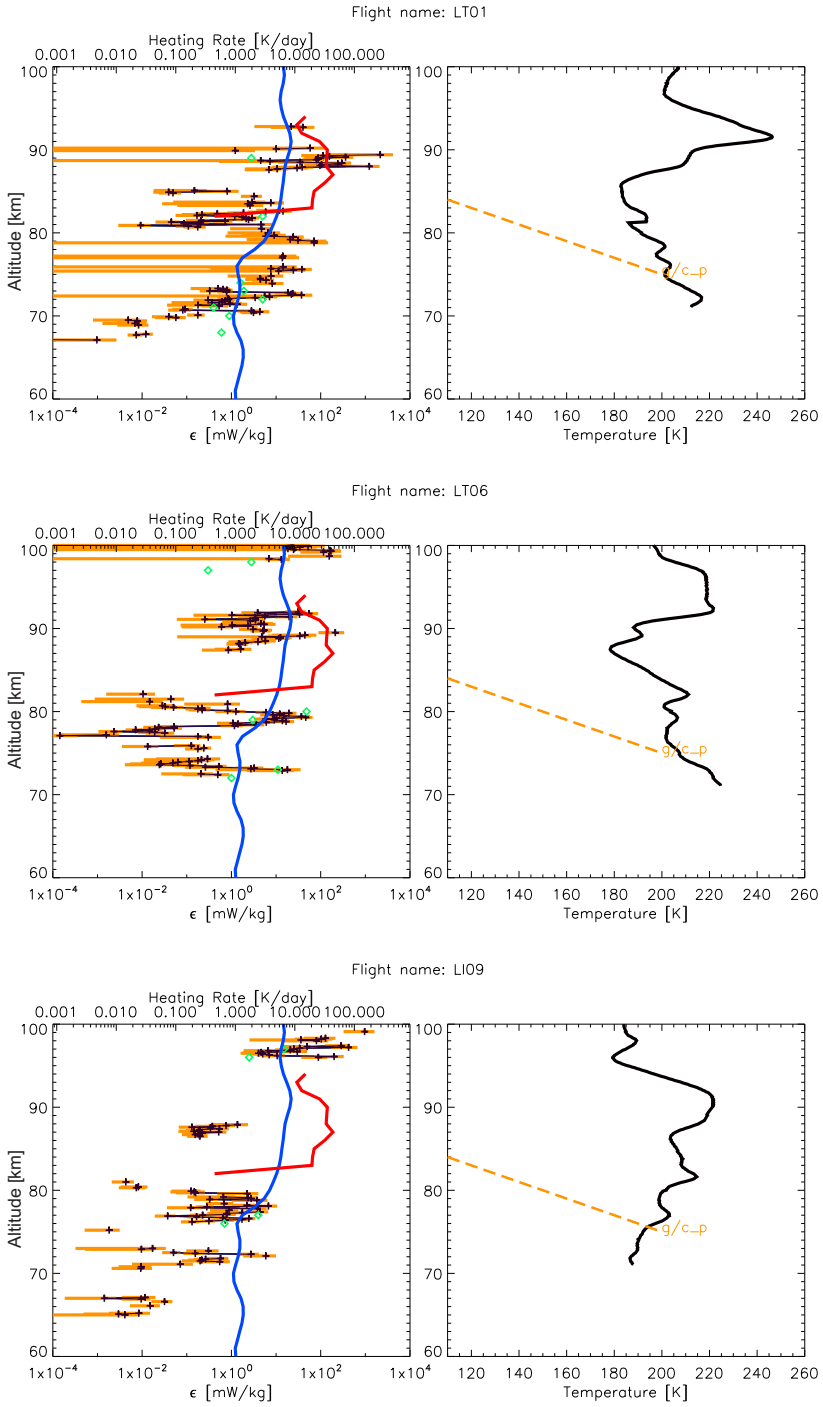

Figure J.4 Individual ε (left column) and temperature (right column) profiles for LT-01 (upper row), LT-06 (middle row) and LI-09 (lower row) flights. In the left panels with black crosses connected with black lines ε-values are given, with ε_{ERR} given as orange bars. As green rectangles ε-values obtained by *Lübken* (1997) are shown for comparison. As blue and red lines mean ε profiles for winter (*Lübken*, 1997) and summer (*Lübken et al.*, 2002) are given respectively. In the right panels temperature profiles are given as black lines, with adiabatic lapse rate (orange dashed lines) given for comparison.

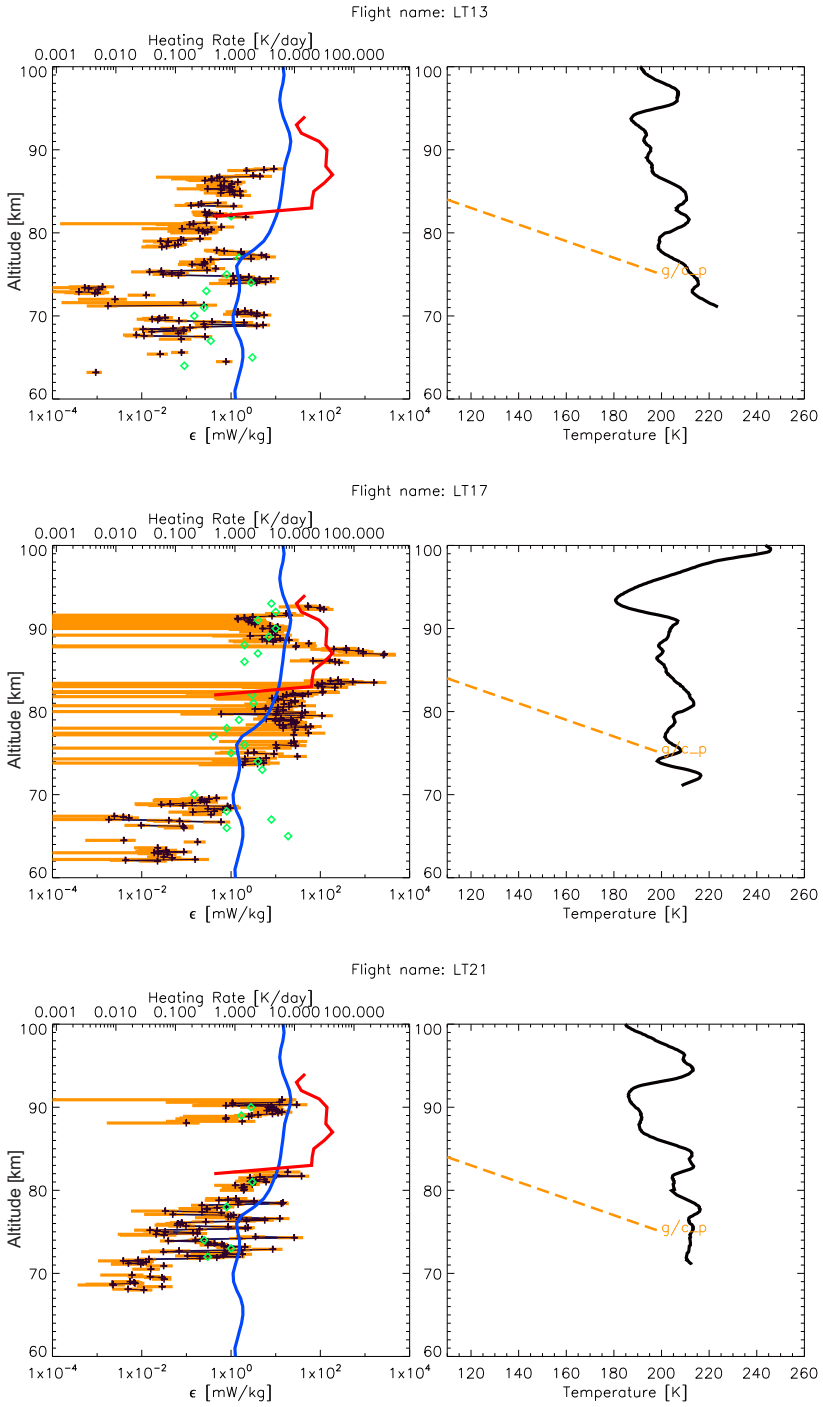

Figure J.5 Individual ε (left column) and temperature (right column) profiles for LT-13 (upper row), LT-17 (middle row) and LT-21 (lower row) flights. In the left panels with black crosses connected with black lines ε-values are given, with ε_{ERR} given as orange bars. As green rectangles ε-values obtained by *Lübken* (1997) are shown for comparison. As blue and red lines mean ε profiles for winter (*Lübken*, 1997) and summer (*Lübken et al.*, 2002) are given respectively. In the right panels temperature profiles are given as black lines, with adiabatic lapse rate (orange dashed lines) given for comparison.

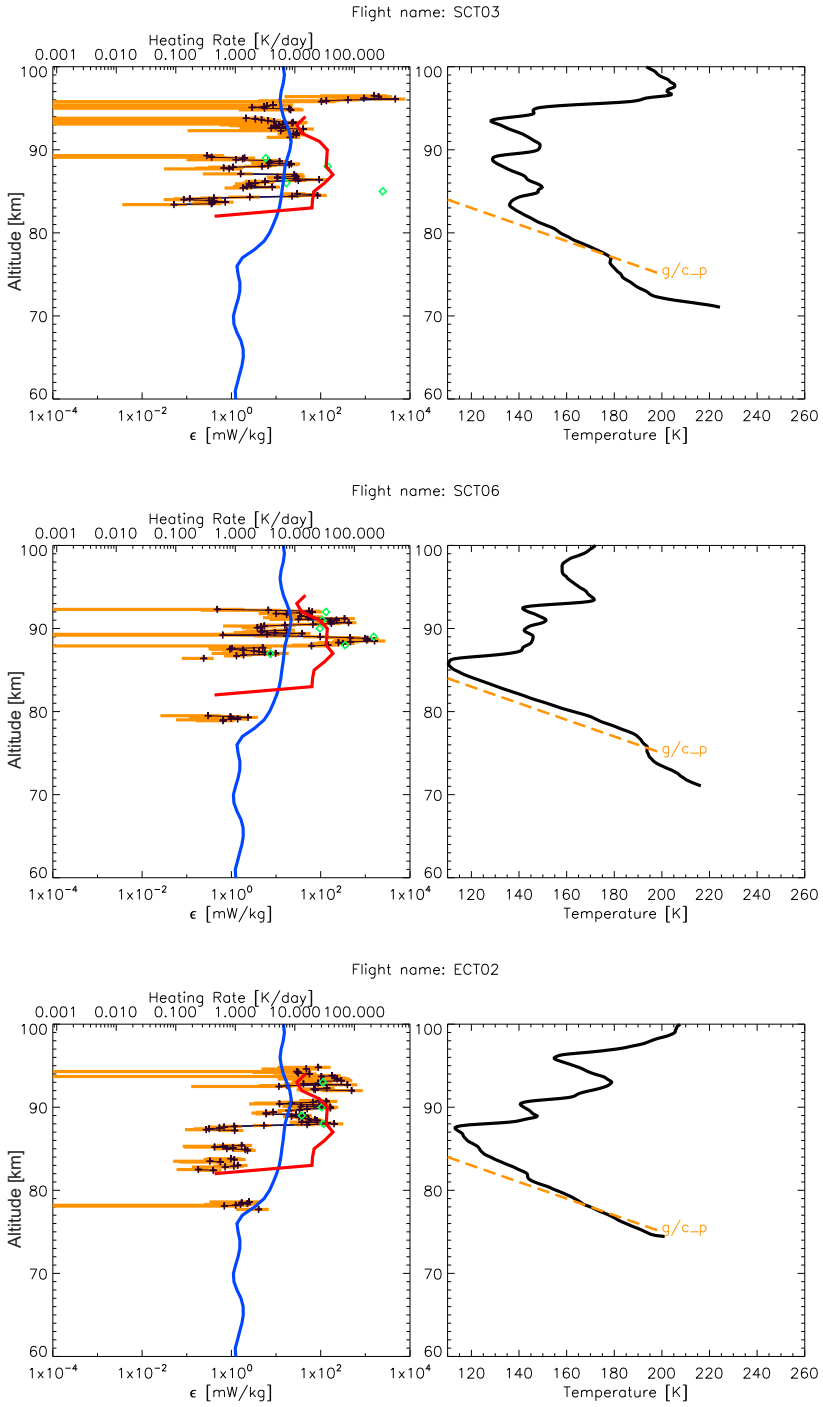

Figure J.6 Individual ε (left column) and temperature (right column) profiles for SCT03 (upper row), SCT06 (middle row) and ECT02 (lower row) flights. In the left panels with black crosses connected with black lines ε-values are given, with ε_{ERR} given as orange bars. As green rectangles ε-values obtained by *Lübken et al.* (2002) are shown for comparison. As blue and red lines mean ε profiles for winter (*Lübken*, 1997) and summer (*Lübken et al.*, 2002) are given respectively. In the right panels temperature profiles are given as black lines, with adiabatic lapse rate (orange dashed lines) given for comparison.

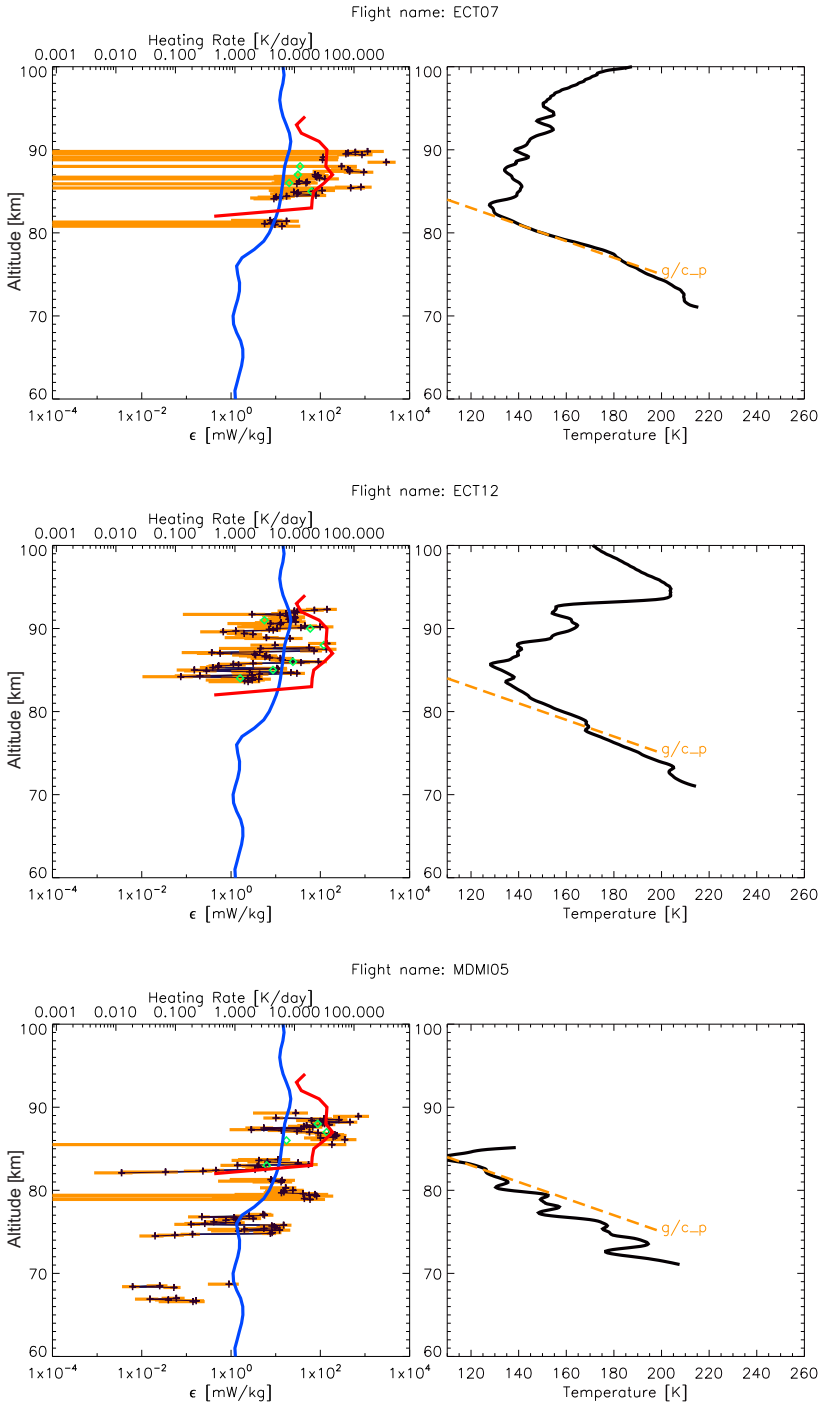

Figure J.7 Individual ε (left column) and temperature (right column) profiles for ECT07 (upper row), ECT12 (middle row) and MDMI05 (lower row) flights. In the left panels with black crosses connected with black lines ε-values are given, with ε_{ERR} given as orange bars. As green rectangles ε-values obtained by *Lübken et al.* (2002) are shown for comparison. As blue and red lines mean ε profiles for winter (*Lübken*, 1997) and summer (*Lübken et al.*, 2002) are given respectively. In the right panels temperature profiles are given as black lines, with adiabatic lapse rate (orange dashed lines) given for comparison.

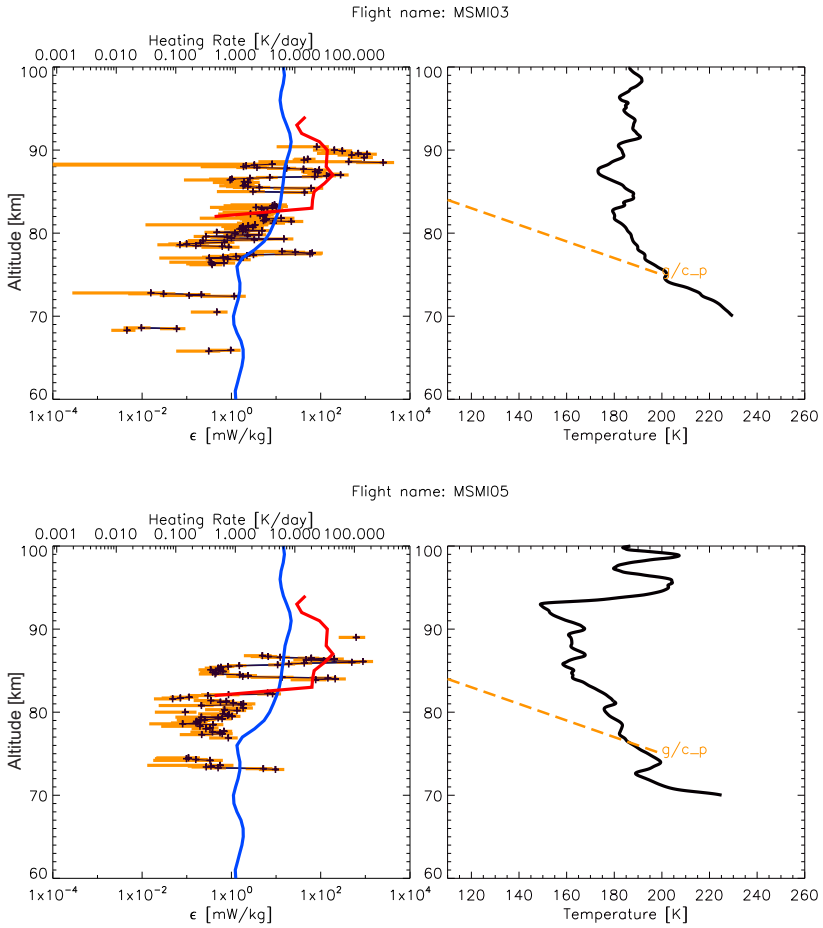

Figure J.8 Individual ε (left column) and temperature (right column) profiles for MSMI03 (upper row) and MSMI05 (lower row) flights. In the left panels with black crosses connected with black lines ε-values are given, with ε_{ERR} given as orange bars. As blue and red lines mean ε profiles for winter (*Lübken*, 1997) and summer (*Lübken et al.*, 2002) are given respectively. In the right panels temperature profiles are given as black lines, with adiabatic lapse rate (orange dashed lines) given for comparison.

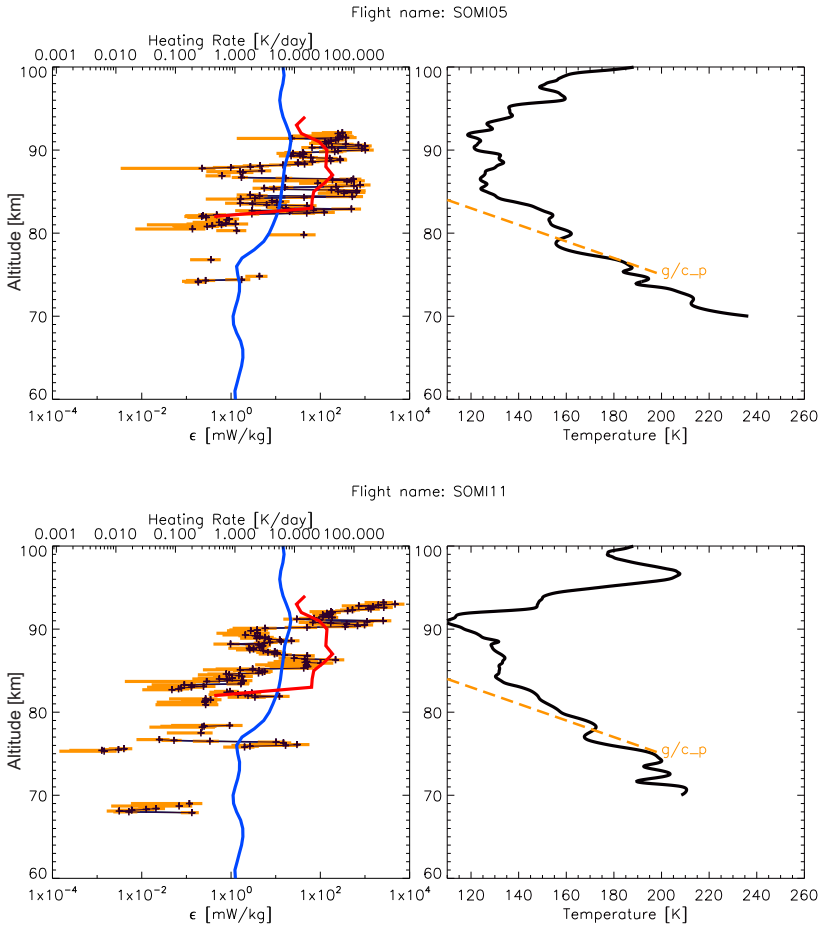

Figure J.9 Individual ε (left column) and temperature (right column) profiles for SOMI05 (upper row) and SOMI11 (lower row) flights. In the left panels with black crosses connected with black lines ε-values are given, with ε_{ERR} given as orange bars. As blue and red lines mean ε profiles for winter (*Lübken*, 1997) and summer (*Lübken et al.*, 2002) are given respectively. In the right panels temperature profiles are given as black lines, with adiabatic lapse rate (orange dashed lines) given for comparison.

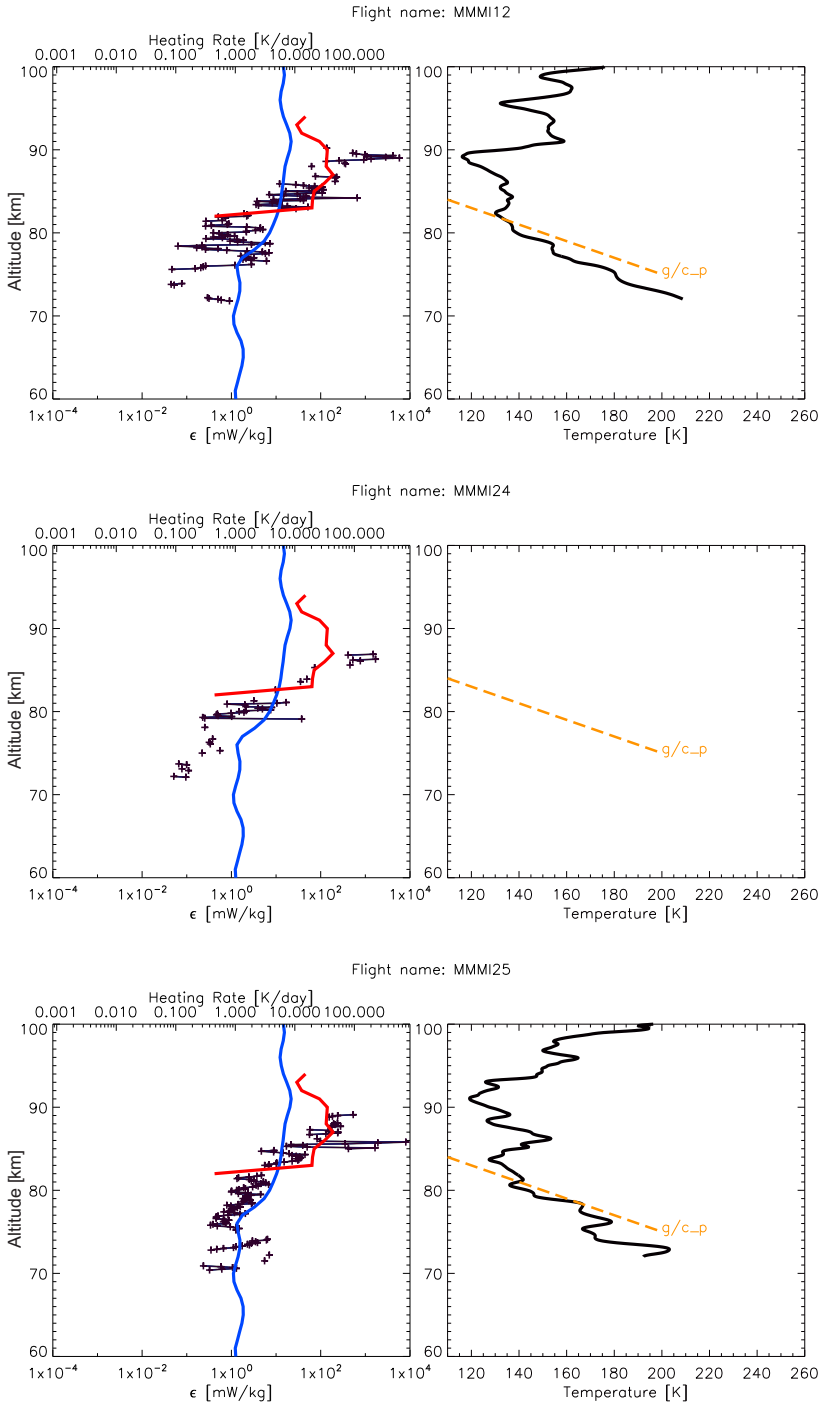

Figure J.10 Individual ε (left column) and temperature (right column) profiles for MMMI12 (upper row), MMMI24 (middle row, no temperature data) and MMMI25 (lower row) flights. In the left panels with black crosses connected with black lines ε-values are given, with ε_{ERR} given as orange bars. As blue and red lines mean ε profiles for winter (*Lübken*, 1997) and summer (*Lübken et al.*, 2002) are given respectively. In the right panels temperature profiles are given as black lines, with adiabatic lapse rate (orange dashed lines) given for comparison.

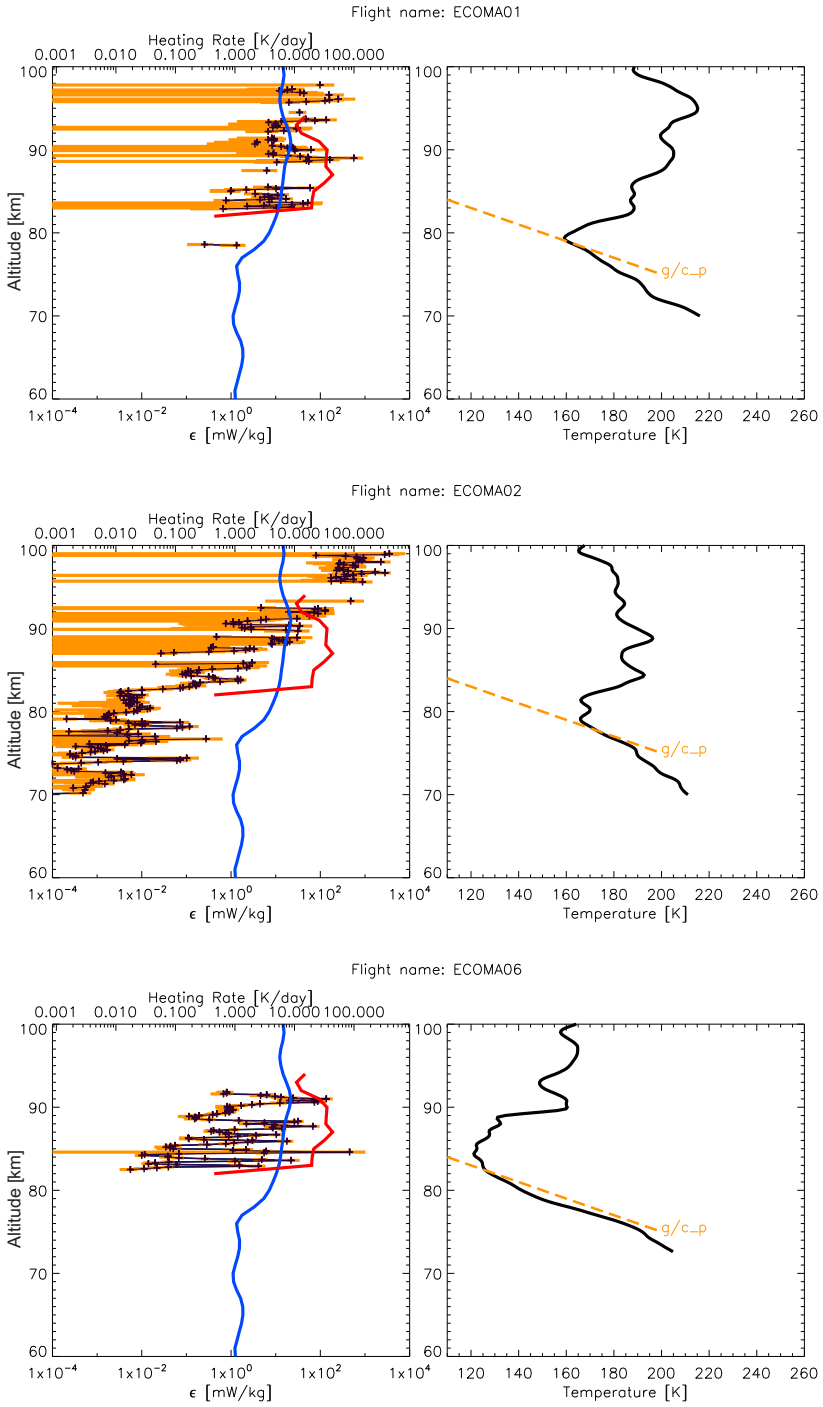

Figure J.11 Individual ε (left column) and temperature (right column) profiles for ECOMA01 (upper row), ECOMA02 (middle row) and ECOMA03 (lower row) flights. In the left panels with black crosses connected with black lines ε-values are given, with ε_{ERR} given as orange bars. As blue and red lines mean ε profiles for winter (*Lübken*, 1997) and summer (*Lübken et al.*, 2002) are given respectively. In the right panels temperature profiles are given as black lines, with adiabatic lapse rate (orange dashed lines) given for comparison.

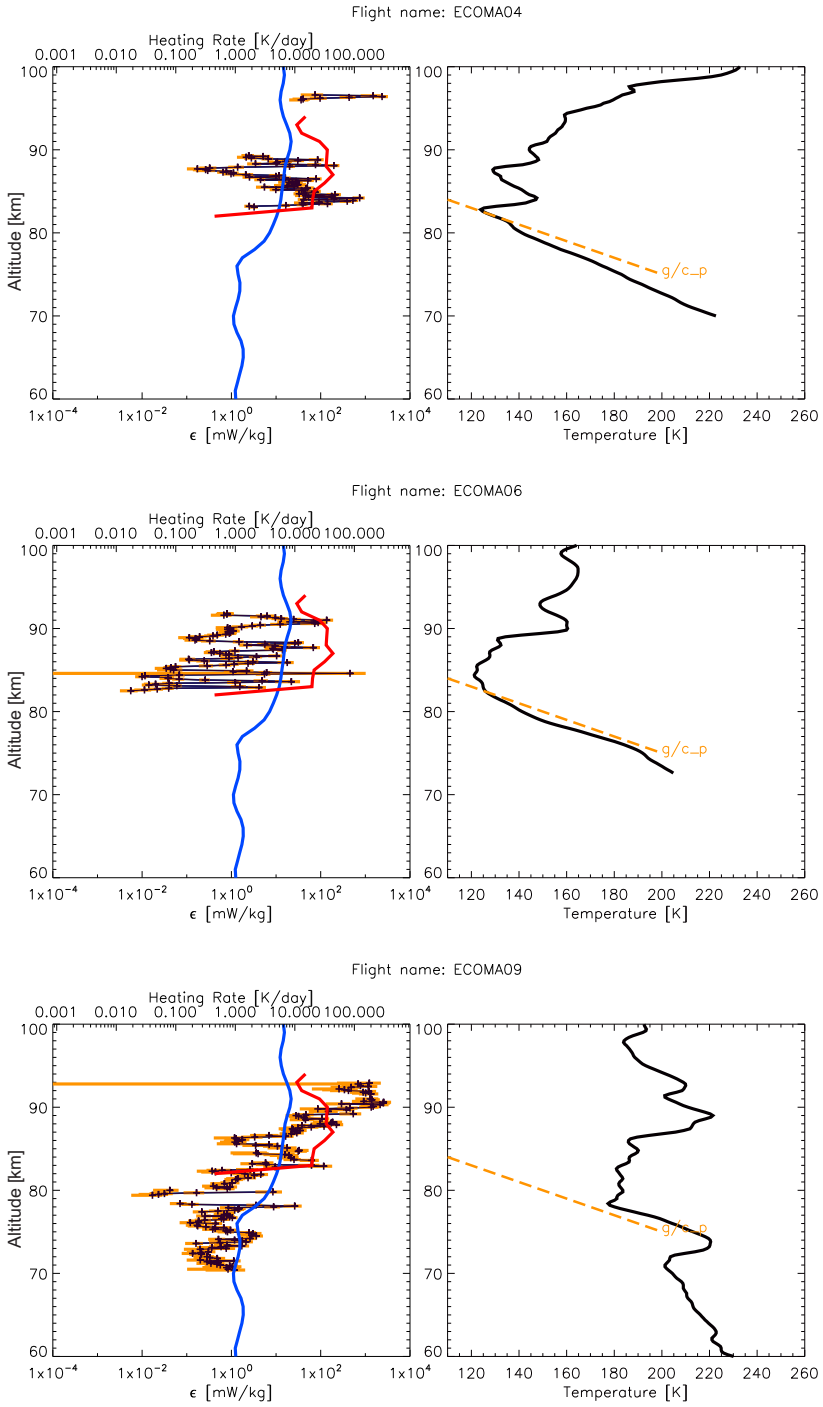

Figure J.12 Individual ε (left column) and temperature (right column) profiles for ECOMA04 (upper row), ECOMA06 (middle row) and ECOMA09 (lower row) flights. In the left panels with black crosses connected with black lines ε-values are given, with ε_{ERR} given as orange bars. As blue and red lines mean ε profiles for winter (*Lübken*, 1997) and summer (*Lübken et al.*, 2002) are given respectively. In the right panels temperature profiles are given as black lines, with adiabatic lapse rate (orange dashed lines) given for comparison.

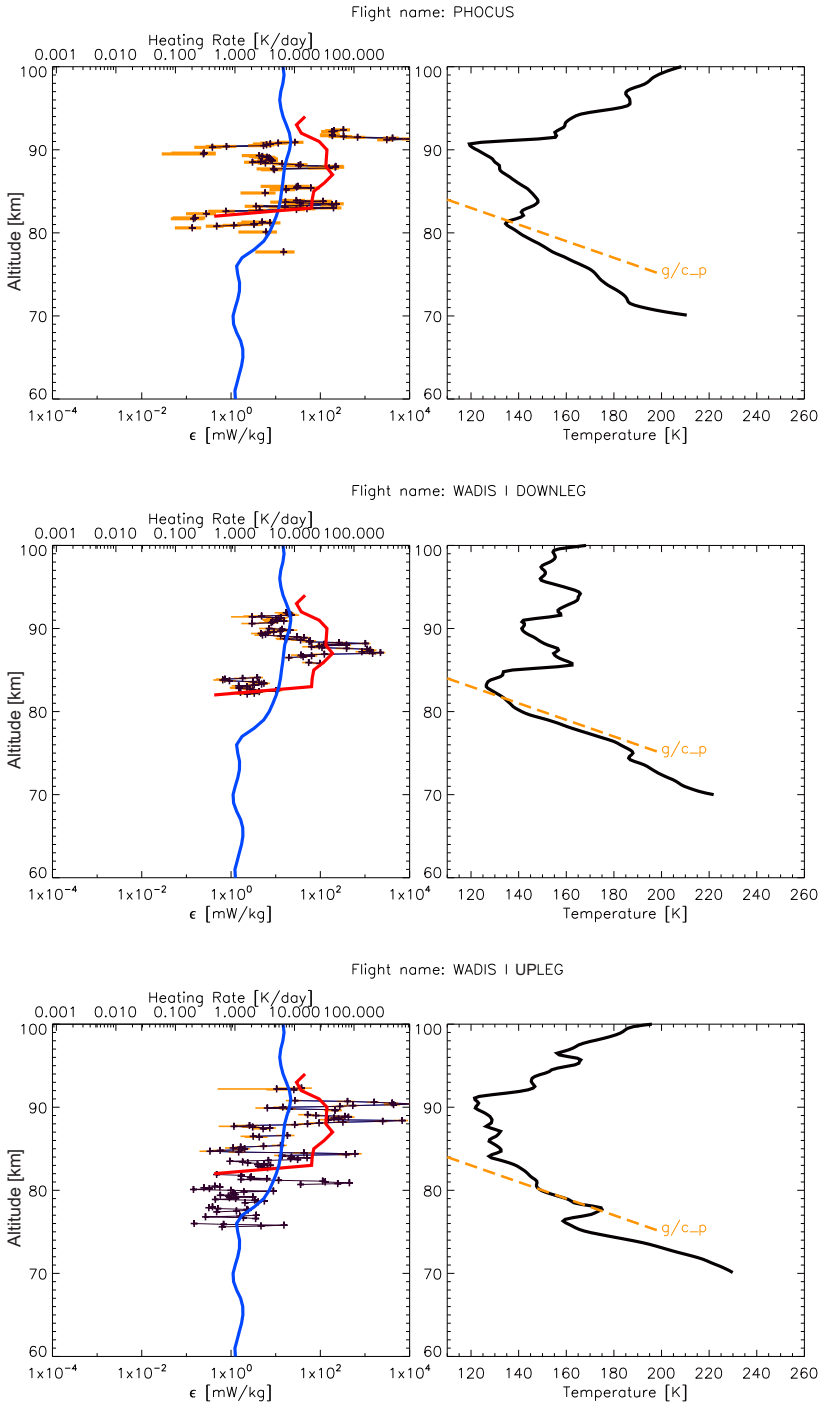

Figure J.13 Individual ε (left column) and temperature (right column) profiles for PHOCUS (upper row) and WADIS1 (downleg - middle row, upleg - lower row) flights. In the left panels with black crosses connected with black lines ε-values are given, with ε_{ERR} given as orange bars. As blue and red lines mean ε profiles for winter (*Lübken*, 1997) and summer (*Lübken et al.*, 2002) are given respectively. In the right panels temperature profiles are given as black lines, with adiabatic lapse rate (orange dashed lines) given for comparison.

Bibliography

Achatz, U., On the role of optimal perturbations in the instability of monochromatic gravity waves, *Phys. Fluids*, *17*(9), 094,107, doi:10.1063/1.2046709, 2005.

Arnold, K. S., and C. Y. She, Metal fluorescence lidar (light detection and ranging) and the middle atmosphere, *Contemporary Physics*, *44*, 35–49, doi:10.1080/00107510302713, 2003.

Batchelor, G. K., *The Theory of Homogeneous Turbulence*, 1953.

Becker, E., Sensitivity of the Upper Mesosphere to the Lorenz Energy Cycle of the Troposphere, *J. Atmos. Sci.*, *66*, 647, doi:10.1175/2008JAS2735.1, 2009.

Becker, E., A. Müllemann, F.-J. Lübken, H. Körnich, P. Hoffmann, and M. Rapp, High Rossby-wave activity in austral winter 2002: Modulation of the general circulation of the MLT during the MaCWAVE/MIDAS northern summer program, *Geophys. Res. Lett.*, *31*, L24S03, doi:10.1029/2004GL019615, 2004.

Belova, E., M. Smirnova, M. T. Rietveld, B. Isham, S. Kirkwood, and T. Sergienko, First observation of the overshoot effect for polar mesosphere winter echoes during radiowave electron temperature modulation, *Geophys. Res. Lett.*, *35*, L03110, doi:10.1029/2007GL032457, 2008.

Blix, T. A., E. V. Thrane, and Ø. Andreassen, In situ measurements of the fine-scale structure and turbulence in the mesosphere and lower thermosphere by means of electrostatic positive ion probes, *J. Geophys. Res.*, *95*, 5533–5548, doi:10.1029/JD095iD05p05533, 1990.

Brown, L. B., A. J. Gerrard, J. W. Meriwether, and J. J. Makela, All-sky imaging observations of mesospheric fronts in OI 557.7 nm and broadband OH airglow emissions: Analysis of frontal structure, atmospheric background conditions, and potential sourcing mechanisms, *J. Geophys. Res.*, *109*, D19104, doi:10.1029/2003JD004223, 2004.

Burchard, H., *Applied turbulence modelling in marine waters, vol. 100 of Lecture Notes in Earth Sciences*, Springer, Berlin, Heidelberg, New York, 2002.

CIRA Working Group, COSPAR International Reference Atmosphere: 0-120 km (1986), *Planetary and Space Science*, *40*, 554–555, doi:10.1016/0032-0633(92)90206-4, 1992.

Collins, R. L., G. A. Lehmacher, M. F. Larsen, and K. Mizutani, Estimates of vertical eddy diffusivity in the upper mesosphere in the presence of a mesospheric inversion layer, *Ann. Geophys.*, *29*, 2019–2029, doi:10.5194/angeo-29-2019-2011, 2011.

Crooks, W. M., Project HICAT an investigation of high altitude clear air tubulence, *Tech. rep.*, Lockheed - California Co Burbank, 1967.

Cutler, L. J., R. L. Collins, K. Mizutani, and T. Itabe, Rayleigh lidar observations of mesospheric inversion layers at Poker Flat, Alaska (65deg N, 147deg W), *Geophys. Res. Lett.*, *28*, 1467–1470, doi:10.1029/2000GL012535, 2001.

Dao, P. D., R. Farley, X. Tao, and C. S. Gardner, Lidar observations of the temperature profile between 25 and 103 km: Evidence of strong tidal perturbation, *Geophys. Res. Lett.*, *22*, doi:10.1029/95GL02950, 1995.

Daubechies, I., *Ten Lectures on Wavelets*, *CBMS-NSF Regional Conference Series in Applied Mathematics*, vol. 61, Society for Industrial and Applied Mathematics, Philadelphia, 1992.

Desaubies, Y., and W. K. Smith, Statistics of Richardson Number and Instability in Oceanic Internal Waves, *Journal of Physical Oceanography*, *12*, 1245–1259, doi:10.1175/1520-0485(1982)012⟨1245:SORNAI⟩2.0.CO;2, 1982.

Dickinson, P. H. G., D. J. MacKinnon, R. Grabowski, H. Wolf, C. Hanuise, J. P. Villain, E. Nielsen, E. V. Thrane, and Ø. Andreassen, Simultaneous observations of E-region irregularities by ground-based and rocket-borne techniques, *J. Atmos. Terr. Phys.*, *47*, 265–281, 1985.

Driscoll, R. J., and L. A. Kennedy, A model for the turbulent energy spectrum, *Phys. Fluids*, *26*, 1228–1233, doi:10.1063/1.864272, 1983.

Duck, T., D. Sipler, J. Salah, and J. Meriwether, Rayleigh lidar observations of a mesospheric inversion layer during night and day, *Geophys. Res. Lett.*, *28*, 3597–3600, 2001.

Duck, T. J., and M. D. Greene, High arctic observations of mesospheric inversion layers, *Geophys. Res. Lett.*, *31*, L02105, doi:10.1029/2003GL018481, 2004.

Dunker, T., U.-P. Hoppe, G. Stober, and M. Rapp, Development of the mesospheric Na layer at 69 °N during the Geminids meteor shower 2010, *Ann. Geophys.*, *31*, 61–73, 2012.

Farge, M., N. K.-R. Kevlahan, V. Perrier, and K. Schneider, Turbulence analysis, modelling and computing using wavelets, in *Wavelets in Physics*, pp. 117–+, 1999.

Fritts, D. C., and M. J. Alexander, Gravity Wave Dynamics in the Middle Atmosphere, *Reviews of Geophysics*, *41*, 2003.

Fritts, D. C., C. Bizon, J. A. Werne, and C. K. Meyer, Layering accompanying turbulence generation due to shear instability and gravity-wave breaking, *J. Geophys. Res.*, *108*, 8452, doi:10.1029/2002JD002406, 2003.

Fritts, D. C., B. P. Williams, C. Y. She, J. D. Vance, M. Rapp, F.-J. Lübken, A. Müllemann, F. J. Schmidlin, and R. A. Goldberg, Observations of extreme temperature and wind gradients near the summer mesopause during the MaCWAVE/MIDAS rocket campaign, *Geophys. Res. Lett.*, *31*, L24S06, doi:10.1029/2003GL019389, 2004.

Fritts, D. C., L. Wang, and J. Werne, Gravity wave-fine structure interactions: A reservoir of small-scale and large-scale turbulence energy, *Geophys. Res. Lett.*, *36*, L19805, doi:10.1029/2009GL039501, 2009a.

Fritts, D. C., L. Wang, J. Werne, T. Lund, and K. Wan, Gravity Wave Instability Dynamics at High Reynolds Numbers. Part I: Wave Field Evolution at Large Amplitudes and High Frequencies, *Journal of Atmospheric Sciences*, pp. 1126–1148, 2009b.

Fritts, D. C., L. Wang, J. Werne, T. Lund, and K. Wan, Gravity Wave Instability Dynamics at High Reynolds Numbers. Part II: Turbulence Evolution, Structure, and Anisotropy, *J. Atmos. Sci.*, *66*, 11491171, 2009c.

Fritts, D. C., L. Wang, and J. Werne, Gravity WaveFine Structure Interactions. Part I: Influences of Fine Structure Form and Orientation on Flow Evolution and Instability, *Journal of Atmospheric Sciences*, *70*, 3710–3734, 2013a.

Fritts, D. C., L. Wang, and J. Werne, Gravity WaveFine Structure Interactions. Part II: Energy Dissipation Evolutions, Statistics, and Implications, *Journal of Atmospheric Sciences*, *70*, 3735–3755, 2013b.

Gan, Q., S. D. Zhang, and F. Yi, TIMED/SABER observations of lower mesospheric inversion layers at low and middle latitudes, *J. Geophys. Res.*, *117*, 2012.

Garcia, R. R., and S. Solomon, The effect of breaking gravity waves on the dynamics and chemical composition of the mesosphere and lower thermosphere, *J. Geophys. Res.*, *20*, 3850–3868, 1985.

Giebeler, J., In-situ Messungen zur Untersuchung der Rolle von Turbulenz bei der Erzeugung von Radarechos in der polaren Mesosphäre im Sommer, Dissertation, Bonn University, BONN-IR-95-28, 1995.

Giebeler, J., F.-J. Lübken, and M. Nägele, CONE - a new sensor for in-situ observations of neutral and plasma density fluctuations, *ESA-SP-355*, 311–318, 1993.

Gille, S. T., A. Hauchecorne, and M.-L. Chanin, Semidiurnal and diurnal tidal effects in the middle atmosphere as seen by Rayleigh lidar, *J. Geophys. Res.*, *96*, 7579–7587, doi: 10.1029/90JD02570, 1991.

Grossmann, A., and J. Morlet, Decomposition of Hardy functions into square integrable wavelets of constant shape, *SIAM Journal on Mathematical Analysis*, *15*(4), 723–736, 1984.

Hall, C. M., T. Aso, and M. Tsutsumi, Atmospheric stability at 90 km, 78^{o}N, 16^{o}E, *Earth, Planets, and Space*, *59*, 157–164, 2007.

Hauchecorne, A., and M.-L. Chanin, Density and temperature profiles obtained by lidar between 35 and 70 km, *Geophys. Res. Lett.*, *7*, 565–568, doi:10.1029/GL007i008p00565, 1980.

Hauchecorne, A., M. L. Chanin, and R. Wilson, Mesospheric temperature inversion and gravity wave breaking, *Geophys. Res. Lett.*, *14*, 933–936, doi:10.1029/GL014i009p00933, 1987.

Hauchecorne, A., M.-L. Chanin, and P. Keckhut, Climatology and trends of the middle atmospheric temperature (33-87 km) as seen by Rayleigh lidar over the south of France, *J. Geophys. Res.*, *96*, 15,297–15,309, doi:10.1029/91JD01213, 1991.

Havnes, O., and M. Kassa, On the sizes and observable effects of dust particles in polar mesospheric winter echoes, *Journal of Geophysical Research (Atmospheres)*, *114*, D09209, doi:10.1029/2008JD011276, 2009.

Havnes, O., C. La Hoz, M. T. Rietveld, M. Kassa, G. Baroni, and A. Biebricher, Dust charging and density conditions deduced from observations of PMWE modulated by artificial electron heating, *Journal of Geophysical Research (Atmospheres)*, *116*(D15), D24203, doi: 10.1029/2011JD016411, 2011.

Heck, W. J., and H. A. Panofsky, Stratospheric mixing estimates from heat flux miasurements, *The Natural Stratosphere of 1974 CIAP Monogr.*, *2*, 6–90 to 6–92, 1975.

Hedin, A. E., Extension of the MSIS thermosphere model into the middle and lower atmosphere, *J. Geophys. Res.*, *96*, 1159–1172, 1991.

Heisenberg, W., Zur statistischen Theorie der Turbulenz, *Zeitschift für Physik*, *124*, 628–657, doi:10.1007/BF01668899, 1948.

Hill, R. J., and S. F. Clifford, Modified spectrum of atmospheric temperature fluctuations and its application to optical propagation, *J. Opt. Soc. America*, *68*, 892–899, 1978.

Hillert, W., F.-J. Lübken, and G. Lehmacher, TOTAL: a rocket-borne instrument for high resolution measurements of neutral air turbulence during DYANA, *J. Atmos. Terr. Phys.*, *56*, 1835–1852, doi:10.1016/0021-9169(94)90013-2, 1994.

Hocking, W. K., The effects of middle atmosphere turbulence on coupling between atmospheric regions, *Journal of Geomagnetism and Geoelectricity*, *44*, 621–636, 1991.

Hocking, W. K., *Small scale dynamics of the upper atmosphere: experimental studies of gravity waves and turbulence*, 51-96 pp., Springer-Verlag, Berlin, Heidelberg, New York, 1996.

Hocking, W. K., The dynamical parameters of turbulence theory as they apply to middle atmosphere studies, *Earth, Planets, and Space*, *51*, 525–541, 1999.

Hocking, W. K., A review of Mesosphere-Stratosphere-Troposphere (MST) radar developments and studies, circa 1997-2008, *J. Atmos. Solar-Terr. Phys.*, *73*, 848–882, doi: 10.1016/j.jastp.2010.12.009, 2011.

Hoffmann, P., M. Rapp, J. Fiedler, and R. Latteck, Influence of tides and gravity waves on layering processes in the polar summer mesopause region, *Ann. Geophys.*, *26*, 4013–4022, doi:10.5194/angeo-26-4013-2008, 2008.

Holschneider, M., Localization properties of wavelet transforms, *Journal of Mathematical Physics*, *34*, 3227–3244, doi:10.1063/1.530073, 1993.

Holton, J. R., The Influence of Gravity Wave Breaking on the General Circulation of the Middle Atmosphere., *J. Atmos. Sci.*, *40*, 2497–2507, doi:10.1175/1520-0469(1983)040⟨2497:TIOGWB⟩2.0.CO;2, 1983.

Holton, J. R., *An introduction to dynamic meteorology*, Academic Press, 1992.

Hultgren, K., H. Körnich, J. Gumbel, M. Gerding, P. Hoffmann, S. Lossow, and L. Megner, What caused the exceptional mid-latitudinal noctilucent cloud event in July 2009, *J. Atmos. Solar-Terr. Phys.*, doi:10.1016/j.jastp.2010.12.008, in press, 2011.

Kavanagh, A. J., F. Honary, M. T. Rietveld, and A. Senior, First observations of the artificial modulation of polar mesospheric winter echoes, *Geophys. Res. Lett.*, *33*, L19801, doi: 10.1029/2006GL027565, 2006.

Kero, A., C.-F. Enell, A. J. Kavanagh, J. Vierinen, I. Virtanen, and E. Turunen, Could negative ion production explain the polar mesosphere winter echo (PMWE) modulation in active HF heating experiments?, *Geophys. Res. Lett.*, *35*, L23102, doi:10.1029/2008GL035798, 2008.

Kolmogorov, A., The Local Structure of Turbulence in Incompressible Viscous Fluid for Very Large Reynolds' Numbers, *Akademiia Nauk SSSR Doklady*, *30*, 301–305, 1941.

Kumar, P., and E. Foufoula-Georgiou, Wavelet analysis for geophysical applications, *35*, 385–412, doi:10.1029/97RG00427, 1997.

La Hoz, C., and O. Havnes, Artificial modification of polar mesospheric winter echoes with an RF heater: Do charged dust particles play an active role?, *J. Geophys. Res.*, *113*, D19205, doi:10.1029/2008JD010460, 2008.

Landau, L. D., E. M. Lifshitz, J. B. Sykes, W. H. Reid, and H. Feshbach, Fluid Mechanics, *14*, 62, doi:10.1063/1.3057567, 1961.

Leblanc, T., and A. Hauchecorne, Recent observations of mesospheric temperature inversions, *J. Geophys. Res.*, *102*, 19,471, doi:10.1029/97JD01445, 1997.

Lehmacher, G., and F.-J. Lübken, Simultaneous observation of convective adjustment and turbulence generation in the mesosphere, *Geophys. Res. Lett.*, *22*, 2477–2480, doi:10.1029/95GL02351, 1995.

Lehmacher, G. A., C. L. Croskey, J. D. Mitchell, M. Friedrich, F.-J. Lübken, M. Rapp, E. Kudeki, and D. C. Fritts, Intense turbulence observed above a mesospheric temperature inversion at equatorial latitude, *Geophys. Res. Lett.*, *33*, L08808, doi:10.1029/2005GL024345, 2006.

Lewalle, J., Tutorial on continuous wavelet analysis of experimental data, Syracuse University, 1995.

Lewalle, J., M. Farge, and K. Schneider, *Wavelet Transforms. Section D 1.6.*, Springer-Verlag, 2005.

Lindzen, R. S., Turbulence and stress owing to gravity wave and tidal breakdown, *J. Geophys. Res.*, *86*, 9707–9714, doi:10.1029/JC086iC10p09707, 1981.

Liu, A. Z., R. G. Roble, J. H. Hecht, M. F. Larsen, , and C. S.Gardner, Unstable layers in the mesopause region observed with na lidar during the turbulent oxygen mixing experiment (tomex) campaign, *J. Geophys. Res.*, *109*, doi:10.1029/2002JD003056, 2004.

Liu, H.-L., M. E. Hagan, and R. G. Roble, Local mean state changes due to gravity wave breaking modulated by the diurnal tide, *J. Geophys. Res.*, *105*, 12,381–12,396, doi:10.1029/1999JD901163, 2000.

Livesey, J. N., W. G. Read, A. Lambert, R. E. Cofield, D. T. Cuddy, L. Froidevaux, R. A. Fuller, R. F. Jarnot, J. H. Jiang, Y. B. Jiang, B. W. Knosp, L. J. Kovalenko, H. M. Pickett, H. C. Pumphrey, M. L. Santee, M. J. Schwartz, P. C. Stek, P. A. Wagner, J. W. Waters, and D. L. Wu, Earth Observing System (EOS). Aura Microwave Limb Sounder (MLS). Version 2.2 Level 2 data quality and desription document, 2007.

Lübken, F.-J., On the extraction of turbulent parameters from atmospheric density fluctuations, *J. Geophys. Res.*, *97*, 20,385, doi:10.1029/92JD01916, 1992.

Lübken, F.-J., Experimental results on the role of turbulence for the heat budget of the upper atmosphere, Habilitation, Bonn University, BONN-IR-93-51, 1993.

Lübken, F.-J., Seasonal variation of turbulent energy dissipation rates at high latitudes as determined by in-situ measurements of neutral density fluctuations, *J. Geophys. Res.*, *102*, 13,441–13,456, 1997.

Lübken, F.-J., Thermal structure of the Arctic summer mesosphere, *J. Geophys. Res.*, *104*, 9135–9149, doi:10.1029/1999JD900076, 1999.

Lübken, F.-J., U. von Zahn, E. V. Thrane, T. Blix, G. A. Kokin, and S. V. Pachomov, In situ measurements of turbulent energy dissipation rates and eddy diffusion coefficients during MAP/WINE, *J. Atmos. Terr. Phys.*, *49*, 763–775, doi:10.1016/0021-9169(87)90018-3, 1987.

Lübken, F.-J., W. Hillert, G. Lehmacher, and U. von Zahn, Experiments revealing small impact of turbulence on the energy budget of the mesosphere and lower thermosphere, *J. Geophys. Res.*, *98*, 20,369, doi:10.1029/93JD02055, 1993.

Lübken, F.-J., K.-H. Fricke, and M. Langer, Noctilucent clouds and the thermal structure near the Arctic mesopause in summer, *J. Geophys. Res.*, *101*, 9489–9508, doi:10.1029/96JD00444, 1996.

Lübken, F.-J., M. Rapp, and P. Hoffmann, Neutral air turbulence and temperatures in the vicinity of polar mesosphere summer echoes, *J. Geophys. Res.*, *107(D15)*, 4273–4277, doi:10.1029/2001JD000\,915, 2002.

Lübken, F.-J., B. Strelnikov, M. Rapp, W. Singer, R. Latteck, A. Brattli, U.-P. Hoppe, and M. Friedrich, The thermal and dynamical state of the atmosphere during polar mesosphere winter echoes, *6*, 13–24, 2006.

Lumley, J. L., The Spectrum of Nearly Inertial Turbulence in a Stably Stratified Fluid, *J. Atmos. Sci.*, *21*, 99–102, doi:10.1175/1520-0469(1964)021⟨0099:TSONIT⟩2.0.CO;2, 1964.

Matsuno, T., A quasi one-dimensional model of the middle atmosphere circulation interacting with internal gravity waves, *J. Meteorol. Soc. Jpn.*, *60*, 215 – 226, 1982.

Meriwether, J. W., and C. Gardner, A review of the mesosphere inversion layer phenomenon, *J. Geophys. Res.*, *105*(12), 405 – 416, 2000.

Meriwether, J. W., and A. J. Gerrard, Mesosphere inversion layers and stratosphere temperature enhancements, *42*, RG3003, doi:10.1029/2003RG000133, 2004.

Müllemann, A., M. Rapp, and F.-J. Lübken, Morphology of turbulence in the polar summer mesopause region during the MIDAS/SOLSTICE campaign 2001, *31*, 2069–2074, doi:10.1016/S0273-1177(03)00230-8, 2003.

Nastrom, G. D., Doppler radar spectral width broadening due to beamwidth and wind shear, *Ann. Geophys.*, *15*, 786–796, doi:10.1007/s00585-997-0786-7, 1997.

Nastrom, G. D., and F. D. Eaton, Turbulence eddy dissipation rates from radar observations at 5-20 km at White Sands Missile Range, New Mexico, *J. Geophys. Res.*, *102*, 19,495, doi:10.1029/97JD01262, 1997.

Nastrom, G. D., and T. Tsuda, Anisotropy of Doppler spectral parameters in the VHF radar observations at MU and White Sands, *Ann. Geophys.*, *19*, 883–888, doi:10.5194/angeo-19-883-2001, 2001.

Novikov, E. A., The energy spectrum of incompressible turbulent flow, *Akademiia Nauk SSSR Doklady*, *139*, 331–334, 1961.

Ramesh, K., S. Sridharan, K. Raghunath, S. Vijaya Bhaskara Rao, and Y. Bhavani Kumar, Planetary wave-gravity wave interactions during mesospheric inversion layer events, *Journal of Geophysical Research (Space Physics)*, *118*, 4503–4515, doi:10.1002/jgra.50379, 2013.

Ramesh, K., S. Sridharan, and S. Vijaya Bhaskara Rao, Causative mechanisms for the occurrence of a triple layered mesospheric inversion event over low latitudes, *Journal of Geophysical Research (Space Physics)*, *119*, 3930–3943, doi:10.1002/2013JA019750, 2014.

Rapp, M., Aerosol layers in the polar summer mesosphere: Interaction with the plasma of the d-region and dependence on temperature and dynamics, Dissertation, 1999.

Rapp, M., Mesospheric aerosol particles studied with in-situ techniques: an overview from the ECOMA project, in *IAGA 11th Scientific Assembly*, Sopron, Hungary, 2009.

Rapp, M., and F.-J. Lübken, Polar mesosphere summer echoes (PMSE): Review of observations and current understanding, *4*, 2601–2633, 2004.

Rapp, M., J. Gumbel, and F.-J. Lübken, Absolute density measurements in the middle atmosphere, *Ann. Geophys.*, *19*, 571–580, 2001.

Rapp, M., F.-J. Lübken, A. Müllemann, G. E. Thomas, and E. J. Jensen, Small scale temperature variations in the vicinity of NLC: Experimental and model results, *J. Geophys. Res.*, *107(D19)*, doi: 10.1029/2001JD001,241, 2002.

Rapp, M., B. Strelnikov, A. Müllemann, F.-J. Lübken, and D. C. Fritts, Turbulence measurements and implications for gravity wave dissipation during the MaCWAVE/MIDAS rocket program, *Geophys. Res. Lett.*, *31*, L24S07, doi:10.1029/2003GL019325, 2004.

Rapp, M., E. Becker, B. Strelnikov, and F.-J. Lübken, The latitude dependence and probability distribution of polar mesospheric turbulence, *Atmospheric Chemistry & Physics Discussions*, *6*, 12,199–12,216, 2006.

Rapp, M., R. Latteck, G. Stober, P. Hoffmann, W. Singer, and M. Zecha, First three-dimensional observations of polar mesosphere winter echoes: Resolving space-time ambiguity, *J. Geophys. Res.*, *116*, A11307, doi:10.1029/2011JA016858, 2011.

Roble, R. G., On the feasibility of developing a global atmospheric model extending from the ground to the exosphere, *Washington DC American Geophysical Union Geophysical Monograph Series*, *123*, 53–67, doi:10.1029/GM123p0053, 2000.

Sassi, F., R. R. Garcia, B. A. Boville, and H. Liu, On temperature inversions and the mesospheric surf zone, *J. Geophys. Res.*, *107*, 4380, doi:10.1029/2001JD001525, 2002.

Schmidlin, F. J., Temperature inversions near 75 km, *Geophys. Res. Lett.*, *3*, 173–176, doi:10.1029/GL003i003p00173, 1976.

Schmidlin, F. J., Derivation and application of temperature corrections for the United States radiosonde, in *Symposium on Meteorological Observations and Instrumentations, 7th, New Orleans, LA, Jan. 14-18, 1991, Preprints (A92-32051 12-47). Boston, MA, American Meteorological Society, 1991, p. 227-231.*, pp. 227–231, 1991.

Schöch, A., G. Baumgarten, and J. Fiedler, Polar middle atmosphere temperature climatology from Rayleigh lidar measurements at ALOMAR (69° N), *Ann. Geophys.*, *26*(7), 1681–1698, 2008.

She, C. Y., J. D. Vance, B. P. Williams, D. A. Krueger, H. Moosmuller, D. Gibson-Wilde, and D. Fritts, Lidar studies of atmospheric dynamics near polar mesopause, *EOS Transactions*, *83*, 289–, doi:10.1029/2002EO000206, 2002.

Shur, G. H., Experimantal studies of the energy spectrum of atmospheric turbulence, *Tr. Tsent. Aerol. Observ.*, *43*, 79–90, 1962.

Singer, W., R. Latteck, D. A. Holdsworth, and T. Kristiansen, A new narrow beam MF radar at 3 MHz for studies of the high-latitude middle atmosphere: System description and first results.

Singer, W., R. Latteck, and D. A. Holdsworth, A new narrow beam Doppler radar at 3 MHz for studies of the high-latitude middle atmosphere, *Advances in Space Research*, *41*, 1488–1494, doi:10.1016/j.asr.2007.10.006, 2008.

Singer, W., R. Latteck, M. Friedrich, M. Wakabayashi, and M. Rapp, Seasonal and solar activity variability of D-region electron density at 69°N, *J. Atmos. Solar-Terr. Phys.*, *73*, 925–935, doi:10.1016/j.jastp.2010.09.012, 2011.

Siva Kumar, V., Y. Bhavani Kumar, K. Raghunath, P. B. Rao, M. Krishnaiah, K. Mizutani, T. Aoki, M. Yasui, and T. Itabe, Lidar measurements of mesospheric temperature inversion at a low latitude, *Ann. Geophys.*, *19*, 1039–1044, doi:10.5194/angeo-19-1039-2001, 2001.

Sridharan, S., M. Suresh, and K. Ramesh, VHF radar observations of mesospheric echoes and their relationship with thermal structure over Gadanki (13.5^{o}N, 79.2^{o}E), *Indian Journal of Radio and Space Physics*, *42*, 364–370, 2013.

States, R. J., and C. S. Gardner, Thermal Structure of the Mesopause Region (80 - 105 km) at 40^{o}N Latitude. Part I: Seasonal Variations, *Journal of Atmospheric Sciences*, *57*, 66–77, doi:10.1175/1520-0469(2000)057⟨0066:TSOTMR⟩2.0.CO;2, 2000.

Stebel, K., U. Blum, K.-H. Fricke, S. Kirkwood, N. J. Mitchell, and A. Osepian, Joint radar/lidar observations of possible aerosol layers in the winter mesosphere, *Journal of Atmospheric and Solar-Terrestrial Physics*, *66*, 957–970, doi:10.1016/j.jastp.2004.03.008, 2004.

Stevens, M. H., D. E. Siskind, S. D. Eckermann, L. Coy, J. P. McCormack, C. R. Englert, K. W. Hoppel, K. Nielsen, A. J. Kochenash, M. E. Hervig, C. E. Randall, J. Lumpe, S. M. Bailey, M. Rapp, and P. Hoffmann, Tidally induced variations of polar mesospheric cloud altitudes and ice water content using a data assimilation system, *J. Geophys. Res.*, *115*, D18209, doi:10.1029/2009JD013225, 2010.

Stober, G., R. Latteck, M. Rapp, W. Singer, and M. Zecha, MAARSY - the new MST radar on Andøya: first results of spaced antenna and Doppler measurements of atmospheric winds in the troposphere and mesosphere using a partial array, *Advances in Radio Science*, *10*, 291–298, doi:10.5194/ars-10-291-2012, 2012.

Strelnikov, B., In situ measurements of small scale neutral and plasma dynamics in the mesosphere/lower thermosphere region, Dissertation, Rostock University, 2006.

Strelnikov, B., M. Rapp, and F.-J. Lübken, A new technique for the analysis of neutral air density fluctuations measured in situ in the middle atmosphere, *Geophys. Res. Lett.*, *30*, 2052, doi:10.1029/2003GL018,271, 2003.

Strelnikov, B., M. Rapp, and F.-J. Lübken, *An introduction to space instrumentation*, chap. In situ density measurements in the mesosphere/lower thermosphere region with TOTAL and CONE instruments, Terra Publishers, Tokyo, 2013.

Sweldens, W., and P. Schröder, Building your own wavelets at home, in *Wavelets in Computer Graphics*, pp. 15–87, ACM SIGGRAPH Course notes, 1996.

Szewczyk, A., B. Strelnikov, M. Rapp, I. Strelnikova, G. Baumgarten, N. Kaifler, T. Dunker, and U.-P. Hoppe, Simultaneous observations of a Mesospheric Inversion Layer and turbulence during the ECOMA-2010 rocket campaign, *Ann. Geophys.*, *31*, 775–785, doi: 10.5194/angeo-31-775-2013, 2013.

Tatarskii, V. I., *The effects of the turbulent atmosphere on wave propagation*, 1971.

Thomas, L., A. Marsh, D. Wareing, I. Astin, and H. Chandra, VHF echoes from the midlatitude mesosphere and the thermal structure observed by lidar, *J. Geophys. Res.*, *101*(12), 867–878, 1996.

Torrence, C., and G. P. Compo, A practical guide to wavelet analysis, *Bullettin of the American Meteorologic Society*, *79*, 61–78, 1998.

Van Zandt, T. E., and D. C. Fritts, A theory of enhanced saturation of the gravity wave spectrum due to increases in atmospheric stability, *Pure and Applied Geophysics*, *130*, 399, 1989.

von Weizsäcker, C., Das Spektrum der Turbulenz bei grossen Reynoldsschen Zahlen, *Zeitschift für Physik*, *12*, 614–627, 1948.

von Zahn, U., G. von Cossart, J. Fiedler, K. H. Fricke, G. Nelke, G. Baumgarten, D. Rees, A. Hauchecorne, and K. Adolfsen, The ALOMAR Rayleigh/Mie/Raman lidar: objectives, configuration, and performance, *Ann. Geophys.*, *18*, 815–833, doi:10.1007/s005850000210, 2000.

Waters, J. W., Microwave limb sounding, *Atmospheric Remote Sensing by Microwave Radiometry*, 1993.

Weinstock, J., Vertical turbulent diffusion in a stably stratified fluid, *J. Atmos. Sci.*, *35*, 1022–1027, 1978.

Weinstock, J., Analytical approximations in the theory of turbulent diffusion, *Phys. Fluids*, *21*, 887–890, doi:10.1063/1.862328, 1978.

Weinstock, J., Energy dissipation rates of turbulence in the stable free atmosphere, *J. Atmos. Sci.*, *38*, 880–883, 1981.

Whiteway, J. A., A. I. Carswell, and W. E. Ward, Mesospheric temperature inversions with overlying nearly adiabatic lapse rate: An indication of a well-mixed turbulent layer, *Geophys. Res. Lett.*, *22*, 1201–1204, doi:10.1029/95GL01109, 1995.

Wolberg, J., *Data Analysis Using the Method of Least Squares. Extracting the Most Information from Experiments*, 2006.

Woods, J. D., On Richardson's Number as a Criterion for Laminar-Turbulent-Laminar Transition in the Ocean and Atmosphere, *4*, 1289–1298, doi:10.1029/RS004i012p01289, 1969.

Wu, D., W. Read, Z. Shippony, T. Leblanc, T. Duck, D. Ortland, R. Sica, P. Argall, J. Oberheide, A. Hauchecorne, P. K. C. She, and D. Krueger, Mesospheric temperature from uars mls: retrieval and validation, *J. Atmos. Solar-Terr. Phys.*, *65*, 2003.

Zimmerman, S. P., and N. V. Loving, Turbulent dissipation and diffusivities in the stratosphere using richardson's technique, *The Natural Stratosphere of 1974 CIAP Monogr.*, *2*, 6–93 to 6–103, 1975.

Selbständigkeitserklärung

Hiermit versichere ich an Eides statt, die vorliegende Arbeit selbständig und ohne fremde Hilfe verfasst, keine außer den von mir angegebenen Quellen und Hilfsmitteln verwandt und die den genutzten Werken inhaltlich oder wörtlich entnommenen Stellen als solche kenntlich gemacht zu haben.

Kühlungsborn, den 25. Juni 2015

(Artur Szewczyk)

Declaration

I hereby declare that this dissertation is the result of my own work and includes nothing which is the outcome of work done in collaboration except where specifically indicated in the text and bibliography.

Kühlungsborn, 25. Juni 2015

(Artur Szewczyk)

I would like to gratefully and sincerely thank to Prof. Dr. Markus Rapp and Prof. Dr. Franz-Josef Lübken for allowing me to work on presented topic in the IAP.

I would like to thank Prof. Gerald Lehmacher for his review of our MIL-paper.

I would like to thank my colleagues from the rocket group, Hans-Jürgen Heckl, Heiner Asmus and Tristan Staszak, and all the colleagues from IAP for really nice time I had in the institute. Also I would like to thank DLR-MORABA team and ASC team for the nice time we had during our rocket campaigns.

I would like to specially thank Dr. Boris Strelnikov for his great support and even greater patience for me during my stay at IAP.

Finally I would like to thanks to my parents, my family and my friends.